Magnesium and Calcium Carbonate Precipitation in Serpentinite-Hosted Alkaline Environments

Natural and Experimental Constraints

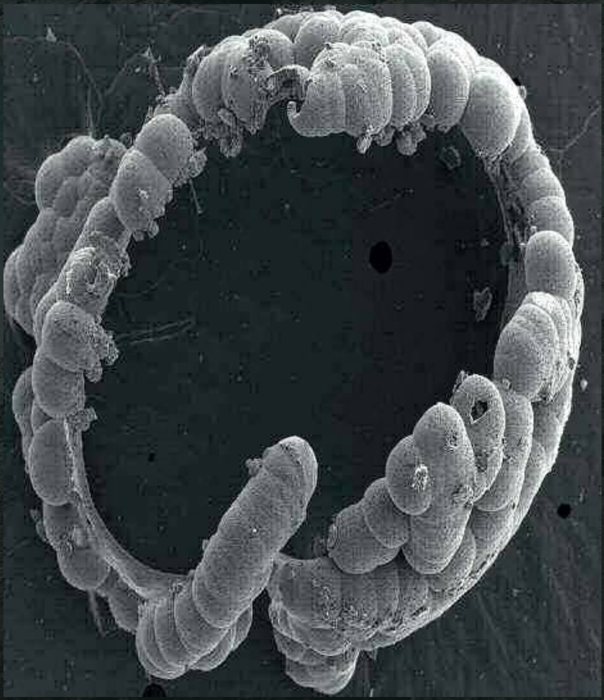

Emmanouil Giampouras

CSIC

IACT
INSTITUTO ANDALUZ DE CIENCIAS DE LA TIERRA

UNIVERSIDAD
DE GRANADA

Programa Doctorado
Ciencias de la Tierra

Tesis Doctoral 2020

CSIC

IACT
Instituto Andaluz de Ciencias de la Tierra

UNIVERSIDAD
DE GRANADA

MAGNESIUM AND CALCIUM CARBONATE PRECIPITATION IN SERPENTINITE-HOSTED ALKALINE ENVIRONMENTS

NATURAL AND EXPERIMENTAL CONSTRAINTS

EMMANOUIL GIAMPOURAS

Ph.D. Thesis – Tesis Doctoral

PhD Program
in Earth Sciences

Programa de Doctorado en Ciencias de la Tierra de la Universidad de Granada

Memoria de Tesis Doctoral presentada por
M.Sc. en Geología Emmanouil Giampouras para optar al grado de
Doctor por la Universidad de Granada

Esta tesis doctoral ha sido dirigida por el
Dr. Juan Manuel García-Ruiz y el Dr. Carlos J. Garrido Marín,
del Instituto Andaluz de Ciencias de la Tierra (CSIC-Universidad de Granada)

En Granada, 20 de febrero de 2020

Editor: Universidad de Granada. Tesis Doctorales
Autor: Emmanouil Giampouras
ISBN: 978-84-1306-534-2
URI: http://hdl.handle.net/10481/62913

Funding: The research presented in this Ph.D. thesis has been funded by the People Programme (Marie Curie Actions) of the European Union's Seventh Framework Programme FP7 (People) under REA grant agreement n° 608001, in the frame of the Marie-Curie Initial Training Network ABYSS, and the F7 (Ideas) European Research Council grant "PROMETHEUS" under REA grant agreement nº 340863. I also acknowledge funding from the Junta de Andalucía research group GIMPY (grant RNM–131). Research and infrastructure grants used in this research have been (co)funded by the European Regional Development Fund (ERFD).

To my parents and sisters

with everlasting love

To my wife Marievi,

my Shangri-La and companion in life

There are no solitary intelligences;
only team effort and hard work
can move human society forward in science and arts.
Everyone should always aim to move to "other places"
If you are not prepared to do so,
then you have already aged.

Hélène Glykatzi-Ahrweiler
(Recteur de l'Académie, Chancelier des Universités de Paris)

Abstract

In continental settings, the interaction of meteoric water with ultramafic rocks generates waters of variable physicochemical characteristics owing to serpentinization and weathering. The discharge of these waters forms aerial alkaline to hyperalkaline spring systems where waters mix, undergo evaporation, and take up atmospheric CO_2, leading to the formation of carbonate minerals. The understanding of natural carbonation taking place in such serpentinite-hosted alkaline environments is critical for assessing the role of this potentially significant sink in the global carbon cycle, and the viability of CO_2 sequestration techniques for safe carbon storage.

Serpentinization-driven, alkaline environments provide critical insights into the natural conditions regarding the capture of atmospheric carbon dioxide through carbon mineralization. The main objective of this Ph.D. thesis is to advance our understanding of serpentinization-related alkaline spring systems and the associated precipitation of carbonate minerals under alkaline conditions. To contribute to this main research goal, the present Ph.D. thesis aims to (i) provide an additional account of how water composition, mixing, and mineral precipitation and textures co-evolve in serpentinization-driven alkaline spring systems in ophiolites, (ii) investigate alkaline spring sites in subcontinental mantle peridotites and associated mineralizations formed by the interaction between hyperalkaline fluids and river waters, and (ii) experimentally investigate the crystallization sequence and morphologies of hydrated magnesium carbonates, and define the conditions under which their nucleation, crystal growth, and transformation take place. These aims have been addressed through the study of natural alkaline springs hosted in exposed oceanic (Samail Ophiolite, Oman) and subcontinental mantle serpentinized peridotites (Ronda peridotites, Spain), and through carbonate crystallization experiments, to fill gaps in our current knowledge on the mechanisms and the conditions characterizing carbonate mineral precipitation in such systems.

In Oman Ophiolite, complex alkaline pool networks include three distinctive water types: i) Mg-type; moderately alkaline ($7.9 < pH < 9.5$), Mg^{2+}–HCO_3^--rich waters, ii) Ca-type; hyperalkaline ($pH > 11.6$), Ca^{2+}–OH^--rich waters, and iii) Mix type; alkaline to hyperalkaline ($9.6 < pH < 11.5$). The sites are characterized by active precipitation and sedimentation in the pools, which is triggered by mixing, evaporation, and uptake of atmospheric CO_2. Hydrated magnesium (hydroxy-) carbonate in Mg-type waters due to evaporation. Crystal morphologies record the effect on the values of supersaturation and supersaturation rates in the pools due to mixing processes, evaporation and CO_2 uptake. Textural evolution of aragonite from crystalline sheaves to spheroidal shapes underlines the different supersaturation rates of calcium carbonate crystallization in Mix-type waters. Geochemical models of mixing between Mg-type and Ca-type waters revealed the evolution of mineral saturation indices under various mixing proportions and their relation to the observed mineralogy and geochemistry of the pool waters.

Ronda waters can be classified into hyperalkaline fluids (10.9 < pH < 12) and river waters (8.5 < pH < 8.9) that are broadly similar to Ca^{2+}–OH^{-}-rich and Mg^{2+}–HCO_3^{-}-rich water types described in serpentinite-hosted alkaline springs in ophiolites. Travertine, crystalline crusts, and sediment deposits comprise the types of solid precipitates observed in Ronda hyperalkaline spring sites. Calcite, aragonite, dolomite and Mg-Al-rich clays are the main mineral phases identified in the spring sites. Aragonite and dolomite contents increase away from the springs and toward the river waters, a process that uniquely reflects the effect of Mg ions on the precipitation of aragonite versus calcite. Dolomite forms during lithification of travertine due to periodic flooding of river water combined with subsequent evaporation.

Low-temperature crystallization experiments in the MgO–CO_2–H_2O system in closed and open systems resulted either in no precipitation (clear drops) or instant precipitation of a cloudy colloidal material of micro- to nano-particles. In closed system experiments, the transformation of the initial colloidal material took place in three stages: i) dissolution of AMC with increasing pH, followed by the formation of nesquehonite, ii) nesquehonite growth with slight pH increase due to the dissolution AMC, and iii) solvent-mediated transformation of nesquehonite into dypingite particles. In open system experiments, evaporation and atmospheric CO_2 diffusion in the solution triggered different crystallization sequences and morphologies compared to the closed system experiments. The solvent-mediated transformation of nesquehonite to dypingite did not occur due to the evaporation of the water. Unlike closed system experiments, dypingite exhibits a wide range of morphologies including chain-like structures, rings and clusters. The chain-like morphologies form after aggregation of dypingite hemispheres triggered by continuous supersaturation due to the evaporation of the solution.

Keywords: *Oman Ophiolite, Ronda peridotites, serpentinization,* CO_2 *sequestration, carbon mineralization, alkaline springs, carbonate precipitation, mixing processes, magnesium ion effect, crystallization experiments, hydrated magnesium carbonates, amorphous magnesium carbonate, nesquehonite, dypingite.*

Extended abstract

In continental settings, the interaction of meteoric water with ultramafic rocks generates waters of variable physicochemical characteristics owing to serpentinization and weathering. The discharge of these waters forms aerial alkaline to hyperalkaline spring systems where waters mix, undergo evaporation, and take up atmospheric CO_2, leading to the formation of carbonate minerals. The understanding of natural carbonation taking place in such serpentinite-hosted alkaline environments is critical for assessing the role of this potentially significant sink in the global carbon cycle, and the viability of CO_2 sequestration techniques for safe carbon storage.

Serpentinization-driven, alkaline environments provide critical insights into the natural conditions regarding the capture of atmospheric carbon dioxide through carbon mineralization. The main objective of this Ph.D. thesis is to advance our understanding of serpentinization-related alkaline spring systems and the associated precipitation of carbonate minerals under alkaline conditions. To contribute to this main research goal, the present Ph.D. thesis aims to (i) provide an additional account of how water composition, mixing, and mineral precipitation and textures co-evolve in serpentinization-driven alkaline spring systems in ophiolites, (ii) investigate alkaline spring sites in subcontinental mantle peridotites and associated mineralizations formed by the interaction between hyperalkaline fluids and river waters, and (ii) experimentally investigate the crystallization sequence and morphologies of hydrated magnesium carbonates, and define the conditions under which their nucleation, crystal growth, and transformation take place. These aims have been addressed through the study of natural alkaline springs hosted in exposed oceanic (Samail Ophiolite, Oman) and subcontinental mantle serpentinized peridotites (Ronda peridotites, Spain), and through carbonate crystallization experiments, to fill gaps in our current knowledge on the mechanisms and the conditions characterizing carbonate mineral precipitation in such systems.

In **Chapter 3**, this thesis investigates how water composition, mixing, and mineral precipitation and textures co-evolve in serpentinization-driven alkaline springs in the Oman Ophiolite (Sultanate of Oman, Oman). Interactions between meteoric water and ultramafic rocks in the Oman Ophiolite generate waters of variable physicochemical characteristics. The discharge of these waters forms complex alkaline pool networks, in which mineral precipitation is triggered by mixing, evaporation, and uptake of atmospheric CO_2.

A systematic and co-localized sampling of waters and solids in two individual spring sites allowed us to determine the saturation state of a range of minerals and correlate them to the different water and precipitate types. The waters of the spring sites are subdivided into three distinctive types: i) Mg-type; moderately alkaline ($7.9 < pH < 9.5$), Mg^{2+}–HCO_3^--rich waters, ii) Ca-type; hyperalkaline ($pH > 11.6$), Ca^{2+}–OH^--

rich waters, and iii) Mix type; alkaline to hyperalkaline ($9.6 < pH < 11.5$) waters with intermediate chemical composition. The sites are characterized by active precipitation and sedimentation in the pools, as well as travertine terraces formed over the ultramafic rocks. The classification of the collected solid samples was made according to their macroscopic features and spatial distribution into five types: i) Crystalline crusts floating on the water surface, ii) rock coatings around the pool rims, iii) flocculent material covering the bottom of the pool and/or being in suspension within the water column, iv) mud-like material forming dam-like formations (rippled terracing) and massive deposits within and adjacent to the pools, and v) lithified structures from active water flow areas and travertine terraces. Lithified structures associated with active flow include dam-like formations and hardened concretions, while travertine terrace samples were collected from areas with no evident —at least currently— active flow.

Similar to weathering environments of ultramafic rocks, this study offers the first report of hydrated magnesium (hydroxy-) carbonate occurrence in Oman Mg-type waters. Nesquehonite forms in these waters via evaporation and transforms into dypingite and hydromagnesite under CO_2-rich conditions. In Ca-type waters, the coupling of atmospheric CO_2 uptake with evaporation leads to the formation of a calcitic crystalline crust on the air-water interface. The crusts are aragonite- and brucite-bearing, where Mg-type and Ca-type waters discharge and vigorously mix in the same pool. Unlike the Mg-type and Ca-type waters, the pools of Mix-type waters host massive aragonite-dominated deposits due to a high Mg/Ca ratio that favors the growth of aragonite over calcite. The hydrodynamics during mixing control brucite precipitation and restrict its formation and accumulation around specific mixing zones, where a continuous supply of Mg of inflowing Mg-type waters takes place.

Crystal morphologies record the effect on the values of supersaturation and supersaturation rates in the pools due to mixing processes, evaporation and CO_2 uptake. Textural evolution of aragonite from crystalline sheaves to spheroidal shapes underlines the different supersaturation rates of calcium carbonate crystallization in flocculent material of Mix-type waters. Aragonite in dams (terraces) of mud-like precipitates shows a self-organized nanocrystalline structure made of co-oriented nano-rods, suggesting nucleation and growth by accretion and not by classical crystal growth mechanisms. In Ca-type waters, CO_2 uptake and evaporation dictate the textural characteristics of calcite both in crystalline crusts and in rock coatings. The texture of crystalline crusts in Mix-type waters is suggestive of an initial stage of aragonite nuclei formation that is followed by subsequent growth of the first crust segments at the air-water interface, likely caused by CO_2 uptake and evaporation.

Geochemical models of mixing between Mg-type and Ca-type waters revealed the evolution of mineral saturation indices under various mixing proportions and their relation to the observed mineralogy and geochemistry of the pool waters. Calcium carbonate (calcite + aragonite) has the highest SI values in Ca-type waters and systematically decreases in Mix-type waters and Mg-type waters that show the lowest SI values. Mg-type waters and Mix-type waters with $pH < 10.5$ are undersaturated with respect to brucite, whereas brucite is supersaturated in Ca-type waters and Mix-type waters with pH > 10.5. All water types are undersaturated with respect to nesquehonite that is close to saturation in Mg-type waters. Ca-type and Mg-type waters are undersaturated with respect to artinite and hydromagnesite. Measured versus estimated (PHREEQC) values of element concentrations in the water samples are well correlated ($R^2 > 0.95$) for K, Na, Cl^-, and Mg, whereas Ca, Al, Si, Sr, Ba, SO_4^{2-} and DIC show a larger dispersion.

In **Chapter 4**, this thesis presents the investigation of alkaline spring sites in subcontinental mantle peridotites, and associated mineralizations formed by the interaction between hyperalkaline fluids and river waters in Ronda peridotite massifs. Ronda waters can be classified into hyperalkaline fluids and river waters that are broadly similar to Ca^{2+}–OH^--rich and Mg^{2+}–HCO_3^--rich water types described in serpentinite-hosted alkaline springs in ophiolites. At the discharge sites of the fluids (fractures or human-made outlets) and ponds along the fluid flow paths, the fluids are hyperalkaline ($10.9 < pH < 12$) and characterized by low Mg and high Na, K, Ca, and Cl^- concentrations. River waters, occurring near the spring sites, are mildly alkaline ($8.5 < pH < 8.9$) and enriched in Mg and DIC compared to Na, K, Ca and Cl^-. The chemical composition of Ronda Mg^{2+}–HCO_3^- river waters is likely due to the hydrolysis of ferromagnesian peridotite minerals in equilibrium with the atmosphere by infiltrated meteoric water and shallow groundwater in the serpentinized peridotite. The Ronda Ca^{2+}–OH^- hyperalkaline fluids are generated by the combination of low-temperature serpentinization reactions from infiltrated surface Mg^{2+}–HCO_3^- river waters —or Ca^{2+}–HCO_3^- waters from near karst aquifers— and deep carbonate precipitation isolated from atmospheric CO_2. Mass balance calculations indicate that the weathering of Ca-bearing peridotite silicates, such as diopside, is a possible source of Ca in Ronda Ca^{2+}–OH^- hyperalkaline fluids; however, it requires steady-state dissolution rates substantially higher than those experimentally determined. Travertine, crystalline crusts, and sediment deposits comprise the types of solid precipitates observed in Ronda hyperalkaline spring sites.

Calcite, aragonite, dolomite and Mg-Al-rich clays are the main mineral phases identified in the spring sites. As illustrated in the Baños del Puerto spring site, calcite-dominated precipitation is due to uptake of atmospheric CO_2 by Ca^{2+}–OH^- hyperalkaline fluids during discharge, and aragonite-dominated precipitation is due to mixing of Ca^{2+}–OH^- hyperalkaline fluids with Mg^{2+}–HCO_3^- river waters. Aragonite and dolomite contents increase away from the springs and toward the river waters, a process that uniquely reflects the effect of Mg ions on the precipitation of aragonite versus calcite. Other potential factors controlling the precipitation of these $CaCO_3$ polymorphs are the Mg/Ca ratio, the CO_2 content, and the temperature of the fluids. Dolomite forms during lithification of travertine due to periodic flooding of river water combined with subsequent evaporation.

In **Chapter 5**, this thesis investigates the crystallization sequence and morphologies of hydrated magnesium carbonates to provide better constraints regarding their nucleation, crystal growth, and transformation in alkaline environments. The experimental procedures included crystallization experiments in the MgO–CO_2–

H_2O system at low temperature under variable pH and reactant concentration to investigate the crystallization sequence and the textural evolution of hydrated magnesium (hydroxy-) carbonates. Two types of experiments were conducted: i) closed system experiments isolated from the atmosphere (in a glove box under Nitrogen), and ii) open system experiments in atmospheric conditions. Mixing of $MgCl_2.6H_2O$ and Na_2CO_3 solutions resulted either in no precipitation (clear drops) or in instant precipitation of a cloudy colloidal material of micro- to nano-particles. Instantly precipitated, colloidal material was amorphous magnesium carbonate (AMC), AMC and nesquehonite, or AMC, nesquehonite, and dypingite.

In closed system experiments, the transformation of the initial colloidal material took place in three stages: i) dissolution of AMC with increasing pH, followed by the formation of nesquehonite prismatic crystals (1 µm – 50 µm), ii) nesquehonite growth (up to 200 µm crystal sizes) with slight pH increase due to the dissolution of AMC, and iii) solvent-mediated transformation of nesquehonite into dypingite particles (< 1 – 5 µm crystal sizes).

In open system experiments, evaporation and atmospheric CO_2 diffusion in the solution triggered different crystallization sequences and morphologies compared to the closed system experiments. Evaporation caused an increase in the values and rates of supersaturation, leading eventually to precipitation in all crystallization wells. Unlike closed system experiments, crystallization in clear drop wells started between 3 and 48 h after the initial mixing. Nesquehonite did not transform into dypingite, as the solution entirely evaporated between 90 and 120 h after initial mixing. This solvent-mediated process cannot take place due to the evaporation of the water, explaining the persistence of nesquehonite in evaporation-affected natural environments. Dypingite exhibits a wide range of morphologies including chain-like structures, rings and clusters. The chain-like dypingite has a hemispherical structure that exhibits interlocking flakes of dypingite at the exterior part, and a compact dypingite substrate in the interior part. This interior part is most likely formed around initial $Mg\text{-}CO_3$-bearing nuclei, while the well-defined dypingite flakes of the exterior part grow at a later stage due to evaporation. The chain-like morphologies form after aggregation of dypingite hemispheres triggered by continuous supersaturation due to the evaporation of the solution.

Keywords: *Oman Ophiolite, Ronda peridotites, serpentinization, CO_2 sequestration, carbon mineralization, alkaline springs, carbonate precipitation, mixing processes, magnesium ion effect, crystallization experiments, hydrated magnesium carbonates, amorphous magnesium carbonate, nesquehonite, dypingite.*

Resumen extendido

En los entornos continentales, la interacción entre el agua meteórica y las rocas ultramáficas genera aguas de características físico-químicas variables debido a la serpentinización y a la meteorización. La descarga de estas aguas forma sistemas de fuentes de aguas alcalinas a hiperalcalinas donde las aguas se mezclan, se evaporan y absorben el CO_2 atmosférico, dando lugar a la formación de minerales carbonatados. Un mejor entendimiento de los procesos carbonatación natural que tiene lugar en estos ambientes alcalinos albergados por serpentinita es fundamental para evaluar el papel de estos procesos en el ciclo global del carbono, y la viabilidad de las técnicas de secuestro de CO_2 para el almacenamiento seguro de carbono mediante mineralización de rocas ultramáficas.

Los manantiales alcalinos asociados a procesos de serpentinización de baja temperatura proporcionan una oportunidad única para investigar las condiciones naturales para la captura permanente de dióxido de carbono atmosférico en diferentes tipos de minerales. El principal objetivo de la presente tesis doctoral es avanzar en nuestra comprensión de los manantiales alcalinos relacionados con la serpentinización y la precipitación de minerales carbonatados que ocurren en estos sistemas alcalinos. Para contribuir a este objetivo principal de investigación, la presente tesis doctoral tiene por objetivos investigar: i) investigar el control de la composición y mezcla de aguas en la precipitación y las texturas minerales en manantiales alcalinos asociados a la serpentinización en complejos ofiolíticos; ii) investigar los manantiales alcalinos en las peridotitas del manto subcontinental y las mineralizaciones asociadas formadas por la interacción entre los fluidos hiperalcalinos y las aguas fluviales; e iii) investigar experimentalmente la secuencia de cristalización y las morfologías de los carbonatos de magnesio hidratados para constreñir las condiciones en que se produce su nucleación, crecimiento cristalino y transformación en sistemas alcalinos. Estos objetivos se han abordado mediante el estudio de manantiales alcalinos naturales en ofiolitas (ofiolita de Samail, Omán) y en macizos de peridotitas del manto subcontinental (peridotitas de Ronda, España), y mediante experimentos de cristalización.

En el **capítulo 3** de esta tesis se investiga cómo la composición del agua de las fuentes y manantiales alcalinos y su mezcla con aguas fluviales influyen en la precipitación de diferentes tipos de minerales y sus texturas en dos manantiales alcalinos asociados a procesos de serpentinización de baja temperatura en la ofiolita de Omán. Las interacciones entre el agua meteórica y las rocas ultramáficas en la ofiolita de Omán generan aguas de características físico-químicas variables. La descarga de estas aguas forma redes complejas de pozas y charcos alcalinos en los que la precipitación de diferentes minerales se genera por una combinación de la mezcla de diferentes tipos aguas, evaporación y absorción del CO_2 atmosférico.

El muestreo sistemático y simultáneo de aguas y sólidos en dos manantiales alcalinos de la ofiolita de Omán nos ha permitido determinar el estado de saturación de las aguas muestreadas en diferentes minerales y correlacionarlos con los diferentes tipos de agua y precipitados observados en estos manantiales. Hemos clasificado las aguas de las fuentes y manantiales alcalinos de Omán en tres tipos principales: i) aguas tipo Mg, que son aguas moderadamente alcalinas ($7,9 < pH < 9,5$) ricas en Mg^{2+}–HCO_3^-; ii) aguas tipo Ca, que son aguas hiperalcalinas ($pH > 11,6$) ricas en Ca^{2+}–OH^-; y iii) aguas de tipo mixto, que son aguas de carácter alcalino a hiperalcalino ($9,6 < pH < 11,5$) con una composición química intermedia entre las dos anteriores. Todos los manantiales investigados en esta ofiolita se caracterizan por la precipitación y sedimentación activa de diferentes minerales en charcos y pozas, así como por la formación de terrazas de travertinos en las rocas ultramáficas sobre los que discurren ocasionalmente. La clasificación de los materiales sólidos muestreados se ha realizado en función de sus características macroscópicas y su distribución espacial. Distinguimos en cinco tipos de materiales sólidos: i) costras cristalinas que flotan en la superficie del agua; ii) revestimientos rocosos alrededor de los bordes de las pozas y charcos; iii) material floculante que cubre el fondo de las pozas o está en suspensión dentro de la columna de agua; iv) material fangoso que forma forma terrazas onduladas y depósitos masivos dentro y adyacentes a las pozas; y v) estructuras litificadas en áreas de flujo activo de agua y terrazas de travertinos. Las estructuras litificadas asociadas con el flujo activo incluyen concreciones endurecidas, mientras que las muestras de terrazas de travertinos se recogieron de zonas sin flujo evidente activo en el momento del muestreo.

Nuestro estudio pone por primera vez en evidencia la presencia de carbonato de magnesio hidratado (hidroxilo) en las aguas de Omán de tipo Mg. La nesquehonita se forma en estas aguas a través de la evaporación y se transforma en dipingita e hidromagnesita en condiciones ricas en CO_2. En las aguas de tipo Ca, la acción simultánea de la captura de CO_2 atmosférico y la evaporación conduce a la formación de una corteza cristalina calcítica en la interfaz aire–agua. En las pozas en las que las aguas de tipo de Mg y Ca descargan simultáneamente y se mezclan vigorosamente, las costras contienen aragonito y brucita. A diferencia de las aguas de tipo Mg y Ca, las pozas con aguas de tipo mixto albergan depósitos masivos dominados por la precipitación de aragonito debido a la alta proporción local de Mg/Ca en el agua lo que favorece el crecimiento del aragonito en lugar de calcita. En estos ambientes mixtos, la hidrodinámica de la mezcla de aguas controla espacialmente la precipitación restringiendo la formación y acumulación de costras alrededor de zonas específicas de mezcla donde existe un suministro continuo de Mg por las aguas de tipo Mg.

Las morfologías de los cristales registran el efecto de la supersaturación y las tasas de supersaturación en las pozas debido a los procesos de mezcla de aguas, evaporación y absorción de CO_2 atmosférico. La evolución de la textura del aragonito desde las gavillas cristalinas a las formas esferoidales se debe a diferentes tasas de supersaturación de la cristalización del carbonato de calcio en el material floculante de las aguas de tipo mixto. El aragonito en las presas y terrazas de los manantiales produce de precipitados parecidos al lodo que muestran una estructura nanocristalina autoorganizada formada de nano-varillas con la misma orientación, sugiriendo la nucleación y el crecimiento por agregación y no por mecanismos clásicos de crecimiento cristalino. En las aguas de tipo Ca, la absorción y evaporación de CO_2 atmosférico controlan las características de la textura de la calcita tanto en las costras cristalinas como en los revestimientos de las rocas ultramáficas. La textura de las costras cristalinas en las aguas de tipo mixto sugiere una etapa inicial de formación de núcleos de aragonito seguida por crecimiento de costras flotantes incipientes en la interfaz aire-agua, probablemente causadas por la captura del CO_2 atmosférico y la evaporación.

Los modelos geoquímicos termodinámicos de mezcla entre las aguas de tipo Mg y las de tipo Ca (mediante el programa PHREEQC) nos permiten investigar los índices de saturación (IS) de minerales bajo diversas proporciones de mezcla de estas aguas y compararlos con la mineralogía y la geoquímica observadas en las aguas de la piscina. El carbonato cálcico (calcita + aragonito) tiene los valores más altos de IS en las aguas de tipo Ca y disminuye sistemáticamente en las aguas mixtas y las de tipo Mg que muestran los valores más bajos de IS. Las aguas de tipo Mg y mixtas con $pH < 10,5$ están subsaturadas con respecto a la brucita, mientras que la brucita está supersaturada en las aguas tipo Ca y las aguas mixtas con $pH > 10,5$. Todos los tipos de agua están subsaturadas con respecto a la nesquehonita que sólo está cerca de la saturación en las aguas de tipo Mg. Las aguas tipo Ca y Mg están subsaturadas con respecto a la artinita y la hidromagnesita. Los valores medidos frente a los estimados de las concentraciones de diferentes elementos en las muestras de agua están bien correlacionados ($R^2 > 0,95$) para K, Na, Cl- y Mg, mientras que el Ca, Al, Si, Sr, Ba, SO_4^{2-} y el contenido en carbono inorgánico disuelto (DIC) muestran una mayor dispersión.

En el **capítulo 4** de esta tesis se presenta la investigación de los manantiales alcalinos en las peridotitas del manto subcontinental, y las mineralizaciones asociadas formadas por la interacción entre aguas hiperalcalinas y las aguas fluviales en los macizos de las peridotitas de Ronda. Las aguas de las peridotitas de Ronda pueden clasificarse en fluidos hiperalcalinos y aguas de río que son similares, respectivamente, a las aguas ricas en Ca^{2+}–OH^- y Mg^{2+}–HCO_3^- descritas en los manantiales alcalinos en ofiolitas. En los lugares de descarga de los fluidos (fracturas o salidas hechas por el hombre) y estanques a lo largo de las trayectorias de flujo de los fluidos, los fluidos son hiperalcalinos ($10,9 < pH < 12$) y se caracterizan por bajas concentraciones de Mg y altas de Na, K, Ca y Cl^-. Las aguas de los ríos, que se producen cerca de los manantiales, son ligeramente alcalinas ($8,5 < pH < 8,9$) y están enriquecidas en Mg y DIC en comparación con Na, K, y Ca. La composición química de las aguas del río en las peridotitas de Ronda son de tipo Mg^{2+}–HCO_3^- y se debe probablemente a hidrólisis de los minerales de ferro-magnesianos de las peridotitas por aguas meteóricas en equilibrio con la atmósfera que discurren en superficie o cómo aguas subterráneas poco profundas que circulan en las fisuras de las serpentinitas. Los fluidos hiperalcalinos de las peridotitas de Ronda son aguas de tipo Ca^{2+}–OH^- que se generan por la combinación de reacciones de serpentinización a baja temperatura de aguas superficiales infiltradas Mg^{2+}–HCO_3^- de ríos o aguas Ca^{2+}–HCO_3^- infiltradas de los acuíferos cársticos adyacentes que evolucionan en acuíferos serpentiníticas profundos generando serpentinización de baja temperatura aisladas del CO_2 atmosférico y precipitando en profundidad carbonatos. Los cálculos de balance de masa indican que el Ca de estas aguas puede provenir de la meteorización de los silicatos de peridotita portadores de Ca, como el diópsido; sin embargo, lo que requeriría tasas de disolución sustancialmente más altas que las determinadas experimentalmente para las bajas temperaturas de este proceso de hidrólisis.

Las costras cristalinas, travertinos y depósitos de sedimentos en pozas son los principales tipos de precipitados sólidos observados en los manantiales hiperalcalinos de las peridotitas de Ronda. La calcita, el aragonito, la dolomita y las arcillas ricas Mg-Al son las principales fases minerales identificadas en los manantiales investigados en las peridotitas de Ronda. Como queda bien ilustrado en el manantial de Baños del Puerto (macizo de peridotita de Ojén), la precipitación dominante de la calcita se debe a la absorción del CO_2 atmosférico por los fluidos hiperalcalinos Ca^{2+}–OH^- durante la su descarga. La precipitación de aragonito en el mismo manantial se debe a la mezcla de los fluidos hiperalcalinos Ca^{2+}–OH^- con las aguas fluviales de escorrentía ricas Mg^{2+}–HCO_3^-. El contenido de aragonito y dolomita aumenta progresivamente desde la surgencia de las aguas hiperalcalinas hacia las aguas del río, lo que refleja de manera única el efecto el pale de los iones Mg en la precipitación de aragonito. Otros factores potenciales que controlan la precipitación de estos polimorfos de $CaCO_3$ son la relación Mg/Ca, el contenido de CO_2 y la temperatura de los fluidos. Por último, la dolomita se forma durante la litificación de los travertinos debido a ciclos de inundación periódica del agua del río combinados con la evaporación.

Finalmente, en el **capítulo 5** de esta tesis se investiga la secuencia de cristalización y las morfologías de los carbonatos de magnesio hidratados con el objetivo de comprender mejor los mecanismos de nucleación, crecimiento cristalino y la transformación de estos minerales en ambientes alcalinos. Los procedimientos han comprendido experimentos de cristalización en el sistema $MgO–CO_2–H_2O$ a baja temperatura, bajo un pH, y una concentración de variables de reactivos para investigar la secuencia de cristalización y la evolución textural de los carbonatos de magnesio hidratados. Se llevaron a cabo dos tipos de experimentos: i) experimentos en sistema cerrado aislado de la atmósfera (en una cabina de guantes en una atmósfera de Nitrógeno); y ii) experimentos en sistema abierto en condiciones atmosféricas. La mezcla de soluciones de $MgCl_2.6H_2O$ y Na_2CO_3 resultó en la ausencia de precipitación o la precipitación instantánea de un material coloidal turbio de micro- a nano-partículas. El material coloidal precipitado instantáneamente es bien carbonato de magnesio amorfo (CMA), CMA y nesquehonita, o CMA, nesquehonita y dipingita.

El muestreo secuencial de experimento con pH variable a diferentes intervalos de tiempo nos ha permitido investigar el efecto del pH y la secuencia de (trans)formación de la fase con el tiempo. En los experimentos en sistema cerrado, la transformación del material coloidal inicial tiene lugar en tres pasos: i) disolución del CMA con un aumento del pH, seguido de la formación de agujas bien definidas de cristales prismáticos de nesquehonita (1 – 50 µm); ii) inicio del crecimiento de la nesquehonita

con un ligero aumento del pH debido a la disolución del CMA; y iii) la transformación de la nesquehonita —mediada por el disolvente— en partículas de dipingita (< 1 – 5 μm).

Los experimentos en sistema abierto están afectados por la captación y difusión del CO_2 atmosférico en la solución y la evaporación, que causaron diferentes secuencias de cristalización y morfologías en comparación con los experimentos en sistema cerrado. La cristalización en sistema abierto comenzó después de 3 hora tras las que s produjeron tasas de supersaturación y precipitación de sólidos en todos los pocillos de del experimento de cristalización debido a la evaporación. A diferencia de los experimentos en sistema cerrado, la nesquehonita no se transforma en dipingita en sistema abierto, ya que la solución se evapora completamente después de 120 horas, evitando el proceso de transformación mediada por el disolvente observado en los experimentos en sistema cerrado. La evaporación de la solución y explica la persistencia de la nesquehonita en los entornos naturales evaporíticos. A diferencia de los experimentos en sistemas cerrados, cuando ésta precipita, la dipingita presenta una amplia gama de morfologías, incluyendo estructuras en forma de cadena, anillos y cúmulos. La dipingita en forma de cadena tiene una estructura semiesférica que exhibe escamas de dipingita entrelazadas en la parte exterior, y un sustrato compacto de dipingita en la parte interior. Las estructuras en forma de cadena se forman después de la agregación de diferentes hemisferios de la dipingita provocados por la supersaturación continúa debido a la evaporación de la solución.

Palabras clave: *ofiolita de Omán, peridotitas de Ronda, serpentinización, secuestro de* CO_2*, mineralización del carbono, fuentes alcalinas, precipitación de carbonatos, procesos de mezcla, efecto del ión magnesio, experimentos de cristalización, carbonatos de magnesio hidratados, carbonato de magnesio amorfo, nesquehonita, dipingita.*

Εκτεταμένη περίληψη

Σε ηπειρωτικές περιοχές, η αλληλεπίδραση μεταξύ μετεωρικού ύδατος και υπερμαφικών πετρωμάτων δημιουργεί νερά διαφόρων φυσικοχημικών χαρακτηριστικών εξαιτίας της σερπεντινίωσης και της αποσάθρωσης. Η έξοδος αυτών των υδάτων στην επιφάνεια σχηματίζει αλκαλικές έως υπεραλκαλικές πηγές, όπου τα ύδατα αναμειγνύονται, υφίστανται εξάτμιση και απορροφούν ατμοσφαιρικό CO_2, οδηγώντας στο σχηματισμό ανθρακικών ορυκτών. Η κατανόηση της δέσμευσης άνθρακα με φυσικές διεργασίες (απόθεση ανθρακικών ορυκτών) που λαμβάνει χώρα σε τέτοια αλκαλικά περιβάλλοντα που φιλοξενούνται σε σερπεντινίτη είναι κρίσιμη για την αξιολόγηση του ρόλου της ως δυνητική δεργασία προσρόφησης στον παγκόσμιο κύκλο του άνθρακα, και της βιωσιμότητας των τεχνικών δέσμευσης CO_2 με σκοπό την ασφαλή αποθήκευση άνθρακα.

Τα αλκαλικά περιβάλλοντα που δημιουργούνται λόγω σερπεντινίωσης παρέχουν σημαντικές γνώσεις για τις φυσικές συνθήκες σχετικά με τη δέσμευση του ατμοσφαιρικού CO_2 μέσω της απόθεσης ανθρακικών ορυκτών. Ο κύριος στόχος αυτού του διδακτορικού είναι να ενισχύσουμε την κατανόηση μας περί των αλκαλικών πηγών που σχετίζονται με τη σερπεντινίωση και την απόθεση ανθρακικών ορυκτών υπό αλκαλικές συνθήκες. Με σκοπό να υλοποιηθεί ο κύριος αυτός ερευνητικός στόχος, το παρόν διδακτορικό στοχέυει (i) να ενισχύσει τις υπάρχοντες γνώσεις σχετικά με τον τρόπο με τον οποίο η σύσταση του νερού, η μίξη και η απόθεση των ορυκτών και οι υφές αναπτύσσονται σε αλκαλικές πηγές που σχετίζονται με την σερπεντινίωση οφιολίθων, (ii) να διερευνήσει τοποθεσίες αλκαλικών πηγών σε περιδοτίτες υποηπειρωτικού μανδύα και την απόθεση σχετικών ορυκτών μέσω της αλληλεπίδρασης μεταξύ υπεραλκαλικών ρευστών και ποτάμιων υδάτων, και (iii) να διερευνήσει πειραματικά την αλληλουχία κρυστάλλωσης και τις μορφολογίες των ένυδρων ανθρακικών ορυκτών του μαγνησίου, και να καθορίσει τις συνθήκες κάτω από τις οποίες λαμβάνουν χώρα η γέννεση και η ανάπτυξη των κρυστάλλων τους, καθώς και ο μετασχηματισμός τους σε άλλες φάσεις. Οι στόχοι αυτοί έχουν επιτευχθεί μέσω της μελέτης των φυσικών αλκαλικών πηγών που φιλοξενούνται σε εκτεθειμένους περιδοτίτες είτε ωκεάνιου (Samail Ophiolite, Ομάν), είτε υποηπειρωτικού μανδύα (Ronda peridotites, Ισπανία), και μέσω πειραμάτων κρυσταλλώσεως ανθρακικών ορυκτών, έτσι ώστε να ενισχύσουμε τις υπάρχουσες γνώσεις μας σχετικά με τους μηχανισμούς και τις συνθήκες που χαρακτηρίζουν την απόθεση ανθρακικών ορυκτών σε τέτοια συστήματα.

Στο **κεφάλαιο 3**, αυτή η διατριβή ερευνά πώς εξελίσσονται ταυτόχρονα η σύσταση των υδάτων, η ανάμειξη και η απόθεση των ορυκτών και οι υφές στις αλκαλικές πηγές που ελέγχονται από τις διεργασίες σερπεντινίωσης των οφιολίθων του Ομάν (Semail Ophiolite). Οι αλληλεπιδράσεις μεταξύ των μετεωρικών υδάτων και των υπερμαφικών πετρωμάτων στους οφιολίθους του Ομάν δημιουργούν ύδατα με ποικίλα φυσικοχημικά χαρακτηριστικά. Η απόρριψη αυτών των υδάτων σχηματίζει σύνθετα δίκτυα κοιλοτήτων με αλκαλικά νερά (δεξαμενές), στα οποία η απόθεση των ορυκτών προκαλείται από την ανάμιξη, την εξάτμιση και την πρόσληψη ατμοσφαιρικού CO_2.

Μια συστηματική και συνυπάρχουσα δειγματοληψία των υδάτων και των στερεών σε δύο ξεχωριστές τοποθεσίες αλκαλικών πηγών μας επέτρεψε να προσδιορίσουμε το επίπεδο κορεσμού μιας ποικιλίας ορυκτών (saturation index) και να τις συσχετίσουμε με τους διαφορετικούς τύπους υδάτων και ορυκτών αποθέσεων. Τα νερά των πηγών υποδιαιρούνται σε τρεις διακριτούς τύπους: i) τύπου Mg (Mg-type), μέτρια αλκαλικά ($7,9 < pH < 9,5$), πλούσια σε Mg^{2+}-HCO_3^- ύδατα, ii) τύπου Ca (Ca-type), υπερκαλκαλικά ($pH > 11,6$), πλούσια σε Ca^{2+}-OH^- ύδατα και iii) μεικτός τύπος (Mix-type)˙ αλκαλικά έως υπεραλκαλικά ($9,6 < pH < 11,5$) ύδατα με ενδιάμεση χημική σύσταση. Οι τοποθεσίες που ερυνήσαμε χαρακτηρίζονται από ενεργή απόθεση και καθίζηση στις δεξαμενές, καθώς και από τραβερτίνη που σχηματίζεται πάνω από τα υπερμαφικά πετρώματα. Η ταξινόμηση των συλλεγέντων στερεών δειγμάτων έγινε σύμφωνα με τα μακροσκοπικά χαρακτηριστικά τους και την χωρική κατανομή τους σε πέντε τύπους: i) Κρυσταλλικές κρούστες (crystalline crusts) που επιπλέουν στην επιφάνεια του νερού, ii) επιστρώσεις αποθετικού υλικού γύρω από τα τοιχώματα των δεξαμενών (rock coatings), iii) κροκιδωτό υλικό (flocculent material) που καλύπτει τον πυθμένα των δεξαμενών και / ή είναι εν αιωρήσει εντός της στήλης ύδατος, iv) λασποειδές υλικό (mud-like) με κυματοειδείς επιφάνειες - ρυτιδώσεις (dam-like) και μαζικές εναποθέσεις εντός και δίπλα στις δεξαμενές και v) λιθοποιημένες δομές από περιοχές ενεργής ροής ύδατος και τραβερτίνη. Οι λιθοποιημένες δομές που σχετίζονται με την ενεργή ροή περιλαμβάνουν αποθέσεις με κυματοειδής δομή και λιθοποιημένα συγκρίματα, ενώ δείγματα τραβερτίνη συλλέχθηκαν από περιοχές που δεν έχουν εμφανή - τουλάχιστον επί του παρόντος - ενεργή ροή.

Ομοίως με τα περιβάλλοντα αποσάθρωσης των υπερμαφικών πετρωμάτων, η παρούσα μελέτη αποτελεί την πρώτη αναφορά ύπαρξης ένυδρων ανθρακικών ορυκτών του μαγνησίου στα ύδατα τύπου Mg στο Ομάν. Σε αυτά τα νερά σχηματίζεται νεσκουεχονίτης (nesquehonite) μέσω της εξάτμισης και μετατρέπεται σε ντιπινγκίτη (dypingite) και υδρομαγνησίτη κάτω από συνθήκες πλούσιες σε CO_2. Στα ύδατα τύπου Ca, η σύζευξη της ατμοσφαιρικής πρόσληψης CO_2 με την εξάτμιση οδηγεί στον σχηματισμό ενός κρυσταλλικού ασβεστούχου φλοιού στην διεπιφάνεια αέρα-νερού. Οι κρούστες αποτελούνται από αραγονίτη και βρουσίτη, όπου εκβάλλουν τα ύδατα τύπου Mg και Ca και αναμειγνύονται στην ίδια δεξαμενή. Αντιθέτως, οι δεξαμενές των υδάτων μεικτού τύπου φιλοξενούν ευμεγέθεις αποθέσεις αραγωνίτη λόγω της υψηλής αναλογίας Mg / Ca που ευνοεί την ανάπτυξη του αραγωνίτη έναντι του ασβεστίτη. Η υδροδυναμική κατά την ανάμιξη ελέγχει χωρικά την απόθεση βρουσίτη και περιορίζει τον σχηματισμό και τη συσσώρευσή του γύρω από συγκεκριμένες ζώνες ανάμιξης, όπου λαμβάνει χώρα μία συνεχής παροχή Mg και υδροξειδίου από τα εισερχόμενα ύδατα τύπου Mg.

Οι κρυσταλλικές μορφολογίες καταγράφουν την επίδραση στις τιμές του υπερκορεσμού (supersaturation state) και στους ρυθμούς υπερκορεσμού (supersaturation rate) στις δεξαμενές λόγω των διαδικασιών ανάμιξης, εξάτμισης και πρόσληψης CO_2. Η μετατροπή της υφής του αραγωνίτη από κρυσταλλικές διπυραμίδες σε σφαιροειδή σχήματα υπογραμμίζει τους διαφορετικούς ρυθμούς υπερκορεσμού της κρυστάλλωσης ανθρακικού ασβεστίου στο κροκιδωτό υλικό των υδάτων μεικτού τύπου. Ο αραγονίτης στις ρυτιδώσεις των λασποειδών αποθέσεων παρουσιάζει μια αυτο-οργανωμένη νανοκρυσταλλική δομή κατασκευασμένη από συν-προσανατολισμένες νανο-ράβδους, γεγονός που υποδηλώνει δημιουργια και ανάπτυξη με προσαύξηση και όχι με τους κλασσικούς μηχανισμούς κρυσταλλογραφίας. Στα ύδατα τύπου Ca, η απορρόφηση και η εξάτμιση του CO_2 καθορίζουν τα χαρακτηριστικά των υφών του ασβεστίτη τόσο στις κρυσταλλικές κρούστες όσο και στις επιστρώσεις αποθετικού υλικού γύρω από τα τοιχώματα των δεξαμενών. Η υφή των κρουστών στα μεικτού τύπου ύδατα υποδηλώνει ένα αρχικό στάδιο σχηματισμού πυρήνων αραγωνίτη που ακολουθείται από ανάπτυξη των πρώτων τμημάτων του φλοιού στη διεπιφάνεια αέρα-νερού, που πιθανώς προκαλείται από πρόσληψη και εξάτμιση CO_2.

Τα γεωχημικά μοντέλα ανάμειξης υδάτων τύπου Mg και Ca αποκάλυψαν την εξέλιξη των δεικτών κορεσμού ορυκτών υπό διάφορες αναλογίες ανάμιξης και τη σχέση τους με την παρατηρούμενη ορυκτολογία και γεωχημεία των υδάτων των δεξαμενών. Το ανθρακικό ασβέστιο (ασβεστίτης + αραγωνίτης) έχει τους υψηλότερους δείκτες κορεσμού στα ύδατα τύπου Ca και συστηματικά μειώνεται στα ύδατα τύπου Mg, τα οποία παρουσιάζουν τις χαμηλότερες τιμές στους δείκτες κορεσμού. Τα ύδατα τύπου Mg και τα μεικτού τύπου ύδατα με $pH < 10.5$ δεν είναι κορεσμένα όσον αφορά στο βρουσίτη, ενώ είναι υπερκορεσμένα στα ύδατα τύπου Ca και στα μεικτού τύπου ύδατα με $pH > 10,5$. Όλοι οι τύποι είναι ακόρεστοι όσον αφορά στο νεσκουεχονίτη που πλησιάζει τον κορεσμό στα ύδατα τύπου Mg. Τα ύδατα τύπου Ca και Mg είναι ακόρεστα όσον αφορά στον αρτινίτη και τον υδρομαγνησίτη. Οι μετρηθείσες έναντι των εκτιμώμενων (PHREEQC) τιμών των συγκεντρώσεων των στοιχείων στα δείγματα νερού παρουσιάζουν ικανοποιητική συσχέτιση ($R^2 > 0,95$) για τα K, Na, Cl και Mg, ενώ αυτές των Ca, Al, Si, Sr, Ba, SO_4^{2-} και DIC δείχνουν μεγαλύτερη διασπορά.

Στο **κεφάλαιο 4**, η παρούσα εργασία παρουσιάζει τη διερεύνηση αλκαλικών πηγών σε περιδοτίτες υποηπειρωτικού μανδύα και τις σχετιζόμενες αποθέσεις που σχηματίζονται από την αλληλεπίδραση των υπεραλκαλικών ρευστών και των ποτάμιων υδάτων στους ορεινούς όγκους των περιδοτιτών της Ronda. Τα ύδατα της Ronda μπορούν να ταξινομηθούν σε υπεραλκαλικά και σε αυτα των ποτάμιων υδάτων που είναι γενικά παρόμοια με αυτά που είναι πλούσια σε Ca^{2+}-OH^- και Mg^{2+}-HCO_3^-, τα οποία περιγράφονται σε αλκαλικές πηγές που φιλοξενούνται σε οφιόλιθους. Στις τοποθεσίες εκρροής των ρευστών (ρωγμές ή ανθρωπογενείς πηγές) και στις δεξαμενές κατά μήκος των διαδρομών ροής τους, τα ρευστά είναι υπεραλκαλικά ($10,9 < pH < 12$) και χαρακτηρίζονται από χαμηλά επίπεδα Mg και υψηλά επίπεδα Na, K, Ca και Cl^-. Τα ποτάμια ύδατα, που εμφανίζονται κοντά στις περιοχές των πηγών, είναι ηπίως αλκαλικά ($8,5 < pH < 8,9$) και εμπλουτισμένα σε Mg και DIC σε σύγκριση με Na, K, Ca και Cl^-. Η χημική σύνθεση των Mg^{2+}-HCO_3^- ποτάμιων υδάτων της Ronda είναι πιθανόν να οφείλεται στην υδρόλυση των σιδηρομαγνησιούχων ορυκτών του περιδοτίτη από το μετεωρικό νερό το οποίο βρίσκεται σε ισορροπία με την ατμόσφαιρα, και τα ρηχούς υδροφόρους ορίζοντες στον σερπεντινιωμένο περιδοτίτη.

Η χημική σύσταση των Ca^{2+}-OH^{-} υπεραλκαλικών ρευστών της Ronda παράγεται από τον συνδυασμό αντιδράσεων σερπεντινώσης χαμηλής θερμοκρασίας από τα διηθημένα Mg^{2+}-HCO_3^{-} επιφανειακά ποτάμια ύδατα —ή από τα Ca^{2+}-HCO_3^{-}ύδατα από τους καρστικούς υδροφόρους ορίζοντες— και την βαθιά απόθεση ανθρακικών ορυκτών σε περιβάλλοντα απομονωμένα από τις ατμοσφαιρικές συνθήκες. Σύμφωνα με τους υπολογισμούς ισορροπίας μάζας, η αποσάθρωση των πυριτικών ορυκτών των περιδοτιτών που φέρουν ασβέστιο, όπως ο διοψίδιος, είναι μια πιθανή πηγή ασβεστίου στα Ca^{2+}-OH^{-} υπεραλκαλικά ρευστά της Ronda˙ ωστόσο, απαιτούνται σταθεροί ρυθμοί διάλυσης, σημαντικά υψηλότεροι από εκείνους που έχουν καθοριστεί πειραματικά. Τραβερτίνης, κρυσταλλικές κρούστες και εναποθέσεις ιζημάτων αποτελούν τους κύριους τύπους των στερεών αποθέσεων που παρατηρούνται στις τοποθεσίες υπεραλκαλικών πηγών της Ronda.

Ο ασβεστίτης, ο αραγωνίτης, ο δολομίτης και οι άργιλοι πλούσιοι σε Mg-Al είναι οι κύριες ορυκτές φάσεις που εντοπίζονται στις μελετημένες πηγές. Όπως φαίνεται στην πηγή Baños del Puerto, οι αποθέσεις που κυριαρχεί ο ασβεστίτης οφείλονατι στην πρόσληψη ατμοσφαιρικού CO_2 από τα Ca^{2+}-OH^{-} υπεραλκαλικά ρευστά κατά την έξοδό τους στην επιφάνεια, και η απόθεση που κυριαρχείται από αραγωνίτη οφείλεται στην ανάμιξη Ca^{2+}-OH^{-} υπεραλκαλικών ρευστών με Mg^{2+}-HCO_3^{-} ποτάμιων υδάτων. Η περιεκτικότητα σε αραγωνίτη και δολομίτη αυξάνεται όσο απομακρυνόμαστε από τα σημεία ανάβλυσης των αλκαλικών πηγών και προς τα ποτάμια ύδατα, μια διαδικασία που αντανακλά την επίδραση των ιόντων μαγνησίου στην απόθεση αραγωνίτη έναντι του ασβεστίτη. Άλλοι δυνητικοί παράγοντες που ελέγχουν την απόθεση αυτών των πολύμορφων ανθρακικού ασβεστίου είναι η αναλογία Mg / Ca, η περιεκτικότητα σε CO_2 και η θερμοκρασία των ρευστών. Ο δολομίτης σχηματίζεται κατά τη διάρκεια της λιθοποίησης του τραβερτίνη λόγω της περιοδικής πλημμύρας των ποτάμιων υδάτων σε συνδυασμό με επακόλουθη εξάτμιση.

Στο **κεφάλαιο 5**, η παρούσα διδιακτορική διατριβή ερευνά την αλληλουχία κρυστάλλωσης και τις μορφολογίες των ένυδρων ανθρακικών όρυκτων του μαγνησίου με σκοπό να οριστεί καλύτερα η γέννεσή τους, η ανάπτυξη των κρυστάλλων τους και ο μετασχηματισμός τους σε αλκαλικά περιβάλλοντα. Οι πειραματικές διαδικασίες περιείχαν πειράματα κρυστάλλωσης στο σύστημα MgO-CO_2-H_2O σε χαμηλή θερμοκρασία υπό μεταβλητό pH και συγκέντρωση αντιδρόντων για να ερευνηθεί η αλληλουχία κρυστάλλωσης και η εξέλλιξη των υφών των ένυδρων (υδροξυ-) ανθρακικών ορυκτών του μαγνησίου. Διεξήχθησαν δύο τύποι πειραμάτων: i) πειράματα κλειστού συστήματος που απομονώθηκαν από την ατμόσφαιρα (σε glove box με άζωτο), και ii) πειράματα ανοικτού συστήματος σε ατμοσφαιρικές συνθήκες. Η ανάμιξη των $MgCl_2.6H_2O$ και των διαλυμάτων Na_2CO_3 οδήγησε είτε σε μηδενική απόθεση (διαυγείς σταγόνες) είτε σε στιγμιαία απόθεση ενός θολού κολλοειδούς υλικού μικρο- έως νανο-σωματιδίων. Το κολλοειδές υλικό που προήλθε από στιγμιαία απόθεση αποτελούταν από άμορφο ανθρακικό μαγνήσιο (AAM), AAM και νεσκουεχονίτη, ή AAM, νεσκουεχονίτη και ντιπινγκίτη.

Στα πειράματα κλειστού συστήματος, ο μετασχηματισμός του αρχικού κολλοειδούς υλικού πραγματοποιήθηκε σε τρία στάδια: i) διάλυση του AAM με

αυξανόμενο pH, ακολουθούμενη από το σχηματισμό κρυσταλλικών στερεών (1 μm - 50 μm), ii) ανάπτυξη νεσκουεχονίτη (μεγέθη κρυστάλλων έως 200 μm) με ελαφριά αύξηση του pH λόγω της διάλυσης του AAM, και iii) μετασχηματισμό του νεσκουεχονίτη, λόγω επίδρασης του διαλύτη, σε σωματίδια ντιπινγκίτη (μεγέθη κρυστάλλων από <1 έως 5 μm).

Στα πειράματα ανοιχτού συστήματος, η εξάτμιση και η διάχυση του ατμοσφαιρικού CO_2 στο διάλυμα πυροδότησαν διαφορετικές αλληλουχίες κρυστάλλωσης και μορφολογίες σε σύγκριση με τα πειράματα κλειστού συστήματος. Η εξάτμιση προκάλεσε αύξηση των τιμών και των ρυθμών υπερκορεσμού, οδηγώντας τελικά σε δημιουργία κρυστάλλων σε όλα τα δοχεία ανάμιξης (δεν υπήρχαν διαυγείς σταγόνες στο τέλος του πειράματος). Σε αντίθεση με τα πειράματα κλειστού συστήματος, η κρυστάλλωση στα δοχεία ανάμιξης διαυγών σταγονών ξεκίνησε μεταξύ 3 και 48 ωρών μετά την αρχική ανάμιξη. Ο νεσκουεχονίτης δεν μεταμορφώθηκε σε ντιπινγκίτη, καθώς το διάλυμα εξατμίστηκε εξ ολοκλήρου μεταξύ 90 και 120 ωρών μετά την αρχική ανάμιξη. Η διεργασία μετασχηματισμού του νεσκουεχονίτη σε ντιπινγκίτη γίνεται υπό τη βοήθεια του διαλύτη και έτσι δεν μπορεί να λάβει χώρα εξαιτίας της εξάτμισης του νερού,. Αυτό εξηγεί την επιμονή του νεσκουεχονίτη σε φυσικά περιβάλλοντα που επηρεάζονται από έντονη εξάτμιση. Ο ντιπινγκίτης παρουσιάζει ένα ευρύ φάσμα μορφολογιών που περιλαμβάνουν δομές που μοιάζουν με αλυσίδα, δακτυλίους και συμπλέγματα κρυστάλλων. Η πρώτη περίπτωση έχει μια ημισφαιρική δομή που παρουσιάζει αλληλοσυνδεόμενες κρυσταλλικές πλάκες ντιπινγκίτη στο εξωτερικό μέρος και ένα συμπαγές υπόστρωμα ντιπινγκίτη στο εσωτερικό μέρος. Αυτό το εσωτερικό μέρος πιθανότατα σχηματίζεται γύρω από τους αρχικούς πυρήνες που φέρουν $Mg\text{-}CO_3$, ενώ οι πλάκες ντιπινγκίτη του εξωτερικού τμήματος αναπτύσσονται σε μεταγενέστερο στάδιο εξαιτίας της εξάτμισης. Οι μορφολογίες που μοιάζουν με αλυσίδα σχηματίζονται μετά από συσσωμάτωση των ημίσφαιρίων ντιπινγκίτη που πυροδοτούνται από συνεχή υπερκορεσμό λόγω της εξάτμισης του διαλύματος.

Λέξεις κλειδιά: *οφιόλιθοι Ομάν, περιδοτίτες Ρόντα, σερπεντινίωση, δέσμευση άνθρακα μέσω ορυκτών, αλκαλικές πηγές, απόθεση ανθρακικών ορυκτών, διεργασίες ανάμιξης υδάτων, δέσμευση* CO_2*, επίδραση ιόντων μαγνησίου, πειράματα κρυστάλλωσης, ένυδρα ανθρακικά του μαγνησίου, άμορφο ανθρακικό μαγνήσιο, νεσκουεχονίτης, ντιπινγκίτης.*

Acknowledgements

First and foremost, I would like to express my sincere gratitude to my supervisors **Prof. Juan Manuel García-Ruiz** and **Dr. Carlos J. Garrido** who trusted me and offered me the opportunity to conduct the present Ph.D. thesis.

Thank you, **Juanma**, for your supportive and kind attitude towards every situation that I had to encounter, creating a healthy environment that helped me to achieve this ultimate goal. Your continuously vigorous enthusiasm made it almost impossible not to transfer it to other people, including myself. So many seminars, congresses, and courses, but also outreach activities and gatherings in beautiful places, all organized by you and your restless spirit for further knowledge and communication; this was a great gift that someone can make to a stressed Ph.D. student. You came up always with fresh ideas and gave me motivation and food for thought for improving every day. Working by your side all these years not only offered me valuable knowledge on many scientific fields where you excel, but I was also, taught how to grow and behave like a scientist. Your ability to synthesize and communicate science and ideas helped me to digest complicated and difficult concepts. At last, I will never forget all the fun moments and fruitful discussions we shared beyond the working hours in bars, restaurants and many more places that you gave me the opportunity to visit.

An equally big thanks goes to you, **Carlos**. You were a paradigmatic tutor regarding many technical and scientific aspects that I had to face during my Ph.D. studies. I learned many valuable things during our lengthy meetings wrapping up everything and producing nice communications. Your specialized points of view, always rational and accurate, were admirable and provided solutions to many occasions that otherwise I would have been lost. I am also, grateful to you for teaching me how to be organized and concise, skills that I needed in my life, and I promise I will try to follow your ways and instructions during my future scientific career. I will never forget you for being always there to motivate me during all the ‘’dark’’ periods of my Ph.D., encourage me to move on, and to congratulate me when I most needed that for our achievements. Honestly, it is not an exaggeration when I say that the completion of this work would have been impossible without your invaluable advice and personal effort. Thank you!

The research stays I conducted out of Spain through the ABYSS network were an important part of my Ph.D., proving useful knowledge, training and results, so I would like to thank all the people involved. First, I am grateful to **Dr. Bénédicte Ménez** and **Dr. Mark Van Zuilen** for all the scientific discussions, technical training and advice during my secondment in IPGP (Paris, France). I am also, especially thankful to **Dr. Wolfgang Bach** not only for the knowledge that so generously offered to me during my research stay in the University of Bremen (Bremen, Germany) but also, for his precious guidance and all the exciting moments we shared during the Oman and Ronda (Malaga, Spain) field trips, in addition to co-authoring my articles. I should not omit to thank the rest group from Bremen University, including **Dario Fussmann**, **Dr. Patrick Monien** and **Dr. Catharina Los** for supporting me during my stay there, for the scientific and technical help, and all the great moments we shared in the deserts of Oman.

Besides, I would like to thank the rest of scientists involved in the ABYSS project, including **Dr. Marguerite Godard** for coordinating the network, **Dr. Damon Teagle**, **Dr. Patrizia Fumagalli**, **Dr. Elisabetta Rampone**, **Dr. Bjorn Jamveit**, **Dr. Jürgen Koepke**, **Dr. Benoit Idelfonse, Olivier Rodriguez, Tim Henstock, Laura Crispini, Håkon Austrheim** and **Dr. Suzanne McEnroe** for organizing priceless training activities and providing stimulating feedback and discussions during various meetings. I should not forget to give thanks to the managers of the ABYSS project, **Chloe** and **Alida**, for the meticulous organization of every activity, so everyone had the opportunity to enjoy it effortlessly.

I would also like to express my gratitude to all the people participating in the Ronda peridotite (Malaga) field trip, including **Dr. Iñaki Vadillo** and **Dr. Pablo Jiménez** (University of Malaga), **Dr. Jennifer Zwicker** and **Dr. Daniel Szmirka** (University of Vienna), **Dr. José Benavente Herrera** (University of Granada), and **Dr. Jörn Peckmann** (University of Hamburg). These people accompanied me, guided me and shared with me their scientific knowledge, each one on his field of expertise that proved to be very useful for the synthesis of the corresponding part of my thesis.

Many special thanks go to all the members of LEC in IACT for welcoming me so warmly in their group, for their invaluable technical, scientific and emotional support through all these years, and for all the unforgettable moments we spend together during dinners, tapas, events, conferences, and many more occasions. Thank you **Paqui**, **Cristóbal**, **Raquel**, **Duane**, **Juan**, **Alfonso**, **Fermin**, **Gabi**, **Jaime**, **Carmen**, as well as **Electra**, **Maritza**, **Joaquín**, **Gan**, **Melese**, **Joti**, **Julian** and **Kevin**. Similarly, I should not omit to sincerely thank all the personnel and

technicians form the Petrology, Geochemistry and Geochronology group of the IACT, including **Alpiste**, **Mayte**, **Károly**, **Claudio**, **Chari** and **Inma** for their continuous help and support in everything I needed, as if not for them it would have been challenging to complete my thesis. I am also thankful to the technicians from the Centro Instrumentación Científica (CIC, University of Granada), including **Isabel Sánchez**, **Isabel Guerra** and **Alicia González Segura** for their patience and the long hours we spent together trying to produce nice results and images for my thesis.

At this point, I would like to express my gratitude to the members of the examination panel, **Dr. Encarnación Ruiz Agudo** (University of Granada), **Dr. Claudio Marchesi** (University of Granada), **Dr. Lourdes Fernández** (Complutense University of Madrid), **Dr. Ana María Alonso Zarza** (Complutense University of Madrid), **Dr. Robin Renaut** (University of Saskatchewan, Canada), and the substitute panel experts, **Dr. Fermin Otálora** (CSIC) and **Dr. Carlos Manuel Rodríguez Navarro** (University of Granada) for their time and interest in this work.

To my dear ABYSS fellows **Carlotta** (or Charlie!), **Val**, **Adriana**, **Karin**, **Sofia**, **Justine**, **Barbara**, **Kristina**, **Zeudia**, **Rachael**, **Tom**, **Pavel**, **Aurélien,** and, of course, my office mate **Manuel**. Thanks for all the eventful, adventurous, and amusing time we spend all together in many places around Europe. I have been so lucky being part of such a great team and network that provided me with new invaluable memories and friends. See you soon!

Special thanks go to my friends and colleagues from IACT for all the happy moments we shared beyond work, for all the emotional and scientific support, for making my working hours more pleasant and for enjoying together the beautiful city of Granada: **Electra**, **Nicole**, **Manu, Erwin**, **Gan, Joaquín, Amel**, **Mari**, **Yassamina**, **Muhammad**, **Annika**, **Károly**, **Marga**, **Bob**, **Álvaro**, **Claudia**, **Laura**, **Ari**, **Dimitris**, **Adrián**, **Rubén**, **Sara**, **Leonardo**, **Melese, Joti, Julien, Kevin**, and many more!

Of course, I should also mention all my other friends of old and new from Greece and other places around the world, for supporting me emotionally through all this overwhelming period of my life and for allowing me to spend the amusing and productive time that helped me move on with more enthusiasm and courage. Thank you from the bottom of my heart!

I should not omit to mention my lovely mother-in-law, who has never faltered as she dealt with many blows and misfortune in her life, giving the best example of endurance and fighting spirit. She was always there for me with her smile and support that can motivate even rocks!

And of course, my dear father-in-law, who was a role model, not only for his intellectual life but also for his moral character and ethics. You will always be an inspiration to me, and I will always miss you.

Here, I would like to give my most special thanks to my family. In a moment like this, you understand how poor are words to express your gratitude towards people who were always there for you, ready to sacrifice everything. Dear mother, I will be forever grateful for advising me to never stop chasing my dreams, and for believing in me even when I did not believe in myself. I am your greatest fan! Dear father, thank you for encouraging me in every step of my life, and for providing me through your sacrifices and struggles, the opportunity to grow as a person and scientist. I owe you everything! I would like to express my profound gratitude to my little twin sisters for their priceless support all these years. Almost literally, we studied and graduated together, providing me with solutions whatever the situation. My dear grandparents, I will always be your son.

Ποτέ δε με αγαπήσατε με λόγια. Πάντα ήσασταν εκεί με πράξεις. Σας ευχαριστώ για όλα όσα έχετε κάνει για μένα. Σας αγαπώ πολύ!

Last, but by no means least, I would like to express my deepest gratitude to my gracious wife, Marievi Papaslioti, who always finds a way to make everything simpler and easier; this thesis is not an exception. She is the boldest and most respectful person I know, and by following her example, it helped me progress and become a better person. Being a geochemist herself, and a successful Doctor in Science, she provided me with invaluable knowledge and constructive advice assisting me to move forward with confidence and determination. I am thankful for her remarkable patience and restless support during these stressful —yet amazing— years *aquí en Graná*, even if she had to do (and complete) her Ph.D. as well. I really must tell her a huge thank you for all the moments of happiness we have shared so far, and for her fathomless generosity that fills me with comfort and serenity. She has a unique skill to give always the best advice, and without her and her brilliance, this achievement would not have been possible. It is a true blessing to have you by my side. Thank you for everything from the bottom of my heart! Σ’αγαπώ!

Contents

PART I – INTRODUCTION, AIMS AND THESIS OUTLINE

PART II – RESULTS

PART III – CONCLUSIONS AND PERSPECTIVES

PART IV – REFERENCES

Part I

INTRODUCTION, AIMS, AND THESIS OUTLINE

1 Introduction

The present chapter includes the background and state of knowledge about the exposure of mantle peridotites on the Earth's surface, the serpentinization and weathering taking place due to their interaction with seawater or meteoric water, and the mineralization processes occurring during these water-rock interactions. It also describes marine and continental alkaline environments developing as a result of water circulation in serpentinized mantle rocks. Moreover, it presents information about the occurrence of (hydrated) Mg-carbonates in serpentinite-hosted alkaline environments, and previous experimental work in the $MgO–CO_2–H_2O$ at low temperature. An introduction to the geological settings of the study areas is given at the end of this chapter.

1.1 Exposures of mantle rocks on Earth's surface

The study of mantle rocks is principally directed towards the understanding of the composition and structure of the Earth's interior (e.g., Carlson, 2003; Helffrich and Wood, 2001; Jackson, 2000), the mechanisms of plate tectonics (e.g., Morris and Ryan, 2003), and the accretion of oceanic and continental crust (e.g., Kelemen et al., 1997; Martinez and Taylor, 2002), among other major geodynamical and petrological topics. However, (bio)geochemical and geological processes triggered during the interaction of fluids with mantle are emerging research fields that are related to different topics of high societal relevance, such as the carbon capture and storage (Kelemen et al., 2011; Kelemen and Matter, 2008; Matter and Kelemen, 2009; Seifritz, 1990), deep carbon cycle (Alt et al., 2013; Dasgupta and Hirschmann, 2010; Kelemen and Manning, 2015; Menzel et al., 2018, 2019), deep subseafloor biosphere (McCollom and Seewald, 2013; Menez et al., 2012), the origin of life (Lane and Martin, 2010; Martin et al., 2008; Martin and Russell, 2007; Sleep et al., 2011), and detection of primitive life (Garcia-Ruiz et al., 2003, 2017).

Exposed parts or fragments of the mantle on the Earth's surface include: i) abyssal peridotites from the oceanic mantle that have been dredged from the ocean floor or recovered from drill cores (e.g., Bonatti et al., 1974; Hamlyn and Bonatti, 1980; Prinz et al., 1976); ii) tectonically emplaced suboceanic; subcontinental and subarc mantle rocks that were exhumed from the upper mantle (e.g., Boudier and Coleman, 1981; Tilley, 1947); and iii) mantle xenoliths erupted in deeply derived volcanic rocks (e.g., Nixon 1973; Pearson et al., 2003).

Abyssal peridotites provide direct information on the uppermost mantle in present-day oceanic settings (e.g., Cann, 1971; Miyashiro et al., 1969), and are limited mid-ocean ridge (MOR) environments (Dick et al., 1984; Niu and Hékinian, 1997), depression deeps (Hékinian et al., 1993), serpentinite seamounts (Parkinson and Pearce, 1998), or passive continental margins (Cornen et al., 1996).

Mantle rocks that have been tectonically emplaced on continental or oceanic crust can be categorized as:

1. The lower ultramafic section of extensive (tens of km) ophiolite or island arc complexes, obducted on continental margins (e.g., the Oman Ophiolite and the Kohistan and Talkeetna Arc complexes – Boudier and Coleman, 1981; Burg et al., 1998; Coleman, 1971; Mehl et al., 2003).
2. Dispersed ultramafic bodies (m to km in size) in suture zones and mountain belts (i.e., the orogenic peridotite massifs – Den Tex, 1969; Thayer, 1960).
3. The exhumed mantle rocks above the sea level by normal faults associated with rifting or transform faults in ocean basins (e.g., Zabargad Island in the Red Sea, St. Paul's islets in the Atlantic, and Macquarie Island in the southwestern Pacific – Dijkstra and Cawood, 2004; Melson et al., 1967; Varne and Rubenach, 1972). This type of tectonically emplaced mantle along with abyssal peridotites are collectively known as "oceanic peridotites" (e.g., Bodinier and Godard, 2014).

In the following sections, we will focus on oceanic and subcontinental mantle peridotites that are the host rocks of the alkaline springs investigated in the present Ph.D. thesis.

1.1.1 Occurrences of abyssal peridotites

Abyssal peridotites can be found in ultraslow- (spreading rate < 1 cm/y), slow- (spreading rate < 3 cm/y), and fast-spreading (spreading rate > 10 cm/y) MORs (**Fig. 1.1**). However, a very limited number of peridotite sites have been reported at fast-spreading MORs (e.g., Hess Deep – Hékinian et al., 1993). The relatively high crustal thickness at fast-spreading ridges (≈ 7 km) and the regular sequence of basalts (1 – 2 km), sheeted dykes (1 – 2 km) and gabbroic rocks (3 – 5 km) could explain the lack of peridotites at fast-spreading MORs (Canales et al., 2003; Ciazela et al., 2015; Warren, 2016; White et al., 1992).

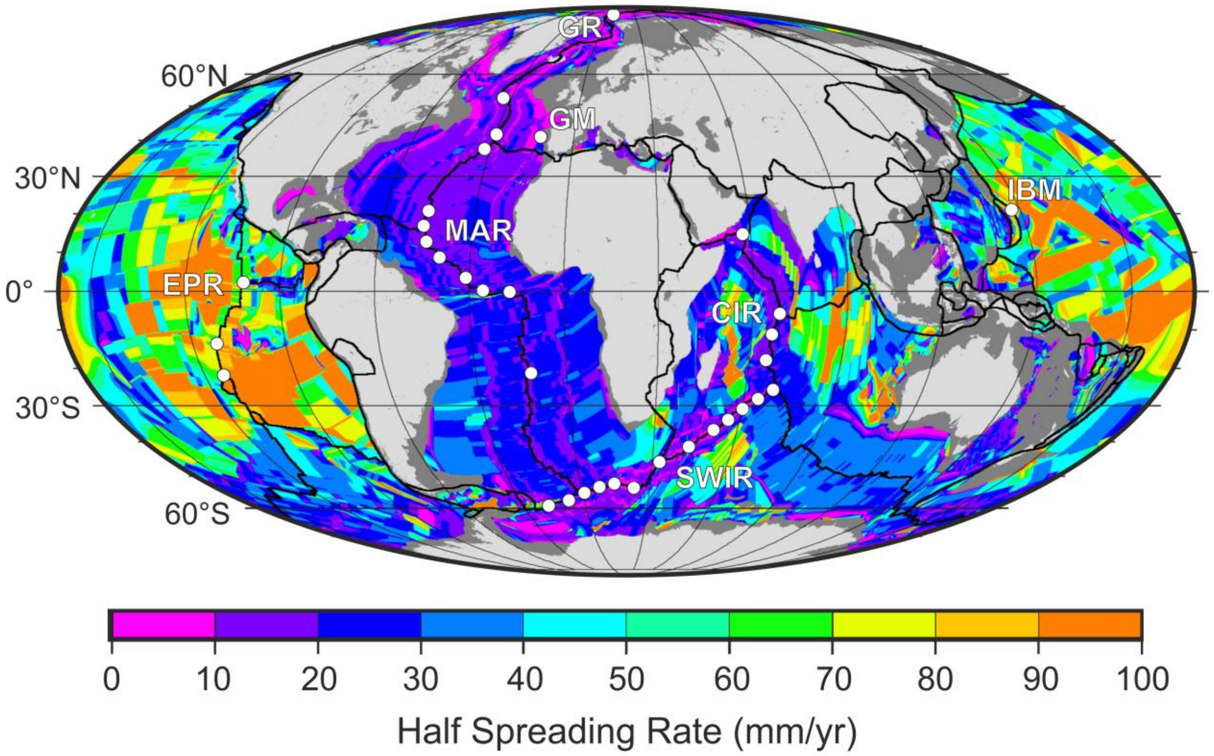

Figure 1.1. *Half spreading rates of ocean crust formation (Müller et al., 2008) and locations where serpentinized abyssal peridotites have been recovered from the seafloor (after Deschamps et al., 2013; Warren, 2016).*

Extensive tectonic windows accommodating upper mantle exposures on the seafloor are most common at slow-spreading MORs. Thus, the abyssal peridotites mostly come from walls of fracture zones or rift mountains in these ridge systems. Samples of this type of peridotites were mainly collected in the slow-spreading Mid-Atlantic and Indian Ocean ridges (e.g., Bonatti et al., 1992; Dick et al., 1984; Godard et al., 2008) and, more recently, at ultraslow-spreading ridges, such as the Southwest Indian Ridge (e.g., Johnson and Dick, 1992; Seyler et al., 2004; Warren and Shimizu, 2010) and the Gakkel Ridge and Lena Trough, Arctic Ocean (Hellebrand et al., 2002; Hellebrand and Snow, 2003). Along both slow- and ultraslow-spreading ridges, abyssal peridotites were also discovered at large exposures of mantle and lower crustal rocks called oceanic core complexes (OCC) (e.g., Boschi et al., 2006; Godard et al., 2009; Ildefonse et al., 2007). These are dome-shaped structures interpreted as parts of the lower crust and/or upper mantle exposed on the seafloor via low-angle normal or detachment faulting (e.g., Cann et al., 1997; Tucholke and Lin, 1994).

Other occurrences of abyssal peridotites can be found at suprasubduction settings (e.g., the Izu–Bonin–Mariana forearc – Parkinson and Pearce, 1998), and at sites related to early stages of the Atlantic opening (Galicia passive margin and the Gorringe Bank – Abe, 2001; Boillot et al., 1988) and Newfoundland margin – Müntener and Manatschal, 2006).

The abyssal peridotites are often affected by oceanic hydrothermal alteration and the degree to which abyssal peridotites are representative of pristine oceanic mantle is still debatable. However, they provide a reference point for understanding processes related to mantle formation and alteration.

1.1.2 Ophiolites and orogenic peridotites in continental settings

The most common types of tectonically emplaced mantle rocks along mountain belts in continental settings include ophiolites and orogenic peridotite massifs (**Fig. 1.2**). Unlike abyssal peridotites, both types are dissociated from the environment where they originally formed (e.g., Bodinier and Godard, 2014). In some cases, the original geodynamic setting of these rocks is uncertain and speculative, rendering it difficult to determine how representative they are regarding mantle compositions (e.g., Menzies and Dupuy, 1991; Nicolas, 1989). However, ophiolites play a crucial role in understanding the function of plate tectonics and the structure of the oceanic crust and upper mantle (Abbate et al., 1985), and orogenic peridotites are an essential window to probe numerous mantle processes (e.g., structure, nature and evolution of lithosphere, asthenosphere, magma genesis, mantle plumes, and metamorphic pathways) (Liou et al., 2007).

Ophiolites represent fragments of upper mantle and oceanic crust (Coleman, 1977; Nicolas, 1989) that were obducted onto continental or oceanic crust during continent-continent and arc-continent collisions (e.g., Dilek and Flower, 2003), ridge-trench interactions (e.g., Lagabrielle et al., 2000), and/or subduction-accretion events (e.g., Cawood et al., 2009). Ophiolites are observed in all major orogenic belts (> 70 ophiolites have been described worldwide) that mark major boundaries between amalgamated plates or accreted terranes (Lister and Forster, 2009) (**Fig. 1.2**).

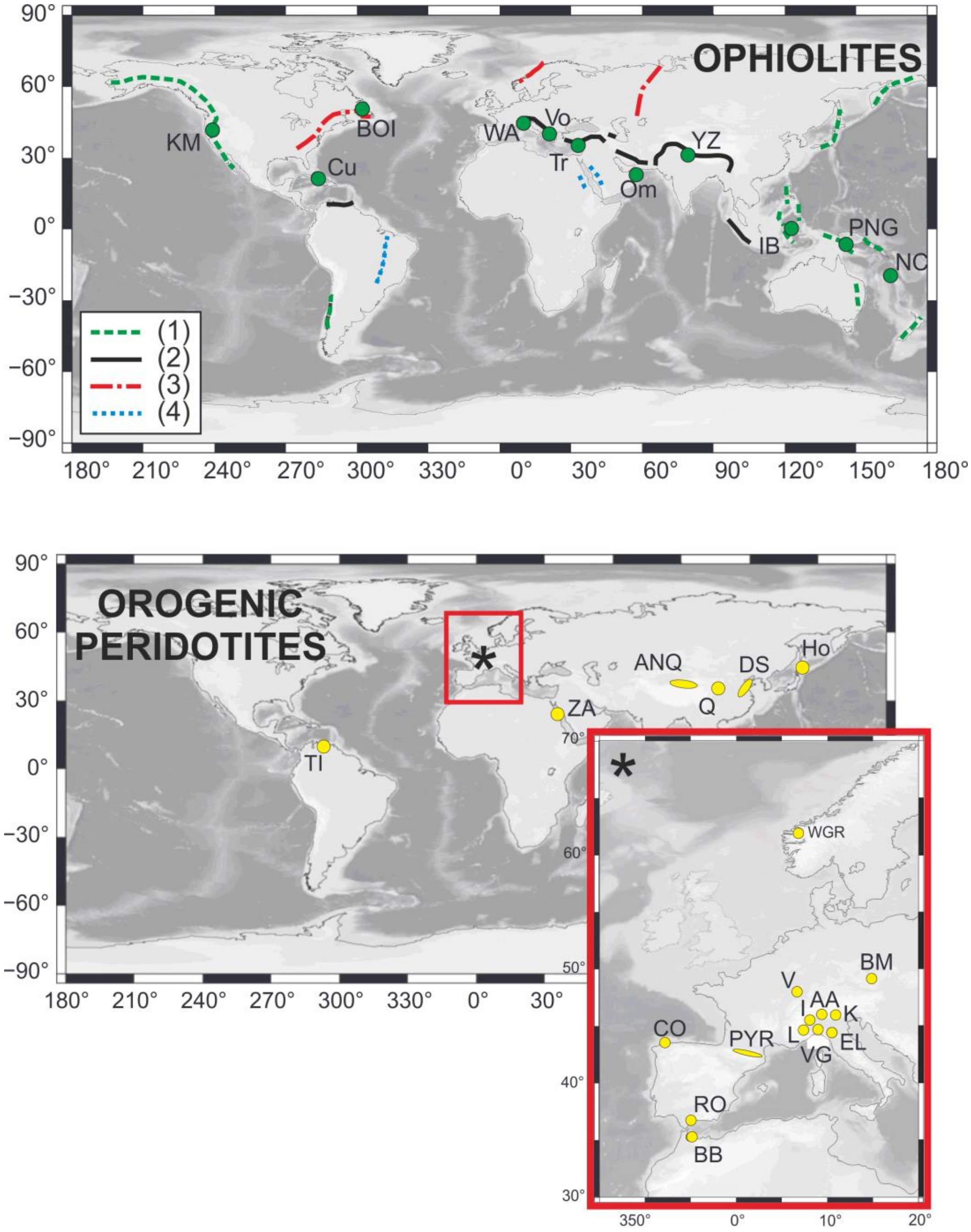

Figure 1.2. ***(Up)*** *Location of the main ophiolitic belts and ophiolite complexes worldwide. (1) Circum-Pacific: KM – Klamath Mountains; NC – New Caledonia; PNG – Papua New Guinea; IB – Indonesian back-arc ophiolites. (2) Himalaya–Alps–Caribbean: YZ – Yarlung Zangbo ophiolites; Om – Semail ophiolite, Oman and U.A.E.; Tr – Troodos, Cyprus; Vo –Vourinos and Pindos, Greece; WA – Western Alps; Cu – Cuba ophiolites. (3) Appalachian–Caledonian belt: BOI – Bay of Islands, Newfoundland. (4) Pan-African belt. (****Down)*** *Location of the main orogenic peridotite occurrences worldwide: TI – Tinaquillo, Venezuela; Ho – Horoman, Hokkaido, Japan; DS – Dabie–Sulu, China; Q – Qinling, China; ANQ – North Qaidam – Altyn-Tagh, China; and ZA – Zabargad, Red Sea, Egypt.* ***Inset:*** *WGR – Western Gneiss Region, Norway; B – Bohemian Massif, Czech Republic, Germany, Austria, and Poland; V – Vosges, France; AA – Alpe Arami, Central Alps, Switzerland; M – Val Malenco, Italy; I – Ivrea zone, Italy; L – Lanzo, Western Alps, Italy; VG – Voltri Group, Italy; EL – External Liguride peridotites, Italy; PYR – Pyrenees, France; RO – Ronda peridotites, Spain; BB – Beni Bousera, Morocco; CO – Cabo Ortegal, Spain (from Bodinier and Godard, 2014)*

A complete ophiolite sequence could be broadly described as a stack of mafic to ultramafic rocks that includes, from bottom to top, tectonized peridotites, cumulate peridotites, and pyroxenites overlain by layered gabbros, sheeted basaltic dikes, a volcanic sequence, and a sedimentary cover (see Penrose Conference, 1972). A number of completely developed ophiolitic complexes have been discovered and studied in the Internal Ligurides (Northern Italy), Troodos (Cyprus), Semail (Sultanate of Oman and the UAE), Xigaze (Tibet), Klamath Mountains (Trinity, California), and the Bay of Islands (Newfoundland, Canada).

Based on the main lithologic variations observed in ophiolitic mantle sections, the Internal Ligurides and the Semail ophiolites may be considered as two end-members from mildly refractory —lherzolite-dominated— mantle section to a strongly refractory —harzburgite-dominated— mantle section, respectively (e.g., Boudier and Nicolas, 1985; Nicolas and Boudier, 2003). Moreover, their geochemistry, structure, and thickness are strongly controlled by spreading rate, proximity to plumes or trenches, mantle temperature and fertility, and the availability of fluids. Thus, they could be also categorized based on their relation to different geodynamic settings: i) subduction-unrelated; continental margins and MORs, and ii) subduction-related; suprasubduction zones and volcanic arcs (see Dilek and Furnes, 2011).

The orogenic peridotite massifs are mostly lherzolite-dominated (e.g., O'Hara 1967), while —in few instances— they can be mainly composed of harzburgites or dunites to pyroxenites, through harzburgites and lherzolites (Bodinier and Godard, 2014). Several orogenic peridotites contain accessory lithologies (e.g., dikes, veins, and veinlets filled with garnet and/or amphibole pyroxenites, hornblendites, gabbros, and diffuse facies of pyroxene-rich or amphibole-bearing peridotites), resulting from the segregation and migration of partial melts or from the interaction between mantle rocks and melt/fluids (e.g., Bodinier et al., 1988; Garrido and Bodinier, 1999).

Based on their predominant petrologic facies and/or their P–T trajectory before exhumation, orogenic peridotites can be characterized from high-pressure (HP) and ultrahigh-pressure (UHP) massifs (e.g., e.g., Central Alps – Ernst, 1981; Pfiffner and Trommsdorff, 1998), over intermediate-pressure (IP) (e.g., Beni Bousera, northern Morocco, and Ronda, southern Spain – Gysi et al., 2011; Lenoir et al., 2001), to low-pressure (LP) exhumed mantle rocks (e.g., Val Malenco in the Eastern Central Alps – Müntener and Hermann, 1996). The orogenic massifs are often related to platform sediments or continental rocks recording extreme metamorphic conditions, from HT at IP or LP (e.g., Beni Bousera (northern Morocco) and

Ronda (southern Spain) massifs – Loomis, 1972) to HP or UHP at variable temperatures (Liou et al., 2007).

The orogenic peridotites show a wide range in size from small bodies (1 – 10 m) embedded in metamorphic sediments (e.g., Pyrenean lherzolites; Fabriès et al., 1991) to extensive ultramafic massifs (up to 450 km^2) comprising the main body of overthrusted tectonic units (e.g., the Ronda peridotite massifs – Tubia and Cuevas, 1986). However, the majority of the lherzolite massifs display intermediate sizes between the examples above (few hundred m to a few km), occurring along thrust sutures or major faults.

1.2 Hydration and carbonation of ultramafic rocks

Most mantle peridotites are harzburgites or lherzolites composed of more than 50 vol% olivine and variable amounts of ortho- and clinopyroxene. Because they are far from equilibrium at weathering and low-temperature metamorphic conditions, these olivine- and pyroxene-rich rocks readily hydrate to form serpentine group minerals when in contact with water. The fate of carbon is closely linked with the hydration of peridotite, which can be carbonated if fluids rich in dissolved inorganic carbon are involved. Natural CO_2 uptake via carbonation of peridotite on the seafloor is a significant carbon sink and an important element of the carbon cycle (e.g., Alt et al. 2012; Früh-Green et al. 2004; Kelemen et al. 2011; Schwarzenbach et al. 2013). On-land, hydration and carbonation result from low-temperature reaction of meteoric water with peridotite, first described in Northern California by Barnes et al. (1967), and later recognized in exposed peridotite bodies worldwide (e.g., Bruni et al. 2002; Cipolli et al. 2004; Kelemen and Matter 2008; Neal and Stanger 1985; Paukert et al. 2012).

In addition to serpentinization, carbonate minerals can form during hydrothermal carbonation and weathering of peridotites and serpentinites (e.g., ophicarbonates and hydromagnesite playas; Kerrick and Connolly, 1998; Power et al., 2009). The types of carbonation depend mainly on the fluid composition and temperature, varying from listvenites at high temperatures (> 150 ºC) to supergene travertine and shallow cryptocrystalline magnesite (< 100 ºC) (e.g., Hansen et al., 2005; Mervine et al., 2014). The fast kinetics of carbonation reactions and the high capacity of serpentinites to buffer CO_2-bearing fluids lead to the rapid precipitation or replacive growth of carbonate minerals in serpentinized peridotites (Andreani et al., 2009; Grozeva et al., 2017). The variations in temperature, solute activities and CO_2 in the fluids lead to different degree of hydration and carbonation of the rock, and thus, different assemblages from brucite-serpentine to talc-magnesite and magnesite-quartz (Klein et al., 2013; Klein and Garrido, 2011; Klein and McCollom, 2013; Menzel et al. 2018; Power et al., 2013) (**Fig. 1.3**).

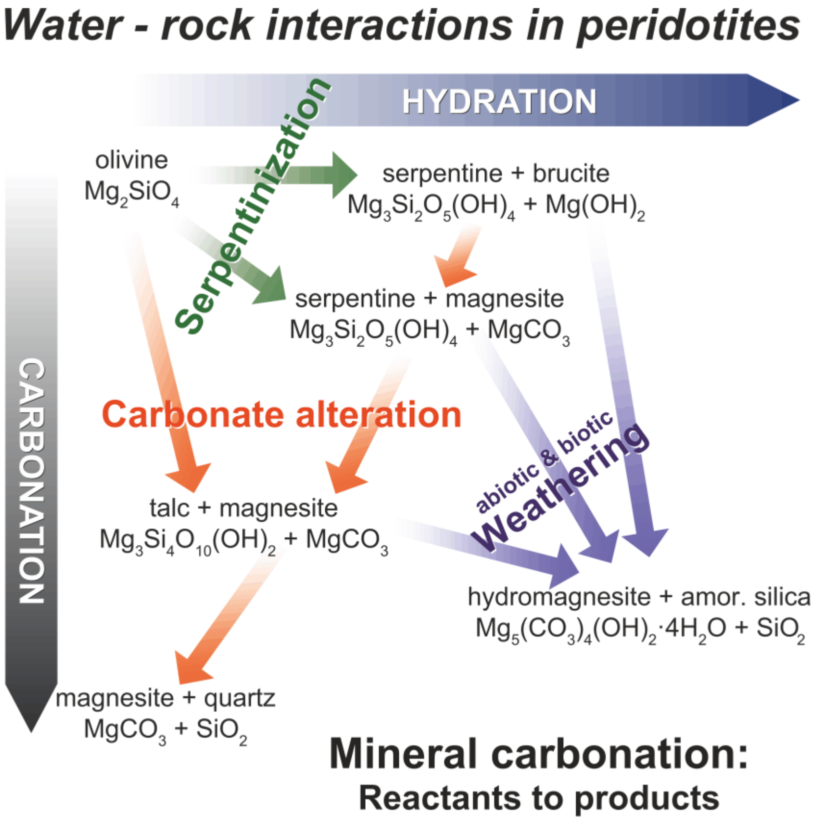

Figure 1.3. *Possible reaction pathways of peridotite and serpentinite alteration at high and low temperatures. These processes include serpentinization, carbonation, and weathering of the rock, leading to different mineral assemblages (From Power et al., 2013).*

1.2.1 Serpentinization of mantle peridotites

Serpentinization takes place in a range of geological settings on Earth, and serpentinites are present in all ancient orogenic belts (Evans et al., 2013) (**Fig. 1.4a**). It mainly occurs at the seafloor (e.g., MORs, OCCs), where exposed oceanic mantle lithosphere comes in contact with seawater, and it continues during subduction of abyssal serpentinites and peridotites (**Fig. 1.4b**). Cannat et al. (2010) argued that serpentinites may constitute up to 25% of the top part of the oceanic lithosphere. In subduction zones, serpentinites occur near the base of the mantle wedge at depths greater than 10 km (Saumur et al., 2010). In some forearc environments, buoyant serpentinites have been exhumed to the seafloor along normal faults and other tectonic processes (e.g., Mariana forearc mud volcanoes; Mottl et al., 2004). This is evidence for the formation of serpentinites in the cold ($T < 650$ °C) leading edge of the mantle wedge in subduction zones when fluxed by fluids derived from pore waters or devolatilization of subducting slab lithologies (Fryer et al., 1999; Hyndman and Peacock, 2003).

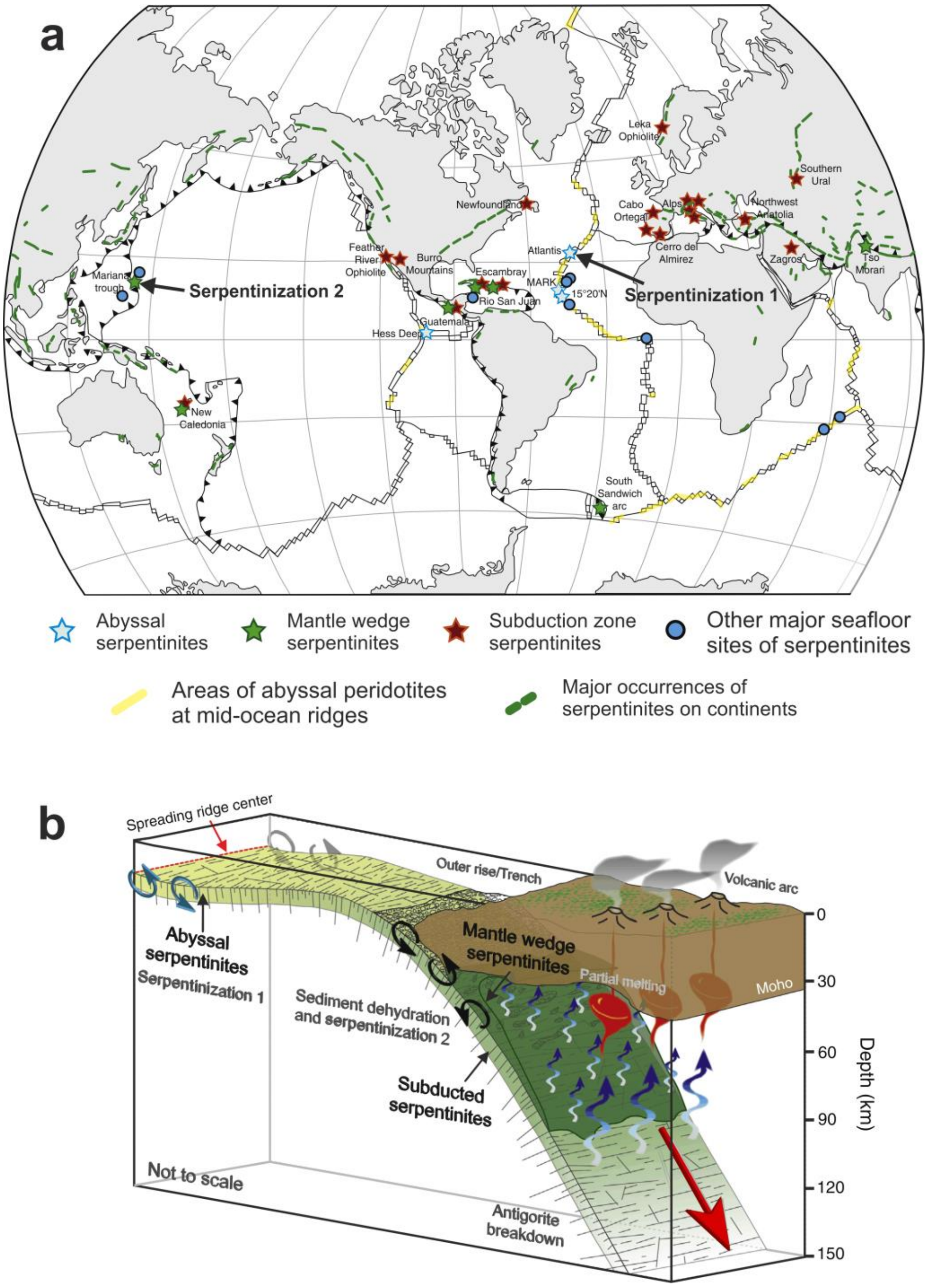

Figure 1.4. ***(a)*** *Worldwide occurrences of abyssal serpentinites (blue star) related to MORs (serpentinization 1), subducted (red star) and mantle wedge serpentinites (green star) (serpentinization 2), major occurrences of serpentinites on continents (green lines) and on seafloor (blue circles), as well as areas of abyssal peridotites at MORs (yellow lines).* ***(b)*** *Schematic sketch illustrating the geological environment of abyssal peridotite serpentinization (serpentinization 1) at MORs, as well as during subduction (serpentinization 2). (after Deschamps et al., 2013; Warren, 2016).*

Serpentinization is a pivotal hydrothermal alteration process of ultramafic rocks that produces unique geochemical environments under unusual geological conditions. Many reports focused on the construction of possible reactions defining mineralogical assemblages during serpentinization (Bach et al., 2006; Frost and Beard, 2007; Kelemen et al., 2011; Klein et al., 2009; Klein and Garrido, 2011; Palandri and Reed, 2004). Fluid-rock interaction reactions result in the transformation of olivine and pyroxene, mainly into hydrous Mg-Fe-phyllosilicates (e.g. serpentine), Mg-hydroxides (brucite), Fe-oxides (e.g. magnetite) and Mg-Ca-carbonates (e.g. magnesite and calcite). Serpentinization demonstrates a variety of different reaction types including hydration (**Eq. 1.1, 1.2**), iron oxidation (**Eq. 1.3**) and carbonation (**Eq. 1.4, 1.5**):

Hydration reactions:

$$3Mg_2SiO_4\ (s) + SiO_2\ (aq) + 6H_2O\ (l) \rightarrow 2Mg_3Si_2O_5(OH)_4\ (s) \tag{1.1}$$

$$4Mg_2SiO_4\ (s) + 6H_2O\ (l) \rightarrow 2Mg_3Si_2O_5(OH)_4\ (s) + 2Mg(OH)_2\ (s) \tag{1.2}$$

Iron oxidation reaction:

$$6Fe_2SiO_4\ (s) + 7H_2O \rightarrow 3Fe_3Si_2O_5(OH)_4\ (s) + Fe_3O_4\ (s) + H_2\ (g) \tag{1.3}$$

Carbonation reactions:

$$4Mg_2SiO_4\ (s) + 4H_2O\ (l) + 2CO_2\ (g) \rightarrow 2Mg_3Si_2O_5(OH)_4\ (s) + 2MgCO_3\ (s) \tag{1.4}$$

$$4Mg_2SiO_4\ (s) + CaMgSi_2O_6\ (s) + 6H_2O\ (l) + CO_2\ (g) \rightarrow 3Mg_3Si_2O_5(OH)_4\ (s) + CaCO_3\ (s) \tag{1.5}$$

At relatively low temperatures (< 150 °C), the reactions result in extremely high pH, commonly above 10. Hyperalkalinity is caused by the OH^- production during the dissolution of the host rock silicates (Palandri and Reed, 2004), and can be further supplemented by the concomitant OH^- and H_2 production during the oxidation of Fe^{2+} contained in the silicates to Fe^{3+} (**Eq. 1.3**) (Chavagnac et al., 2013a). The combination of the produced H_2 and CO_2 or CO under highly reducing conditions leads to the formation of methane (**Eq. 1.6**) and other organic compounds (Bach et al., 2004; Klein et al., 2014; McCollom and Bach, 2009; Ménez et al., 2018).

$$4H_2\ (g) + CO_2\ (g) \rightarrow CH_4\ (g) + 2H_2O\ (l) \tag{1.6}$$

The combination of redox gradients, abiotic production of hydrogen, and higher carbon molecules make serpentinization environments strong candidates to host the emergence of life on Earth or even other planets (Ménez et al., 2012; Russell et al., 2010).

In continental settings, ultramafic rocks share the same chemical characteristics of hydrothermal systems in seafloor peridotite: reaction of meteoric water with peridotites results in the development of high-pH, production of H_2 and CH_4, and precipitation of Ca-Mg-carbonates (e.g., Barnes and O'Neil 1969; Boulart et al., 2013; Bruni et al. 2002; Kelley et al. 2005; Neal and Stanger 1985; Paukert et al., 2012).

1.2.2 Weathering of serpentinized rocks

In principle, peridotites are considered low-permeability crystalline rocks, although a fraction of sufficient rainfall can be stored in shallow and weathered layers (Andreo et al., 1993; Andreo and Gervilla, 2007). The weathering rate of serpentinized rocks is strongly related to carbonation rates and the viability engineered solutions for carbon capture and storage (Matter and Kelemen, 2009; Power et al., 2013). The weathering rate of partially or completely serpentinized peridotites is controlled by many factors such as rock composition, climate, water chemistry, pH, and biological activity (Baumeister et al., 2015; Hausrath et al., 2008; Lewis et al., 2006; Power et., 2013). Serpentine minerals are relatively unstable in near-surface conditions and weather quickly into other layer silicates, such as smectite and vermiculite (Dixon, 1989; Hseu et al., 2007; Rabenhorst et al., 1982). Baumeister et al., (2015) underlined the importance of the rock porosity and initial composition of serpentine minerals, reporting the mineral dissolution sequence in weathered serpentinites from the Klamath Mountains (California, U.S.A.). The sequence from most to least weathered was Fe-rich pyroxene > antigorite > Mg-rich lizardite > Al-rich lizardite, showing the critical role of pyroxene content and Fe, Mg and Al proportions in the minerals of the rock. Moreover, microbial activity may enhance the dissolution of serpentinized peridotites and induce carbonate precipitation in weathering environments (e.g., hydromagnesite – magnesite playas; Power et al; 2014; Renaut and Stead, 1990), by altering the water chemistry, pH, and redox conditions (Ferris et al. 1994; Schwartzman and Volk 1989).

Similar to serpentinization-related fluids, the interaction reactions during weathering of peridotites alters the chemical composition of the circulating waters from meteoric into Mg-Si-rich, alkaline ($pH = 8 - 9.5$) waters (e.g., Barnes and O'Neil 1969; Neal and Stanger 1985;

Palandri and Reed, 2004). Carbonation of serpentinites due to weathering has been reported in various environments such as alkaline springs (Kelemen and Matter, 2008; Matter and Kelemen 2009), hydromagnesite playas (Power et al., 2009), and serpentinite mine shafts and tailings (Beinlich and Austrheim, 2012). Hydrated Mg-carbonate minerals are associated with low-temperature weathering environments of serpentine minerals and brucite (e.g., Beinlich and Austrheim, 2012; O'Neil and Barnes, 1971; Power et al., 2014; 2019; Ulven et al., 2017). Their formation is likely related to uptake of atmospheric CO_2 by Mg-rich waters coupled to evapoconcentration (Power et al., 2019). Significant abundances of hydrated Mg-carbonate minerals may develop at depth as carbonated surfaces become buried or as a consequence of ongoing reaction after burial (e.g., Pronost et al. 2012). Continental weathering sequesters an estimated 300 million tonnes of CO_2 each year, while serpentinites contribute a disproportionately high share of weathering products despite representing only a small proportion of crustal rocks (Seifritz 1990).

1.3 Serpentinite-related alkaline waters in marine and continental environments

Alkaline fluids are strongly related to serpentinization and weathering of mantle rocks both in marine and continental settings. The produced alkaline waters (*cf. Sec. 1.2*) play a key role in the carbonation of the host rock, as well as in the capture of CO_2 after their discharge. Most studies of marine peridotite-hosted hydrothermal systems have focused on serpentinization near mid-ocean ridges (e.g., Charlou et al. 2002; Früh-Green et al. 2003; Kelley et al. 2001; Schmidt et al. 2007), while continental alkaline environments can be observed —together with the hosting peridotites— all around the globe (**Fig. 1.5**).

On-land alkaline waters can originate either from weathering or serpentinization of mantle rocks by meteoric water. These water-rock interactions alter the water chemistry, forming two evolved water types of entirely different chemical composition. In shallow aquifers, reactive meteoric water generates $Mg–HCO_3$-rich waters via weathering of peridotite. Deeper water percolation produces a highly alkaline Ca–OH-rich groundwater, probably influenced by serpentinization. The Oman Ophiolite is the most typical location to observe both $Mg–HCO_3$-rich and Ca–OH-rich water types emerging from partially serpentinized peridotites (e.g., Chavagnac et al., 2013a; Neal and Stanger, 1985; Paukert et al., 2012).

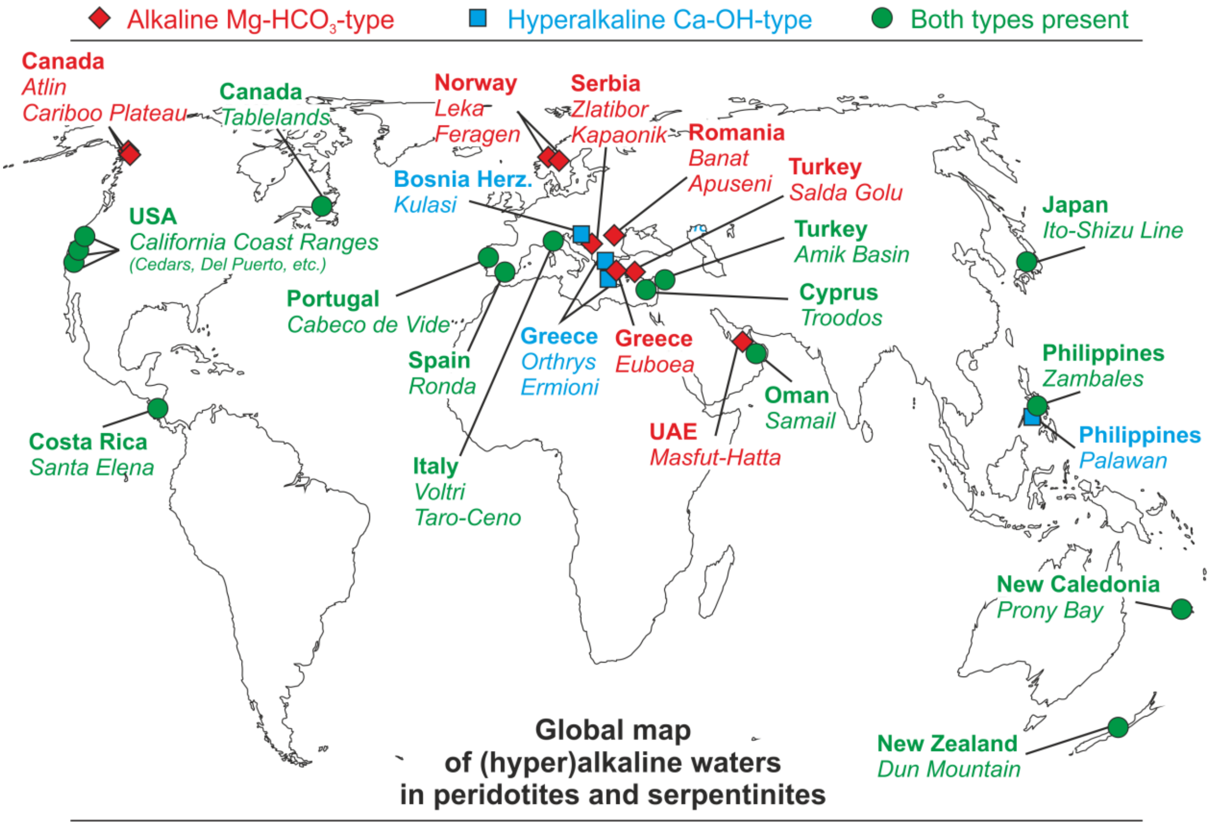

Figure 1.5. *Global map showing the sites hosting alkaline to hyperalkaline waters related to peridotites and serpentinites. In red are the sites hosting only Mg–HCO_3-type waters. In blue are the sites hosting only Ca–OH-type waters. In green are the site hosting both types of waters.*

However, several localities of alkaline waters worldwide have been studied, where one or both water types are present; U.A.E.: Uqba, 1991; Etiope et al., 2015, U.S.A.: Barnes et al., 1972; Blank et al., 2009; Morrill et al., 2013, Canada: Power et al, 2014; Szponar et al.,2013, Costa Rica: Sánchez-Murillo et al., 2014, New Caledonia: Monnin et al, 2014, New Zealand: Pawson, 2015, Philippines: Cardace et al., 2015, Japan: Homma and Tsukahara, 2008; Suda et al., 2017, Turkey: D'Alessandro et al., 2016; Russell et al., 1999; Yuce et al., 2014, Serbia: Doljak et al., 2016; Oudech and Djokic, 2015; Todorovic et al., 2016, Bosnia and Herzegovina: Barnes et al., 1978; Etiope et al., 2017; Miocic and Samardzic, 2016, Cyprus: Neal and Shand, 2002, Italy: Boschetti and Toscani, 2008; Bruni et al., 2002; Cipolli et al., 2004, Romania: Nicula and Baciu, 2019; Rosca et al., 2016, Norway: Beinlich and Austrheim, 2012; Daae et al., 2013; Okland et al., 2012, Greece: D'Alessandro et al., 2018; Etiope et al., 2013; Voutsis et al., 2015, Portugal: Marques et al., 2008, and Spain: Etiope et al., 2016. Hydromagnesite playas in Atlin (Canada) and serpentinite mine tailings in Feragen ophiolites (Norway) are two characteristic examples of Mg–HCO_3-rich waters generation due to weathering of ultramafic rocks (e.g., Beinlich and Austrheim, 2012; Power et al., 2014).

Occurrences of CH_4 and H_2 have been broadly documented in marine serpentinite-hosted hydrothermal fields (e.g., Lost City), and serpentinization-driven hyperalkaline springs (e.g., Oman, Philippines, Italy, among others; see Etiope and Whiticar, 2019). The observed variability of H_2/CH_4 ratios in the different gas-producing sites worldwide may reflect different stages of serpentinization that produce fluids from H_2-dominated (e.g., Lost City, Semail, Oman) to CH_4-dominated (Voltri, Italy) (Boulart et al., 2013).

1.3.1 Hydrothermal vents of alkaline fluids in marine serpentinites

Hydrothermal activity in marine environments (**Fig. 1.6**) plays an essential role in Earth's evolution by modifying the composition of oceanic crust, affecting ocean chemistry, forming ore deposits, global element cycles, and providing energy for thriving microbial communities. Also, serpentinization and carbonation of peridotite are exothermic processes and may contribute to hydrothermal circulation (Schuiling 1964; Fyfe 1974; Kelley et al. 2001; Emmanuel and Berkowitz 2006).

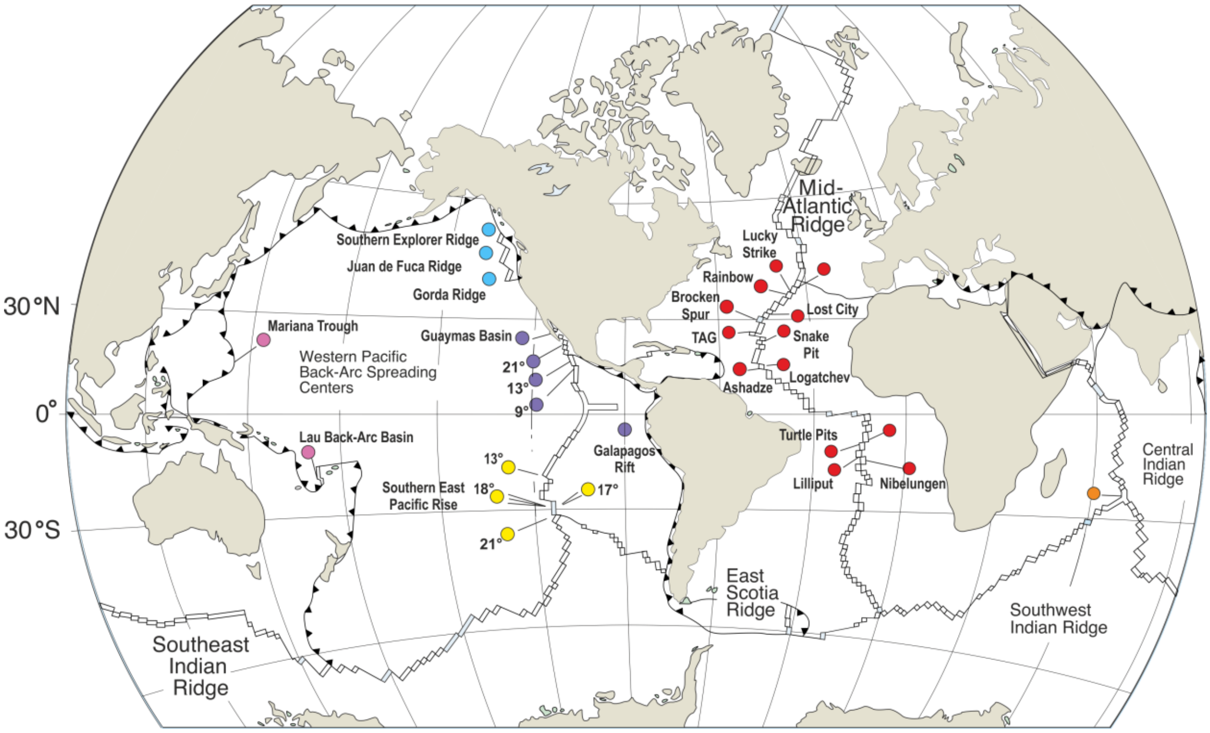

Figure 1.6. *Map of major hydrothermal vents at MORs and subduction zones (From Konn, 2009).*

Along divergent margins, numerous marine hydrothermal systems of high temperature (> 300 °C), high metal concentration, and acidic pH (2 – 3) have been discovered in serpentinized ultramafic rocks (e.g., Longatchev; Batuev et al., 1994). Unlike these systems, Lost City is the only known serpentinization-driven hydrothermal field (**Fig. 1.7**) that shows relatively low temperature (40 – 90 ºC), high pH (9 – 11), high H_2/CH_4 ratios, and low metal concentrations (Kelley et al., 2001; Kelley et al., 2005; Proskurowski et al., 2006). This system is hosted in serpentinized peridotites of an oceanic core complex (Atlantis massif) near the Mid-Atlantic Ridge at 30 °N. The discharge of the active venting fluids into the seawater leads to the formation of large carbonate chimneys (up to 60 m above the seafloor), which consist of variable mixtures of calcite, aragonite and brucite (Ludwig et al., 2005). The highly reducing conditions of the serpentinizing environments allow the development of abiotic organic compounds (Lang et al., 2010) and host a broad and specific community of microorganisms (Brazelton et al., 2006). Kelley et al. (2001) suggested that, whereas other vent sites have a magmatic heat source, Lost City may be heated by exothermic hydration of peridotite, while exothermic heating via peridotite carbonation may also be necessary (Kelemen and Matter 2008).

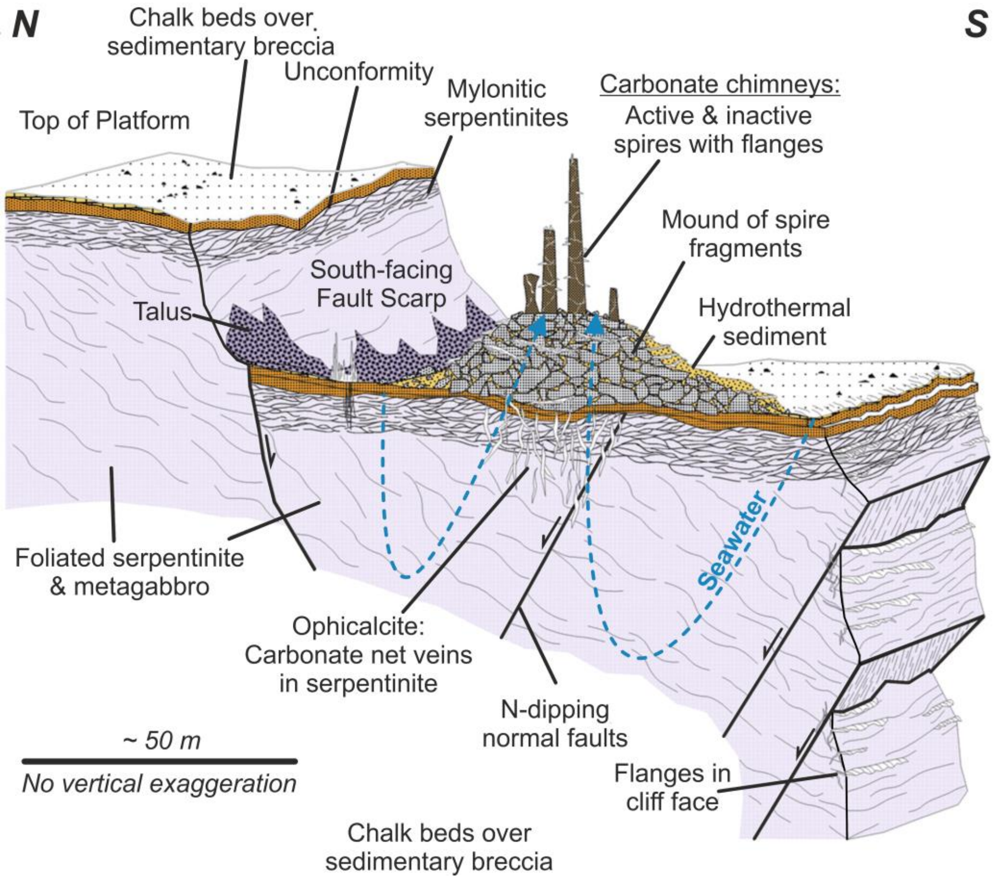

Figure 1.7. *Sketch showing geologic and tectonic relationships at Lost City. Hydrothermal structures are located on a faulted down-dropped block of variably altered and deformed crust composed predominantly of serpentinite. Active serpentinization of the peridotites by seawater generates alkaline fluids that form carbonate chimneys (calcite+aragonite+brucite) upon their discharge (After Kelley ey al., 2005).*

Even lower-temperature (< 40 °C), peridotite-hosted, hydrothermal alkaline vents form carbonate chimneys just offshore from Prony Bay in New Caledonia (Monnin et al., 2014). The existence of additional terrestrial low-salinity, high-pH waters that discharge into the New Caledonia southern lagoon creates a peculiar mixed subaerial – subaquatic alkaline spring system (Monnin et al., 2014).

In submarine forearc environments, the reaction of hanging wall peridotite above subduction zones with hydrothermal fluids is evidenced by serpentine mud volcanoes and associated carbonate chimneys (e.g., Mottl et al. 2004). In Mariana forearc, several low-temperature (~ 2 °C) hydrothermal systems are associated with serpentinite-hosted mud-volcanoes. These systems are H_2 – CH_4-producing, hyperalkaline (pH up to 12.5), and are able to sustain high biomass communities (Takai et al., 2005).

1.3.2 Aerial alkaline springs in continental settings

In continental settings, surface alkaline waters (e.g., springs, playas) and aquifers in serpentinized peridotites are the manifestations of low-temperature alteration and weathering of their host rocks. The vast majority of these alkaline environments are located in ophiolites (e.g., Oman, U.S.A., Cyprus, Norway, New Zealand, among others), while few sites are hosted in subcontinental mantle orogenic peridotites (e.g., Italy, Spain, Portugal). Low-temperature reactions between meteoric water and ultramafic rocks take place in many steps, based on different subsurface flow paths. These different flow paths dictate the generation of the two types of alkaline to hyperalkaline waters (**Fig. 1.8**).

The hydrolysis of ferromagnesian peridotite and serpentinite minerals by meteoric water in open —CO_2- and O_2-rich— shallow aquifers leads to the increase of Ca, Mg, Si, and dissolved inorganic carbon (DIC) in the water (**Eq. 1.7**). These water-rock interactions result in the formation of mildly alkaline (pH = 7.5 – 9.5) Mg–HCO_3 groundwater, also known as Type I waters (e.g., Barnes et al., 1967; Barnes and O’Neil, 1969). These waters are strongly related to weathering of ultramafic rocks and precipitation of (hydrated) magnesium carbonate minerals, which is —in some cases— mediated by microorganisms (e.g., Power et al., 2009; McCutcheon et a., 2014; Renaut et al., 1993).

$$Mg_2SiO_4\ (s) + 4CO_2\ (g) + 2H_2O\ (l) \rightarrow 2Mg^{2+} + 4HCO_3^{-} + SiO_2\ (aq) \qquad (1.7)$$

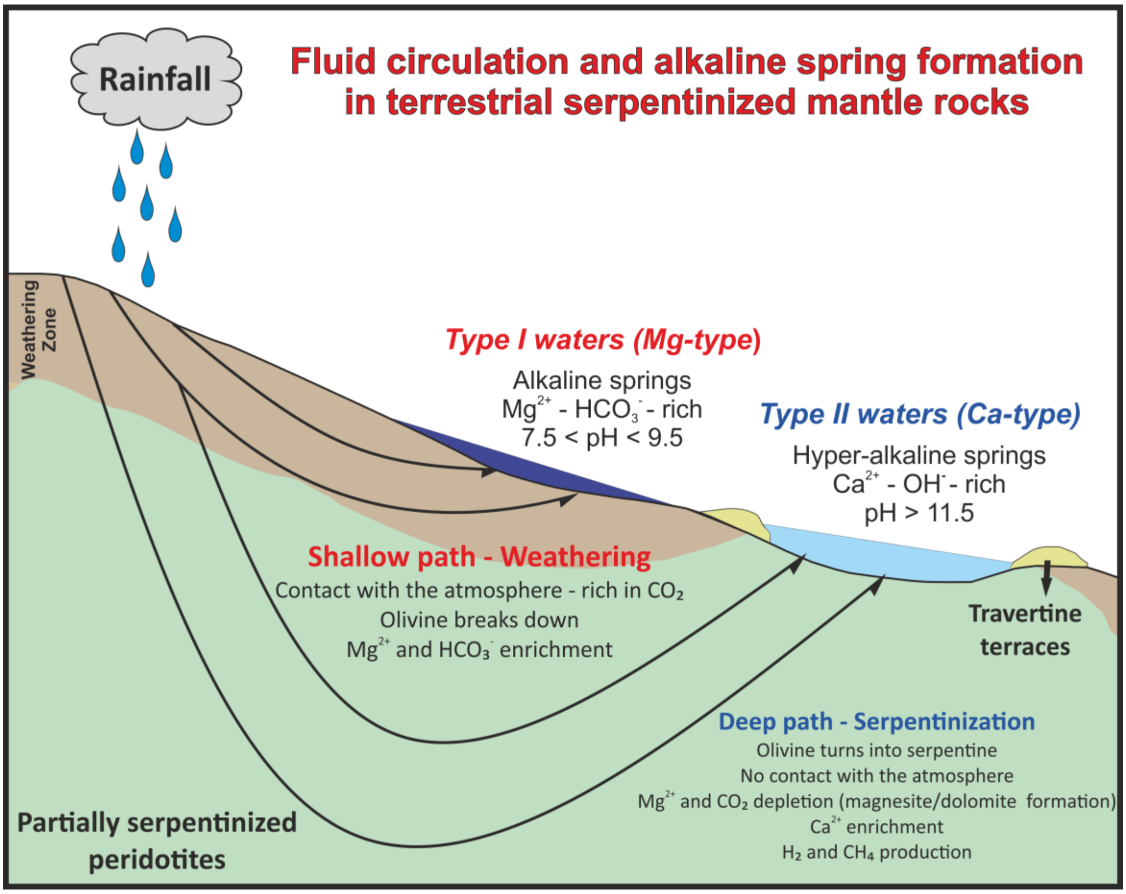

Figure 1.8. *Schematic illustration of the possible groundwater pathways leading to different water types in serpentinized peridotites. Type I (red) is CO_2-rich groundwater that follows near-surface pathways through the vadose zone and shallow fault systems. Weathering of the peridotite leads to the generation of $Mg–HCO_3$-type waters. Deeper fluid percolation and isolation from the atmosphere leads to the formation of CO_2-depleted Type II groundwater (blue). This process triggers serpentinization, creating hyperalkaline Ca–OH-type waters. Travertine terraces form by Ca–OH waters via CO_2 uptake. (after Mervine et al., 2014).*

Deeper meteoric or already evolved water (e.g., Mg-HCO_3-type) infiltration in the peridotites, cutting off the contact with the atmospheric CO_2 and O_2. These isolated waters become hyperalkaline (pH up to 12) due to H^+ consummation and OH^- release during dissolution reactions of Fe-Mg-silicates (**Eq. 1.8**) that can be enhanced by iron oxidation reactions (Chavagnac et al., 2013a; Kelemen et al., 2011; Palandri and Reed, 2004). The chemical profile of these waters is characterized by very low Mg and DIC concentrations, as reaction with the peridotites results in the formation of serpentine and carbonate minerals. Although both Mg and Ca are released from primary forsterite and pyroxenes, Mg is preferentially incorporated into reaction products such as serpentine, brucite, and magnesite. Thus, although Ca is a minor constituent of the peridotite, contained mainly in pyroxene minerals, its concentration in the generated waters rises, as it is excluded almost completely from serpentine and clay minerals (Kelemen et al., 2011).

$$4Mg_2SiO_4 + CaMgSi_2O_6 + 7H_2O = 3Mg_3Si_2O_5(OH)_4 + Ca^{2+} + 2OH^- \quad (1.8)$$

When the hyperalkaline waters emerge to the surface, they react with the atmosphere or mix with shallow groundwater or surface waters. These processes feed the waters with CO_2 and trigger Ca-carbonate precipitation in the form of travertine terraces, stream conglomerates, and shallow vein networks (**Eq. 1.9**).

$$Ca^{2+}(aq) + 2OH^-(aq) + CO_2\,(aq\ or\ g) = CaCO_3\ (s) + H_2O\ (l) \quad (1.9)$$

Other secondary minerals reported co-existing with Ca-carbonates in alkaline springs include mainly brucite, and traces of hydromagnesite, dypingite and layered double hydroxides (e.g., Anraku et al., 2009; Chavagnac et al., 2013b; Neal and Stanger, 1984; Mervine et al., 2014; Olsson et al., 2014).

The present research investigates the geochemistry and mineralogy in alkaline spring systems from serpentinized ultramafic rocks in ophiolites (Oman) and orogenic subcontinental peridotites (Ronda, Spain) that host both Mg–HCO_3-type and Ca–OH-type waters generated by weathering and serpentinization, respectively.

1.4 Crystallization experiments in the MgO–CO_2–H_2O system at low temperature

The formation of Mg-carbonate minerals during the weathering of silicates and hydroxides is a naturally occurring process that could be utilized to store CO_2 artificially. Numerous geo-engineered carbon mineralization proposals have been evaluated at laboratory and pilot-scale, involving subsurface injection of CO_2 into basalts and peridotites (Gislason and Oelkers, 2014; Kelemen and Matter, 2008; Matter et al., 2016; Power et al., 2013a, b), passive carbonation of ultramafic mine tailings (e.g., Beinlich and Austrheim, 2012; Harrison et al., 2013; McCutcheon et al., 2015; Power et al., 2010; Wilson et al., 2009), and accelerated mineralization using high pressure–high temperature reactors (Gerdemann et al., 2007; Lackner et al., 1995). Another related approach for CO_2 sequestration that can also induce carbonate precipitation is enhanced weathering. This process artificially accelerates the natural weathering and requires the emplacement of fine-grained mafic or ultramafic rocks in natural weathering environments (e.g., Hartmann et al., 2013; Montserrat et al., 2017; Rigopoulos et al., 2018). In addition to their natural occurrence and use for CO_2 storage, hydrated Mg-carbonates are promptly linked to the construction of engineered barriers for nuclear waste storage (Xiong and Lord, 2008), exploitation of Mg resources, (Cheng et al., 2009; Cheng and Li, 2009; Dong et al., 2008; Wang et al., 2008), and MgO production (Cheng et al., 2009; Wang and Li, 2012).

Assessment of the CO_2 storage capacity and security requires knowledge of the stability, solubility, and formation sequence of the carbonate minerals. The relative stability and solubility of numerous Mg-carbonates has been investigated (e.g., Ballirano et al., 2013; Bénézeth et al., 2011; Berninger et al., 2014; Gautier et al., 2014; Hänchen et al., 2008; Harrison et al., 2019; Hopkinson et al., 2008, 2012; Königsberger et al., 1999; Xiong, 2011; Zhang et al., 2006). **Table 1.1** lists the most common $MgCO_3$-bearing phases that have been discovered and investigated so far in nature and laboratory experiments. In general, more hydrated Mg-carbonate phases are more stable than less hydrated phases: magnesite > hydromagnesite > dypingite > nesquehonite > lansfordite (Canterford et al., 1984; Langmuir, 1965). For example, dypingite can be a precursor for the formation of hydromagnesite (Davies and Bubela, 1973; Hopkinson et al., 2008), a mineral suitable for safe CO_2 storage at surface conditions (e.g., Power et al., 2009; 2014). Furthermore, the transformation processes of metastable Mg-carbonates play a key role in the isotopic signature for tracing CO_2 cycling and sequestration (e.g., Beinlich and Austrheim, 2012; Falk et al., 2016; Oskierski et al., 2013, 2016; Mervine et al., 2014; Shirokova et al., 2013), and assessing the mobility of toxic metals that can be incorporated in the crystal structure (Hamilton et al., 2016).

Table 1.1 *Most common $MgCO_3$-bearing phases and their chemical formulas.*

No. of MgO/mol	No. of H_2O/mol	No. of CO_2/mol	Compound	Chemical formula
1	-	1	Magnesite	$MgCO_3$
1	2	1	Barringtonite	$MgCO_3·2H_2O$
1	3	1	Nesquehonite	$MgCO_3·3H_2O$
1	5	1	Lansfordite	$MgCO_3·5H_2O$
2	1.5	1	Pokrovskite	$Mg_2(CO_3)(OH)_2·0.5H_2O$
2	4	1	Artinite	$Mg_2(CO_3)(OH)_2·3H_2O$
5	5	4	Hydromagnesite	$Mg_5(CO_3)_4(OH)_2·4H_2O$
5	6	4	Dypingite	$Mg_5(CO_3)_4(OH)_2·5H_2O$
5	5-6	4	Giorgiosite	$Mg_5(CO_3)_4(OH)_2·5\text{-}6H_2O$
7	25	5	Shelkovite	$Mg_7(CO_3)_5(OH)_4·24H_2O$

Due to the strong hydration of aqueous Mg, the formation of magnesite is kinetically inhibited at low temperatures and is rarely observed to form in crystallization experiments at temperature < 60 °C (e.g., Deelman, 2011; Hänchen et al., 2008; Saldi et al., 2009;). Instead, hydrated Mg-magnesium carbonates are consistently identified in field and laboratory studies, often co-existing and transforming under variable conditions (e.g. Ballirano et al., 2013; Davies and Bubela, 1973; Hopkinson et al., 2008; Harrison et al., 2015; Power et al., 2014; Wilson et al., 2009). The unclear precipitation mechanisms and wide range of potential occurrence of multiple metastable hydrated Mg-carbonates, makes difficult the prediction for the formation of a specific phase, and thus the evaluation of the CO_2 storage efficiency (Hänchen et al., 2008; Hopkinson et al., 2008; Königsberger et al., 1999; Kristova et al., 2014; Montes-Hernandez et al., 2012).

Nesquehonite and dypingite are the most common phases during the interaction of Mg-rich waters with CO_2 at low temperatures, with nesquehonite forming by equilibrated with the atmosphere waters and/or evaporative conditions (Königsberger et al., 1999; Power et al., 2007; Schaef et al., 2011; Xiong and Lord, 2008; Zhao et al., 2010), while dypingite under lower than the atmospheric P_{CO_2} values and/or presence of microbial activity (e.g., Mavromatis et al., 2012; McCutcheon et al., 2014; Power et al., 2007; Shirokova et al., 2013; Wilson et al., 2010). Nesquehonite, dypingite and hydromagnesite are thoroughly examined via a large number of studies regarding its thermal stability (e.g., Ballirano et al., 2010; Jauffret et al., 2015; Lanas and Alvarez, 2004; Morgan et al., 2015), and the impacts of temperature, pH, saturation state, solubility, and solution composition on nucleation, kinetics, and crystal morphology and size (Chaka et al., 2014, 2016; Cheng et al., 2009; Cheng and Li, 2010; Ding et al., 2016; Di Lorenzo et al., 2014; Hanchen et al., 2008; Harrison et al., 2019; Wang et al., 2008; Wang and Li, 2012; Zhang et al., 2006; Zhao et al., 2013). However, further experimental study on the factors and mechanisms controlling crystallization sequences and textural features of hydrated Mg-carbonates is required in order to shed light on the conditions, under which they nucleate, grow and transform.

1.5 Geological setting of the study areas

1.5.1 Serpentinized peridotites in the Semail Ophiolite, Oman

The Samail Ophiolite, located in the Sultanate of Oman and the United Arab Emirates, is considered the largest and best-exposed ophiolite in the world. The ophiolite is a thrust sheet of oceanic crust and upper mantle that was emplaced onto the Arabian continental margin during the closure of the Tethyan ocean in the late Cretaceous (initiated ~95 Ma; Coleman 1981; Hacker et al. 1996).

The mantle section is underlain by the metamorphic sole (metamorphosed oceanic sediments and volcanic rocks), the relatively unmetamorphosed oceanic sediments and volcanic rocks of the allochthonous Hawasina nappes, and the autochthonous continental shelf and parautochthonous continental slope deposits (thick carbonate deposits resting on pre-Permian crystalline basement) (Glennie et al., 1974). Tilting and erosion have exposed ophiolite sections from 0 to 15 km below the paleo-seafloor, providing outcrop exposures of igneous and hydrothermal processes at oceanic spreading centers (e.g., Gregory and Taylor 1981; Kelemen et al. 1997; Pallister and Hopson 1981; Van Tongeren et al. 2008).

Many studies have focused of hydrothermal processes in the lower crust (e.g., Bosch et al., 2004; Van Tongeren et al. 2008), as well as on mantle peridotite hydration and carbonation (e.g., Mervine et al., 2014; Paukert et al., 2012). In Oman, carbonate-altered peridotite is present as travertine and carbonate veins in serpentinized peridotite associated with active hyperalkaline waters, and fully-carbonated listvenite, representing older high-temperature systems. The hydrology and the geochemistry of groundwater and mineral deposits associated with alkaline springs formed have been documented in a series of studies in the last 40 years (e.g., Dewandel et al., 2004, 2005; Matter et al., 2006; Neal and Stanger 1983, 1984, 1985; Stanger 1986; Stanger et al. 1988; Stanger and Neal 1994; Weyhenmeyer, 2000). Clark and co-workers studied the stable isotope and radiocarbon record of travertine formation from peridotite-hosted alkaline springs (Clark and Fontes 1990; Clark et al. 1992). Recent studies have investigated these alkaline systems in greater detail, adding extensive mineralogical analyses, isotopic data, quantitative estimates of carbonation rates and geochemical reaction path models (e.g., Chavagnac et al. 2013a, b; Kelemen and Matter 2008; Kelemen et al. 2011; Matter and Kelemen 2009; Paukert et al. 2012).

1.5.2 Subcontinental mantle peridotites in Ronda, SW Spain

The Ronda (S. Spain) and Beni Bousera (N. Morocco) peridotite massifs are segments of subcontinental lithospheric mantle tectonically emplaced on the internal metamorphic crustal units of the Betic and Rif belts, respectively (e.g., Afiri et al., 2011; Bruguier et al., 2009; Frets et al., 2014; Garrido et al., 2011; Reuber et al., 1982). These internal units correspond to the Alpujárride and Sebtide complexes exposed together with the Ronda and Beni Bousera massifs, respectively. They consist of metamorphic crustal rocks with an increasing metamorphic grade towards the contact with the peridotites, reaching granulite facies (Platt et al., 2013). The Ronda massif is one of the largest exposures of subcontinental lithospheric mantle, covering an area of c. 450 km^2. The massifs include the Ronda, Ojén, and Carratraca peridotite bodies, and they are composed mainly of spinel lherzolites, harzburgites, minor dunites, and subordinate pyroxenite layers that are generally parallel to the foliation of their host peridotites (e.g., Garrido et al., 2011; Garrido and Bodinier, 1999; Lenoir et al., 2001; Obata, 1980; Pearson et al., 1993; Reisberg, 1988). Mantle pyroxenites from Ronda massifs demonstrate a wider range of major element abundances and O isotopic variability than the peridotites, showing extreme variations in their Nd and Sr isotopic compositions (e.g., Frey et al., 1985; Garrido and Bodinier, 1999; Kumar et al., 1996; Obata, 1980; Varas-Reus et al., 2016). From top to bottom these, three main tectono-metamorphic domains have been recognized in the Ronda massifs (Frets et al., 2014; Lenoir et al., 2001; Soustelle et al., 2009; Van der Wal and Vissers, 1993, 1996; Varas-Reus et al., 2016):

i. Garnet-spinel mylonite domain, in direct contact with the overlying metamorphic crustal units and including stretched and boudinaged garnet pyroxenite layers.
ii. Spinel (± garnet) tectonite domain composed of highly foliated porphyroclastic spinel peridotites and garnet pyroxenite.
iii. Granular spinel peridotite domain that consists of coarse grained spinel peridotites with intercalated spinel pyroxenite layers.

In Ronda, a narrow (c. 200 – 400 m wide) recrystallization front has been observed and described at the transition between the spinel tectonites and granular peridotites (Van der Wal and Vissers, 1993; Lenoir et al., 2001; Vauchez and Garrido, 2001). Ronda massifs are characterized by a late plagioclase tectonite domain that overprints the other domains, and attests for partial re-equilibration of peridotites in the plagioclase lherzolite facies (Hidas et al., 2013a, 2015; Lenoir et al., 2001; Van der Wal and Vissers, 1996). According to several geochronological studies in peridotites and pyroxenites, and in their metamorphic country rocks (e.g., Esteban et al., 2011; Loomis, 1975; Pearson and Nowell, 2004; Reisberg et al., 1989), the emplacement of both Ronda peridotites took place early Miocene (19 – 23 Ma). This emplacement was probably triggered by rapid extension, producing an extremely attenuated continental lithosphere in the westernmost Mediterranean (e.g., Platt et al., 2005).

In the peridotite massifs, most rainfall generates surface runoff and only a small fraction infiltrates in the weathered zone (Andreo and Gervilla, 2007). The discharge of groundwater occurs as streams/rivers and springs with weak flow rates. The surface streams and rivers are slightly mineralized (electrical conductivity = 100 – 200 μS/cm), and show circum-neutral pH values (7 – 9) (Etiope et al., 2016). Numerous spring waters are widespread in the peridotites due to the deep circulation of water along the main faults of the peridotite massifs (Vadillo et al., 2015). These types of springs are hyperalkaline and they are characterized by dissolved CH_4 (0.1 – 3.2 mg/) of abiotic origin (Etiope et al., 2016).

2 Thesis Aims and Outline

2.1 Motivation

The present Ph.D. thesis is part of the European Commission FP–7 Marie Curie Initial Training Network (ITN) “ABYSS” on reactive geological systems from the mantle to the abyssal sub-seafloor. The objective of ITN ABYSS is to train Early Stage Researchers (ESR) in geodynamics, mineralogy, hydrodynamics, thermodynamics, and (bio)geochemistry of mid-ocean ridge processes and their environmental and economic impacts. The motivation behind the ITN ABYSS is to make significant advances and in the understanding of the coupled tectonic, magmatic, hydrothermal and (bio-) geochemical mechanisms that control the structure and composition of the oceanic lithosphere. One of the targets of the ABYSS project is to investigate the carbon mineralization in hydrothermally altered mantle rocks; in particular, explore the couplings between chemical, mechanical and hydrodynamic processes as well as the effect of transport, and fluid and rock compositions on rates and products of reactions in open hydrothermal systems.

Within the framework of the ABYSS project, the present thesis aims to contribute to a better understanding of the role of low-temperature carbonation in atmospheric carbon dioxide sequestration through the study of natural examples of carbon mineralization in serpentinization-related alkaline environments and the conduction of crystallization experiments of carbonate minerals. Moreover, the present Ph.D. thesis is part of the PROMETHEUS[1] project, an ERC Advanced Grant that aims to carry out an in-depth investigation of the nature of mineral structures and the role of mineral self-organization in extreme alkaline geological environments. The PROMETHEUS project seeks to improve our understanding of the early geological and biological history of Earth by pushing forward the unexplored field of inorganic biomimetic pattern formation. The investigation of geologically-feasible scenarios for early Earth conditions requires the investigation of the global scale serpentinization of ultramafic rocks under alkaline and highly reducing conditions, and the textural and morphological features of carbonate minerals precipitating from serpentinization-driven alkaline fluids.

---

[1] Project Prometheus (ERC Advanced Grant) (http://prometheus-erc.eu/).

2.2 Aims

The main objective of this Ph.D. thesis is to advance our understanding of serpentinization-related alkaline spring systems and associated precipitation of carbonate minerals under alkaline conditions. Serpentinization-driven, alkaline environments provide critical insights into the natural conditions for the capture of atmospheric carbon dioxide through carbon mineralization. To contribute to this main research goal, the present Ph.D. thesis aims to:

i. provide an additional account of how water composition, mixing, and mineral precipitation and textures co-evolve in serpentinization-driven alkaline spring systems in ophiolites.

ii. investigate alkaline spring sites in subcontinental mantle peridotites and associated mineralizations formed by the interaction between hyperalkaline fluids and river waters.

iii. experimentally investigate the crystallization sequence and morphologies of hydrated magnesium carbonates, and define the conditions under which their nucleation, crystal growth, and transformation take place.

These aims have been addressed through the study of natural alkaline springs hosted in exposed oceanic (Samail Ophiolite, Oman) and subcontinental mantle serpentinized peridotites (Ronda peridotites, Spain), and through carbonate crystallization experiments, to fill gaps in our current knowledge on the mechanisms and the conditions characterizing carbonate mineral precipitation in such systems.

To accomplish the first aim, I conducted a systematic sampling of waters and solids samples from two alkaline spring sites in the Wadi Tayin Massif of the Samail Ophiolite, Oman. The determination of water composition and detailed mineralogical and textural study of samples allowed us to examine the effects of geochemistry and hydrodynamics on mineral precipitation. This study complements our current knowledge of carbonation in serpentinization-related alkaline springs by providing thorough documentation of mineralogy, textures and crystal morphologies coupled to water geochemistry. I further used thermodynamic modeling to determine the saturation state of a wide range of minerals and compare it to the mineralogy and (macroscopic and microscopic) textural features of the precipitates collected from the alkaline water pools.

To address the second aim, I investigated water and solid samples from five alkaline spring sites in the Ronda peridotite massifs (SW Spain). The water samples included hyperalkaline fluids and river waters, and the solid samples involved mineral precipitates and travertines observed in the sampling sites. I carried out a detailed study of the chemical composition of the waters and the mineralogy and textures of the solid precipitates in order to determine the geochemical and mineralogical characteristics of the alkaline spring sites, and assess how the interaction between hyperalkaline fluids and river waters affects the mineral precipitation.

Finally, in order to tackle the third goal, I carried out a series of crystallization experiments in the $MgO–CO_2–H_2O$ system. The experiments involved unseeded mixing of lab-synthesized solutions in a closed and an open system . I monitored the crystallization sequence , morphological characteristics and changes in the solution pH to screen the conditions of hydrated magnesium carbonate precipitation under different reactant concentrations, pH, CO_2, and silica contents . The experiments provide new constraints on the nucleation , crystal growth, and transformation conditions and mechanisms of formation of hydrated magnesium carbonates.

2.3 Structure of the Thesis

The current Thesis comprises four main parts. **Part I** contains an introduction to the background and state-of-knowledge of the subject (**Chapter 1**), the research motivation, aims, and overview of the structure of the thesis (**Chapter 2)**. For clarity and consistency, the methodological aspects of the research are addressed in their respective chapters in Part II.

Part II includes **Chapters 3**, **4** and **5**, which present the main findings and results of the three aims of my Ph.D. thesis. **Chapter 3** addresses the first aim of the thesis, presenting a detailed study of the Samail Ophiolite (Oman) alkaline spring systems under a geochemical, mineralogical and hydrodynamical perspective. The results of this study have been published in the JCR journal *Chemical Geology*[2]. **Chapter 4** presents the results of the geochemical and mineralogical investigation of the alkaline spring sites in the Ronda peridotite massifs. This chapter has been published in the JCR journal *Lithos*[3]. **Chapter 5** is a draft of a manuscript that

---

[2] Giampouras, M., Garrido, C.J., Bach, W., Los, C., Fussmann, D., Monien, P., García-Ruiz, J.M., 2020. On the controls of mineral assemblages and textures in alkaline springs, Samail Ophiolite, Oman. *Chemical Geology*. DOI: https://doi.org/10.1016/j.chemgeo.2019.119435

[3] Giampouras, M., Garrido, C.J., Zwicker, J., Vadillo, I., Smrzka, D., Bach, W., Peckmann, J., Jiménez, P., Benavente, J., García-Ruiz, J.M., 2019. Geochemistry and mineralogy of serpentinization-driven hyperalkaline springs in the Ronda peridotites. *Lithos*. DOI: https://doi.org/10.1016/j.lithos.2019.105215

addresses the third aim of the thesis and reports the results of the experimental crystallization and morphogenesis of various hydrated magnesium carbonate phases under variable alkaline conditions.

Part III presents the main conclusions of the thesis and open questions for future investigations (**Chapter 6**). **Part IV** provides the bibliography used and references cited throughout the thesis.

In addition to the JCR publications cited above, the results of the present thesis have been disseminated at different international conferences and meetings, including a poster in the 5th International School of Crystallization (2016; Granada), a talk and a poster in the EGU General Assembly (2016; Vienna, Austria), a poster in the AGU Fall Meeting (2017; New Orleans, U.S.A.), a 3-minute thesis (3MT) presentation at the ABYSS Meeting (Granada, Spain, 2017), a poster in the Final FLOWS Conference (Granada; 2017), and a talk at the 5th Granada–Münster Discussion Meeting (Granada, Spain, 2017). The research of the thesis has further been communicated to the broader audience in one outreach article and one video in the ABYSS *SeaRocksBlog*[4].

---

[4] https://searocksblog.wordpress.com/2016/01/07/the-crystal-society-an-introduction/; https://searocksblog.wordpress.com/2016/05/19/an-ocean-on-land/

Part II

RESULTS

3 On the controls of mineral assemblages and textures in alkaline springs, Samail Ophiolite, Oman[1]

3.1 Introduction

Serpentinization-driven processes have recently been identified to affect a vast range of environments on the Earth's (sub-)surface. These processes are highly relevant for currently debated issues, such as carbon capture and storage (Kelemen et al., 2011; Kelemen and Matter, 2008; Matter and Kelemen, 2009; Seifritz, 1990), the deep carbon cycle (Alt et al., 2013; Dasgupta and Hirschmann, 2010; Kelemen and Manning, 2015; Menzel et al., 2018, 2019), the origin of life (Lane and Martin, 2010; Martin et al., 2008; Martin and Russell, 2007; Sleep et al., 2011), and the detection of primitive life (Garcia-Ruiz et al., 2003, 2017).

Serpentinization is the process of hydrothermal alteration of peridotite and other olivine-rich rocks, producing particular geochemical environments under different geological conditions (e.g., Schrenk et al., 2013). Many studies have provided insights into the diversity of the fluid-rock interaction reactions leading to different mineralogical assemblages during serpentinization processes (Bach et al., 2006; Frost and Beard, 2007; Kelemen et al., 2011; Klein et al., 2009; Klein and Garrido, 2011; Palandri and Reed, 2004). Depending on the fluid and rock compositions, fluid-peridotite reactions at moderate to low temperatures result in the transformation of primary olivine and pyroxene, mainly into hydrous Mg-Fe-phyllosilicates (e.g., serpentine), magnesium hydroxide (brucite), Fe-oxides (e.g., magnetite), and Ca-Mg-carbonates (e.g., magnesite and calcite).

The Lost City hydrothermal field (LCHF) is a characteristic example of marine serpentinization, and is hosted in an oceanic core complex (Atlantis massif) near the Mid-Atlantic Ridge at 30°N (Kelley et al., 2001). Fluids in LCHF show relatively low temperature (40 − 90 °C), high pH (9 − 11), high H_2/CH_4 ratio, and low metal concentrations (Kelley et al., 2005; Proskurowski et al., 2006). Active fluid venting leads to the formation of carbonate chimneys that consist of variable mixtures of calcite, aragonite, and brucite (Ludwig et al., 2006). In continental subaerial settings, serpentinization of ophiolites and subcontinental

---

[1] *This chapter has been published in Giampouras, M., Garrido, C. J., Bach, W., Los, C., Fussmann, D., Monien, P., & García-Ruiz, J. M., 2020. On the controls of mineral assemblages and textures in alkaline springs, Samail Ophiolite, Oman. Chemical Geology. DOI: https://doi.org/10.1016/j.chemgeo.2019.119435*

mantle peridotites by meteoric waters is typically linked to the formation of terrestrial alkaline spring systems (among others, in Oman: Chavagnac et al., 2013a; Neal and Stanger, 1985; Paukert et al., 2012, Turkey: Yuce et al., 2014, U.S.A.: Barnes et al., 1972; Blank et al., 2009; Morrill et al., 2013, Costa Rica: Sanchez-Murillo et al., 2014, Bosnia: Barnes et al., 1978, Cyprus: Neal and Shand, 2002, Italy: Bruni et al., 2002; Cipolli et al., 2004, Canada: Szponar et al., 2013, Portugal: Marques et al., 2008, and Spain: Etiope et al., 2016; Giampouras et al., 2019). There are also examples of mixed subaerial and subaquatic alkaline spring systems; Monnin et al. (2014) showed that serpentinization-affected meteoric water in Prony Bay (New Caledonia) discharges in a lagoon area, where it mixes with seawater forming carbonate concretions. In Aqua de Ney springs in California, Boschetti et al. (2017) suggested that the release of fossil seawater due to slab dehydration influenced the chemical profile of the hyperalkaline fluids before their discharge.

In terrestrial subaerial environments, the formation of the alkaline springs is the consequence of the infiltration and reactive percolation of meteoric waters in ultramafic rock aquifers. This process triggers numerous water-rock reactions that eventually lead to the generation of two distinctive types of waters, generally known as “Type I” and “Type II” waters (Barnes et al., 1967; Barnes and O’Neil, 1969). Type I waters are Mg^{2+}–HCO_3^--rich waters associated with shallow water flow paths in the ultramafic aquifer (**Fig. 3.1**), where waters are in equilibrium with the atmosphere and cause the chemical weathering of the host ultramafic rock minerals (**Eq. 3.1**) via reactions such as:

$$\underset{\textit{(Olivine)}}{4\ Mg_2SiO_4} + 4\ CO_2 + 2\ H_2O \rightarrow 2\ Mg^{2+} + 4\ HCO_3^- + SiO_2\ (aq) \qquad (3.1)$$

Type II waters are Ca^{2+}–OH^--rich and their genesis requires deeper reactive percolation flow paths through the ultramafic bedrock (**Fig. 3.1**), where groundwater becomes isolated from the atmosphere triggering low-temperature serpentinization of olivine and pyroxene (**Eq. 3.2)** via reactions such as:

$$\underset{\textit{(Olivine)}}{4\ Mg_2SiO_4} + \underset{\textit{(Pyroxene)}}{CaMgSi_2O_6} + 7\ H_2O \rightarrow \underset{\textit{(Serpentine)}}{3\ Mg_3Si_2O_5(OH)_4} + Ca^{2+} + 2\ OH^- \qquad (3.2)$$

Type II waters are hyperalkaline (pH >11) due to OH^- production during the dissolution of the host rock silicates (Palandri and Reed, 2004). The increase of the water pH could be supplemented by the concomitant OH^- and H_2 production during the oxidation of Fe^{2+} contained in the silicates to Fe^{3+} (Chavagnac et al., 2013a).

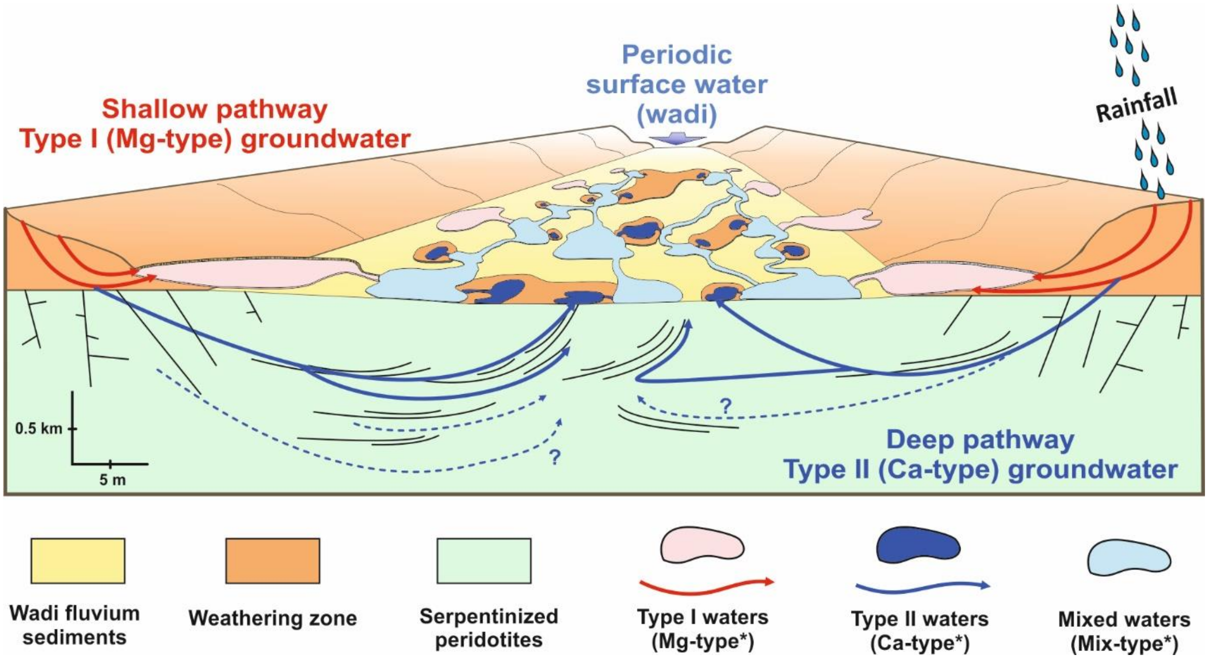

Figure 3.1. *Schematic illustration of the possible groundwater pathways and the different water types characterizing the spring systems. Modified after Mervine et al. (2014). Type I (red line) is CO_2-rich groundwater that follows near-surface pathways through the vadose zone and shallow fault systems. Deeper fluid percolation and isolation from the atmosphere leads to the formation of CO_2-depleted Type II groundwater (blue line). Mixing between these two waters upon discharge forms pools of mixed waters (light blue). Dashed lines show potential deeper water percolation in the peridotites. The horizontal scale represents only the frontal part of the sketch without taking into account the perspective of the image. *The terms "Mg-type", "Ca-type", and "Mix-type" are used in the present study to describe Type I, Type II, and mixed waters arising upon mixing between Type I and Type II waters, respectively.*

Studies of the terrestrial alkaline spring systems hosted in the Oman Ophiolite have provided a very detailed account of their geochemistry and mineralogy (69 sites in Neal and Stanger, 1983, 1984, 1985 and Stanger, 1986; 14 sites in Paukert et al., 2012; and 26 sites in Chavagnac et al., 2013a). These studies have identified the characteristic two water types previously described in terrestrial alkaline spring sites in ophiolites: moderately alkaline (pH = 7.5 − 9.5) Mg^{2+}–HCO_3^--rich (Type I), and hyperalkaline (pH > 11) Ca^{2+}–OH^--rich waters (Type II). The two water types mix upon their discharge and eventually form complex hydrological networks observed in different spring sites throughout the Oman Ophiolite (**Fig. 3.1**). Paukert et al. (2012) reported that these surface mixed waters are alkaline to hyperalkaline (pH between 8.5 and 11.9), showing variable Ca^{2+} (0.2 to 1.7 mmol/L), Mg^{2+} (0.02 to 2.5 mmol/L), and Dissolved Inorganic Carbon (DIC) (0.07 to 4.5 mmol/L) concentrations. In terms of their mineralogy, previous studies showed that calcium carbonate precipitation dominates the alkaline springs, while magnesium hydroxides are occasionally present. Hydromagnesite

(Mervine et al., 2014), dypingite (Olsson et al., 2014) and layered double hydroxides (LDH) (Anraku et al., 2009; Chavagnac et al., 2013b) have been reported in some spring sites.

In submarine serpentinite-hosted alkaline systems, mixing between discharging alkaline fluids and seawater is the key driver of mineral precipitation (Kelley et al., 2005; Ludwig et al., 2006). In terrestrial alkaline spring systems, mixing between differently sourced waters may also, govern the precipitation and cause much of the geochemical and mineralogical diversity in the alkaline springs (e.g., Chavagnac et al., 2013a, 2013b; Falk et al., 2016; Leleu et al., 2016; Morrill et al., 2013; Neal and Stanger, 1985; Paukert et al., 2012; Szponar et al., 2013). A trademark of the Oman alkaline springs is the well-developed hydrological systems formed by the coeval production and, subsequent mixing, of hyperalkaline (Ca^{2+}–OH^{-}-rich) and moderately alkaline (Mg^{2+}–HCO_3^{-}-rich) water types (Chavagnac et al., 2013a; Neal and Stanger, 1985; Paukert et al., 2012).

In this study, we investigated two individual spring sites in the Oman Ophiolite, where mixing of the two water types is widespread and imposes a primary control of water composition and mineral precipitation. Although similar studies have been previously carried out in the Oman alkaline springs (Chavagnac et al., 2013a, 2013b), the present research complements these studies by providing a thorough documentation of the mineralogy, textures and crystal morphologies coupled to a conceptual geochemical and mineralogical mapping of the different pools in the spring sites. We conducted a systematic —downstream— sampling of waters and solids from numerous pools in the spring sites with the aim to examine the function of the spring sites under a geochemical, mineralogical and hydrodynamical perspective. The joint collection of water and solid samples from the same pool (each sampling point) allows us to determine the saturation state of a wide range of minerals and compare it to the mineralogy and (macroscopic and microscopic) textural features of the precipitates. This detailed pool-by-pool investigation enables us to provide an additional account of how water composition, mixing, and mineral precipitation co-evolve in the alkaline spring systems.

3.2 Geological setting and alkaline spring sites

The Samail Ophiolite (Sultanate of Oman and the United Arab Emirates) is one of the largest exposures of oceanic lithosphere on land and is composed of twelve (12) distinct massifs lined up along the NE part of the Arabian plate (**Fig. 3.2a**). The ophiolites represent the topmost of a stack of nappes thrusted over autochthonous carbonate rocks (Hajar supergroup), which lie on top of a pre-Permian crystalline basement (e.g., Coleman, 1981; Glennie et al., 1973; Searle and Cox, 2002). The nappes consist of ~47 km of crustal rocks (layered gabbros, sheeted dikes,

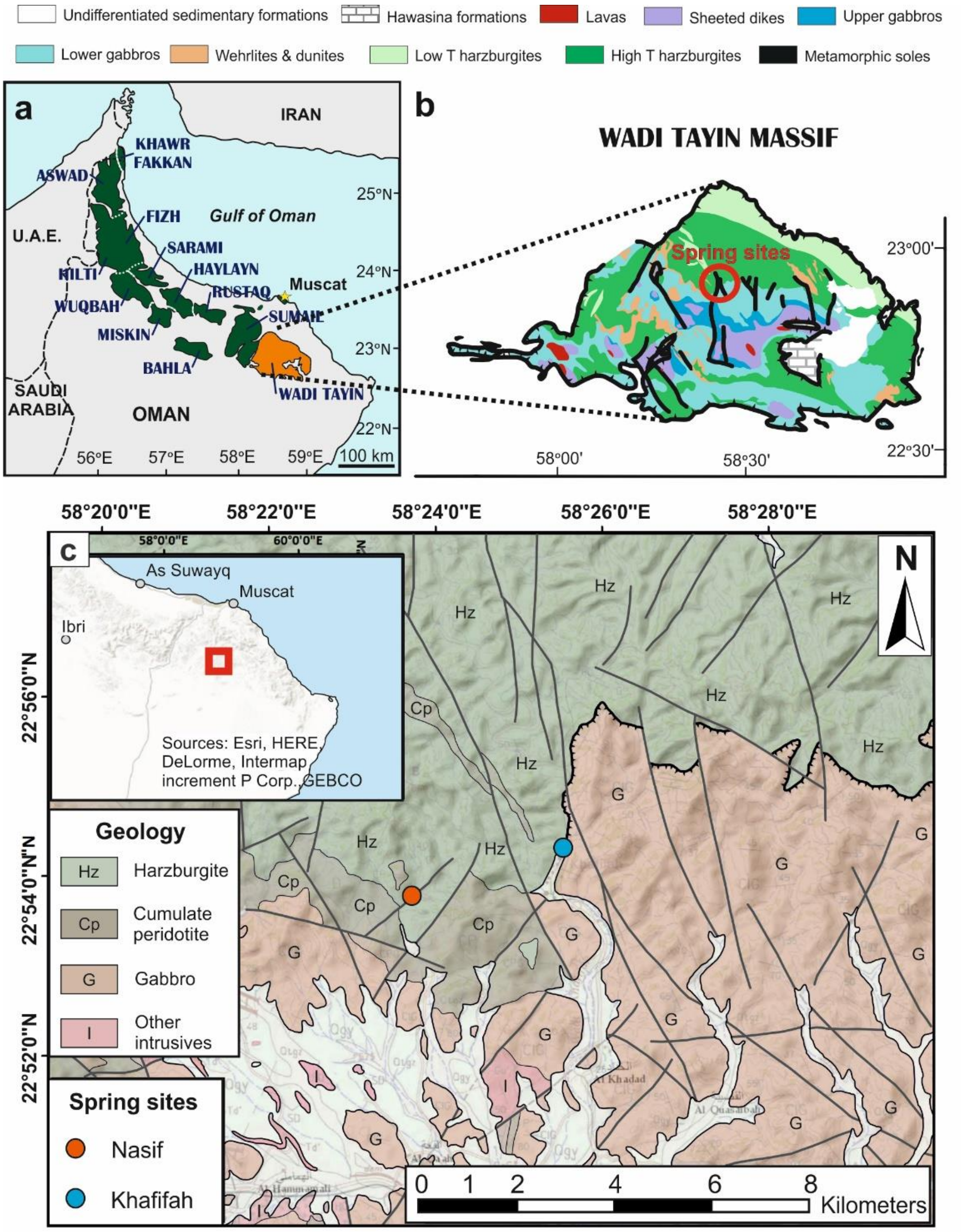

Figure 3.2. Geology of the studied spring sites in the Samail Ophiolite, Wadi Tayin massif, Sultanate of Oman. ***(a)*** *The Oman Ophiolite (green) is located in the northeastern part of the Arabian plate and is composed of twelve (12) large structural massifs (names indicated in blue). Modified after Godard et al. (2003).* ***(b)*** *Geology of Wadi Tayin massif (orange in* ***(a)****), where the present study took place. The sampling sites, Nasif and Khafifah, are located within the red circle. Modified after Nicolas et al. (2000).* ***(c)*** *Local geological map of the two spring sites, Nasif and Khafifah. Modified after de Gramont et al. (1986).*

and volcanics) and ~10 km of variably serpentinized (~30 − 80%) upper mantle section (harzburgites and dunites) (e.g., Coleman, 1981; Glennie et al., 1973; Godard et al., 2000; Hanghoj et al., 2010; Lippard et al., 1986; Monnier et al., 2006; Nicolas et al., 2000). A large portion of the serpentine has probably formed during sub-oceanic hydrothermal alteration prior to the exposure of the ophiolites on land (e.g., Boudier et al., 2010). However, the partially serpentinized peridotites continue to experience on-going water-rock interactions at low temperatures (< 60 °C) (Kelemen et al., 2011; Miller et al., 2016; Neal and Stanger, 1985; Streit et al., 2012).

The present study focuses on two alkaline spring systems; the Nasif and Khafifah sites (80 km south of Muscat; **Fig. 3.2c**). Both sites are hosted in partially serpentinized ultramafic rocks from the Wadi Tayin massif (**Fig. 3.2b**), and they host a number of springs and water pools that form complex hydrological networks (**Fig. 3.1**). The first site (Nasif: 58°23′39.03″E, 22°53′43.23″N) is located NNW of Al Hayema town in wadi Nasif, and is hosted in partially serpentinized harzburgites of the mantle section that are highly fractured and weathered. The second site (Khafifah: 58°25′30.87″E, 22°54′14.23″N) is located N of Al Hayema town in wadi Khafifah (also known as Qafeefah). The Khafifah site is located at the end of the southeastern oriented wadi Khafifah and is placed in partially serpentinized harzburgites with minor dunite. However, the valley that hosts the Khafifah site represents an important tectonic boundary, as it separates harzburgites of the mantle section from gabbros belonging to the crustal section. In earlier communications, the Nasif site has been referred to as “Les Lauriers Roses” and the Khafifah site as “Rencontre de la Colombe” (Chavagnac et al., 2013a, 2013b).

3.3 Methods

3.3.1 Field methods

3.3.1.1 Sampling

We collected fifty-five (55) solid samples of fresh precipitates and lithified structures associated with alkaline and hyperalkaline waters in the spring sites. The sites are characterized by active precipitation and sedimentation in the pools, and travertine terrace occurrnce over the ultramafic rocks. We classified the collected solid samples according to their macroscopic features and spatial distribution into five types: i) Crystalline crusts floating on the water surface (**Fig. 3.3a**), ii) rock coatings around the pool rims (**Fig. 3.3b**), iii) flocculent material covering the bottom of the pool and/or being in suspension within the water column (**Fig. 3.3c**),

iv) mud-like material forming dam-like formations (rippled terracing) and massive deposits within and adjacent to the pools (**Fig. 3.3d**), and v) lithified structures from active water flow areas (**Fig. 3.3e**) and travertine terraces (**Fig. 3.3f**). Lithified structures associated with active flow include dam-like formations and hardened concretions (**Fig. 3.3e**), whilst travertine terrace samples were collected from areas with no evident —at least currently— active flow.

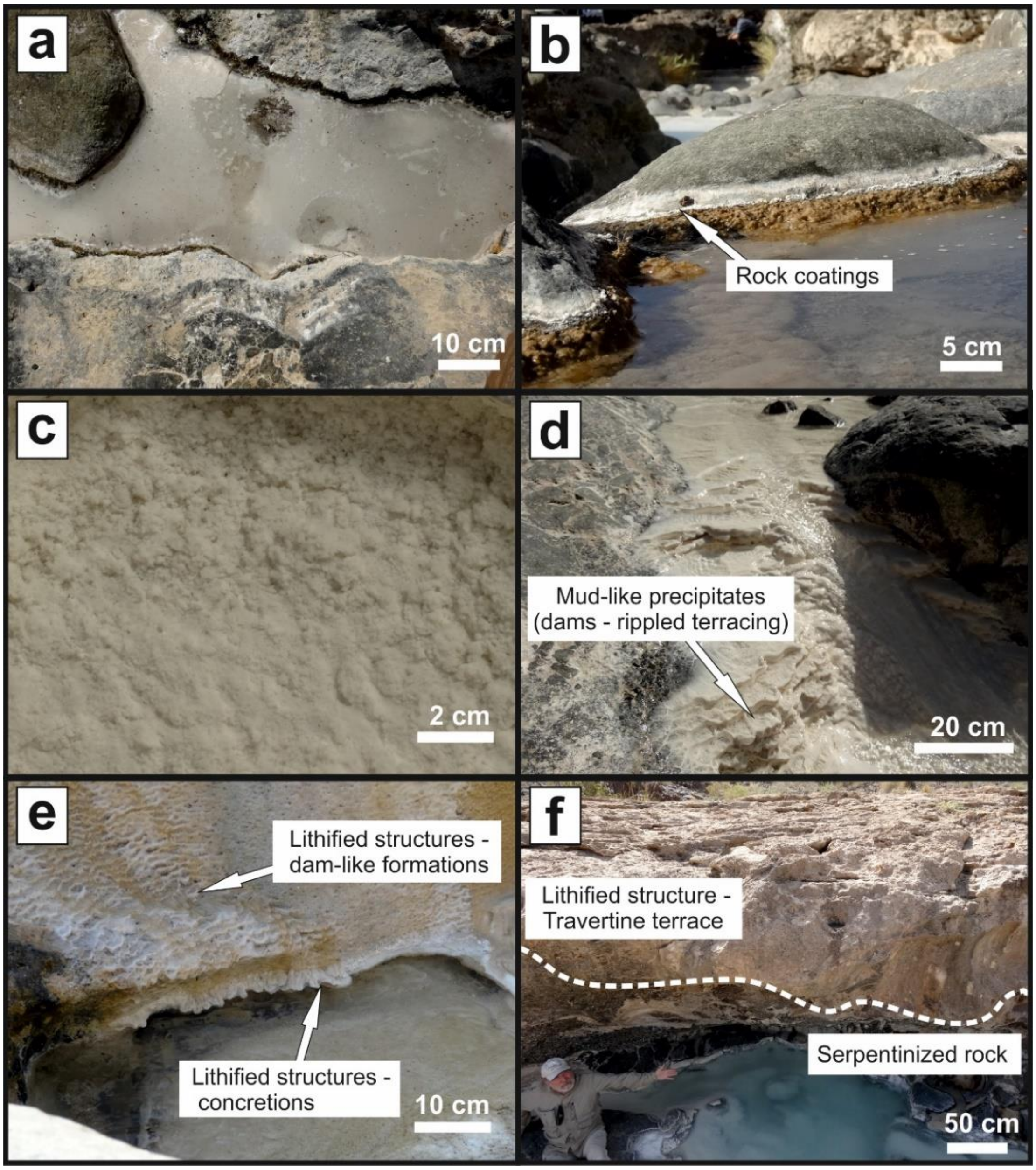

Figure 3.3. *Photographs of the types of the collected solid samples.* ***(a)*** *Crystalline crusts floating on the water surface,* ***(b)*** *rock coatings around the pool rims,* ***(c)*** *flocculent material covering the pool bottom and/or being suspended in the water column,* ***(d)*** *mud-like precipitates forming dam like structures (rippled terracing) and massive deposits around streams and pools,* ***(e)*** *lithified structures (dam-like formations and concretions) from active water flow areas, and* ***(f)*** *travertine terraces lying on the ultramafic rocks.*

Thirty (30) water samples were taken from several pools and their contributors (spring outlets) by using 50 mL syringes (PE/ PP), which were pre-rinsed with sample material. Sampling from deeper parts was conducted using a telescope sampling collector (Burkle, Germany) equipped with a rinsed 500 mL polyethylene bottle. The waters from each sampling point were filtered through (pre-flushed) cellulose acetate membrane syringe filters (Sartorius Minisart Plus, pore diameter 0.45 µm) and directly filled into three different 10 mL polyethylene vials for alkalinity titration (pre-cleaned with ultrapure water, without headspace), trace metal analysis (pre-conditioned with distilled 5 % HNO_3 and sample was fixed by adding 100 µL of distilled concentrated HNO_3), and anion analysis (pre-cleaned with ultrapure water).

3.3.1.2 In-situ measurements

Water samples were analyzed for pH, temperature, and electrical conductivity (EC) using a Hanna Instruments HI 98129 handheld tester, which was recalibrated daily. Alkalinity was directly measured in the field within 1 h after sampling. For this purpose, 10 mL of each sample was poured into a 20 mL polystyrene container under stirring, using a portable magnetic stirrer (IKAR Topolino Mobil). Under continuous stirring, 0.1 M hydrochloric acid (Titrisol, Merck, Germany) was added in 20 − 30 µL steps until a pH value between 3.5 and 4.3 was reached. The pH was monitored using a WTW Multi 3430 IDS portable meter, equipped with an IDS pH electrode (SentixR 940) during the entire alkalinity measurement process. Considering the change in the pH value and the volume of HCl added, the alkalinity (Alk.; **Eq. 3.3**) can be calculated as:

$$Alk.\left(\frac{mol}{L}\right) = \frac{[(V_{\mathrm{HCl}} \cdot c_{\mathrm{HCl}}) - 10^{-\mathrm{pHfinal}} \cdot \frac{(V_0 + V_{\mathrm{HCl}})}{f_{\mathrm{H+}}} + 10^{-\mathrm{pHstart}} \cdot \frac{V_0}{f_{\mathrm{H+}}}]}{V_0} \quad (3.3)$$

where V_0 represents the initial sample volume, V_{HCl} and C_{HCl} is the volume and the concentration of the added acid, pH_{start} symbolizes the initial pH value of the sample, pH_{final} is the final pH value after the end of the titration, and f_{H+} stands for the activity coefficient of H^+ ions (1.0 for freshwater). In order to determine the accuracy and the precision of the method, a 2.5 M $NaHCO_3$ solution was measured on a daily basis as a control. Precision was better than 0.5 % and accuracy was < 3.3 %. Dissolved inorganic carbon (DIC) was calculated using the following alkalimetric titration equation (**Eq. 3.4**) given in Stumm and Morgan (1996):

$$C_T\left(\frac{mmol}{L}\right) = 1000 \cdot \frac{\left(\frac{Alk.}{1000} + [H^+] - [OH^-]\right)}{(\alpha_1 + 2\alpha_2)} \quad (3.4)$$

where C_T is the sum of the concentrations of carbonic species in the aqueous solution, and α_1, α_2 are the values of ionization fractions of carbonic acid. The ionization fractions were estimated using the equilibrium constants, $K_1 = [H^+][HCO_3^-]/[H_2CO_3]$ for HCO_3^- and $K_2 = [H^+][CO_3^{2-}]/[HCO_3^-]$ for CO_3^{2-}.

3.3.2 Analytical techniques

Water samples were analyzed for major (Ca, K, Mg, Na, Si) and trace elements (Ba, Sr) by inductively coupled plasma optical emission spectroscopy using a Varian Vista Pro ICP-OES device. Sulfate (SO_4^{2-}) and chloride (Cl^-) concentrations in water samples were determined using a Metrohm 882 Compact IC Plus ion chromatograph (IC). Analytical accuracy obtained from the measurement of certified reference materials (TMDW-A, IAPSO seawater) was better than 0.25 % for IC analyses and better than 8 % for Ca, K, Mg, Si, Ba, Sr, and 13.8 % for Na regarding the ICP-OES measurements. Further element analyses on 10-fold diluted water samples were conducted using a double-focusing magnetic sector field inductively coupled plasma mass spectrometer (Thermo Finnigan Element2™, Germany).

The mineralogy of the samples was determined by powder X-ray diffraction (XRD), using a PANalytical MPD diffractometer with a Bragg-Brentano parafocusing geometry and Cu K_α radiation (operating at 40 mA and 45 kV). Instrument configuration included programmable divergence slits in the incident and diffracted beams, placement of a 0.25° fix anti-scatter slit in the incident path and a PSD detector PIXel. Data processing was conducted by using the software HighScore Plus from PANalytical X'Pert PRO (mineral database: Pdf2HSP/PAN-ICSD). Mineral quantification was defined by the peak refining method described in Rietveld (1969). Recently formed precipitates collected from the spring sites were analyzed both wet and dried in order to detect hydrated, labile phases that might be present within the pools. The textural characterization and semi-quantitative chemical analysis of the solid samples were carried out at the Centro de Instrumentación Científica (CIC) of the University of Granada (Granada, Spain) using a Field Emission Scanning Electron Microscope (FE-SEM) ZEISS AURIGA (In- Lens mode at 3 kV) and an Environmental SEM (ESEM) FEI Quanta 400 (SE mode at 5 kV and BSE mode at 12 kV). Complementary analysis of mineral phases and textures was carried out at CIC using a FE-SEM Zeiss Supra 40Vp connected to a Renishaw In Via Raman spectrometer fitted with a Nd:YAG 532 nm laser and a near infrared diode 785 nm laser, with maximum powers of 500 mW and 100 mW, respectively. The SEMs were equipped with Energy Dispersive X-ray Spectrometers (EDS).

3.4 Results

3.4.1 Chemical composition of alkaline waters

The physicochemical parameters (Appendix **Fig. A−3.1**) and chemical composition of the collected water samples are presented in **Tables 3.1 and 3.2**, respectively. We subdivided the waters into three types according to their chemical and hydrological characteristics: i) Mg-type; moderately alkaline ($7.9 < pH < 9.5$), Mg^{2+}–HCO_3^--rich waters, ii) Ca-type; hyperalkaline ($pH > 11.6$), Ca^{2+}–OH^--rich waters, and iii) Mix-type; alkaline to hyperalkaline ($9.6 < pH < 11.5$) waters with intermediate chemical composition. In the present study, we use the terms “Mg-type” instead of Mg^{2+}–HCO_3^--rich waters (Type I) and “Ca-type” instead of Ca^{2+}–OH^--rich waters (Type II). We also use the term “Mix-type” to refer to all the waters formed by the mixing between Mg-type and Ca-type waters (**Fig. 3.1**).

The two studied spring sites are small-scale, hydrological networks of pools formed upon the discharge of Ca-type and Mg-type waters (**Fig. 3.4a**). Mg-type waters occur in spring and run-off waters forming pools with diameters from 0.5 to 2 m, and emanate from rock fractures usually associated with soils **(Fig. 3.4b**). They have high Mg (1.4 − 7.2 mmol/L) and DIC (4 − 14.6 mmol/L) concentration, and relatively low Ca concentration (0.2 − 0.4 mmol/L).

Ca-type waters include shallow pools (in most cases up to 0.5 m in diameter) with a thin crystalline crust floating on the water surface (**Fig. 3.4c**). They show high Ca concentration (up to 2 mmol/L), low DIC (0.4 − 1.7 mmol/L), and virtually no Mg (0.001 − 0.02 mmol/L). Ca-type waters form isolated pools discharging from either tectonic fractures or small cracks and fissures in the ultramafic rocks. The hydrological network of the pools develops through mixing of the run-off waters of the two different spring water types (**Figs. 3.1; 3.4a**). Pools of Mix-type waters —that are predominant in the two spring sites— show great variability in diameter (0.5 − 7 m) and habitually display a turquoise color (**Fig. 3.4d**).

Mix-type waters have variable Ca (0.1 − 0.6 mmol/L) and Mg (0.02 − 2 mmol/L) concentrations, intermediate between Mg-type and Ca-type waters, and DIC values between 0.7 and 3.8 mmol/L. The graph in **figure 3.5** highlights the categorization of the three different water types, based on the relationship between Ca/Mg ratio and pH.

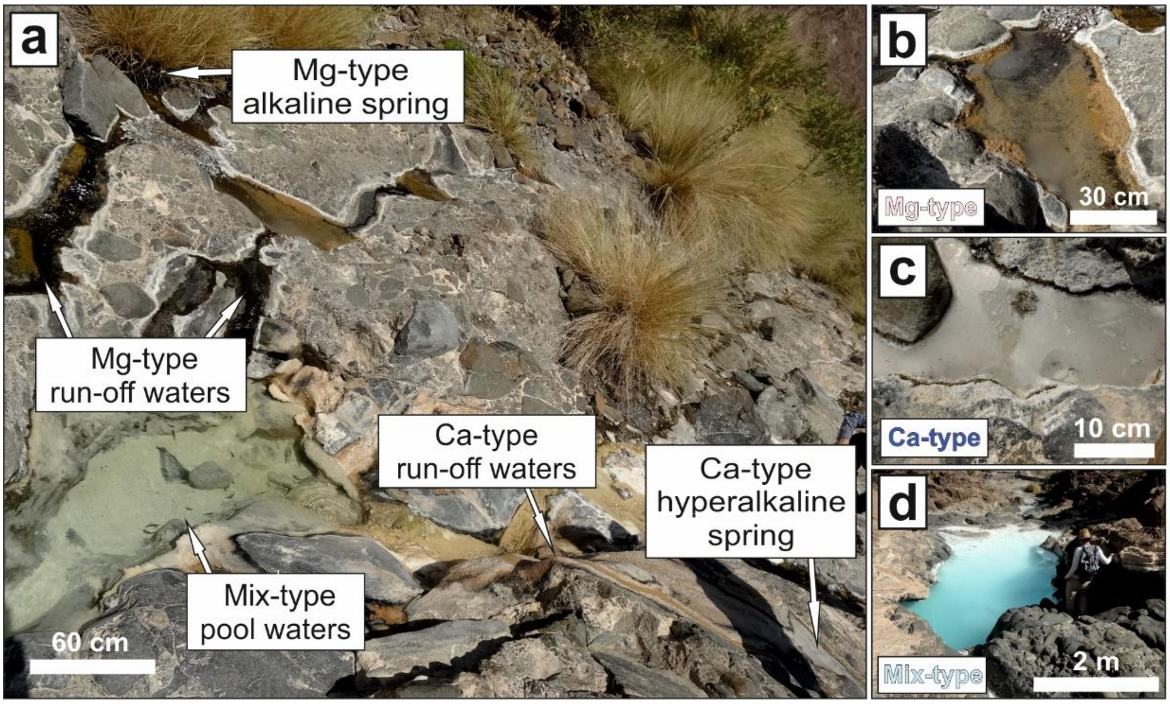

Figure 3.4. *Hydrological network and water types in the Nasif site, forming upon the discharge of circulating waters in the peridotites.* ***(a)*** *Overview photograph showing the type of springs, pools and run-off waters in the Nasif spring site. Upstream to downstream direction is from top-right to bottom-left.* ***(b)*** *Mg-type waters mantled by white rock coatings.* ***(c)*** *Ca-type waters hosting a crystalline crust floating on their surface.* ***(d)*** *Mix-type waters; often demonstrating turquoise-colored waters.*

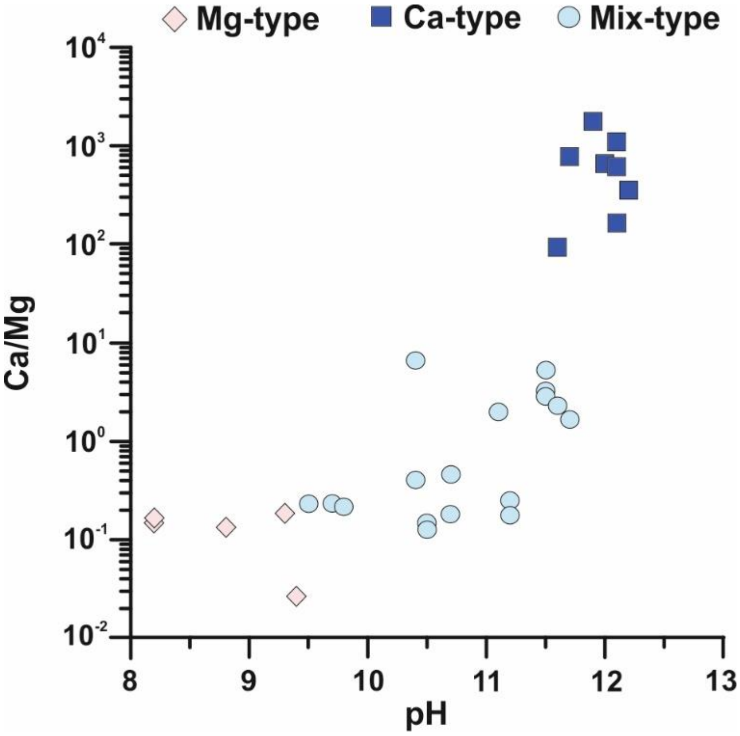

Figure 3.5. *Graph showing the relationship between Ca/Mg ratio and pH in the different water types. Mg-type waters are mildly alkaline and show low Ca/Mg ratios. Ca-type waters are hyperalkaline and show high Ca/Mg ratios. Mix-type waters demonstrate a wide range in pH values and intermediate Ca/Mg ratios.*

Table 3.1. *General sample information and physicochemical parameters of water samples.*

Sample ID	Location	Coord.		pH	Temp	Cond.	Alk.
		Easting	Northing		(°C)	(µS/cm)	(meq/L)
Mg-type							
OM15-1W	Nasif	58°23′41.47″	22°53′44.20″	8.2	29.6	603	4.6
OM15-2W	Nasif	58°23′41.34″	22°53′44.11″	8.8	29.8	599	4.0
OM15K-2W	Khafifah	58°25′27.13″	22°54′16.93″	9.4	20.5	2705	15.5
OM15K-7W	Khafifah	58°25′27.24″	22°54′16.43″	8.2	20	640	5.5
OM15K-23W	Khafifah	58°25′31.27″	22°54′15.13″	9.3	24.1	455	2.6
Ca-type							
OM15-4W	Nasif	58°23′40.76″	22°53′43.99″	11.7	30.2	1183	4.1
OM15-9W	Nasif	58°23′40.38″	22°53′44.00″	11.6	32.2	1365	3.3
OM15K-1W	Khafifah	58°25′27.19″	22°54′17.10″	12	26.3	1710	5.4
OM15K-3W	Khafifah	58°25′27.28″	22°54′17.01″	12.2	20.1	1691	4.9
OM15K-4W	Khafifah	58°25′27.24″	22°54′16.92″	12.1	20.2	1560	4.9
OM15K-9W	Khafifah	58°25′27.36″	22°54′16.41″	11.9	28.4	1790	3.5
OM15K-11W	Khafifah	58°25′27.67″	22°54′16.37″	12.1	26.6	1724	5.8
OM15K-14W	Khafifah	58°25′28.19″	22°54′16.25″	12.1	25.4	1894	6.2
Mix-type							
OM15-3W	Nasif	58°23′40.77″	22°53′44.10″	11.2	30.2	890	1.3
OM15-5W	Nasif	58°23′40.65″	22°53′44.01″	9.5	29.4	610	3.8
OM15-6W	Nasif	58°23′40.56″	22°53′43.99″	9.7	29.3	614	4.0
OM15-8W	Nasif	58°23′40.39″	22°53′43.86″	10.5	29.9	630	2.1
OM15-11W	Nasif	58°23′39.56″	22°53′43.43″	10.7	29.2	642	2.0
OM15-12W	Nasif	58°23′39.03″	22°53′43.23″	10.5	26.9	595	1.9
OM15K-5W	Khafifah	58°25′27.21″	22°54′16.55″	11.7	19.5	969	2.7
OM15K-6W	Khafifah	58°25′27.29″	22°54′16.55″	10.7	20	718	2.9
OM15K-8W	Khafifah	58°25′27.25″	22°54′16.25″	9.8	22.9	666	3.5
OM15K-10W	Khafifah	58°25′27.46″	22°54′16.34″	10.4	23.5	713	2.6
OM15K-13W	Khafifah	58°25′27.74″	22°54′16.00″	11.2	22.2	790	3.0
OM15K-16W	Khafifah	58°25′28.56″	22°54′15.83″	11.6	23.5	954	2.5
OM15K-18W	Khafifah	58°25′29.09″	22°54′15.47″	11.5	23.6	912	2.5
OM15K-19W	Khafifah	58°25′29.21″	22°54′15.19″	10.4	23.9	1039	2.3
OM15K-20W	Khafifah	58°25′29.95″	22°54′15.19″	11.5	24	927	npm[a]
OM15K-21W	Khafifah	58°25′30.67″	22°54′14.33″	11.5	22.5	927	npm
OM15K-22W	Khafifah	58°25′30.87″	22°54′14.23″	11.1	23.3	818	1.9

[a] Not possible to measure.

Table 3.2. *Major ion and trace element chemistry of water samples.*

Sample ID	Ba (µmol/L)	Ca (mmol/L)	K (mmol/L)	Mg (mmol/L)	Na (mmol/L)	Si (mmol/L)	Sr (µmol/L)	Cl^- (mmol/L)	SO_4^{2-} (mmol/L)	DIC (mmol/L)
Mg-type										
OM15-1W	0.044	0.382	0.029	2.497	0.869	0.391	2.705	0.982	0.378	4.713
OM15-2W	0.044	0.317	0.029	2.430	1.003	0.297	2.648	1.222	0.478	4.040
OM15K-2W	0.604	0.183	0.279	7.167	16.921	0.112	0.262	16.623	0.649	14.66
OM15K-7W	0.692	0.425	0.021	2.837	1.110	0.335	2.762	1.424	0.358	5.810
OM15K-23W	0.801	0.249	0.051	1.373	1.618	0.145	1.016	1.657	0.292	2.521
Ca-type										
OM15-4W	0.029	1.793	0.127	0.002	5.228	0.006	1.335	5.121	0.002	0.993
OM15-9W	0.029	1.603	0.118	0.017	4.850	0.006	1.278	4.814	0.006	1.006
OM15K-1W	2.709	1.954	0.162	0.003	6.055	0.006	1.586	5.176	0.007	1.319
OM15K-3W	1.260	1.666	0.149	0.005	6.255	0.005	1.472	5.364	0.008	1.329
OM15K-4W	2.381	1.703	0.140	0.010	6.072	0.009	1.507	5.190	0.008	1.422
OM15K-9W	1.995	2.035	0.143	0.001	6.277	0.003	1.404	5.244	0.005	0.379
OM15K-11W	0.990	1.944	0.150	0.002	7.151	0.003	1.405	5.941	0.005	1.661
OM15K-14W	1.405	2.043	0.154	0.003	6.886	0.024	1.518	5.503	0.005	1.705
Mix-type										
OM15-3W	bdl[a]	0.141	0.095	0.578	3.992	0.112	0.137	4.028	0.120	0.709
OM15-5W	0.029	0.460	0.041	2.019	1.619	0.256	2.305	1.804	0.407	3.655
OM15-6W	0.022	0.431	0.047	1.891	1.892	0.238	1.666	2.056	0.379	3.765
OM15-8W	bdl	0.147	0.073	1.176	3.058	0.151	0.183	3.095	0.231	1.565
OM15-11W	0.007	0.188	0.080	1.066	3.354	0.137	0.205	3.254	0.212	1.329
OM15-12W	0.015	0.152	0.079	1.043	3.336	0.123	0.171	3.311	0.214	1.451
OM15K-5W	0.801	0.611	0.120	0.373	5.194	0.043	0.856	4.671	0.063	1.168
OM15K-6W	0.626	0.339	0.104	0.749	4.589	0.088	0.787	4.163	0.126	2.016
OM15K-8W	0.670	0.292	0.078	1.384	3.678	0.162	1.187	3.365	0.207	3.183
OM15K-10W	0.837	0.357	0.097	0.901	4.347	0.115	0.536	3.898	0.144	1.773
OM15K-13W	0.881	0.177	0.099	1.016	4.301	0.109	0.194	3.770	0.176	1.912
OM15K-16W	0.786	0.499	0.121	0.220	5.459	0.055	0.377	4.520	0.099	1.018
OM15K-18W	0.619	0.459	0.122	0.162	5.529	0.052	0.331	4.588	0.093	1.011
OM15K-19W	0.910	0.124	0.203	0.019	8.686	0.044	0.662	7.575	0.012	1.756
OM15K-20W	1.966	0.446	0.124	0.140	5.694	0.050	0.377	4.673	0.086	npm[b]
OM15K-21W	2.287	0.351	0.127	0.069	5.890	0.039	0.285	4.807	0.076	npm
OM15K-22W	0.721	0.150	0.130	0.076	6.029	0.035	0.126	4.873	0.081	0.999

[a] Below detection limit.

[b] Not possible to measure.

3.4.2 Mineralogy and textures

We have identified five mineral groups in the studied spring sites (**Table 3.3**): anhydrous carbonates (calcite, aragonite, and dolomite), hydroxides (brucite), layered double hydroxides (LDH; hydrotalcite), hydrated carbonates (nesquehonite), and hydrated hydroxy-carbonates (dypingite, hydromagnesite and artinite). Olivine and serpentine group minerals —identified in a fraction of the samples— are most likely detritus from the ultramafic host rocks, and quartz probably derives from wind-blown dust from the nearby Wahiba Sands desert (40 km SE from the spring sites). The detailed mineralogy and description of the collected solid samples are given in **Table 3.4**. In addition, we determined the frequency and the proportional content of each identified mineral phase in all sample types. **Table 3.5** summarizes the percentage of the identified mineral phases to the total mineralogical index in each sample type, and **Table 3.6**, presents the wt% range in mineral composition for each type of solid samples. All samples contain calcium carbonate phases, and brucite is present in 22% of them. Hydrated magnesium (hydroxy-) carbonates (nesquehonite, dypingite, hydromagnesite and artinite), LDH, and dolomite are found in 7%, 2% and 2% of the total number of collected samples, respectively.

Table 3.3. *Chemical formulas and mineral groups of mineral phases identified in the spring sites.*

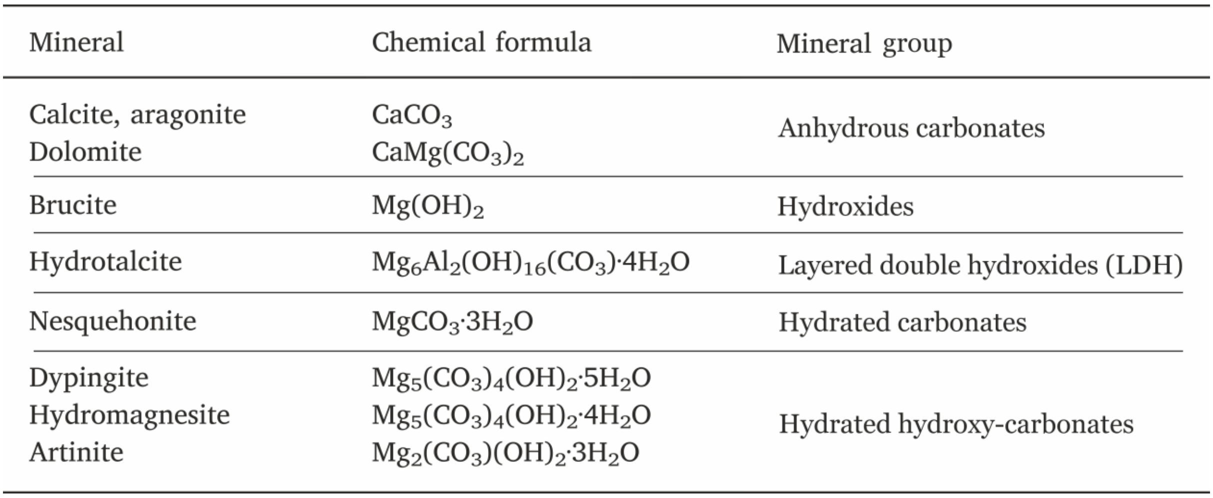

Mineral	Chemical formula	Mineral group
Calcite, aragonite Dolomite	$CaCO_3$ $CaMg(CO_3)_2$	Anhydrous carbonates
Brucite	$Mg(OH)_2$	Hydroxides
Hydrotalcite	$Mg_6Al_2(OH)_{16}(CO_3)\cdot 4H_2O$	Layered double hydroxides (LDH)
Nesquehonite	$MgCO_3\cdot 3H_2O$	Hydrated carbonates
Dypingite Hydromagnesite Artinite	$Mg_5(CO_3)_4(OH)_2\cdot 5H_2O$ $Mg_5(CO_3)_4(OH)_2\cdot 4H_2O$ $Mg_2(CO_3)(OH)_2\cdot 3H_2O$	Hydrated hydroxy-carbonates

3.4.2.1 Crystalline crusts

We identified two types of crystalline crusts in the spring sites: i) calcitic crusts (90 − 100 wt%; **Table 3.6**) in Ca-type waters, and ii) aragonite-dominated crusts (60 − 72 wt%) in Mix-type waters. Calcitic crusts in Ca-type waters are thin (< 1 mm) and form on the air–water interface. They are rather homogeneous and almost exclusively composed of aggregates of subhedral {120} calcite crystals (up to 40 μm), growing laterally to the air–water interface towards the water column (**Fig. 3.6a**). Patches of subhedral to anhedral calcite crystals (< 4 μm) can be also observed in between the main subhedral calcite crystals (**Fig. 3.6a**).

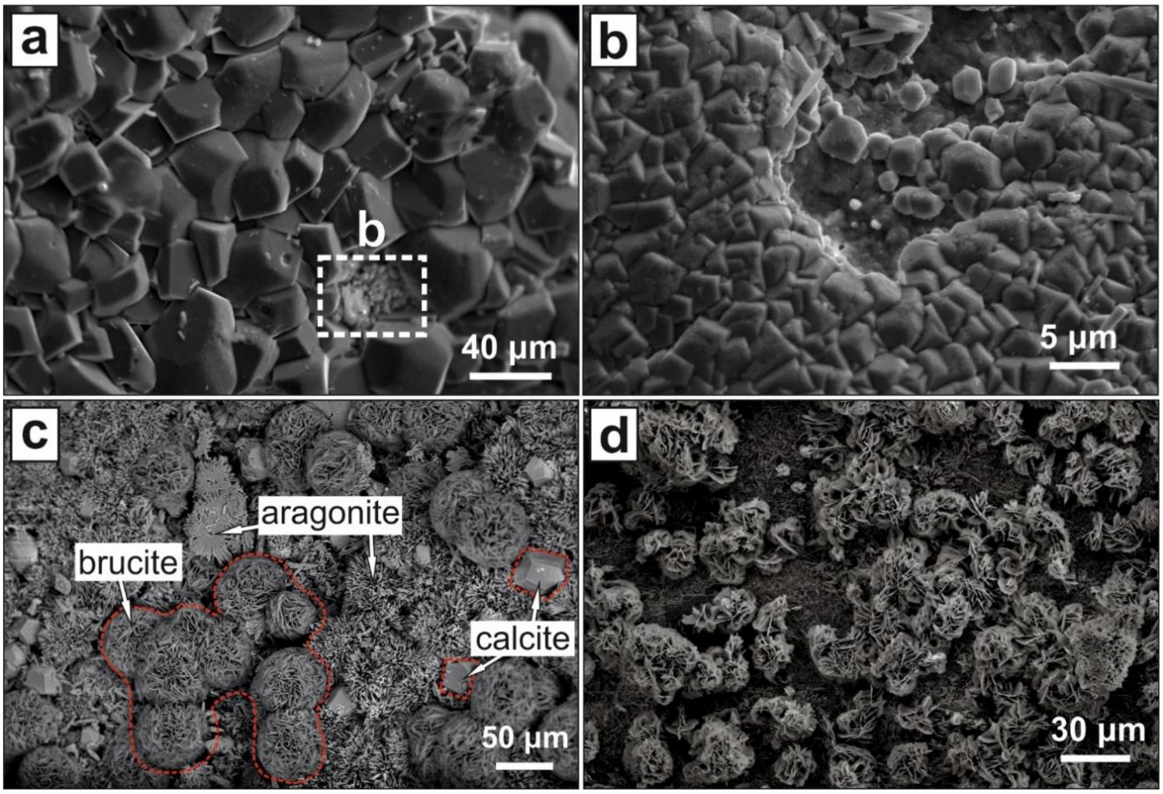

Figure 3.6. *SEM images of crystalline crusts precipitating on the surface of Ca-type and Mix-type waters.* ***(a)*** *Calcite-dominated crystalline crust in Ca-type waters.* ***(b)*** *Zoomed-in image of the calcite crystals from the inset in* ***(a)****, showing patches of subhedral to anhedral calcite crystals in between larger calcite crystals.* ***(c)*** *Aragonite–brucite–calcite assemblage in a crystalline crust in Mix-type waters.* ***(d)*** *Hydromagnesite and brucite clusters grow on an aragonitic crust in Mix-type waters.*

Crystalline crusts in Mix-type waters are rare and occur where Mg-type and Ca-type spring water outlets discharge in the same pool. They typically form near the outlet of Ca-type waters, and their growth is restricted towards the central parts of the pool. Unlike Ca-type water crusts, the mineralogy in Mix-type water crusts is heterogeneous and is composed of aragonite (50 − 75 wt%), brucite (10 − 35 wt%), calcite (4 − 12 wt%), and sometimes hydromagnesite (0 − 15 wt%) (**Fig. 3.6c, d**). Aragonite exhibits acicular, needle-like morphologies, with needle-like crystal sizes ranging from < 1 − 20 μm. In the aragonite-dominated crusts, dispersed euhedral to subhedral (5 − 30 μm) calcite crystals grow on the aragonitic crust surface (**Fig. 3.6c**). Brucite occurs as single spheres (avg. diameter of 40 μm) made of interlocking flakes (**Fig. 3.6c**), and hydromagnesite as rosette clusters with flower-like morphologies of variably spaced flaky crystals (**Fig. 3.6d**).

3.4.2.2 Rock coatings

The rock coating materials mantle some Mg-type and Ca-type pools just above the water surface. The mineralogy of rock coatings in Mg-type waters is diverse and includes calcium carbonate phases (0 − 15 wt% calcite and aragonite), hydrated magnesium carbonates (5 − 70 wt% nesquehonite, 0 − 25 wt% dypingite, 0 − 12 wt% hydromagnesite and 0 − 5 wt% artinite), and halite (0 − 20 wt%) (**Fig. 3.7**). Aragonite occurs as individual, spindle crystals (< 15 µm; **Fig. 3.7a**), and calcite as subhedral crystal clusters (< 40 µm; **Fig. 3.7b**). Nesquehonite exhibits variably sized, prismatic crystals (40 − 2000 µm; **Fig. 3.7b, c**) and dypingite and hydromagnesite show rosettes (< 40 µm) made of flaky crystals (**Fig. 3.7c**). Halite —formed during evaporation at the edges of the pools— appears as integrating {111} octahedral crystals (**Fig. 3.7a**) or crusts on the surfaces of other minerals (**Fig. 3.7c**).

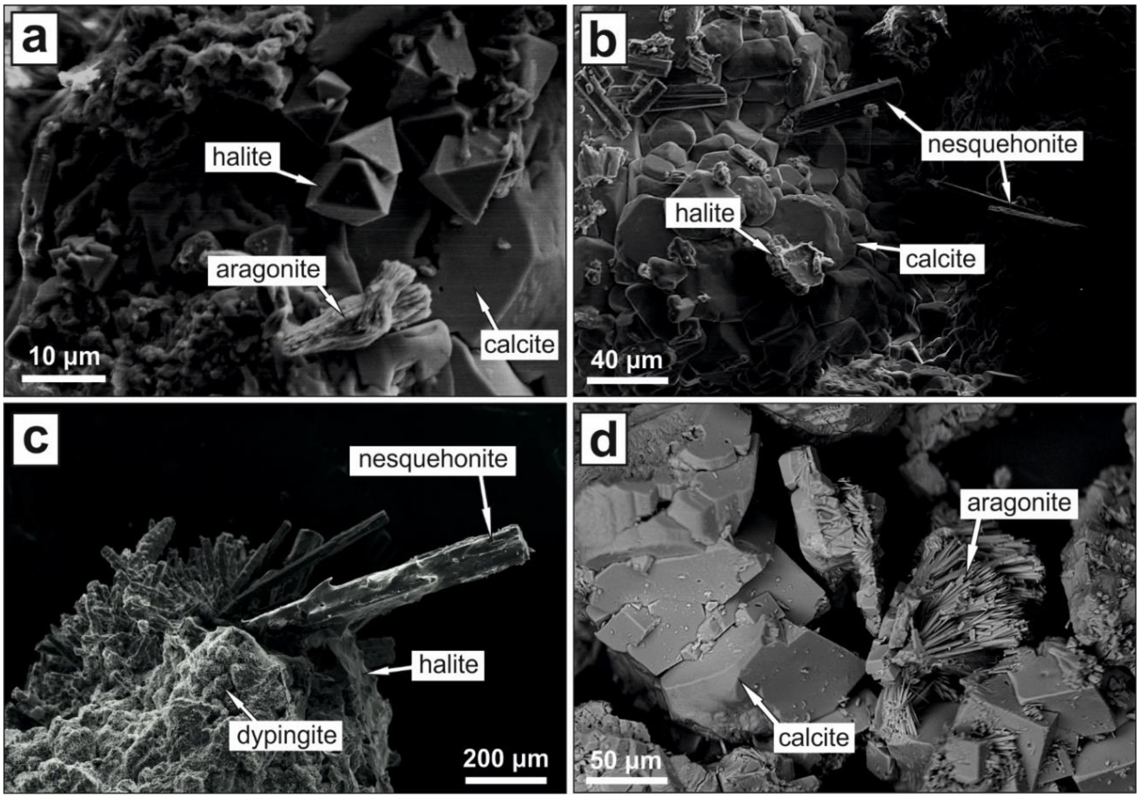

***Figure 3.7.** SEM images of rock coatings precipitating around the pools. **(a)** Mineral assemblage of calcite, octahedral halite and spindle-like aragonite in Mg-type waters of the Nasif site. **(b)** Prismatic nesquehonite, calcite with curved edges and halite in Mg-type waters of the Nasif site. **(c)** Large prismatic crystals of nesquehonite grow on rosette-like aggregates of dypingite in Mg-type waters. **(d)** Acicular aragonite crystals associated with calcite crystals with curved edges in Ca-type waters.*

Rock coatings in Ca-type waters are made of calcite (70 − 90 wt%) and aragonite (10 − 30 wt%) showing subhedral to euhedral crystals (**Fig. 3.7d**). Integrating, euhedral {104} calcite crystals (up to 50 μm) co-exist with {120} curved edged calcite (up to 120 μm), which exhibits step growth (**Fig. 3.7d**). Where present, aragonite shows acicular morphologies of tubular crystals ranging in size from 5 to 80 μm (**Fig. 3.7d**).

3.4.2.3 Flocculent material

The flocculent material consists of particles in suspension within the water column that eventually form unconsolidated deposits at the bottom of the pools. They mostly occur in the Mix-type waters; we have only found one sample of this sample type in Ca-type waters at the Khafifah site (sample OM15K−01A−P; **Table 3.4**). Aragonite (5 − 25 μm) is the main component of the flocculent particles (75 − 100 wt%) and exhibits diverse textures including initial crystalline sheaves, dumbbell, wheat-sheaf, and acicular-spheroidal morphologies (**Fig. 3.8a**). Brucite crystals, with low degree of crystallinity, and flakes of LDH phases are occasionally attached to aragonite particles (**Fig. 3.8b;** Appendix **Fig. A−3.2**).

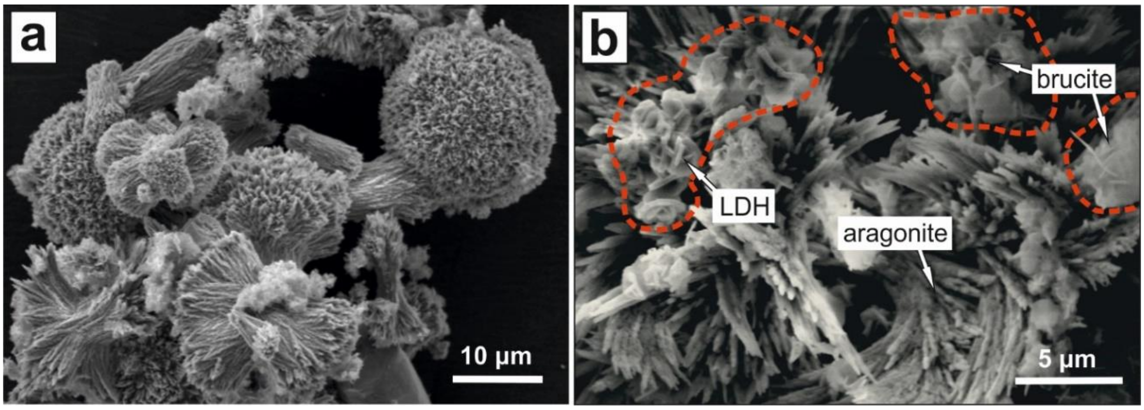

Figure 3.8. *SEM images of flocculent material depositing at the bottom of the pools and/or being in suspension within the water column.* ***(a)*** *Textural variability of aragonite including initial crystalline sheaves, dumbbell, wheat-sheaf, and acicular-spheroidal morphologies in Mix-type waters.* ***(b)*** *Brucite and LDH (hydrotalcite) crystals found attached on aragonite crystals in Mix-type waters.*

3.4.2.4 Mud-like precipitates

Mud-like precipitates are white to yellow/brown material only occurring in Mix-type waters. They mainly form at shallow parts of the pool network, such as the pool and stream edges, or shallow areas of Mix-water pools. Occasionally, mud-like precipitates form dams (rippled terracing) in pools and streams associated with active water flow. Aragonite is the predominant mineral phase (63 − 100 wt%) in mud-like precipitates, displaying a homogeneity in morphological and textural features (crystal sizes range from < 1 μm to 15 μm) (**Fig. 3.9a**). The most common aragonite morphologies are spindle (c. 80 vol%; **Fig. 3.9b**) followed by spheroidal aragonite clusters made of small (< 3 μm) needle-like crystals (**Fig. 3.9b**). Calcite (0 − 37 wt%; 2 − 5 μm in size) and brucite (0 − 16 wt%; < 500 nm in size) are occasionally associated with needle-like aragonite (**Fig. 3.9c**). In some cases, aragonite shows penetration twinning with crystal sizes varying from < 1 μm to 10 μm (**Fig. 3.9d**).

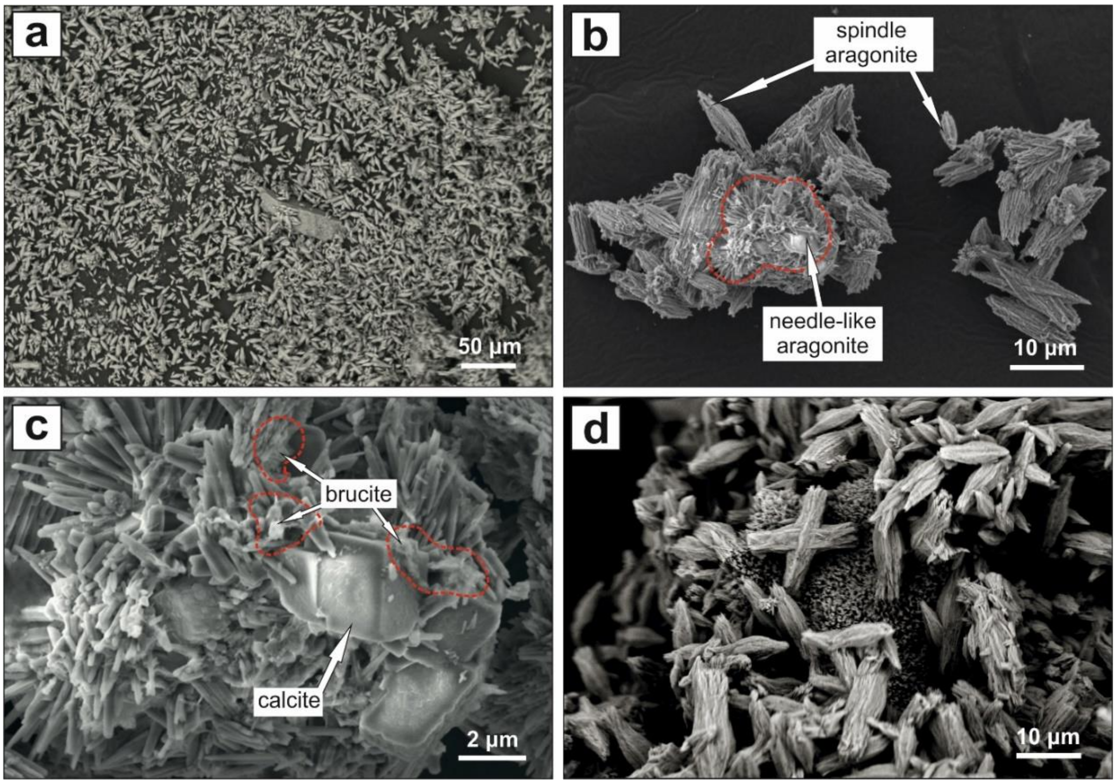

Figure 3.9. *SEM images of mud-like precipitates forming inside and around the pools and streams.* ***(a)*** *Overview of aragonite-dominated mud-like precipitates.* ***(b)*** *Spindle and needle-like morphologies of aragonite crystals and crystal aggregates in mud-like precipitates.* ***(c)*** *Needle-like clusters of aragonite along with calcite and brucite crystals.* ***(d)*** *Aragonite crystals exhibiting (cruciform) penetration twinning sit on spheroidal needle-like aragonite.*

3.4.2.5 Lithified structures

Samples of lithified structures include dam-like formations, concretions associated with active water flow, and travertine terraces on ultramafic rocks that are presently unrelated to active water flow. Dam-like formations are whitish, yellowish or reddish, and they are commonly associated with microbial mats. Calcite is the dominant phase of the dam-like formations (85 − 100 wt%) and exhibits an internal layering that terminates into curved and sharp edges on the exterior part (**Fig. 3.10a**). Small amounts of needle-like aragonite (0 − 15 wt%) can be observed at the external parts of the dams (**Fig. 3.10a**).

The concretions consist of aragonite (55 wt%), brucite (36 wt%), and calcite (9 wt%), and they are locally observed in restricted zones, where run-off Ca-type waters mix with Mg-type or Mix-type waters. Aragonite occupies the lower part of the concretions (in contact with the ultramafic bedrock), and shows a massif cementation texture that becomes needle-like (< 5 µm) at the exterior part (facing the water column). Brucite displays a compact texture with narrow spaces between the flaky crystals that compose the brucite clusters (**Fig. 3.10b**).

Calcite is the main component (76 − 90 wt%) of travertine samples, whilst aragonite (5 − 14 wt%) and dolomite (0 − 8 wt%) are present as minor phases. Traverine samples display recrystallization textures with variable crystal sizes (from < 1 µm to > 200 µm), different generations of vein networks, and chaotic and colloformic textural features (**Fig. 3.10c**). Clasts of serpentinite, Fe-oxides, and Cr-spinel from the ultramafic host rocks occasionally occur in the carbonate matrix of the travertine (**Fig. 3.10d**).

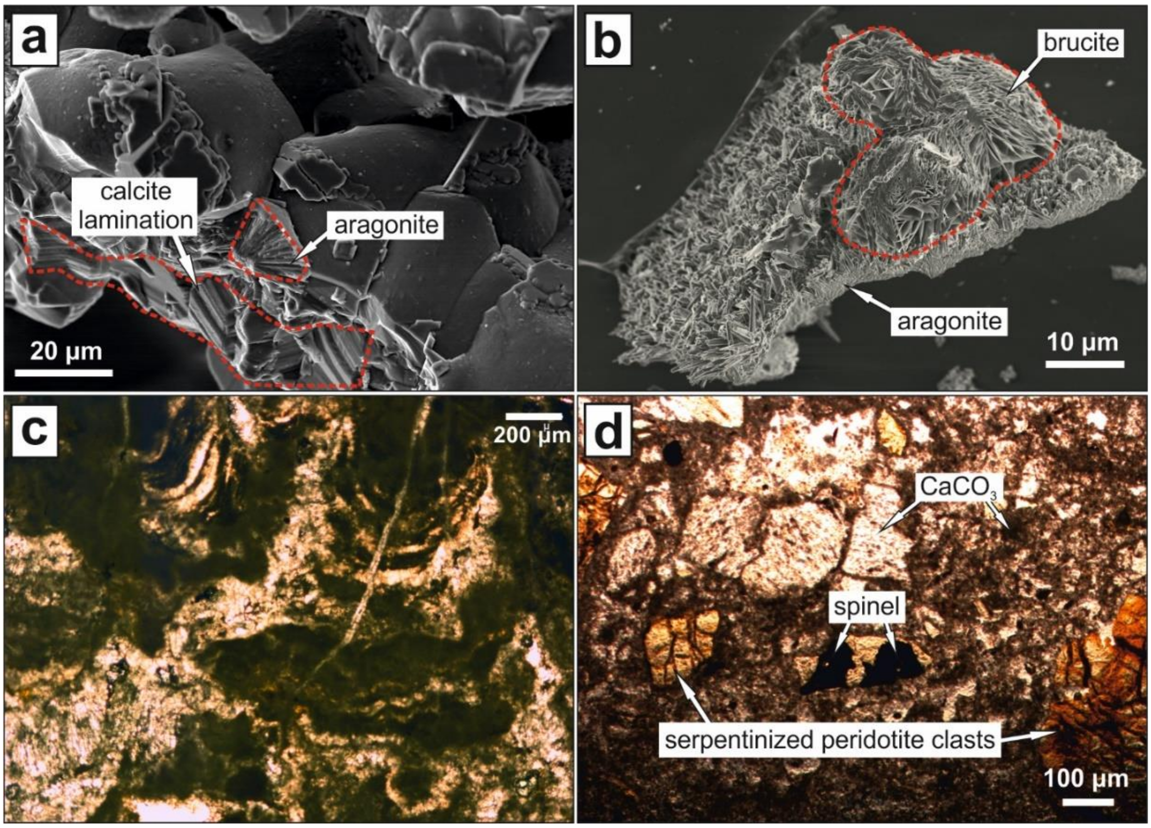

Figure 3.10. *SEM and optical microscope images of lithified structures associated with Ca-type and Mix-type waters or collected from travertine terraces.* ***(a)*** *SEM image of calcite-dominated dam-like structures associated with active flow of Ca-type waters. The dams exhibit an internal layering that terminates into a curved and smoothened exterior part. Needle-like aragonite occurs at the external part of the dam.* ***(b)*** *SEM image of concretions containing brucite clusters that grow on a substrate of acicular aragonite. This type of sample occurs at the mixing zones where Ca-type waters mix with Mg-type or Mg-rich Mix-type waters.* ***(c)*** *Optical microphotograph of travertine thin section exhibiting colloformic and chaotic textures of calcium carbonate (transmitted light).* ***(d)*** *Optical microphotograph of travertine thin section composed of clasts from the serpentinized host rocks that are entrapped in the calcium carbonate matrix (transmitted light).*

Table 3.4. *Mineralogy of solid sample types collected from the spring sites.*

Sample	Site	Water type	Sample type description	Mineralogy	
				Major	Minor
OM15-02B-R	Nasif	Mg-type	Rock coatings	Calcite	Aragonite, halite, nesquehonite
OM15-03A-P	Nasif	Mix-type	Crystalline crust	Aragonite	Brucite, calcite, hydromagnesite
OM15-03B-P	Nasif	Mix-type	Crystalline crust	Aragonite, brucite	Calcite
OM15-03C-Pa	Nasif	Mix-type	Mud-like (pool)	Aragonite, brucite	Calcite
OM15-03C-Pb	Nasif	Mix-type	Mud-like (pool)	Aragonite	Calcite
OM15-03D-P	Nasif	Mix-type	Mud-like (pool)	Aragonite	–
OM15-03E-P	Nasif	Mix-type	Flocculent material (pool)	Aragonite, calcite, brucite	Quartz, hydromagnesite
OM15-04A-P	Nasif	Ca-type	Crystalline crust	Calcite	Aragonite
OM15-04B-R	Nasif	Ca-type	Rock coatings	Calcite	Aragonite
OM15-05F-P	Nasif	Mix-type	Mud-like (stream)	Aragonite	Calcite
OM15-05G-P	Nasif	Ca-type	Lithified structures (dam-like)	Calcite	Aragonite
OM15-05H-P	Nasif	Mix-type	Lithified structures (concretions)	Aragonite, brucite	Calcite
OM15-06A-P	Nasif	Mix-type	Mud-like (stream)	Calcite, aragonite	–
OM15-06B-P	Nasif	Mix-type	Mud-like (stream)	Aragonite	–
OM15-08A-P	Nasif	Mix-type	Mud-like (pool)	Aragonite	–
OM15-08B-P	Nasif	Mix-type	Flocculent material (pool)	Aragonite	–
OM15-08C-P	Nasif	Mix-type	Mud-like/dam (stream)	Aragonite	–
OM15-08D-P	Nasif	Mix-type	Mud-like/dam (stream)	Aragonite	–
OM15-08E-P	Nasif	Mix-type	Mud-like/dam (stream)	Aragonite	–
OM15-08F-P	Nasif	Mix-type	Flocculent material (stream)	Aragonite, brucite	Calcite
OM15-08G-P	Nasif	Mix-type	Mud-like/dam (stream)	Aragonite	–
OM15-08H-P	Nasif	Mix-type	Mud-like/dam (stream)	Aragonite	–
OM15-08I-P	Nasif	Mix-type	Mud-like/dam (stream)	Aragonite	–
OM15-09A-P	Nasif	Ca-type	Mud-like (pool)	Aragonite, calcite, brucite	–
OM15-10A-P	Nasif	Mix-type	Mud-like/dam (stream)	Aragonite	–
OM15-10B-Pa	Nasif	Mix-type	Mud-like (pool)	Aragonite	Calcite
OM15-10B-Pb	Nasif	Mix-type	Mud-like (pool)	Aragonite	–

Table 3.4. *Mineralogy of solid sample types collected from the spring sites. (continued)*

Sample	Site	Water type	Sample type description	Mineralogy	
				Major	Minor
OM15-10D-Ra	Nasif	–	Travertine terrace	Mg-calcite, aragonite	–
OM15-10D-Rb	Nasif	–	Travertine terrace	Calcite, dolomite	Aragonite, chrysotile
OM15-10E-P	Nasif	Mix-type	Mud-like/dam (stream)	Aragonite	–
OM15-12B-Pa	Nasif	Mix-type	Mud-like (pool)	Aragonite	Calcite
OM15-12B-Pb	Nasif	Mix-type	Mud-like (pool)	Aragonite	–
OM15K-01A-P	Khafifah	Ca-type	Flocculent material (pool)	Aragonite, calcite	Brucite
OM15K-01B-P	Khafifah	Ca-type	Crystalline crust	Aragonite, calcite	–
OM15K-02A-R	Khafifah	Mg-type	Rock coatings	Nesquehonite, dypingite, hydromagnesite	Calcite, aragonite, halite, (Cl-)artinite
OM15K-02B-R	Khafifah	Mg-type	Rock coatings	Nesquehonite, dypingite, hydromagnesite	Halite, calcite, aragonite, artinite, quartz
OM15K-03A-P	Khafifah	Mix-type	Mud-like/dam (stream)	Aragonite, calcite	Quartz
OM15K-05B-P	Khafifah	Mix-type	Mud-like/dam (stream)	Aragonite, calcite	Brucite
OM15K-05B-P	Khafifah	Mix-type	Flocculent material (pool)	Aragonite	Brucite, calcite, LDH (hydrotalcite)
OM15K-07A-R	Khafifah	Mg-type	Rock coatings	Nesquehonite	Dypingite, hydromagnesite, halite, aragonite, quartz
OM15K-09A-P	Khafifah	Mix-type	Mud-like (pool)	Calcite	Aragonite
OM15K-10A-P	Khafifah	Mix-type	Mud-like (pool)	Aragonite, calcite	–
OM15K-10C-P	Khafifah	Mix-type	Mud-like (pool)	Aragonite, calcite	–
OM15K-12A-P	Khafifah	Mix-type	Mud-like (pool)	Aragonite, calcite	–
OM15K-12B-P	Khafifah	Mix-type	Flocculent material (pool)	Aragonite	Calcite
OM15K-13C-P	Khafifah	Mix-type	Flocculent material (pool)	Aragonite, calcite	Brucite
OM15K-13D-P	Khafifah	Mix-type	Flocculent material (pool)	Aragonite	–
OM15K-13E-Pa	Khafifah	Mix-type	Mud-like (pool)	Aragonite, halite	–
OM15K-13E-Pb	Khafifah	Mix-type	Mud-like (pool)	Aragonite, halite	–
OM15K-14A-P	Khafifah	Ca-type	Crystalline crust	Calcite	–
OM15K-14A-P	Khafifah	Ca-type	Crystalline crust	Calcite	–
OM15K-14B-Pa	Khafifah	Ca-type	Crystalline crust	Calcite	Aragonite
OM15K-14-R	Khafifah	–	Travertine terrace	Calcite	Aragonite, chrysotile, Fe-oxides, Cr-spinel
OM15K-15A-P	Khafifah	Mix-type	Mud-like/dam (stream)	Aragonite	–
OM15K-17A-P	Khafifah	Mix-type	Mud-like/dam (stream)	Aragonite, brucite	–

Table 3.5. *Percentages of mineral phases to the total mineralogical index in each solid sample type.*

Solid sample type	Site	$CaCO_3$ (calcite/aragonite)	Dolomite	Brucite	Hydrated Mg- carbonates	LDH
Crystalline crusts	Nasif	100%	0%	66.6%	33.3%	0%
	Khafifah	100%	0%	0%	0%	0%
Rock coatings	Nasif	100%	0%	0%	50%	0%
	Khafifah	100%	0%	0%	100%	0%
Flocculent material	Nasif	100%	0%	66.6%	33.3%	0%
	Khafifah	100%	0%	60%	0%	20%
Mud-like precipitates	Nasif	100%	0%	10%	0%	0%
	Khafifah	100%	0%	20%	0%	0%
Lithified structures	Nasif	100%	25%	25%	0%	0%
	Khafifah	100%	0%	0%	0%	0%

Table 3.6. *Compositional range of mineral phases by solid sample type found in the different water type*

Solid sample type	Water type	Calcite	Aragonite	Dolomite	Brucite	Nesquehonite	Dypingite	Hydromagnesite	Artinite	LDH
Crystalline crusts	Ca-type	90–100	0–10	–	–	–	–	–	–	–
	Mix-type	5–15	50–70	–	10–35	–	–	0–10	–	–
Rock coatings	Mg-type	0–15	0–5	–	–	5–70	0–25	0–15	0–5	–
	Ca-type	70–90	10–30	–	–	–	–	–	–	–
Flocculent material	Ca-type	10	74	–	12	–	–	–	–	–
	Mix-type	0–15	75–100	–	0–15	–	–	–	–	0–4
Mud-like precipitates	Mix-type	0–37	63–100	–	0–16	–	–	–	–	–
Lithified structures:										
i) Travertine terraces	–	76–90	5–14	0–8	–	–	–	–	–	–
ii) Dam-like formations	Ca-type	85–100	0–15	–	–	–	–	–	–	–
iii) Concretions	Mix-type	9	55	–	36	–	–	–	–	–

[a] Values in wt%

3.4.3 Thermodynamic models

3.4.3.1 Mineral saturation indices

The mineral saturation indices (SIs) in the investigated water samples (Appendix **Fig. A‒3.3**) were calculated using the geochemical speciation and reaction path modeling code PHREEQC (Parkhurst and Appelo, 1999) and the wateq4f database. **Figure 3.11** shows the SI of potential mineral phases as a function of the partial pressure of CO_2 ($P_{\mathrm{CO_2}}$) in the three water types from

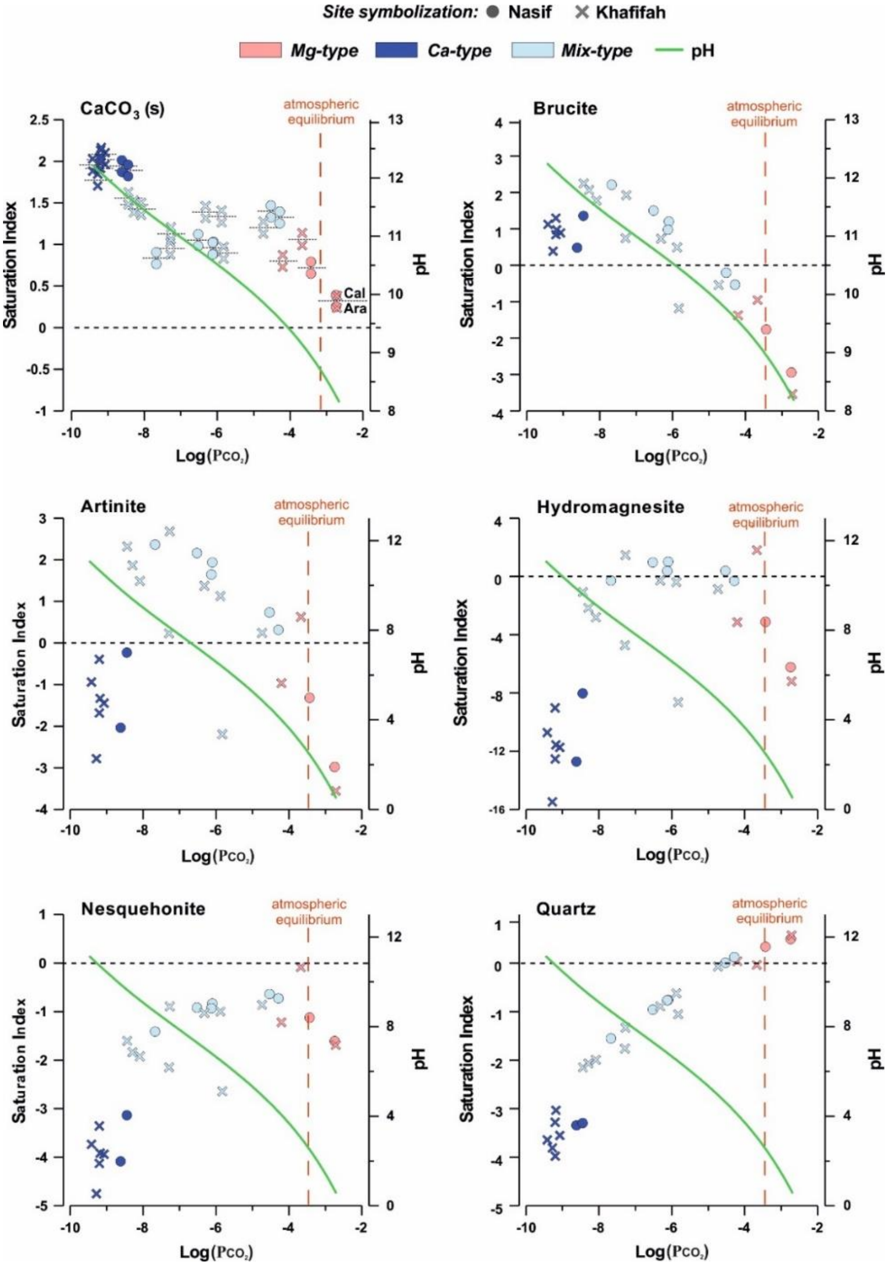

Figure 3.11. Saturation index of potential mineral phases versus the Log($P_{\mathrm{CO_2}}$) in the different water types of the two spring sites. The pH-curve in the diagrams (green line) is filled through actual data measured on-site. The $CaCO_3$ (s) diagram (up left) plots saturation index values for calcite (top-above the line) and aragonite (bottom-below the line) for each sample.

the Nasif and Khafifah spring sites. Calcium carbonate (calcite + aragonite) has the highest SI values in Ca-type waters (avg. SI = 1.95) and systematically decreases in Mix-type waters (avg. SI = 1.33) and Mg-type waters (avg. SI = 0.85) that show the lowest SI values. Mg-type waters and Mix-type waters with $pH < 10.5$ are undersaturated with respect to brucite (avg. SI = −2), whereas brucite is supersaturated in Ca-type waters and Mix-type waters with $pH > 10.5$ (avg. SI = 1). All water types are undersaturated with respect to nesquehonite that is close to saturation in Mg-type waters. Ca-type and Mg-type waters are undersaturated with respect to artinite and hydromagnesite. The SIs of these minerals increase in Mix-type waters, where hydromagnesite is supersaturated in some samples, and artinite is supersaturated (avg. SI = 1.2) in most samples. Quartz SIs are positively correlated with P_{CO_2} that corresponds to a transition from quartz-undersaturated Ca-type waters to quartz-saturated Mg-type waters. Most Khafifah waters show lower P_{CO_2} values than Nasif waters, indicating that Khafifah waters are less equilibrated with the atmosphere.

3.4.3.2 Mixing model

The spatial distribution and the undisturbed nature of the pools in the Nasif site allow to accurately compare the water chemical compositions derived by analytical techniques to those acquired by mixing model calculations. The positive correlation ($r^2 = 0.9992$) of conservative tracers, such as Cl^- and Na, points that the physicochemical variability of the Nasif site waters is due to variable mixing of two water end-members with the highest and lowest Cl^- and Na concentrations, respectively. To evaluate the role of water mixing in mineral precipitation, we performed mixing model calculations using the PHREEQC-MIX command. For modeling, we use as end-members pristine Ca-type (OM15−1W) and Mg-type spring water samples (OM15−4W) with the highest and lowest Cl^- and Na concentrations (**Table 3.2**), respectively. The modeling was computed to mix the Mg-type water end-member with the Ca-type end-member under a mixing ratio step of 0.01 (1%) (**Fig. 3.12**). This permits to follow and examine the SI of the minerals under all the intermediate mixing ratios between the two pristine end-members (100% = 1; **Fig. 3.12**) of Mg-type and Ca-type waters.

Figure 3.12 models the evolution of the SIs of selected mineral phases, $CO_2(g)$ and pH with increasing mixing fraction —from left to right— of the Ca-type water end-member. Calcite and aragonite are supersaturated for all mixing fractions and their SIs reach a plateau, where Ca-type water mixing fraction is between 0.3 and 1 (**Fig. 3.12**). Brucite becomes saturated at Ca-type water mixing fraction > 0.25, where pH is > 9.8. Brucite SI value continues to increase (c. 2.5) up to 0.95 Ca-type water mixing fraction, where it rapidly decreases (**Fig. 3.12**). Artinite reaches saturation at 0.12 Ca-type water mixing fraction, where the pH value is11.2 (**Fig. 3.12**). Similar to brucite, artinite presents an extreme SI value decrease between 0.95 and 1 Ca-type water mixing fraction that leads to its undersaturation. Hydromagnesite — which SI values display a bell-shaped curve— is supersaturated between 0.15 and 0.8 Ca-type water mixing fraction (**Fig. 3.12**). Nesquehonite is undersaturated for all mixing fractions; its SI increases in the 0 − 0.15 Ca-type water fraction interval, while it decreases with increasing Ca-type water mixing fraction (0.4 − 1) (**Fig. 3.12**).

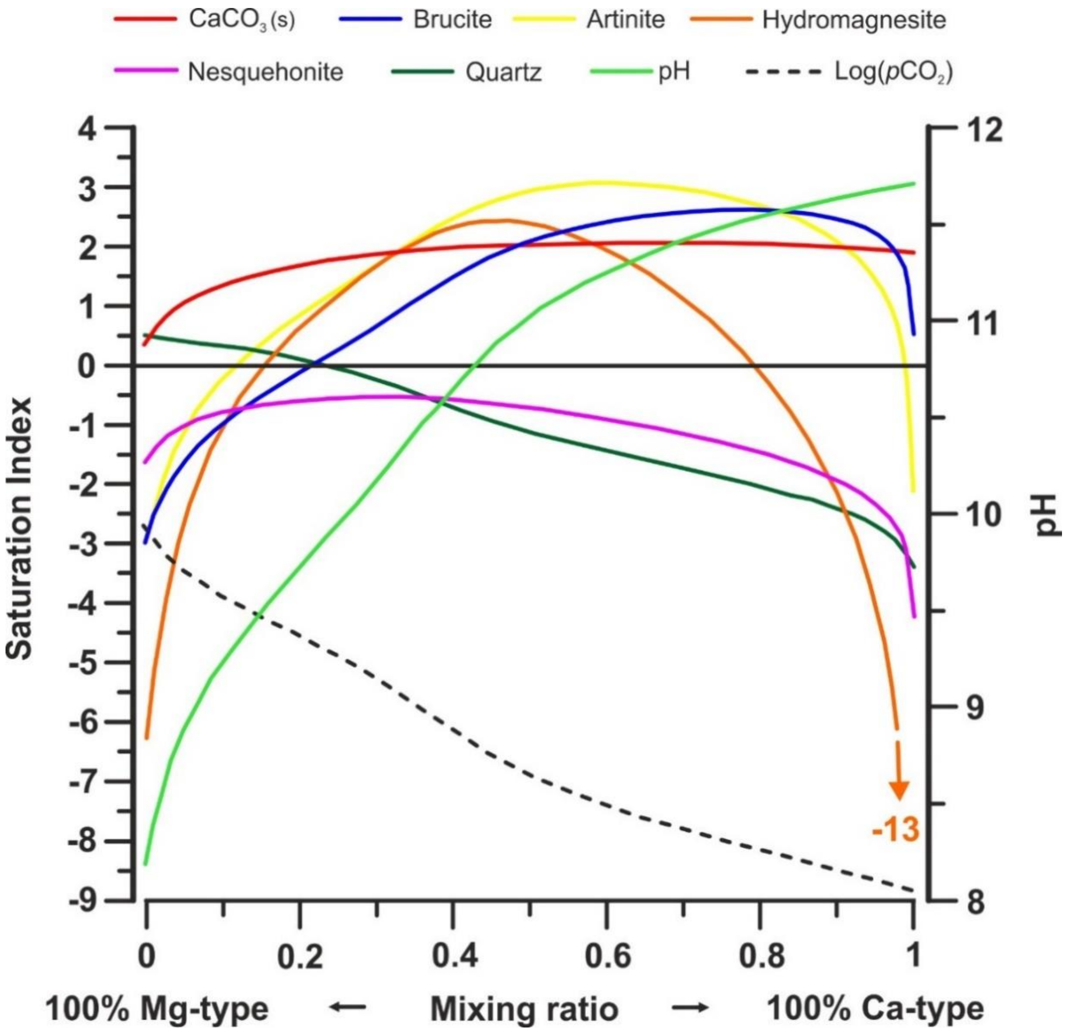

Figure 3.12. *Saturation index, pH, and CO_2 evolution during gradual mixing of Mg-type and Ca-type waters. Water sample OM15–1W was used as the end-member for pristine Mg-type waters and sample OM15–4W as the end-member for pristine Ca-type waters (see* ***Table 3.2****). The step of mixing ratios in the model is 0.01 (1%), starting from 100% Mg-type water (at 0 on the x axis) and ending up with 100% Ca-type water (at 1 on the x axis).*

The same water samples used as end-members for the mixing model in **figure 3.12** were also used to calculate the theoretical mixing proportion of Mg-type and Ca-type water type in each collected water sample from the Nasif spring site (**Fig. 3.13**).

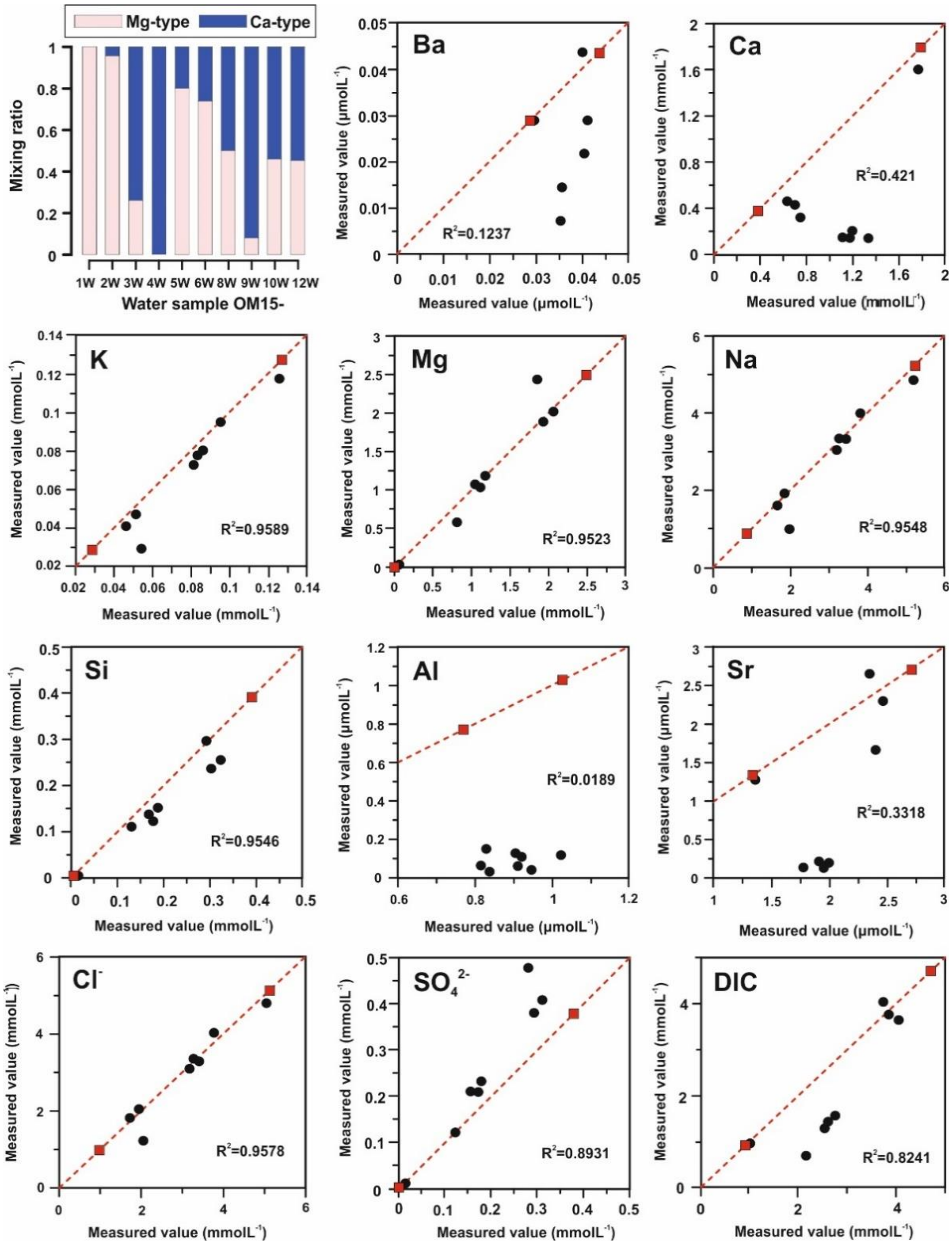

*Figure 3.13. Plots of measured (analytical) versus estimated (PHREEQC) concentrations using the collected water samples from the Nasif spring site. Water sample OM15–1W was used as the end-member for Mg-type waters and sample OM15–4W as the end-member for Ca-type waters (see **Table 3.2**). Red squares represent the values of the two end-members. The black circles correspond to the rest water samples. Red dashed line represents the indicative mixing trend.*

Measured (analytical) versus estimated (PHREEQC) values of element concentrations (**Fig. 3.13**) in the Nasif water samples are well correlated (R2 > 0.95) for K, Na, Cl^- and Mg, whereas Ca, Al, Si, Sr, Ba, SO_4^{2-} and DIC show a larger dispersion and correlation. Estimated values of Ba, Sr, Ca, K, Si, Al, DIC are higher than the measured ones in the majority of the samples, whereas SO_4^{2-} shows higher measured values.

3.5 Discussion

3.5.1 Groundwater flow paths of Oman alkaline springs

In the Oman spring systems, the proximity between the outlets of Mg-type and Ca-type water springs —somewhere spaced close together c. 1 m— (**Fig. 3.4a**) raises the question of what are the underground flow paths of these two types of water. In the Oman Ophiolite, groundwater circulation occurs in the near-surface horizon of fissured serpentinized peridotite, and to a lesser extent, along deeper fractures (Dewandel et al., 2003). Although tectonic structures (e.g., faults) might act as deep groundwater pathways of Oman hyperalkaline Ca-type springs, these springs randomly emanate from bedrock fissures unrelated to these tectonic structures, indicating that they follow other groundwater permeability pathways in the fissured aquifer. On the contrary, Mg-type spring waters generally follow tectonic contacts, emanating from fractured zones often associated with soils. The similar chemistry of meteoric-derived Mg-type spring waters and surface wadi waters (e.g., Paukert et al., 2012) suggests that they were both produced due to weathering processes taking place in the shallow serpentinized peridotite aquifer (Barnes and O'Neil, 1969; Dewandel et al., 2004).

The contrasting difference in the daily temperature fluctuations between Ca-type and Mg-type spring waters likely indicates that they are fed by groundwater from different depth horizons. The temperature of Ca-type hyperalkaline waters is rather constant (30 − 32 °C) and is likely indicative of deep groundwater. The daily temperature of Mg-type spring waters fluctuates as much as 10 − 12 °C showing that they are fed from shallower groundwater horizons. The differences in temperature fluctuations support that, before their discharge, Ca-type and Mg-type waters probably circulate along distinct flow paths, and that their underground mixing was likely limited. Rempfert et al. (2017) argued, however, that subsurface mixing of both water types could be the cause for enhancing the chemical disequilibria that promotes the growth of some microbial communities in Oman Ophiolite deep aquifers. Although the chemical profile of Ca-type and Mg-type waters greatly differs, underground mixing —at least to some degree and at specific aquifer parts— is a possible scenario. Further research is needed to develop a better understanding of the pathways and processes controlling the groundwater circulation and mixing of both water types, and their impact on their chemistry and any potentially triggered precipitation.

3.5.2 Hydrodynamics, geochemistry and active precipitation in the Oman spring systems

The hydrology and hydrodynamics of the Oman spring systems are pivotal to understand the variations in the chemistry of Mix-type waters and the chemical, mineralogical, and textural characteristics of their mineral precipitates (**Fig. 3.14**). In the following subsections we discuss the various mineral phases and textures associated with the different water types, and how they are linked to the hydrological features and hydrodynamics characterizing the spring sites.

3.5.2.1 Hyperalkaline Ca-type waters

Deep-rooted Ca-type waters discharge —apparently scattered— throughout the spring sites, feeding regularly the pool waters with hyperalkaline waters upstream to downstream (**Fig. 3.14**). The depletion of Ca-type waters in DIC dictates atmospheric CO_2 uptake as one of the main contributors for carbonate precipitation. In addition, the slow Ca-type water flow rates ($Q = 0.1 - 0.5$ L/s; Leleu et al., 2016) and the shallow nature of Ca-type pools promote evaporation under the arid climate conditions of Oman.

A thin (< 1 mm) crystalline crust on the water surface (**Fig. 3.3a**) is the main characteristic of hyperalkaline Ca-type waters. Crystalline crusts in Ca-type water pools and flow paths are mainly made of calcite (90 − 100 wt%; **Table 3.6**) that precipitates due to coupled effects of atmospheric CO_2 uptake and evaporation (e.g., Chavagnac et al., 2013b; Clark et al., 1992; Falk et al., 2016). The absence of Mg^{2+} ions and the low Mg/Ca ratio in Ca-type waters favor the precipitation of calcite (Folk, 1994; Pentecost, 2005), as well as the low dissolved CO_2 content (**Fig. 3.11**) inhibits aragonite precipitation (Jones, 2017a). In the absence of Mg ions, evaporation and CO_2 hydroxylation lead to extreme supersaturation rates and massive precipitation of calcite (Jones, 2017a). These fast supersaturation rates (Clark et al., 1992; Falk et al., 2016) in Ca-type waters could lead to the formation of initial calcite nuclei that remain attached to the air–water interface due to surface tension. This process may explain the presence of patches with small calcite crystals (< 4 μm) (**Fig. 3.6b**) in between the typical subhedral calcite crystals (up to 40 μm) in Ca-type crystalline crusts (**Fig. 3.6a**). Further evaporation in the pool can lead to high supersaturation and promote the observed precipitation of larger calcite crystals that use the initial small crystals as nucleation surface.

Evaporation of Ca-type waters produces a coating rim of precipitation on the rock around the pools (**Fig. 3.3b**). Similar to crystalline crusts, these rock coatings are calcite dominated (70 − 90 wt%; **Table 3.6**). The calcite crystals from rock coatings (**Fig. 3.7d**) and crystalline crusts (**Fig. 3.6a**) share similar sizes and morphologies that record the possible effects of evaporation on the textures of this sample type during precipitation. The curved edges of calcite crystals (**Fig. 3.7d**) are associated with high supersaturation (Gonzalez et al., 1992) with respect to calcium carbonate as a result of the high concentration of Ca in the evaporating waters. Slow evaporation rates could lead to kinetically-controlled high-quality crystals (Jones, 2017b), which is supported by the co-existence of euhedral {104} calcite crystals along with {120} calcite with curved edges and evident step-growth crystallization (**Fig. 3.7d**).

Figure 3.14. *Conceptual model of the Oman alkaline spring systems. The spring sites host different types of waters that are characterized by several types of precipitates with various textural characteristics. Water mixing, atmospheric CO_2 uptake, and evaporation are the main drivers of precipitation and textural differentiation of mineral phases occurring in the spring systems.*

3.5.2.2 *Mg-type and wadi waters*

Unlike Ca-type waters, Mg-type waters are more scarce and less dispersed, often merging with surface wadi waters before mix with Ca-type waters. In most cases, the Mg-type and wadi waters (Q is up to 20 L/s) in the peridotites are perennial and their flow is higher than that of the Ca-type water (Dewandel et al., 2004). This constant water flow leads to influxes of large Mg-type water volumes in pool network, especially near the Mg-type spring outlets. The fraction of the Mg-type waters in the Mix-type waters decreases upstream to downstream, as the number of the Ca-type springs feeding the pool network increases.

The precipitation in Mg-type waters is limited including only rock coatings around the pool rims. Our study is the first report of broad occurrence of hydrated magnesium (hydroxy-) carbonates in the Oman Ophiolite Mg-type waters. Since most of the Oman Mg-type waters are undersaturated with respect to hydrated Mg-carbonate, evaporation is the most plausible factor controlling their precipitation. Hydrated magnesium (hydroxy-) carbonates are indicative of evaporative environments characterized by CO_2 degassing and high CO_2 content (e.g., Levy et al., 1999; Müller et al., 1972; Power et al., 2009; Power et al., 2019). Nesquehonite can be formed due to evapoconcentration around the Mg-type pools (**Fig. 3.14**) through cycles of recharge and subsequent evaporation of the pool waters. The large size (up to 2 mm) and the high quality of nesquehonite crystals in Mg-type waters (**Fig. 3.7c**) could indicate slow supersaturation rates, probably due to slow evaporation of the —lower in temperature compared to Ca-type (Appendix **Fig. A−3.1**)— Mg-type waters.

In the Khafifah spring site, one Mg-type water pool (i.e., OM15K−02W; **Table 3.2**) is supersaturated with respect to hydromagnesite (SI = 2) and artinite (SI = 0.8) (**Fig. 3.11**). The interaction of water with soil potentially accounts for its high Mg DIC concentration —that plays a crucial role in the precipitation of hydrated Mg-carbonates (Ferrini et al., 2009; Kloprogge et al., 2003; Power et al., 2019)— and favored the precipitation of hydrated Mg-carbonates (25 wt% nesquehonite and 70 wt% dypingite; **Table 3.6**). The XRD analysis showed that artinite in Mg-type pools is chlorartinite, a Cl-rich artinite variety, where OH^- is replaced by Cl^- in the crystal lattice. Co-precipitation of chlorartinite and nesquehonite is common in Cl-rich evaporitic environments (Mignardi et al., 2011). Hydromagnesite only occurs in the Khafifah water pools with DIC > 5 mmol/L, attesting for precipitation in a CO_2-rich environment (Power et al., 2019).

Alternatively, the precipitation of hydrated Mg-carbonates may also be due to the increase of the OH^- concentration during the influx of Ca-type waters in Mg-type pools. In this scenario, evaporation would control nesquehonite precipitation, while the precipitation of dypingite, hydromagnesite, and artinite is governed by the pH increase (Power et al., 2007; Zhang et al., 2006) during Ca-type water influx events. These influx events could explain the observed transformation process of nesquehonite to dypingite in **figure 3.15**, where a pseudomorph of dypingite forms after a prismatic crystal of nesquehonite. This could also imply a potential recharge of the pool with alkaline Mg-type waters. In both cases, the inserted fluid is undersaturated with respect to nesquehonite and initiates its dissolution. Subsequently, supersaturation with respect to dypingite or hydromagnesite could create an interfacial layer, where the product mineral may take on the crystal morphology of the parent (pseudomorphic replacement; **Fig. 3.15**) (Power et al., 2019 and references therein). This process is known as *interface-coupled dissolution–precipitation* (Ruiz-Agudo et al., 2014). In addition, the influence of Mg-type waters by Ca-type water influxes could introduce high amounts of OH^- in the pool leading to nesquehonite conversion into dypingite and/or hydromagnesite (Power et al., 2007; Zhang et al., 2006).

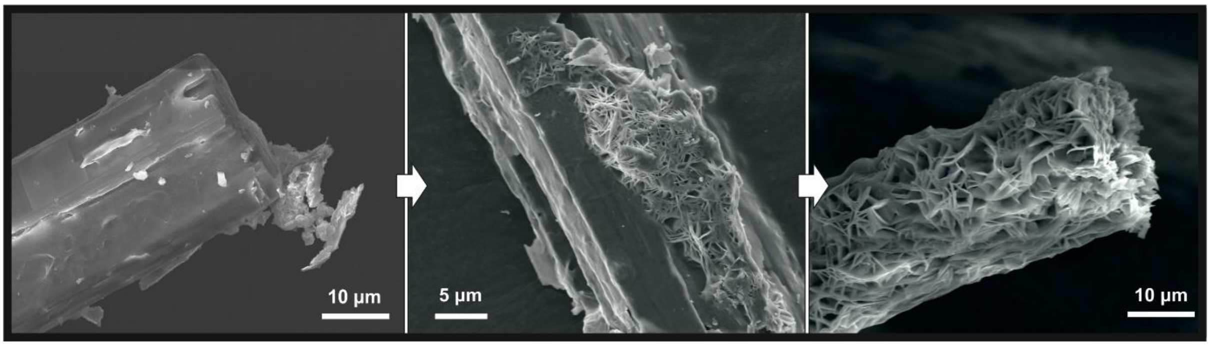

Figure 3.15. *The transformation process of nesquehonite into dypingite (pseudomorph crystal) in Mg-type waters. Prismatic crystal of nesquehonite (left) get completely converted to dypingite flakes (right) via interface-coupled dissolution–precipitation (middle).*

3.5.2.3 Mix-type waters

Massive calcium carbonate deposits —mud-like precipitates and flocculent material— are systematically associated with Mix-type water pools, pointing that mixing of Ca-type and Mg-type waters is the primary cause for the precipitation of these deposits. Based on the stable isotope signature of calcium carbonates, Falk et al. (2016) proposed that the main precipitation mechanisms of these deposits was both water mixing and atmospheric CO_2 uptake; however, calcium carbonates with an atmospheric CO_2 uptake isotopic composition may have been formed in Ca-type pools and transported to the Mix-type pools by the water flow. Due to the relatively low SI of calcium carbonate (SI = 0.6 − 1.7; **Fig. 3.11**) in Mix-type waters — compared to other travertine forming environments (Leleu et al., 2016; Pentecost, 2005)— evaporation may have also played a role in the formation of these deposits.

Aragonite is the dominant calcium carbonate phase in Mix-type water pools due to the higher Mg concentration and Mg/Ca ratio relative to those in Ca-type waters (**Table 3.6**) (e.g., Chavagnac et al., 2013b; Falini et al., 1994; Jones, 2017a; Lin and Singer, 2009; Pokrovsky, 1998, and references therein). In some cases, Mg-type and Ca-type waters discharge simultaneously into the same pool and create peculiar Mix-type pools (**Fig. 3.14**; e.g., OM15−03W). These Mix-type pools share a mixture of mineralogical and textural characteristics that reflect a strong influence from both Mg-type and Ca-type waters on mineral precipitation; aragonite–brucite (hydromagnesite)–calcite crystalline crusts (**Table 3.4**; OM15−03B−P) and aragonite–brucite (hydromagnesite)–calcite mud-like and flocculent material deposits (**Table 3.4**; OM15−03C−Pa) form, respectively, around Ca-type and of Mg-type spring outlets (**Fig. 3.14**).

The texture of crystalline crusts in Mix-type waters is suggestive of an initial stage of aragonite nuclei formation that is followed by subsequent growth of the first crust segments at the air-water interface, likely caused by CO_2 uptake and evaporation (**Fig. 3.16**; Stage I). In a second stage (**Fig. 3.16**; Stage II), further growth of semi-spherical acicular aragonite takes place leading to the expansion of the crust. The growth of aragonite is unaffected by the presence of Mg ions, which remain —at least initially— in solution and suppress aragonite transformation into calcite (Berner, 1975; Kitamura, 2001; Reddy and Wang, 1980). The continuous growth of the crust leads to the development of an aragonitic layer that completely covers the water surface and becomes the substrate for later growth of brucite and calcite crystals (**Fig. 3.16**; Stage III). The development of the crystalline crust provides a non-turbulent environment and a physical substratum that promotes the growth of well-defined microplates of magnesium hydroxide, resulting in a better ordering of brucite crystals. In contact with atmospheric CO_2, brucite transforms to hydromagnesite, artinite or nesquehonite, what would account for the presence of hydromagnesite in some crystalline crusts (**Fig. 3.6d**) (Botha and Strydom, 2001; Hostetler et al., 1966; Simandl et al., 2008; Zhao et al., 2009). In the late crystallization stage (**Fig. 3.16**; Stage III), formation of brucite in the crystalline crusts decreases the Mg/Ca ratio of Mix-type waters, triggering the heterogeneous nucleation of calcite on the aragonitic crust surface. The euhedral shape of these crystals formed in this stage (**Fig. 3.16**) is indicative of slow crystal growth that was favored by the sluggish atmospheric

CO_2 diffusion into water pools due to the formation of the crystalline crust (Chavagnac et al., 2013b; Olsson et al., 2014).

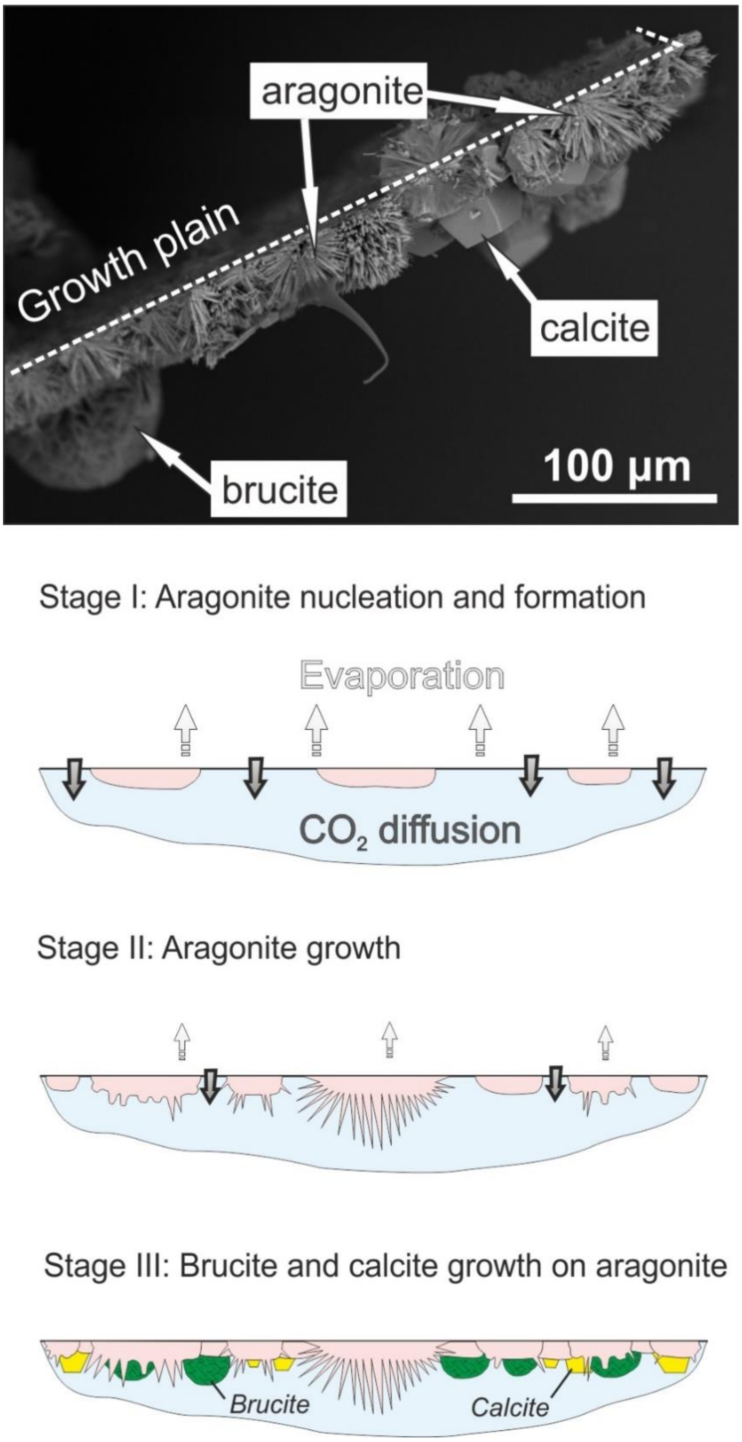

Figure 3.16. *Growth process of crystalline crusts in Mix-type waters. At initial crystallization stage, aragonite nucleates at the air–water interface due to evaporation and* CO_2 *uptake (**Stage I**). Further evaporation and* CO_2 *diffusion and uptake leads to aragonite growth, and the development of the crystalline crust at the air–water interface (**Stage II**). Aragonite crystals act as a growth substrate for brucite and calcite, as well as a barrier for further* CO_2 *diffusion in the water (**Stage III**).*

Aragonite particles from a single sample of flocculent material in Mix-type pools (**Fig. 3.14**) exhibits a large textural diversity (**Fig. 3.8a**) that reflects their formation under different supersaturation values and rates. The aragonite particle textures record an evolutionary path from an initial crystalline sheaf towards acicular, sphere-like aragonite (**Fig. 3.17**). Higher supersaturation and faster supersaturation rates lead to aragonite formation that exhibits branching, displaying a splitting process at the growth front of the crystal (Rowling, 2004). This process creates fan-like morphologies at the tips of aragonite crystals that eventually form spherical aragonite morphologies **(Fig. 3.17**) (Gránásy et al., 2005). Unlike mud-like precipitates, the aragonite textures in flocculent material record the changes in the values of supersaturation and supersaturation rates associated with environments of vigorous water mixing (e.g., in Mix-type pools where Mg-type and Ca-type waters discharge simultaneously) or rapid CO_2 uptake and evaporation (e.g., near the air–water interface).

The deposition and development of dam-like formations (rippled terracing) is controlled by water hydrodynamics, in particular the bedrock morphology and local obstacles to the water flow paths (Hammer et al., 2007; Hammer et al., 2010) (**Fig. 3.3d**). Aragonite in dams (terraces) of mud-like precipitates show a self-organized nanocrystalline structure made of co-oriented nano-rods (**Fig. 3.18**), suggesting nucleation and growth by accretion and not by classical crystal growth mechanisms. Diverging rod-made branches lead to wheat-sheaf shapes, whereas converging ones lead to spindle crystals with mesocrystalline structure (**Fig. 3.18**). These structures could also be attributed to self-organization of aragonite mesocrystals, leading to crystals formed by crystalline subunits (Cölfen and Mann, 2003; Jones, 2017b; Meldrum and Cölfen, 2008; Zhou et al., 2009). The homogeneity of mineralogy (aragonite: 63 − 100 wt%; **Table 3.6**) and textures (**Fig. 3.9a**) in mud-like precipitates imply non variable saturation values and supersaturation rates. These steady conditions can be established in low energy environments of the pool networks, such as the mid-parts of shallow pools and the outmost parts of streams and pools. Indeed, these environments are the most common areas within the spring sites, where mud-like dams tend to form.

Apart from crystalline crusts, brucite is uncommon in streams, but locally precipitates — occasionally forming brucite-bearing concretions (**Fig. 3.3e**)— in restricted mixing zones, where Ca-type waters come in contact with Mg-type and Mix-type waters (**Fig. 3.14**). In these mixing zones, the water flow is slow, indicating the critical role of hydrodynamics on brucite occurrence. The relatively more energetic water flow of streams may prevent brucite settling and favor its dissolution (Chavagnac et al., 2013b), while mixing zones with slow water flow promotes the settling and/or preservation of brucite.

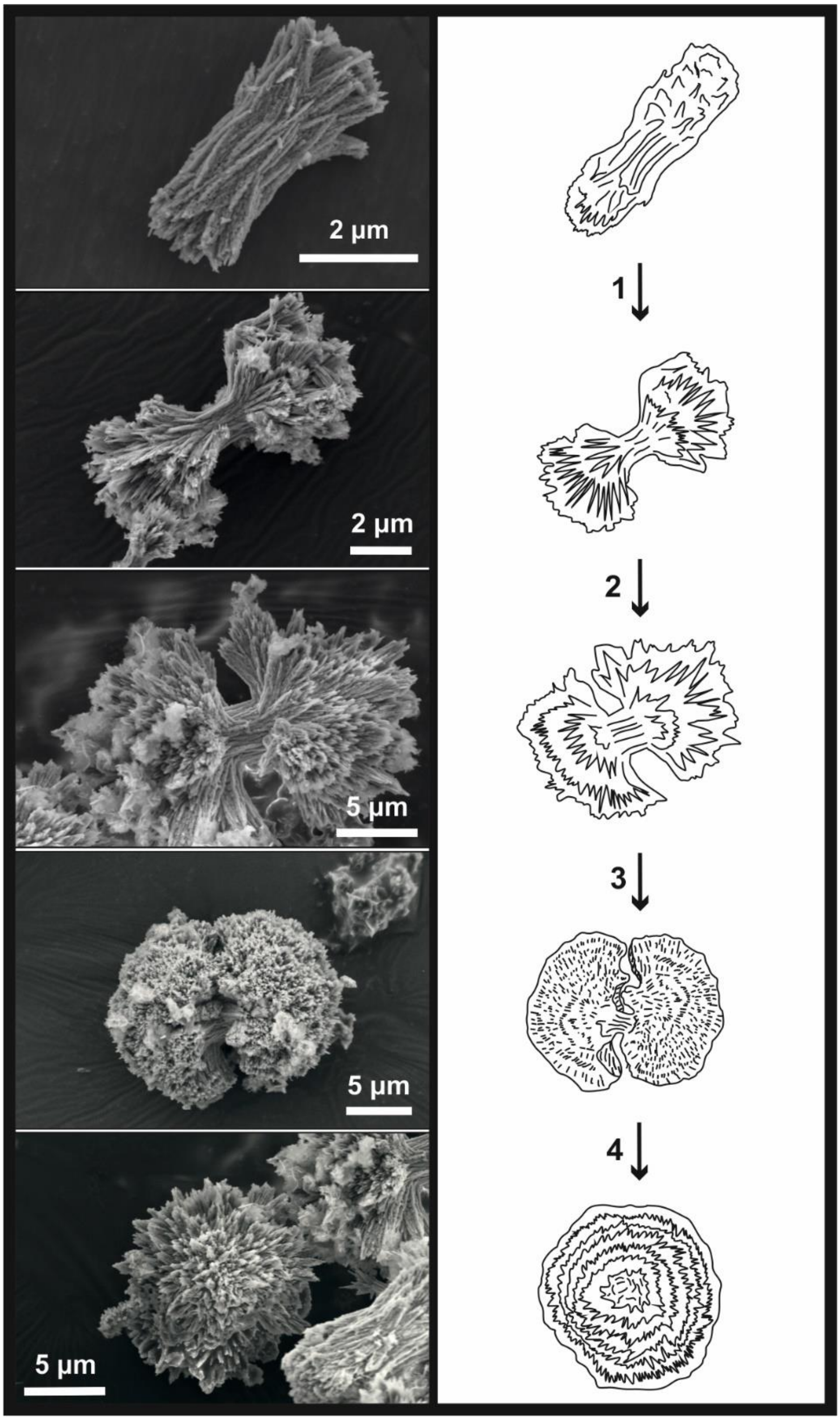

Figure 3.17. SEM images (left) and sketches (right) describing the textural evolution of aragonite in flocculent material. Branching and splitting processes lead from an initial crystalline sheaf, over wheat-sheaf and dumbbell, to an acicular-spheroidal morphology.

The crystals of brucite in the concretions (**Fig. 3.3e**) display a distortion bending and a narrowing of the internal distances between the crystal flakes (**Fig. 3.10b**). These textural features likely indicate an on-going cementation process around mixing zones, where the hyperalkaline Ca-type waters come in contact with Mg-type or Mix-type waters under slow water flow conditions. At the parts of the concretions that aragonite growth is not inhibited by brucite, open-space crystallization of acicular, needle-like aragonite is favored (**Fig. 3.10b**). Unlike Mix-type crystalline crusts, brucite crystals in mud-like and flocculent material (for frequency see **Table 3.5**) show smaller crystal sizes (< 5 μm) and lower degree of crystallinity (**Fig. 3.8b**) than brucite in the crystalline crusts (**Fig. 3.6c**). This textural feature is possibly indicative of faster supersaturation rates during vigorous mixing of Ca-type with Mg-type or Mg-rich Mix-type waters, where the steady supply of Mg^{2+} and OH^{-} keeps the water supersaturated with respect to brucite. In some cases, brucite occurs in mud-like and flocculent material from Mix-type water pools that are located away from mixing zones. This may indicate that brucite had formed elsewhere and was transported by the water flow in these pools. Nevertheless, according to our mixing model, the highest values of brucite supersaturation (SI = 2.5; **Fig. 3.12**) are attained where the Ca-type mixing fraction is between 0.5 and 0.9. This is in agreement with the calculated Mg-type – Ca-type ratios (see **Fig. 3.13**) characterizing the natural Mix-type pools, where brucite was actually found (Appendix **Fig. A−3.4**).

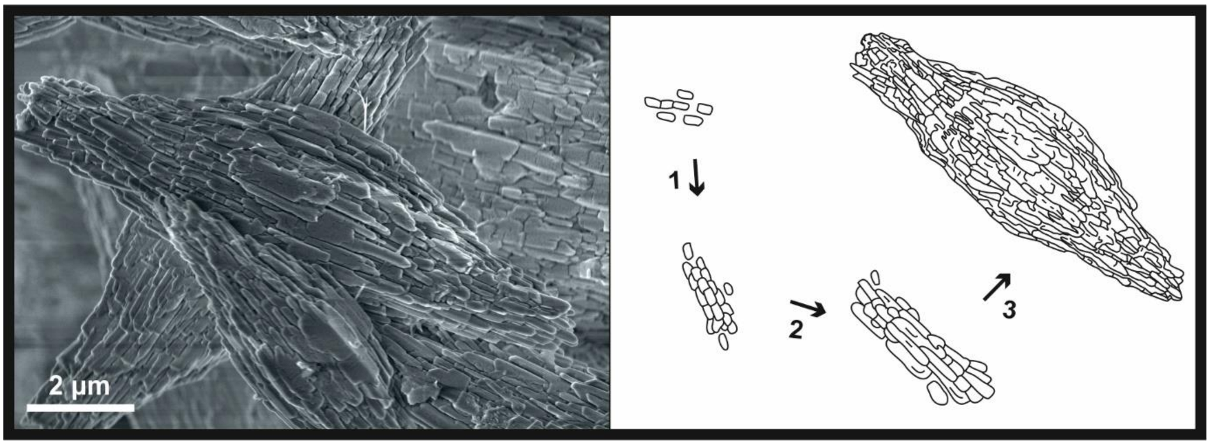

Figure 3.18. *SEM image (left) and sketch (right) describing the spindle aragonite crystals that form due to the aggregation of aragonite nano-rods via self-assembly processes in the dams of mud-like precipitates.*

3.1.1 Development of travertine terraces

Preserved travertine terraces in Oman (**Fig. 3.3f**) —forming over the past 50 ka (Mervine et al., 2014)— are extensive carbonate formations that mainly form via CO_2 uptake from the hyperalkaline Ca-type waters (Falk et al., 2016). In most cases, the travertine terraces develop in association with Ca-type springs and appear to have a close genetic relation to lithified dam-like structures (**Fig. 3.3e**). Before reaching the form we observe today, travertine terraces experience early stages of cementation and lithification processes that can be identified in the lithified dam-like structures. Calcite exhibits internal lamination and undefined crystal boundaries (**Fig. 3.10a**) recording the conversion of well-shaped crystals into the observed chaotic textures of the travertines. Similarly, aragonite structure is affected by cementation processes and displays a compact texture by narrowing the space between the needle-like crystals (**Fig. 3.10a**). Compact textures of aragonite could indicate its gradual transformation into more stable calcite (Pentecost, 2005 and references within), which is the major component of Oman travertine terraces (**Table 3.6**). In some parts of the lithified dams, calcite crystals exhibit concentric cavities, which often crosscut crystal boundaries (Appendix **Fig. A−3.5**). These cavities on calcite surfaces could be created by gas bubbles that are attached to the growth substrate (Aquilano et al., 2003; Taylor and Chafetz, 2004). Calcite starts forming on the bubble surface leaving an empty space at the place where the bubble was present. This kind of pores on calcite surface may also be associated with specific cellular functions (e.g., self-protection mechanisms, presence of polysaccharidic capsule) processed by several microbial communities (e.g., cyanobacteria) during calcium carbonate precipitation (Bundeleva et al., 2014; Martinez et al., 2010). Such impurities on calcite may create disorganization and irregular crystallization surfaces that eventually lead to the perplexing textures observed in post-lithification travertine.

The lithified dam-like structures are exclusively associated with active Ca-type waters that run-off from Ca-type springs (**Fig. 3.4; Fig. 3.14**). The dominance of calcite over aragonite in these dam-like structures (**Table 3.6**) point to their precipitation directly from Ca-type waters without any indication of mixing with Mg-type waters. Alternations of active and inactive flow of Ca-type waters could trigger multiple recrystallization events that effect the development of the dam-like structures and subsequently the travertine terraces. Dehydration-hydration periods have an impact on calcite growth and reactivity (Fenter and Sturchio, 2012 and references within) that could lead to the chaotic and colloformic textures of the travertine terraces (**Fig. 3.10c**). The strong presence of active carbonate precipitation due to mixing requires further assessment regarding its contribution and incorporation to the travertine terrace build-up.

3.2 Appendices

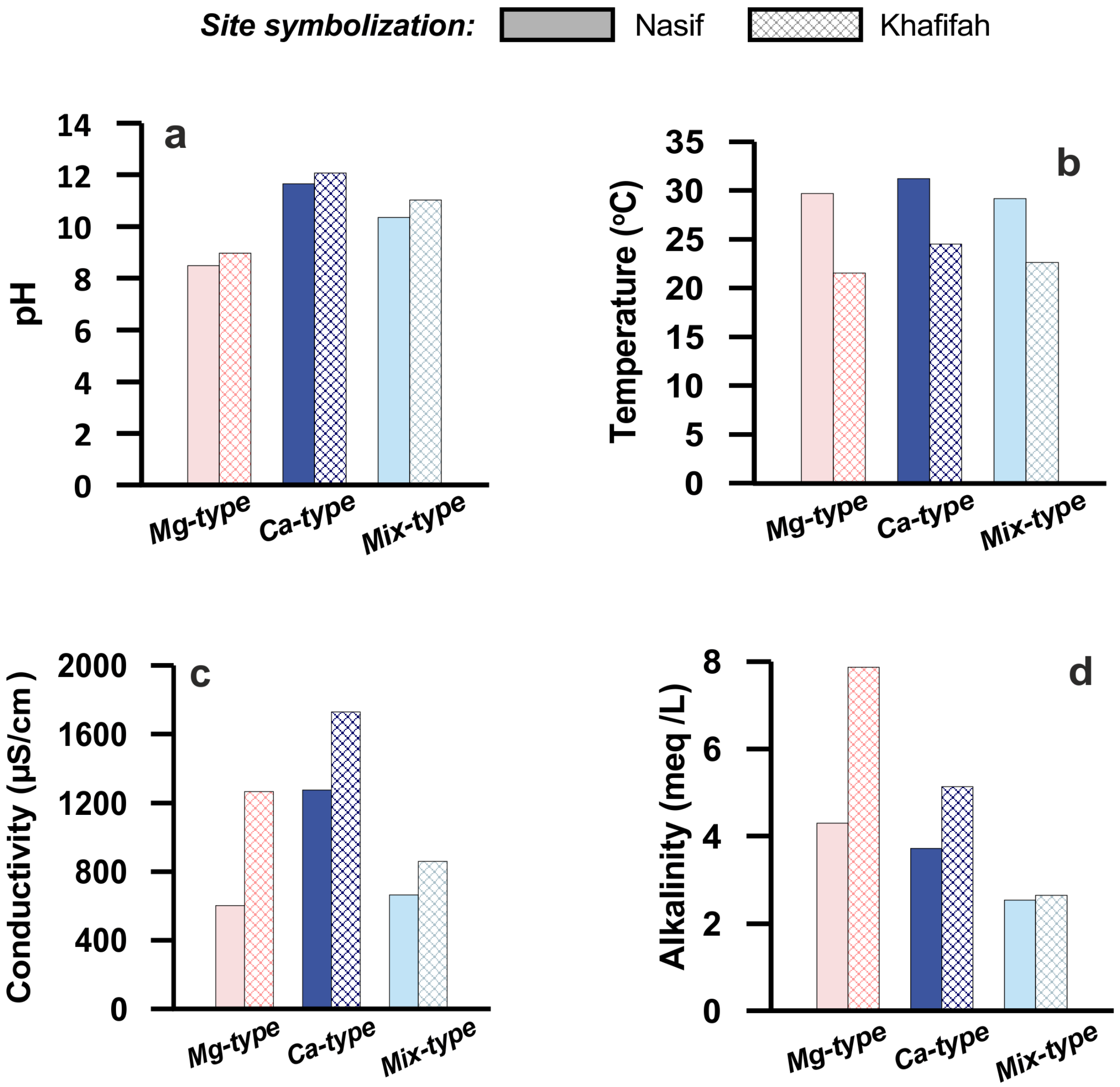

Figure A-3.1. *Comparative bar charts of average values of water parameters of each water type in the two spring sites. Bar charts**:** **(a)** pH, (**b**) temperature, (**c**) conductivity, and (**d**) alkalinity.*

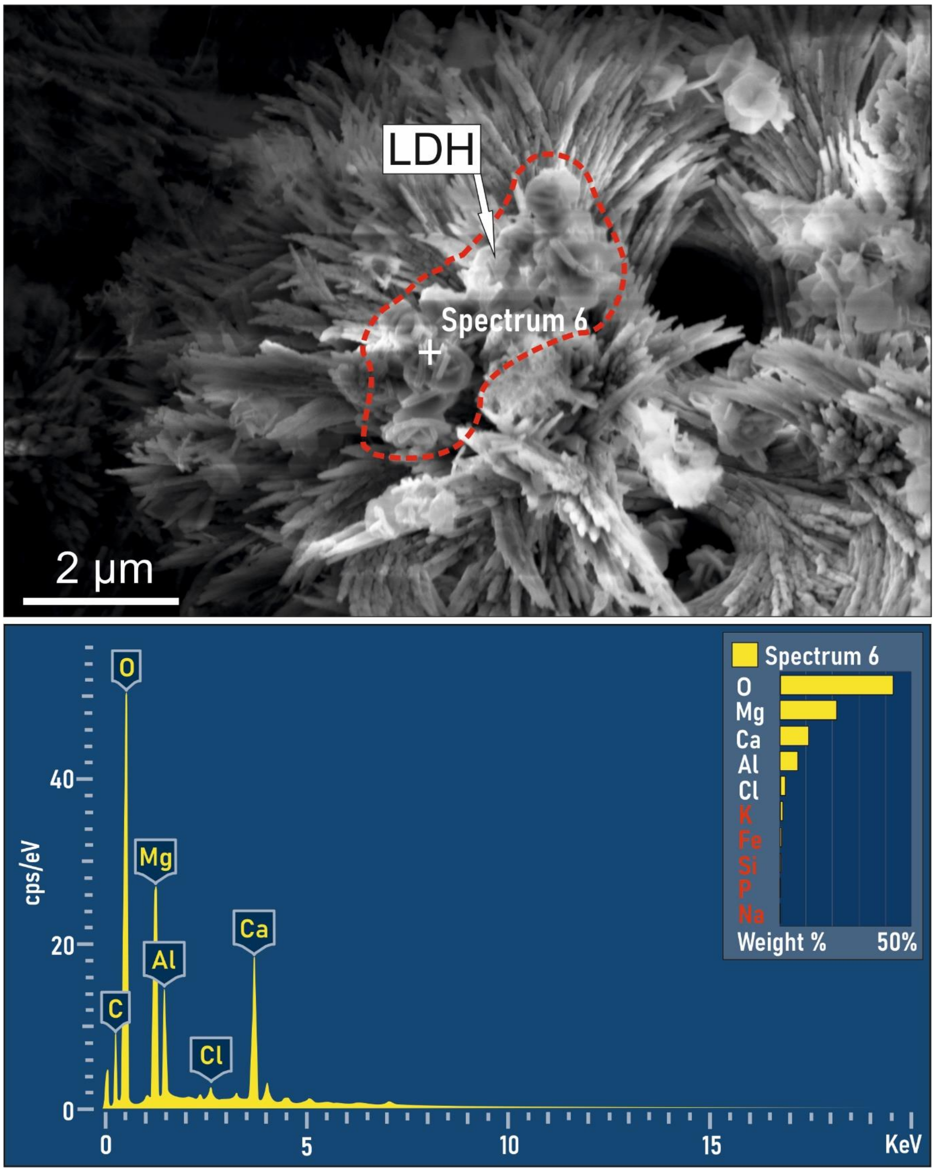

Figure A-3.2. *SEM image (up) of LDH flaky crystals growing on acicular aragonite. EDX analysis (down) showing the Mg and Al in the LDH (hydrotalcite) crystal structure.*

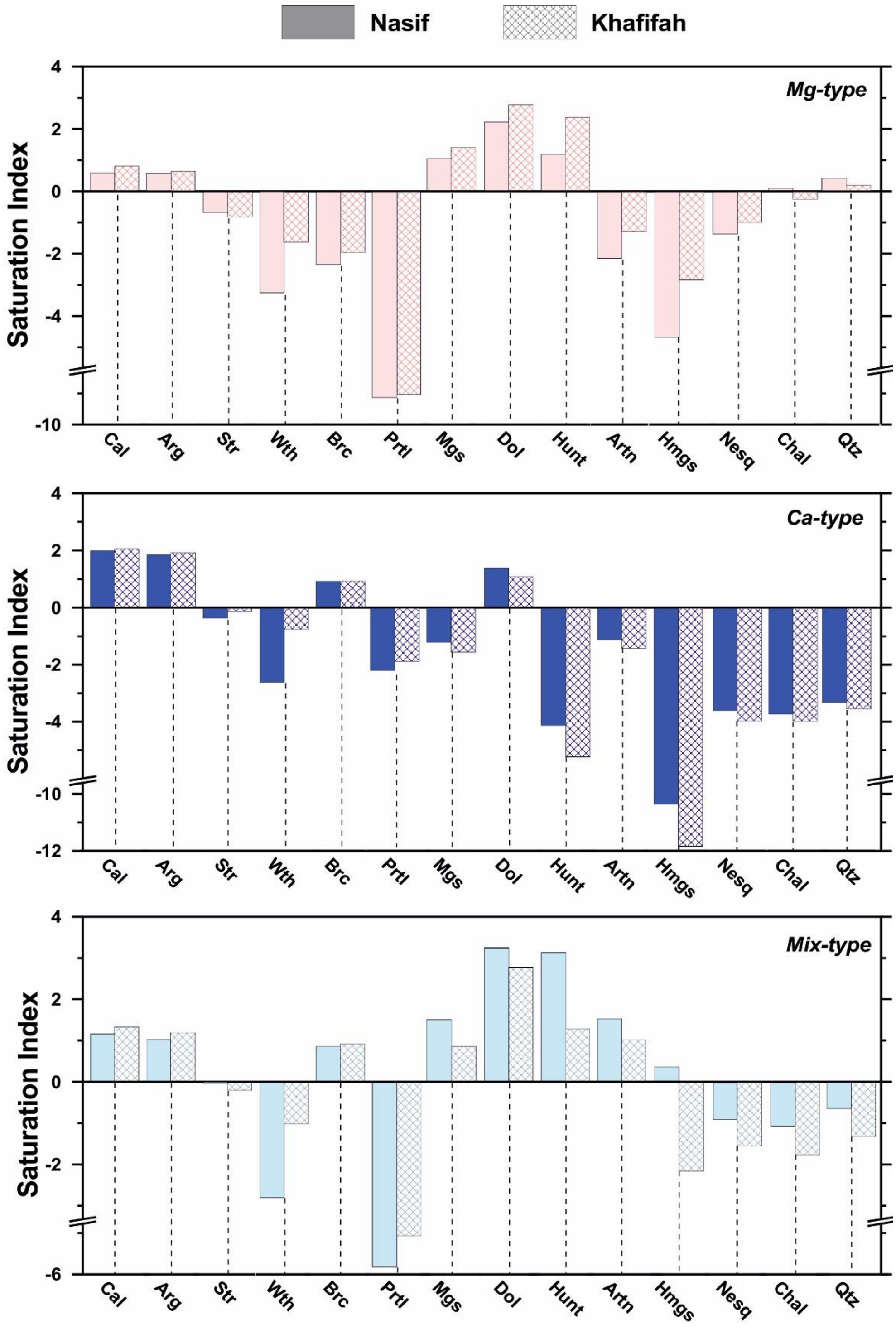

Figure A-3.3. *Average values of saturation indices of potential mineral phases (carbonates, hydroxides and* SiO_2 *polymorphs) in Mg-, Ca- and Mix-type waters for the Nasif and Khafifah spring sites.* ***Cal:*** *calcite,* ***Ara:*** *aragonite,* ***Str:*** *strontianite,* ***Wth:*** *witherite,* ***Brc:*** *brucite,* ***Prtl:*** *portlandite,* ***Mgs:*** *magnesite,* ***Dol:*** *dolomite ,* ***Hunt :*** *huntite ,* ***Artn :*** *artinite ,* ***Hmgs :*** *hydromagnesite ,* ***Nesq :*** *nesquehonite,* ***Chal:*** *chalcedony,* ***Qtz:*** *quartz.*

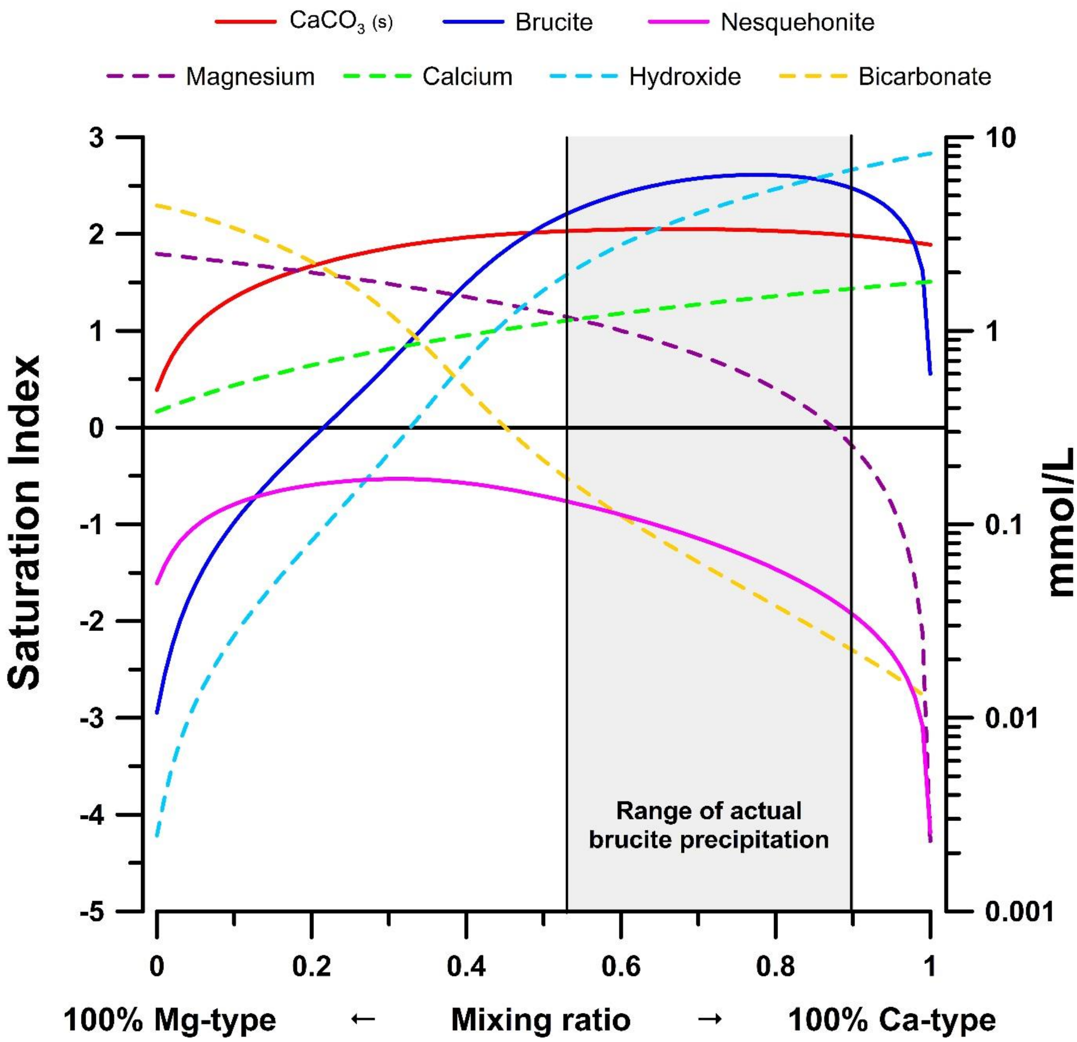

Figure A-3.4. *Relationship between SI evolution of occurring mineral phases in the pools (calcite, aragonite, brucite and nesquehonite) and concentration variations of the main ion species of the water types (Ca, Mg, OH^- and HCO_3^-) during gradual mixing model. The mixing model and the end-member waters used for its construction are described in section **3.4.3**, and they are identical with the model in **figure 3.12**. The grey area on the plot corresponds to sampled Mix-type water pools with modeled Mg- and Ca-type mixing proportions (see **Fig. 3.13**) in which brucite has been identified.*

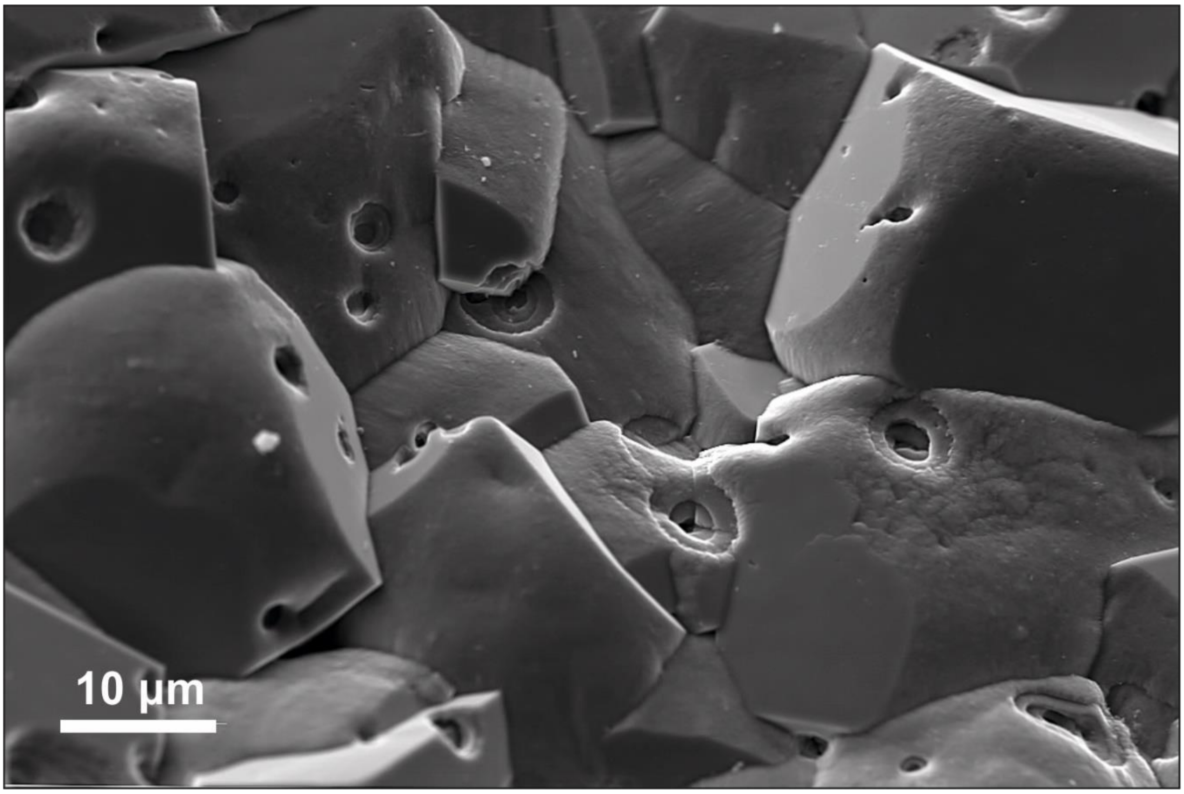

Figure A-3.5. *Concentric cavities on calcite surface crosscutting crystal boundaries in lithified dam-like structures.*

4 Geochemistry and mineralogy of serpentinization–driven hyperalkaline springs in the Ronda peridotites[1]

4.1 Introduction

Carbonation processes associated with hyperalkaline fluids and serpentinization of peridotite have recently attracted much attention because of their relevance to carbon capture and storage (Kelemen et al., 2011; Klein and Garrido, 2011; Matter and Kelemen, 2009), the role of carbonation of serpentinite in the deep carbon cycle (Alt et al., 2012, 2013; Dasgupta and Hirschmann, 2010; Kelemen and Manning, 2015; Menzel et al., 2018, 2019), the origin of prebiotic organic chemistry (Martin et al., 2008; Martin and Russell, 2007; Sleep et al., 2011), and the detection of primitive life (García-Ruiz et al., 2003, 2017).

Active serpentinization in the ocean sub-seafloor generates fluid vents with carbonate chimneys —up to 60 m in height— composed of mixtures of calcite, aragonite, and brucite (Ludwig et al., 2006). The Lost City hydrothermal field is a unique example of active serpentinization system in the Atlantis massif oceanic core complex near the Mid-Atlantic Ridge at 30° N (Kelley et al., 2001). In this vent field, the discharging alkaline to hyperalkaline fluids (pH: 9 − 11) show relatively low temperature (40 − 90 °C), high H_2/CH_4 ratios, and low concentrations of metals (Kelley et al., 2005; Proskurowski et al., 2006). Alkaline to hyperalkaline springs also occur off-shore in continental settings, where hyperalkaline fluids form during deep circulation of meteoric waters in tectonically emplaced and variably serpentinized ophiolites and subcontinental lithosphere mantle peridotites. In these continental peridotites, the exposure of serpentinite-hosted hyperalkaline (pH > 11) fluids to atmospheric conditions induces carbon mineralization (Neal and Stanger, 1984). Carbonate precipitation from continental serpentinite-hosted hyperalkaline fluids are documented, among other places, in the Samail Ophiolite (Oman) (Chavagnac et al., 2013a; Neal and Stanger, 1983; Paukert et al., 2012), California Coast Range (USA) (Barnes and O'Neil, 1971; Blank et al., 2009; Morrill et al., 2013), Bay of Islands (Canada) (Cardace et al., 2009), Santa Elena Ophiolite (Costa Rica)

---

[1] *This chapter has been published in Giampouras, M., Garrido, C.J., Zwicker, J., Vadillo, I., Smrzka, D., Bach, W., Peckmann, J., Jiménez, P., Benavente, J., García-Ruiz, J.M., 2019. Geochemistry and mineralogy of serpentinization-driven hyperalkaline springs in the Ronda peridotites. Lithos. DOI: https://doi.org/10.1016/j.lithos.2019.105215*

(Sánchez-Murillo et al., 2014) and the Ligurian ophiolites (Italy) (Chavagnac et al., 2013a; Cipolli et al., 2004). In addition, alkaline springs in Prony Bay ophiolites (New Caledonia) are an example of carbonate precipitation by meteoric-origin hyperalkaline fluids, which are subsequently affected by seawater (Monnin et al., 2014). The increasing interest in carbon mineralization for the removal of carbon dioxide from the atmosphere has fuelled research on carbonate formation in serpentinite-hosted alkaline fluids in continental settings such as caverns, hot springs, and lacustrine environments (Lacelle et al., 2009; Leleu et al., 2016; Pentecost, 2005).

In the Ronda peridotites (Betic Cordillera, S. Spain) (**Fig. 4.1**), previous studies have documented more than 70 alkaline to hyperalkaline springs, which chemistry and related mineralization are still barely known (Etiope et al., 2016; Vadillo et al., 2016). Here, we present a detailed study of the geochemistry of hyperalkaline fluids and river waters, and the associated mineral phases and textures characterizing the alkaline spring sites in the Ronda peridotites. The present study is aimed at better constraining the carbonation processes in serpentinite-hosted alkaline fluids in one of the largest exposures of subcontinental mantle peridotites worldwide.

4.2 The Ronda peridotites

The Gibraltar arc in the westernmost Mediterranean is bounded by the Alpine Betic and Rif orogenic belt that surrounds the Neogene Alborán Sea basin (**Fig. 4.1a**). This arc-like mountain belt was formed as the result of a complex Cenozoic evolution of subduction initiation, slab fragmentation, and rollback in the central and western Mediterranean in a context of slow convergence between Africa and Europe (e.g., Balany_a et al., 1997; Booth-Rea et al., 2015; Faccenna et al., 2004; Guerrera et al., 2005; Lonergan and White, 1997; Platt et al., 2013; Royden, 1993). These geodynamic processes resulted in the crustal emplacement of large bodies of subcontinental mantle peridotites that now crop out in the internal zones of the western Betics (the Ronda peridotites) and the Rif (Beni Bousera peridotites) mountain belts (**Fig. 4.1a**) (Frets et al., 2014; Garrido et al., 2011; Hidas et al., 2013a; Marchesi et al., 2012; Mazzoli et al., 2013; Obata et al., 1980; Précigout et al., 2013; Tubía et al., 1997; Van der Wal and Vissers, 1996).

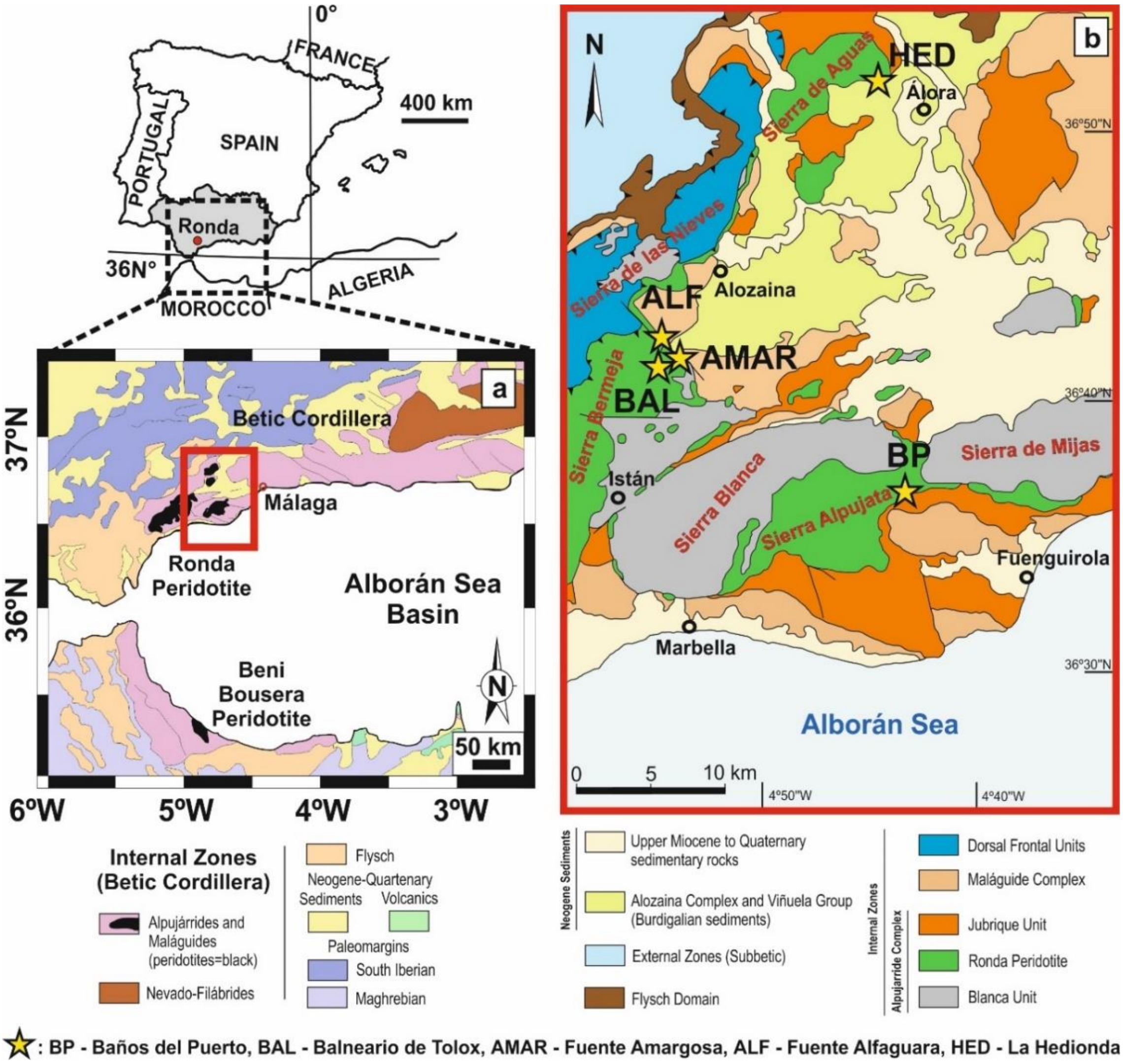

Figure 4.1. *Geological maps of the Betic-Rif orogen and the western Betic Cordillera.* ***(a)*** *Simplified geological map of the main tectonic domains and units of the Betic-Rif orogenic belt showing the location of the Ronda peridotites (Betic Cordillera, S. Spain) and the Beni Bousera Peridotite (Rif Belt, N. Morocco). The red rectangle indicates the area shown in* ***Fig. 4.1b*** *(modified after Hidas et al., 2013a).* ***(b)*** *Enlarged geological map of the western sector of the internal zones of the Betic Cordillera showing the location of the investigated serpentinite-hosted hyperalkaline spring sites (yellow stars) in eastern Sierra Bermeja (Ronda peridotite massif; BAL: Balneario de Tolox; AMAR: Fuente Amargosa; ALF: Fuente Alfaguara), western Sierra Alpujata (Ojén peridotite massif; BP: Baños del Puerto), and northwestern Sierra de Aguas (Carratraca peridotite massif; HED: La Hedionda) (modified after Acosta-Vigil et al., 2014; Mazzoli and Martin Algarra, 2011).*

In the Betic Cordillera, several mantle peridotite massifs —here collectively referred to as “the Ronda peridotites”— occur in the westernmost Alpujárride complex, a tectonic unit of the internal zones of the Betics that is structurally sandwiched between the Maláguide and the Nevado-Filábride complexes (**Fig. 4.1a**). The westernmost Alpujárride complex includes the Jubrique and Blanca crustal units that overlie and underlie, respectively, the Ronda peridotite massif (**Fig. 4.1 a & b**) (Balanyá et al., 1997; Tubía et al., 1997). The Jubrique unit is a highly attenuated (≤ 5 km) crustal section composed of non-metamorphic to greenschist carbonates underlain by a crustal sequence of increasing metamorphic grade towards the upper contact with the peridotite massif. The Blanca Unit (**Fig. 4.1b**) underlies below the Ronda peridotite and is composed of variably deformed, high temperature–low pressure schists, marbles, and migmatitic gneisses (Acosta-Vigil et al., 2014; Tubía et al., 1997).

Covering an area of c. 450 km^2, the Ronda peridotites are one of the largest outcrops of subcontinental mantle peridotite worldwide (Obata et al., 1980; Tubía et al., 1997). These ultramafic massifs are mostly composed of spinel and plagioclase peridotite (lherzolite, minor harzburgite and subordinate dunite) and minor garnet lherzolite, with occasional layers of garnet- spinel- and plagioclase-pyroxenites, and rare gabbro veins and chromitite pods (Bodinier et al., 2008; Garrido and Bodinier, 1999; Garrido et al., 2011; Gervilla and Leblanc, 1990; González-Jiménez et al., 2017; Lenoir et al., 2001; Obata et al., 1980; Soustelle et al., 2009; Tubia et al., 2004; Van der Wal and Vissers, 1996). The Ronda peridotites encompass several massifs exposed in the mountain ranges of Sierra Bermeja (Ronda massif), Sierra Alpujata (Ojén massif), and Sierra de Aguas (Carratraca massif) (**Fig. 4.1b**). The massifs are in tectonic contact with different crustal lithologies of the Jubrique and the Blanca units of the western Alpujarrides, and the frontal units of the western internal zones of the Betics (Martín Algarra, 1987) (**Fig. 4.1b**).

4.3 Hyperalkaline springs in the Ronda peridotites

We studied five hyperalkaline spring sites in the westernmost part of the Ronda peridotites (**Fig. 4.1b; Table 4.1**). Etiope et al. (2016) investigated the stable isotope signatures and ^{14}C age of gases occurring in these spring sites and confirmed that they show isotopic signatures similar to other continental hyperalkaline springs associated with active serpentinization. The spring sites investigated in the present study generally occur near the contact of peridotites with crustal rocks (**Fig. 4.1b**). Fuente Amargosa (AMAR), Fuente Alfaguara (ALF) and Balneario de Tolox (BAL) springs are located in the eastern part of Sierra Bermeja —the Ronda peridotite massif— near the village of Tolox (**Fig. 4.1b**), and the La Hedionda (HED) spring is located in SE Sierra de Aguas —Carratraca peridotite massif— near the village of Álora (**Fig. 4.1b**). In these springs, the hyperalkaline fluids emanate from rock fractures (ALF) or human-made pipes and fountains (BAL, AMAR, and HED).

The Baños del Puerto (BP) (**Fig. 4.2**) —in the Ojén massif, SW Sierra Alpujata (**Fig. 4.1b**)— is a serpentinite-hosted spring system near the riverside of the Alaminos river. We

Table 4.1. *General sample information and water chemistry parameters.*

Sample ID	Peridotite Massif	Coordinates		pH	T	Cond.	Alk.
		N	W		(°C)	(µS/cm)	(meq/L)
Hyperalkaline fluids							
HED	Carratraca	36°50′34.55″	4°43′57.72″	11.3	21.0	857	2.32
AMAR	Ronda	36°41′21.24″	4°54′39.92″	11.8	18.2	1257	5.08
BAL	Ronda	36°40′44.44″	4°54′34.34″	11.4	16.9	478	1.54
ALF	Ronda	36°41′35.12″	4°55′00.56″	12.0	18.9	1100	6.02
BP1	Ojén	36°35′42.18″	4°43′32.11″	11.5	21.6	636	2.33
BP1/SK	Ojén	36°35′42.11″	4°43′32.26″	11.5	20.1	586	1.21
BP2	Ojén	36°35′41.76″	4°43′32.12″	11.5	20.2	718	2.73
BP3	Ojén	36°35′42.12″	4°43′32.33″	10.9	20.1	1859	1.79
BP4	Ojén	36°35′42.32″	4°43′32.42″	11.4	20.3	1156	2.47
BP5	Ojén	36°35′42.41″	4°43′32.54″	9.6	20.8	3015	15.13
River waters							
ALF/R	Ronda	36°41′34.98″	4°55′01.51″	8.8	16.8	412	5.26
BPR/DO	Ojén	36°35′41.84″	4°43′32.38″	8.9	17.7	621	8.32
BPR/UP	Ojén	36°35′43.10″	4°43′33.02″	8.5	17.6	550	8.37

selected this spring site for the comprehensive investigation of hyperalkaline fluids and river waters, and the associated mineralogy.

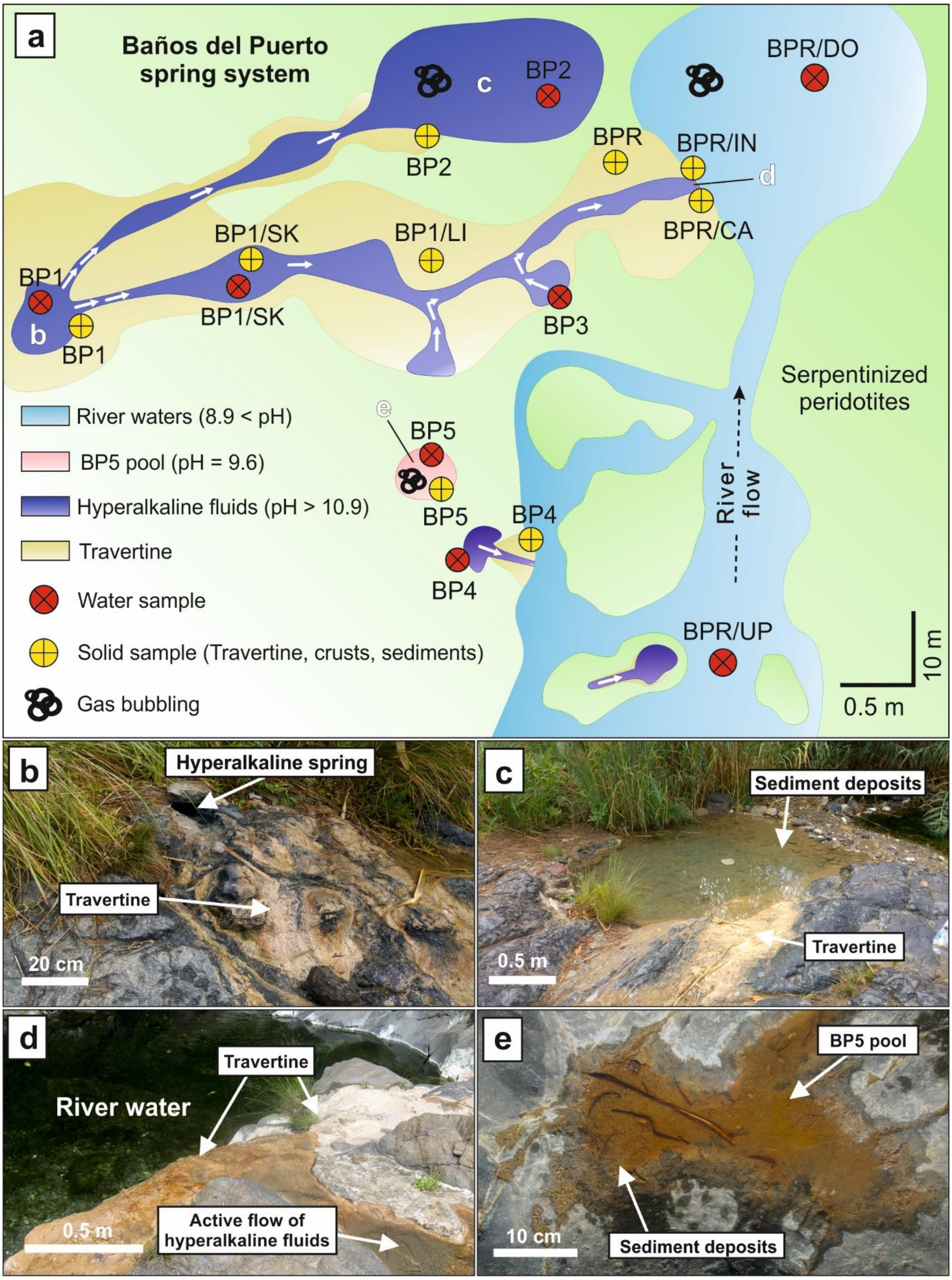

Figure 4.2a shows a map of the BP spring system; the hyperalkaline fluids emanate from fractures in serpentinized peridotites (e.g., BP1, BP3, and BP5; **Fig. 4.2a & b**) and flow downstream stagnating at shallow pools along several flow paths (e.g., BP1/SK and BP2; **Fig. 4.2a & c**). The hyperalkaline fluids discharge at the riverside, where they mix with the Alaminos river waters (**Fig. 4.2 a & d**). Rarely, small and isolated shallow reddish pools occasionally occur in this spring site (e.g., BP5; **Fig. 4.2a & e**). Intermittent methane bubbling (Etiope et al., 2016) is observed in some pools (e.g., BP2 and BP5; **Fig. 4.2a**) and in the river at the confluence with the hyperalkaline streams.

In Ronda hyperalkaline spring sites, the main types of precipitates are travertines, crystalline crusts and sediments (**Fig. 4.2c & e**). Crystalline crusts occur as thin films floating on the surface of hyperalkaline pools, while sediments —referred to as "flocs" in the Oman alkaline springs (e.g., Falk et al., 2016)— are unconsolidated solid precipitates on the bottom of the pools. Pentecost (2005) defines travertine as the inorganic process of calcium carbonate precipitation through the transfer (evasion or invasion) of carbon dioxide from or to a groundwater source. In this study, we refer to travertine as the solid precipitates at the spring discharging outlets, and to lithified terraces in former and current flow paths of hyperalkaline fluids (**Fig. 4.2b – d**). All the studied hyperalkaline spring sites are characterized by different extents of travertine precipitation and build-up of lithified terraces.

The HED and AMAR sites (**Fig. 4.1b**) show only minor amounts of travertine, and the BAL site contains only sediments. The ALF site hosts travertine precipitating around the outlet of the hyperalkaline spring, and crystalline crusts forming on the surface of the discharging fluids. The BP site has abundant travertine, crystalline crusts, and sediments depositing in various pools. No evident precipitation was observed at the riverbeds (**Fig. 4.2a**).

◄ ***Figure 4.2.*** *Overview of the Baños del Puerto site (BP).* ***(a)*** *Sketch of the serpentinite-hosted BP hyperalkaline spring system in Sierra Alpujata (**Fig. 4.1b**) near Alaminos river. The BP site hosts numerous springs of hyperalkaline fluids discharging from fractures in the serpentinized peridotites. The hyperalkaline fluids flow (white arrows) towards the riverside, locally stagnating in shallow pools, and eventually mixing with the Alaminos river waters. Also shown are travertine zones on bedrock, sampling locations of solid (yellow circles) and water (red circles) samples, and sites with gas bubbling. The IDs of water (e.g., BP1) and solid (e.g., BP1/SK) samples in the figure correspond to the IDs presented in **Tables 4.1** and **4.2** for the water samples and in **Table 4.3** for the solid samples.* ***(b)*** *Picture of travertine forming around the hyperalkaline spring (BP1; label **b** in **Fig. 4.2a**).* ***(c)*** *Picture of spring–pool systems of hyperalkaline fluids (BP2; label **c** in **Fig. 4.2a**) with travertine and sediment deposits, and periodic gas bubbling.* ***(d)*** *Picture of the confluence and mixing area of hyperalkaline fluids and river waters (label **d** in **Fig. 4.2a**). Note the presence of travertine on the bedrock along the flow path of hyperalkaline fluids and the development of thick travertine at the mixing zone with river waters.* ***(e)*** *Picture of the red-colored isolated pool, BP5, showing the sediment bed on the bottom of the pool (label **e** in **Fig. 4.2a**).*

4.4 Sampling

We sampled water and —where present— solid samples of mineralization from the hyperalkaline spring sites, some of which also accommodate river waters (i.e., ALF and BP sites). Solid samples were taken from travertines, crystalline crusts, and sediments (cf. *section **4.3***). Where available, we collected travertine samples at the spring discharging outlets, along the flow paths, and from lithified terraces.

We collected water samples from the discharging outlets (e.g., BP1 spring in **Fig. 4.2b**) and pools (e.g., BP2 pool in **Fig. 4.2c**) of hyperalkaline fluids, and at selected sites, from nearby river waters (e.g., **Fig. 4.2d**). We sampled hyperalkaline waters from the discharging outlets of the BAL, AMAR, ALF, and HED springs (**Table 4.1**), and one sample of the river waters in the ALF site (**Table 4.1**). In the BP site, we sampled hyperalkaline fluids from discharging outlets and pools, river waters, and waters from an isolated, red-colored pool (**Fig. 4.2a**). The locations of these samples are given in **Table 4.1**.

Water samples were taken using 50 mL syringes (PE/PP) with cellulose acetate membrane filters (Sartorius Minisart Plus; pore diameter 0.45 mm) that were previously rinsed with the sampled water. The water samples were split into three 10 mL polyethylene vials —cleaned with milliQ water— for the measurement of alkalinity, cations and trace metals, and anions, respectively. The vials for the determination of alkalinity were filled without headspace, while the vials for cation and trace metal analyses were preconditioned with 5 % HNO_3 (distilled), and 100 mL of concentrated HNO_3 (distilled) were added to the water samples.

4.5 Methodology

4.5.1 In situ measurements of physicochemical parameters of waters

We determined in situ the pH (± 0.01), temperature (± 0.4 ºC), total dissolved solids (± 1 %) and electrical conductivity (± 1 %) of water samples using a Hanna Instruments HI 9813-5 portable meter. We measured the alkalinity within 1 h after sampling by pouring 10 mL of the water sample into a 20 mL polystyrene container on a portable magnetic stirrer; after measurement, 0.1 M HCl (Titrisol, Merck, Germany) was added in 20 µL steps under continuous stirring until attaining a pH value between 3.5 and 4.3. The **equation 4.1** was used to calculate the alkalinity (Alk.) as follows:

$$Alk.\left(\frac{mol}{L}\right) = \frac{\left[(V_{\mathrm{HCl}} \cdot c_{\mathrm{HCl}}) - 10^{\text{-pHfinal}} \cdot \frac{(V_0 + V_{\mathrm{HCl}})}{f_{\mathrm{H+}}} + 10^{\text{-pHstart}} \cdot \frac{V_0}{f_{\mathrm{H+}}}\right]}{V_0} \quad (4.1)$$

where V_0 is the initial sample volume, V_{HCl} and C_{HCl} are, respectively, the volume and the concentration of the acid added, $\mathrm{pH_{start}}$ and $\mathrm{pH_{final}}$ are, respectively, the pH at the start and end of the titration, and $f_{\mathrm{H+}}$ is the activity coefficient of $\mathrm{H^+}$ ions (1.0 for freshwater). A 2.5 M $\mathrm{NaHCO_3}$ solution was measured as a control in order to determine the accuracy and the precision of the method. Precision was better than 0.6 % and accuracy was < 3.4 %.

Dissolved inorganic carbon (DIC) was calculated using the alkalimetric titration equation (**Eq. 4.2**) of Stumm and Morgan (1996):

$$C_T\left(\frac{mmol}{L}\right) = 1000 \cdot \frac{\left(\frac{Alk.}{1000} + [H^+] - [OH^-]\right)}{(\alpha_1 + 2\alpha_2)} \quad (4.2)$$

where C_{T} is the sum of the concentrations of carbonic species in the aqueous solution, and α_1 and α_2 are the values of ionization fractions of carbonic acid. Ionization fractions were estimated using the equilibrium constants, $\mathrm{K_1 = [H^+][HCO_3^-]/[H_2CO_3]}$ for $\mathrm{HCO_3^-}$, and $\mathrm{K_2 = [H^+][CO_3^{2-}]/[HCO_3^-]}$ for $\mathrm{CO_3^{2-}}$.

4.5.2 Analyses of solid and water samples

The mineralogy of solid samples was determined by XRD, using a PANalytical MPD diffractometer (40 mA and 45 kV) at the Andalusian Institute of Earth Sciences (IACT, Granada, Spain). Instrument configuration included programmable divergence slits in the incident and diffracted beams, placement of a 0.25° fix anti-scatter slit in the incident path and a PSD detector PIXel. Data processing was conducted using the software HighScore Plus from PANalytical X'Pert PRO (mineral database: Pdf2HSP/PAN-ICSD). Mineral quantification was defined by peak refining method described in Rietveld (1969). The observation and semi-quantitative analysis of solid samples was carried out at the Centro de Instrumentación Científica (CIC) of the University of Granada (Granada, Spain) using a Field Emission ZEISS AURIGA (InLens mode at 3 kV) and a Variable Pressure SEM FEI QEMSCAN 650F (SE mode at 5 kV and BSE mode at 12 kV) Scanning Electron Microscope (SEM), both equipped with Energy Dispersive X-ray Spectrometers (EDS).

Water samples were analyzed for major (Ca, K, Mg, Na, Si, P) and trace elements (Ba, Sr, Al, Fe) by inductively coupled plasma optical emission spectroscopy (ICP-OES) using a Varian Vista Pro ICP-OES at the University of Bremen. The analyses were conducted within two weeks after sampling. Sulfate (SO_4^{2-}) and chloride (Cl^-) concentrations were determined using a Metrohm 882 Compact IC Plus ion chromatograph (IC) at the University of Bremen. The relative error (%) for SO_4^{2-} and Cl^- is 1.9 % and 1.4 %, respectively, and it was obtained from the measurement of certified reference material (CRM) TMDW-A/IAPSO (seawater). The percentage errors (%) for the ICP-OES measurements were obtained by using the SLEW-3/evisa (estuarine water) and SLRS-5/evisa (river water) CRMs and they are < 5 % for Ca, Ba, Mg, Na, Si, Sr, Al and Fe, 10 % for K, and 24 % for P.

4.5.3 PHREEQC modelling

The Saturation Index (SI) of the relevant mineral phases in the sampled waters was calculated using the PHREEQC-2 code (Parkhurst and Appelo, 2005) and the wateq4f.dat database (Ball and Nordstrom, 1991). Negative SI indicates that the solutions are undersaturated with respect to a given mineral and its dissolution is thermodynamically favored over precipitation; positive SI indicates that mineral precipitation is favored, and SI of zero (0) shows that the mineral phase is in equilibrium with the solution. We removed from the dataset serpentine-group minerals, diopside, talc, and other minerals that, though could be supersaturated (SI > 5) in the investigated alkaline fluids, do not precipitate in alkaline terrestrial systems (Paukert et al., 2012; Chavagnac et al., 2013b). We use PHREEQC-2 to model the chemical variations of the waters induced by a gradual CO_2 partial pressure (P_{CO_2}) decrease (cf. *section* ***4.6.1***) to simulate non-reactive isolation of the waters from the atmosphere. The step of P_{CO_2} decrease was −0.25 bar, and the final P_{CO_2} of the waters was −9.17 bar. The model used Ronda river waters (BPR/DO in **Table 4.2**) and Ca–HCO_3-rich waters from the Turón river valley in eastern Serranía de Ronda (Barberá and Andreo, 2015).

4.6 Results

4.6.1 Classification of Ronda alkaline and hyperalkaline waters

Based on their chemistry and physical characteristics, we classify Ronda waters into hyperalkaline fluids and river waters (**Fig. 4.3**; **Fig. 4.4**):

i. Hyperalkaline fluids are characterized by high pH (10.9 − 12) (**Table 4.1**), low Mg (0.0007 to ~0.06 mmol/L) and high Na (up to ~4.6 mmol/L), K (up to ~0.34 mmol/L), Ca (up to ~1.9 mmol/L), and Cl^- (up to ~4.5 mmol/L) concentrations compared to those of river waters (**Fig. 4.3a & b**). Hyperalkaline fluids display relatively constant DIC/Ca ratios and fall close to the Ca apex in the Ca – DIC – Si diagram (**Fig. 4.3d**). On the contrary, these fluids show variable DIC/Mg ratios plotting along the DIC – Si side (**Fig. 4.3e**). They correspond to water samples taken from —natural or human-made— discharging outlets, and pools formed along the flow path of the hyperalkaline discharging outlets (i.e., in the BP site; **Fig. 4.2b, d & e**).

ii. River waters are samples taken from rivers at the ALF and BP sites (**Fig. 4.1**). They are enriched in Mg (up to ~2.8 mmol/L) and DIC (up to ~8.3 mmol/L) compared to Na, K, Ca and Cl^- (**Fig. 4.3a & b**), are mildly alkaline ($8.5 < pH < 8.9$) (**Table 4.1**), and have high alkalinity (**Fig. 4.3b & c**). They fall near the DIC – Si side in the Ca – DIC – Si ternary plot (**Fig. 4.3d**) and have DIC/Mg ratios between 3 and 4 (**Fig. 4.3**).

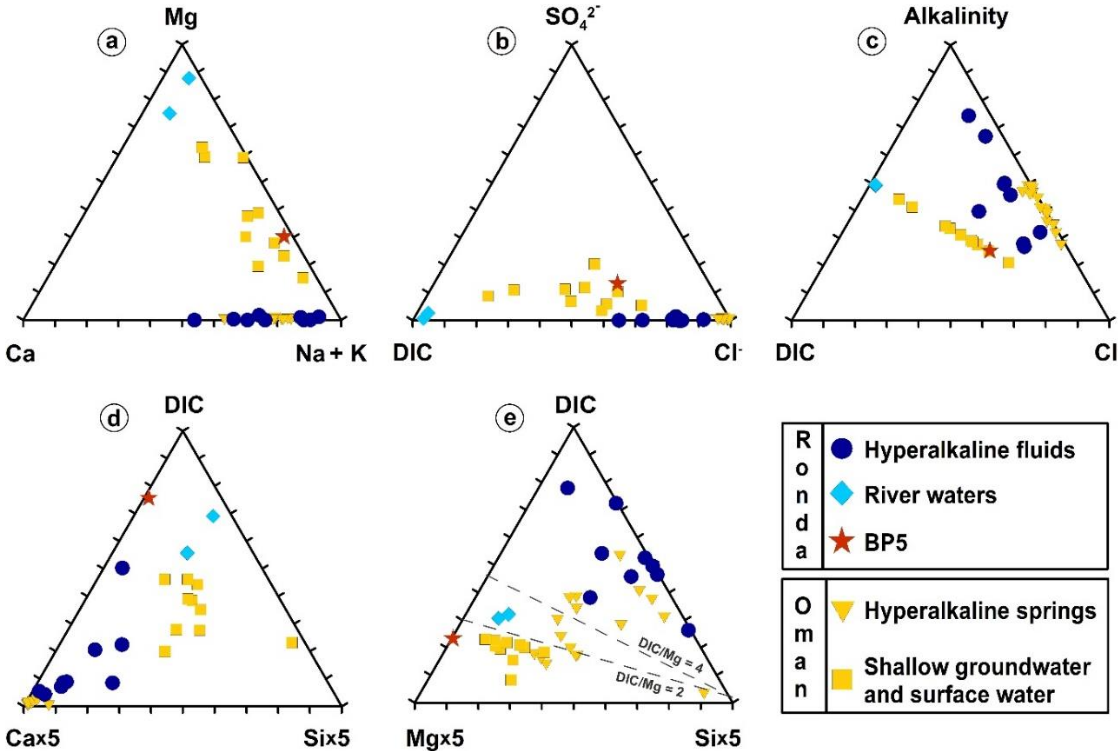

Figure 4.3. *Ternary classification diagrams of Ronda collected waters (this study) and waters from Samail ophiolites in Oman (Paukert et al., 2012).* ***(a)*** *Mg – Ca – Na + K,* ***(b)*** SO_4^{2-} *– DIC –* Cl^-*,* ***(c)*** *Alkalinity – DIC –* Cl^-*,* ***(d)*** *Ca – DIC – Si and* ***(e)*** *Mg – DIC – Si.*

iii. The BP5 —a red-colored pool (**Fig. 4.2c**)— water sample is unlike other alkaline water sample from our study and is characterized by relatively high temperature in the high-end range of hyperalkaline fluids (20.8 °C), and intermediate pH (9.6) between those of river waters and hyperalkaline fluids (**Fig. 4.4a**). It shows the highest conductivity (3015 mS/cm) and alkalinity (15.13 meq/L) (**Fig. 4.4b & c**) and demonstrates low Ca concentration compared to Mg, Na and K (**Fig. 4.3a**). Furthermore, the BP5 falls near the DIC apex in the Ca – DIC – Si diagram (**Fig. 4.3d**) and near the Mg apex in the Mg – DIC – Si diagram (**Fig. 4.3e**).

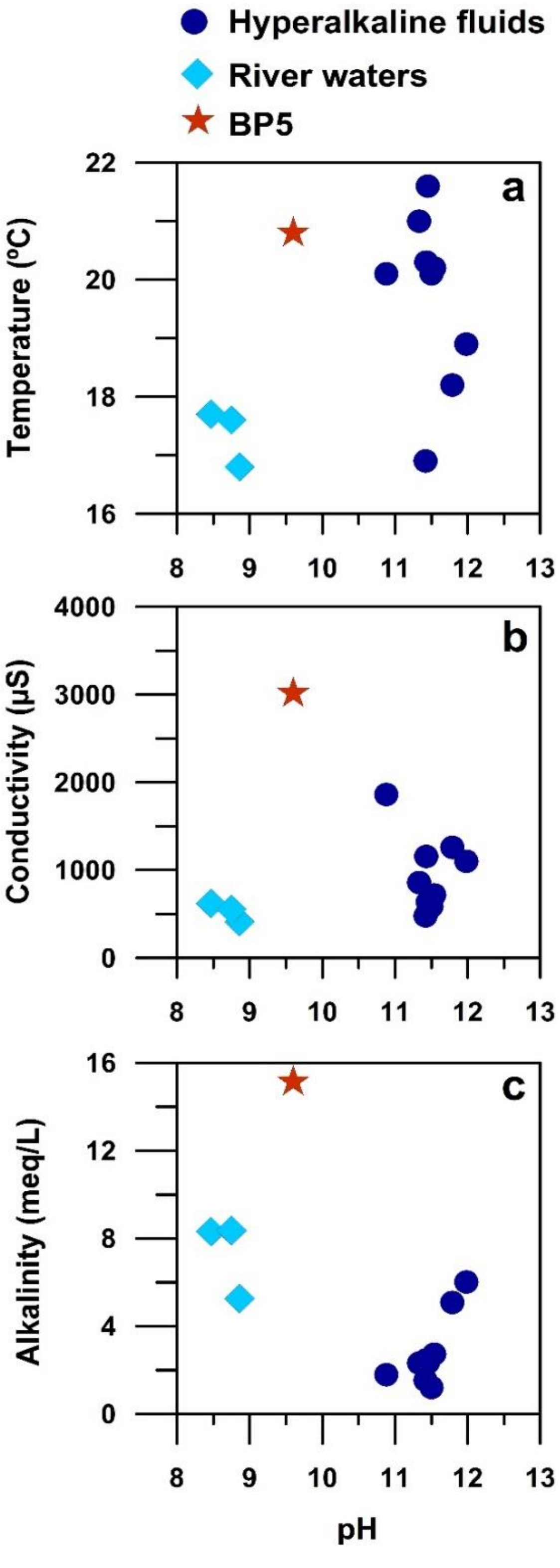

Figure 4.4. *Water parameters of the collected samples . **(a)** Temperature , **(b)** conductivity , and **(c)** alkalinity of water samples versus pH.*

Overall, the chemistry of Ronda alkaline waters is within the range of Ca–OH (i.e., Ca^{2+}–OH^--rich) and Mg–HCO_3 (i.e., Mg^{2+}–HCO_3^--rich) water types described in ophiolite-hosted alkaline springs (e.g., Barnes et al., 1967; Barnes and O'Neil, 1969; Cipolli et al., 2004; Neal and Shand, 2002; Neal and Stanger, 1985) (**Fig. 4.3**; **Fig. 4.4;** Appendix **Fig. A−4.1**). The composition of Ronda hyperalkaline fluids and river waters are similar to that of hyperalkaline springs and run-off or surface waters —river and shallow groundwater— in the Oman Ophiolite (**Fig. 4.3a – c**). Ronda river waters have higher Mg and DIC than Oman surface waters.

Ronda hyperalkaline fluids have a higher conductivity (avg. of 892 mS/cm) and are hotter (avg. of 19.9 °C) (**Fig. 4.4a & b**) and less alkaline (avg. 2.68 meq/L) (**Fig. 4.4c**) than Ronda river waters (avg. of 17.2 °C, 528 mS/cm and 7.31 meq/L, respectively). Compared to other alkaline spring sites worldwide, Ronda river waters (5 − 8.5 meq/L; **Fig. 4.4c**) display a similar range of alkalinity to the Troodos Mg–HCO_3 waters (4.5 − 9.4 meq/L; Neal and Shand, 2002), and a more restricted range of alkalinity than the Taro-Ceno Valleys Mg–HCO_3 waters (1 − 10.2 meq/L; Boschetti and Toscani, 2008). The Oman Ophiolite Mg–HCO_3-rich, mildly alkaline waters are less alkaline (2.5 − 4.5 meq/L; Chavagnac et al., 2013b) than Ronda river waters (**Fig. 4.4c**). The alkalinity of hyperalkaline fluids in the Troodos (2.3 − 6 meq/L; Neal and Shand, 2002), Gruppo di Voltri ophiolites (0.5 − 4.4 meq/L; Cipolli et al., 2004), and Samail Ophiolite (Chavagnac et al., 2013b) are similar to those in the Ronda peridotites (1.2 − 6 meq/L; **Fig. 4.4c**).

Temperature and pH of waters from our study —measured in October 2017— are similar (within 0.6 − 1.7 °C, and < 1 for pH) to those measured by Etiope et al. (2016) in the same springs in March and June 2014, pointing to a limited annual and seasonal variability of temperature and pH of Ronda peridotite waters. The temperature of ultramafic-hosted fluids in continental springs, such as in Ronda, are generally lower than those of alkaline fluids in submarine vents like the Lost City hydrothermal field (40 − 90 °C) (Kelley et al., 2001) (**Fig. 4.5**).

Other continental serpentinite-hosted hyperalkaline fluid sites show similarly low temperatures (**Fig. 4.5**); the New Caledonia and Cyprus alkaline springs display temperatures in the range of 10 − 30 °C (Barnes et al., 1978; Monnin et al., 2014; Neal and Shand, 2002), and those in the Taro-Ceno valleys are c. 13 °C (Boschetti and Toscani, 2008). The temperature of Ronda alkaline waters is similar to those of serpentinite-hosted alkaline fluids of the Cabeço de Vide (avg. of 19.5 °C) (Marques et al., 2008) and Liguria ophiolites (Chavagnac et al., 2013b).

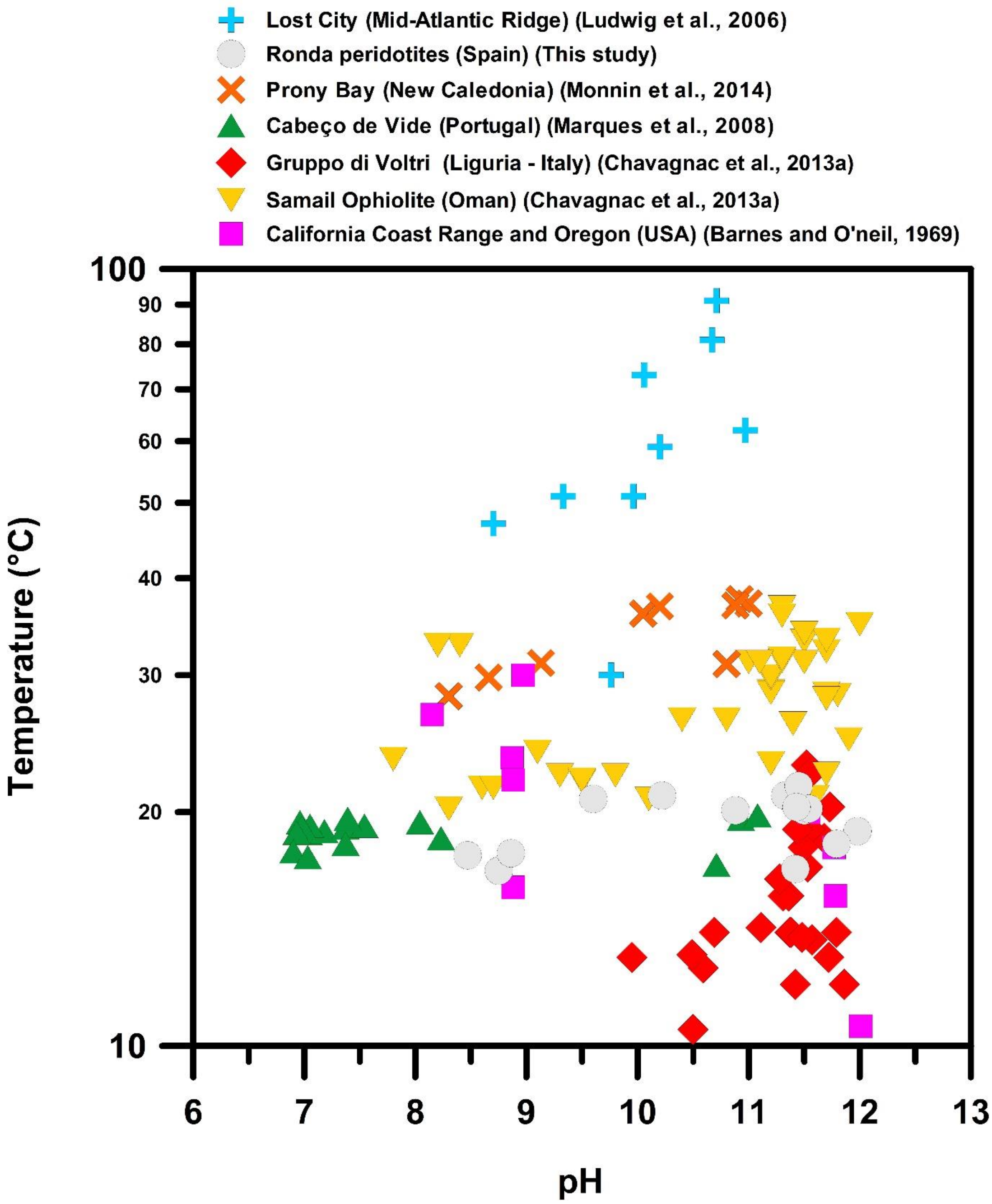

Figure 4.5. Plot of the temperature versus pH of various serpentinite-hosted alkaline fluid sites worldwide.

4.6.2 The chemical composition of Ronda peridotite waters

Ronda water samples altogether show a positive correlation between Na and Cl^- (**Fig. 4.6**). Similar correlations have been reported in other serpentinite-hosted spring sites and ascribed to variable extents of evaporation or mixing with surface freshwater or seawater (Chavagnac et al., 2013a; Monnin et al., 2014). The pH gap observed between Ronda hyperalkaline fluids (pH > 10.9) and river waters (pH < 8.9) (**Fig. 4.4**) points to limited mixing of both water types at the time of sampling. Therefore, the Na – Cl^- correlation in Ronda water most likely reflects differences in the salinity of waters due to variable extents of evaporation. The effect of evaporation is particularly significant for the hyperalkaline fluid and BP5 samples. Hyperalkaline fluids in discharging outlets and pools —with intermediate Na and Cl^- concentrations— record moderate to great extent of evaporation; the fluids in the BP5 pool underwent the highest evaporation as attested by their unusually high Na and Cl^- concentrations (**Fig. 4.6**).

The chemistry of Ronda waters is shown in **figure 4.7**. The Ca concentration versus pH is rather scattered (**Fig. 4.7a**). The Mg, Si, SO_4^{2-} and DIC concentrations show a decrease from

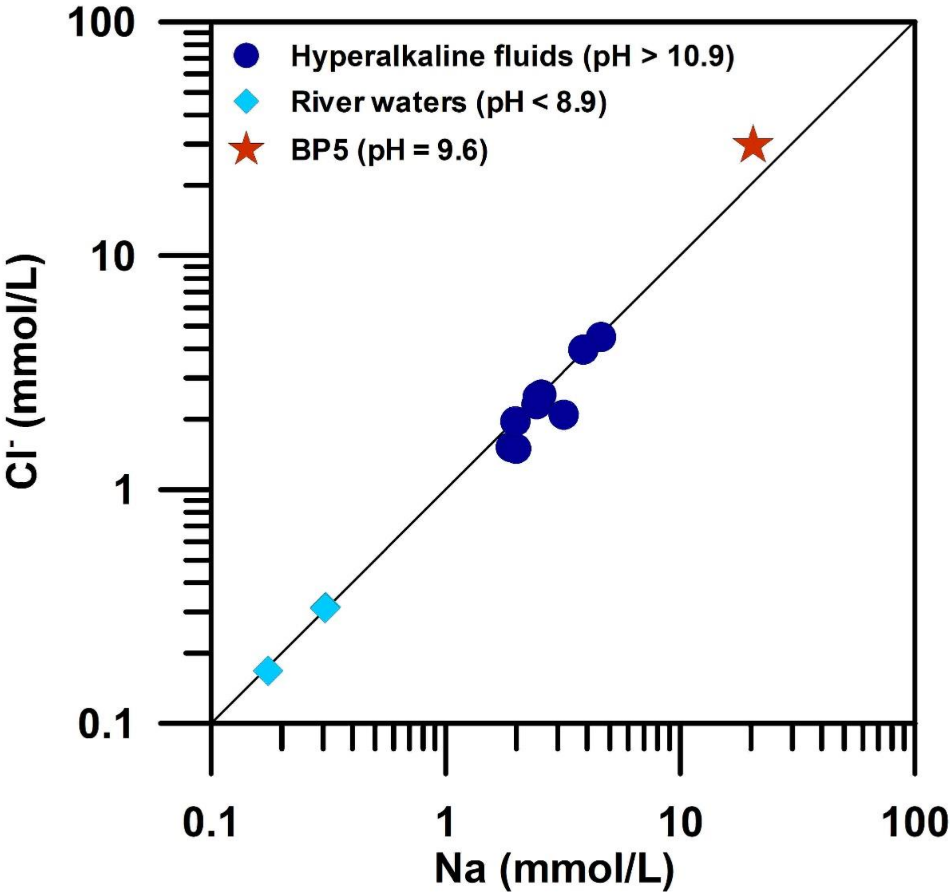

__Figure 4.6.__ Na vs. Cl– diagram defining the different water types around the evaporation line.

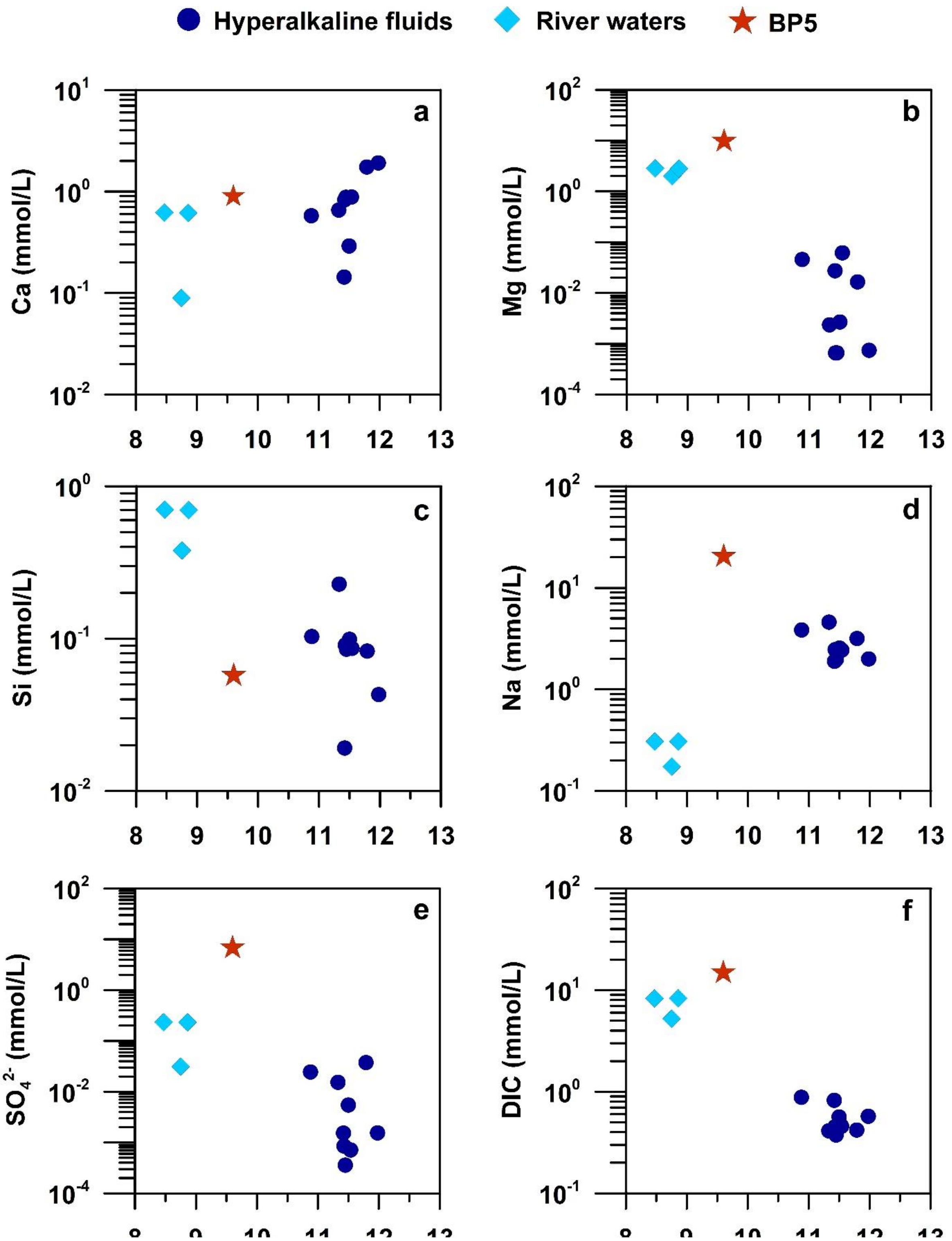

Figure 4.7. *Major element concentrations plotted against pH for the different water types in Ronda spring sites.*

Table 4.2. *Major ion and trace element chemistry of water samples.*

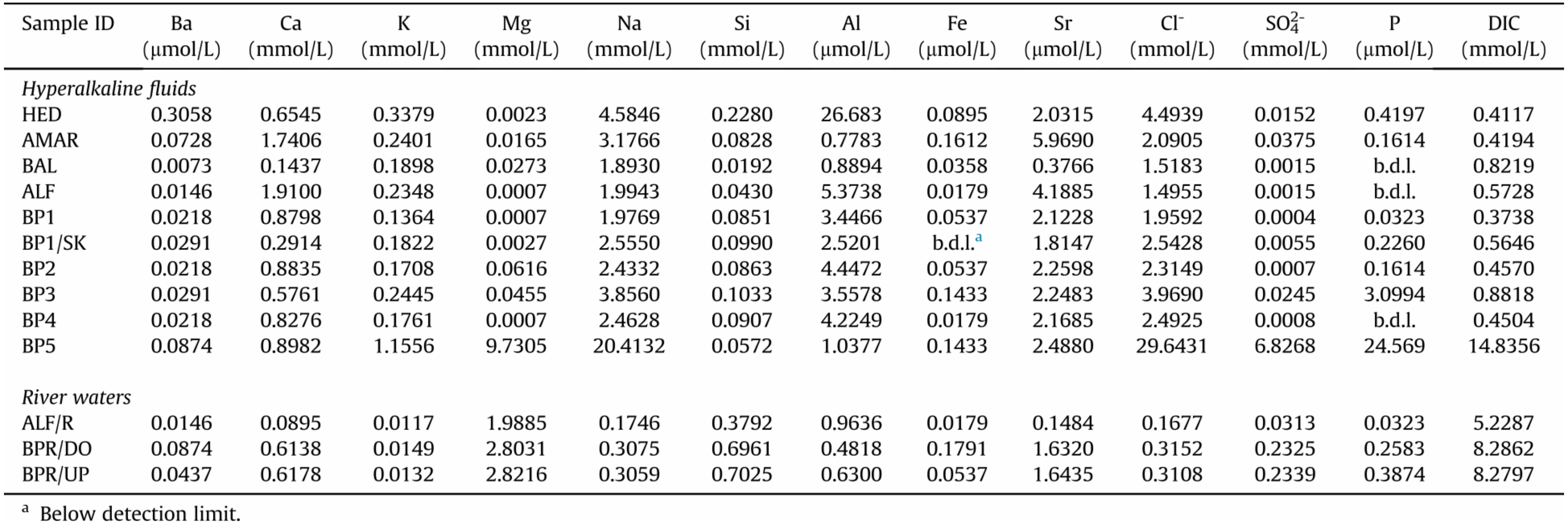

Sample ID	Ba (μmol/L)	Ca (mmol/L)	K (mmol/L)	Mg (mmol/L)	Na (mmol/L)	Si (mmol/L)	Al (μmol/L)	Fe (μmol/L)	Sr (μmol/L)	Cl^- (mmol/L)	SO_4^{2-} (mmol/L)	P (μmol/L)	DIC (mmol/L)
Hyperalkaline fluids													
HED	0.3058	0.6545	0.3379	0.0023	4.5846	0.2280	26.683	0.0895	2.0315	4.4939	0.0152	0.4197	0.4117
AMAR	0.0728	1.7406	0.2401	0.0165	3.1766	0.0828	0.7783	0.1612	5.9690	2.0905	0.0375	0.1614	0.4194
BAL	0.0073	0.1437	0.1898	0.0273	1.8930	0.0192	0.8894	0.0358	0.3766	1.5183	0.0015	b.d.l.	0.8219
ALF	0.0146	1.9100	0.2348	0.0007	1.9943	0.0430	5.3738	0.0179	4.1885	1.4955	0.0015	b.d.l.	0.5728
BP1	0.0218	0.8798	0.1364	0.0007	1.9769	0.0851	3.4466	0.0537	2.1228	1.9592	0.0004	0.0323	0.3738
BP1/SK	0.0291	0.2914	0.1822	0.0027	2.5550	0.0990	2.5201	b.d.l.[a]	1.8147	2.5428	0.0055	0.2260	0.5646
BP2	0.0218	0.8835	0.1708	0.0616	2.4332	0.0863	4.4472	0.0537	2.2598	2.3149	0.0007	0.1614	0.4570
BP3	0.0291	0.5761	0.2445	0.0455	3.8560	0.1033	3.5578	0.1433	2.2483	3.9690	0.0245	3.0994	0.8818
BP4	0.0218	0.8276	0.1761	0.0007	2.4628	0.0907	4.2249	0.0179	2.1685	2.4925	0.0008	b.d.l.	0.4504
BP5	0.0874	0.8982	1.1556	9.7305	20.4132	0.0572	1.0377	0.1433	2.4880	29.6431	6.8268	24.569	14.8356
River waters													
ALF/R	0.0146	0.0895	0.0117	1.9885	0.1746	0.3792	0.9636	0.0179	0.1484	0.1677	0.0313	0.0323	5.2287
BPR/DO	0.0874	0.6138	0.0149	2.8031	0.3075	0.6961	0.4818	0.1791	1.6320	0.3152	0.2325	0.2583	8.2862
BPR/UP	0.0437	0.6178	0.0132	2.8216	0.3059	0.7025	0.6300	0.0537	1.6435	0.3108	0.2339	0.3874	8.2797

[a] Below detection limit.

river water towards hyperalkaline fluid composition, while Na concentration displays the opposite trend (**Fig. 4.7b – f**). Hyperalkaline fluids are enriched in Ca (up to ~1.9 mmol/L) and depleted in Mg (avg. of 0.06 mmol/L) and DIC (avg. of 0.63 mmol/L). River waters contain higher Mg (up to ~2.8 mmol/L), Si (up to ~0.7 mmol/L) and DIC (up to ~8.3 mmol/L) concentration than hyperalkaline fluids. Compared to river waters, hyperalkaline fluids show higher Na, K, Al, and Cl^- concentrations, while Fe, Ba, Sr, and SO_4^{2-} concentrations are similar in both water types. Fluid from the BP5 pool has an unusual chemical composition characterized by very high Mg, Na, K, Cl^-, and DIC, as well as 1 to 4 orders of magnitude higher P and SO_4^{2-} concentrations than the other Ronda water types (**Table 4.2**). Generally, Mg, Si, SO_4^{2-} and DIC concentrations of river waters and hyperalkaline fluids display opposite trends with pH (**Fig. 4.7**).

Figure 4.8 displays the composition of Ronda waters normalized to Cl^- to better depict the primary chemical variations of waters that undergo variable extends of evaporation upon fluid discharge (Chavagnac et al., 2013b; Monnin et al., 2014). The Ca/Cl^- and Na/Cl^- ratios versus pH of Ronda hyperalkaline fluids (**Fig. 4.8a & d**) display positive covariations that are more patent than in the non-normalized plots (cf. **Fig. 4.7a & d**). Otherwise, the plots of Cl-normalized elemental variations are less scattered but display similar trends for Mg, Si, SO_4^{2-}, and DIC versus pH than the non-normalized concentrations, demonstrating that evaporation has not greatly obliterated the primary compositional trends of the Ronda hyperalkaline fluids and river waters. Saturation indices of minerals and PCO_2 of waters

The saturation index (SI) for different minerals in the studied Ronda waters are shown in **figure 4.9**. Calcite and aragonite are saturated in hyperalkaline fluids and river waters, showing a higher supersaturation in hyperalkaline fluids (calcite avg. SI = 1.4 and aragonite avg. SI = 1.2; **Fig. 4.9a & b**) than in river waters (calcite avg. SI = 0.8 and aragonite avg. SI = 0.6; **Fig. 4.9a & b**). Dolomite [$CaMg(CO_3)_2$] is supersaturated in river waters (avg. SI = 2.5; **Fig. 4.9c**) and the majority of hyperalkaline fluids (avg. SI = 1.2; **Fig. 4.9c**). The BP5 pool water displays the highest SI values for calcite (1.8), aragonite (1.7), and dolomite (5). Magnesite [$MgCO_3$] is supersaturated in the BP5 pool (2.5) and river waters (1.2) (**Fig. 4.9d**), while is undersaturated in the hyperalkaline fluids (**Fig. 4.9d**). The hydrated magnesium carbonate phases nesquehonite [$MgCO_3 \cdot 3H_2O$] and artinite [$Mg_2(CO_3)(OH)_2 \cdot 3H_2O$] are generally undersaturated in the hyperalkaline fluids and river waters (average SI < −1.5; **Fig. 4.9e & f**) except for fluids from the BP2 —supersaturated in artinite— and BP5 pools —supersaturated in nesquehonite and artinite— (**Fig. 4.9e & f**). Brucite [$Mg(OH)_2$] is supersaturated (**Fig. 4.9g**)

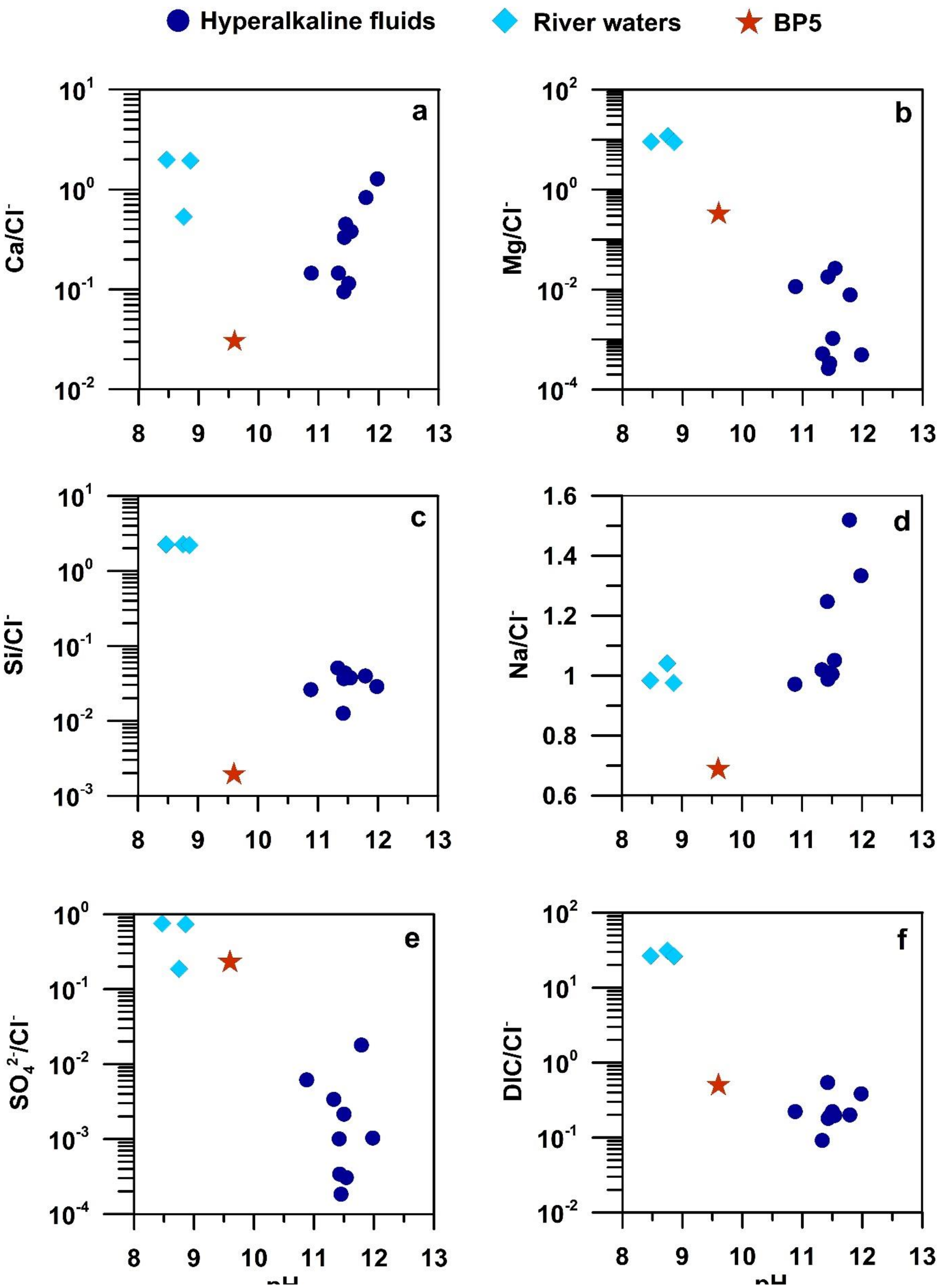

Figure 4.8. *Cl-normalized major element concentrations plotted against pH for the different water types in Ronda spring sites.*

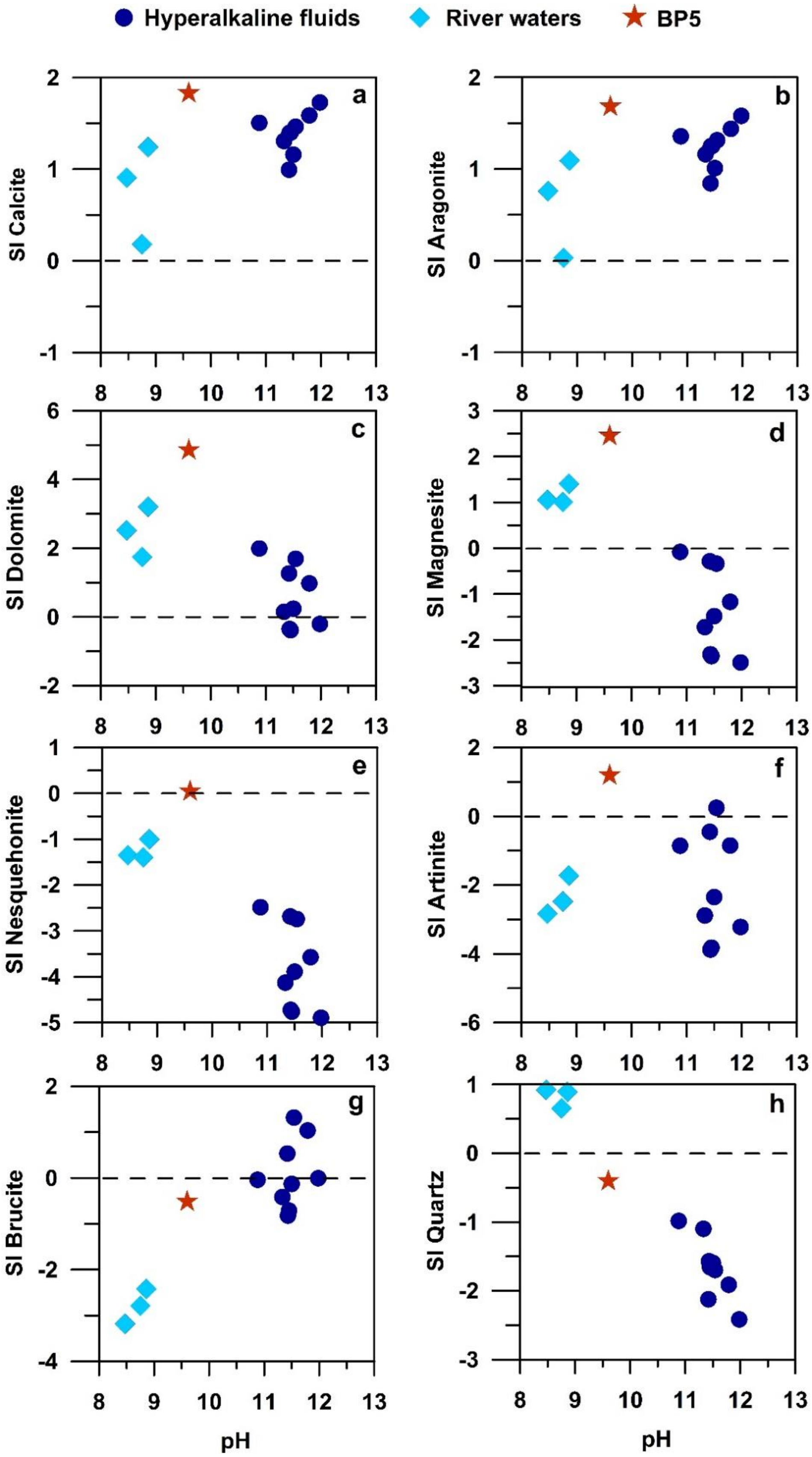

__Figure 4.9.__ Saturation indices (SI) versus the pH of potential minerals in different water types of Ronda spring sites. Horizontal dashed black line indicates the equilibrium state (SI = 0).

in hyperalkaline fluids that exhibit the highest Mg concentrations (BAL, AMAR, and BP2 sites; [Mg] > 10^{-2}) (**Table 4.2**; **Fig. 4.7b**), and slightly undersaturated in the rest of the hyperalkaline fluids, and in the river waters and BP5 pool waters (**Fig. 4.9g**). Quartz is saturated in river waters (avg. SI = 0.8) and unsaturated in the hyperalkaline and BP5 fluids (**Fig. 4.9h**).

Altogether, the calculated P_{CO_2} for Ronda alkaline waters is negatively correlated with pH (**Fig. 4.10**). River water P_{CO_2} values reflect equilibration with the atmosphere, while hyperalkaline fluids show lower P_{CO_2} values in disequilibrium with the atmosphere. The P_{CO_2} of the BP5 pool water (−3.96 bar) is intermediate between those of river waters and hyperalkaline fluids (**Fig. 4.10**), indicating conditions closer to atmospheric equilibrium.

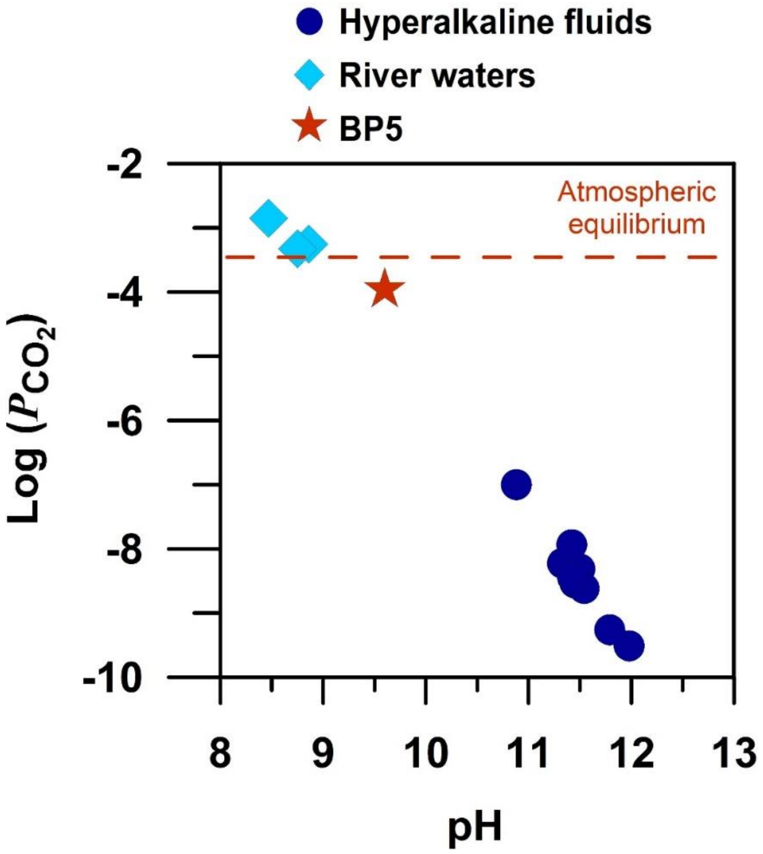

Figure 4.10. *Calculated* P_{CO_2} *versus the pH of different water types in Ronda spring sites. Horizontal dashed red line represents the point at which the waters are in equilibrium with Earth's atmosphere (*$P_{CO_2} = -3.42$ *bar).*

4.6.3 Mineralogy and textures of the precipitates

Minerals identified the Ronda spring sites are mainly calcite and aragonite, and minor dolomite and Mg-Al-rich clays (**Table 4.3**). Other minerals (e.g., serpentine group minerals and quartz) (**Table 4.3**) are likely detritus.

4.6.3.1 HED, AMAR, BAL and ALF sites

Calcite is the predominant or single phase (**Table 4.3**) in travertine formed by hyperalkaline fluids at the HED, AMAR and ALF sites (**Fig. 4.1b**). Rhombohedral calcite (up to 60 mm crystal size) at the HED site shows poor crystallinity due to cementing processes (**Fig. 4.11a**). In the BAL site (**Fig. 4.1b**), aragonite exhibits dumbbell, cruciform, and spindle-like morphologies (**Fig. 4.11b**). Calcite is the main mineral of crystalline crusts, where it forms aggregates of euhedral to subhedral {104} crystals (10 − 60 mm) that grow laterally to the air-water interface (**Fig. 4.11c**). A three-dimensional growth of calcite crystals takes place at the crust–water interface, while the crust side facing the atmosphere is flat due to non-occurring crystallization (**Fig. 4.11c**). Minor branched, spindle-like aragonite crystals (**Fig. 4.11d**) are also present in the crust at the ALF site. The aragonite crystal size (10 − 20 mm) is relatively constant in all solid samples (cf. *section* ***4.3***).

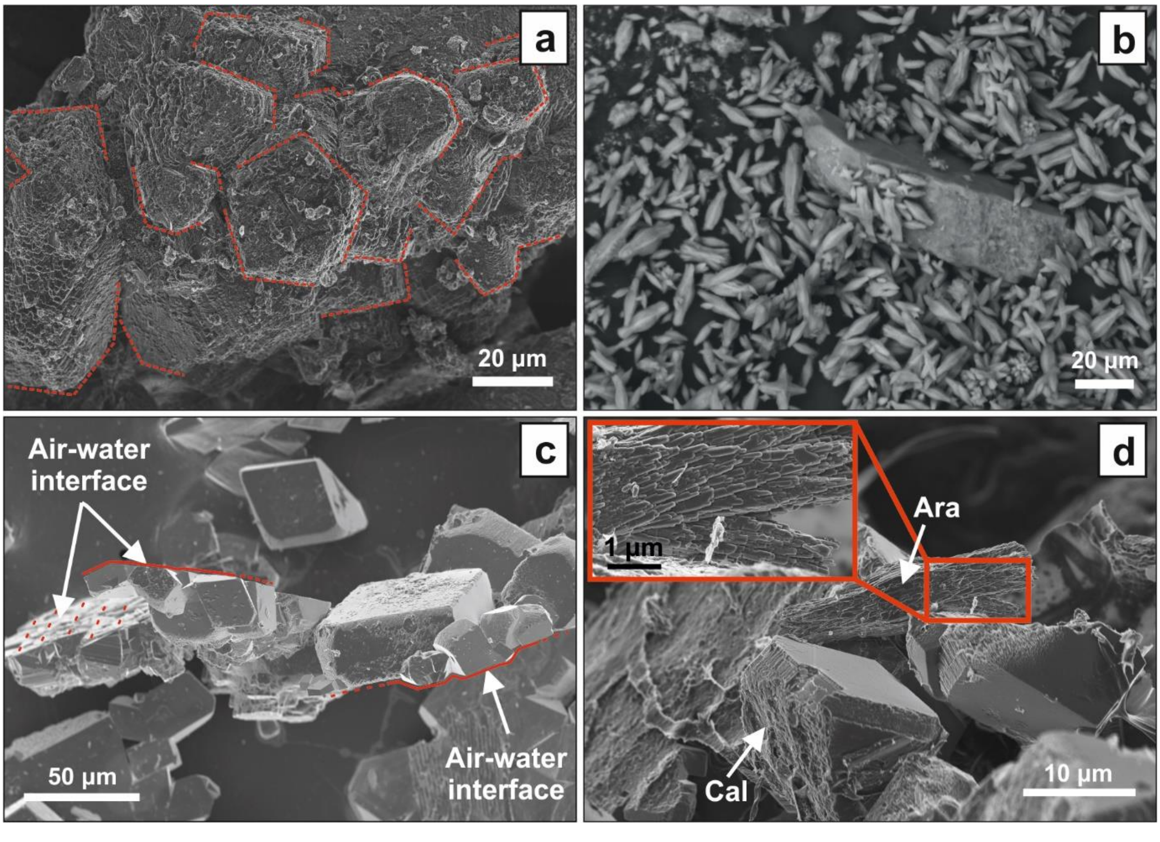

Figure 4.11. *Mineral phases and textures from HED, BAL and ALF sites.* ***(a)*** *Sample of calcite dominated travertine at the discharging outlet of HED spring site. Crystal boundaries (red dashed lines) of calcite get degraded due to lithification processes.* ***(b)*** *Dumbbell, cruciform and spindle aragonite in the BAL spring site.* ***(c)*** *Calcitic crystalline crust forming at the air–water interface in the ALF spring site. The side facing towards the air is flat, while calcite crystals grow towards the water column and exhibit euhedral {104} crystals.* ***(d)*** *Calcite (Cal)-dominated crystalline crust with minor aragonite (Ara) from the ALF site.* ***Inset:*** *Zoom in the branching phenomenon of aragonite crystals.*

Table 4.3. *Location, description, and mineralogy of solid samples.*

Sample ID	Site	Sample description	Mineralogy (minor phases)
HED	Carratraca	White travertine precipitate from a pipe	Mg-calcite (vermiculite)
AMAR	Ronda	White travertine precipitate from human-made fountain	Calcite (aragonite)
BAL	Ronda	White sediment from the bottom of a water tank	Aragonite
ALF	Ronda	Travertine terrace around the hyperalkaline spring	Calcite (vermiculite)
ALF/SK	Ronda	Crystalline crust floating on water surface	Calcite (aragonite)
BP1	Ojén	Travertine terrace around human-made well	Calcite
BP1/SK	Ojén	Crystalline crust floating on water surface	Calcite
BP1/LI	Ojén	Lithified travertine terrace	Mg-calcite (dolomite, quartz, chrysotile, lizardite, unidentified clay)
BP2	Ojén	Yellowish travertine precipitate from human-made pond	Calcite
BP4	Ojén	Travertine terrace at the river bank	Mg-calcite (aragonite)
BP5	Ojén	Sediment from BP5 pond	Dolomite (aragonite, quartz, chrysotile, lizardite, unidentified clay)
BPR	Ojén	Travertine terrace before the river bank	Calcite, aragonite
BPR/CA	Ojén	Travertine terrace hanging over the river bank	Aragonite, calcite (dolomite, vermiculite)
BPR/IN	Ojén	Submerged travertine terrace in the river water	Aragonite, calcite (dolomite)

4.6.3.2 Baños del Puerto site

Samples from the BP site contain variable proportions of calcite and aragonite, with calcite ratio ranging from 35 to 100%. Travertines at the hyperalkaline fluid discharging outlets are mostly composed of calcite (**Table 4.3**; **Fig. 4.2b**) with chaotic and colloformic textures (**Fig. 4.12a**) typical of the onset of travertine formation (Pentecost, 2005). Travertines formed at the mixing areas of hyperalkaline fluids and river waters (**Table 4.3**; **Fig. 4.2a, c & d**) are rich in aragonite with spherulitic morphologies (up to 100 mm in diameter) (**Fig. 4.12b**). Aragonite in the BP site is associated with Mg-Al-rich clays, possibly vermiculite (**Fig. 4.12c**). Dolomite is a minor component of lithified travertines, and a major phase in the BP5 pool (**Fig. 4.2e**), where it occurs as subhedral to euhedral crystals up to 300 mm in size in the pool sediments (**Fig. 4.12d**).

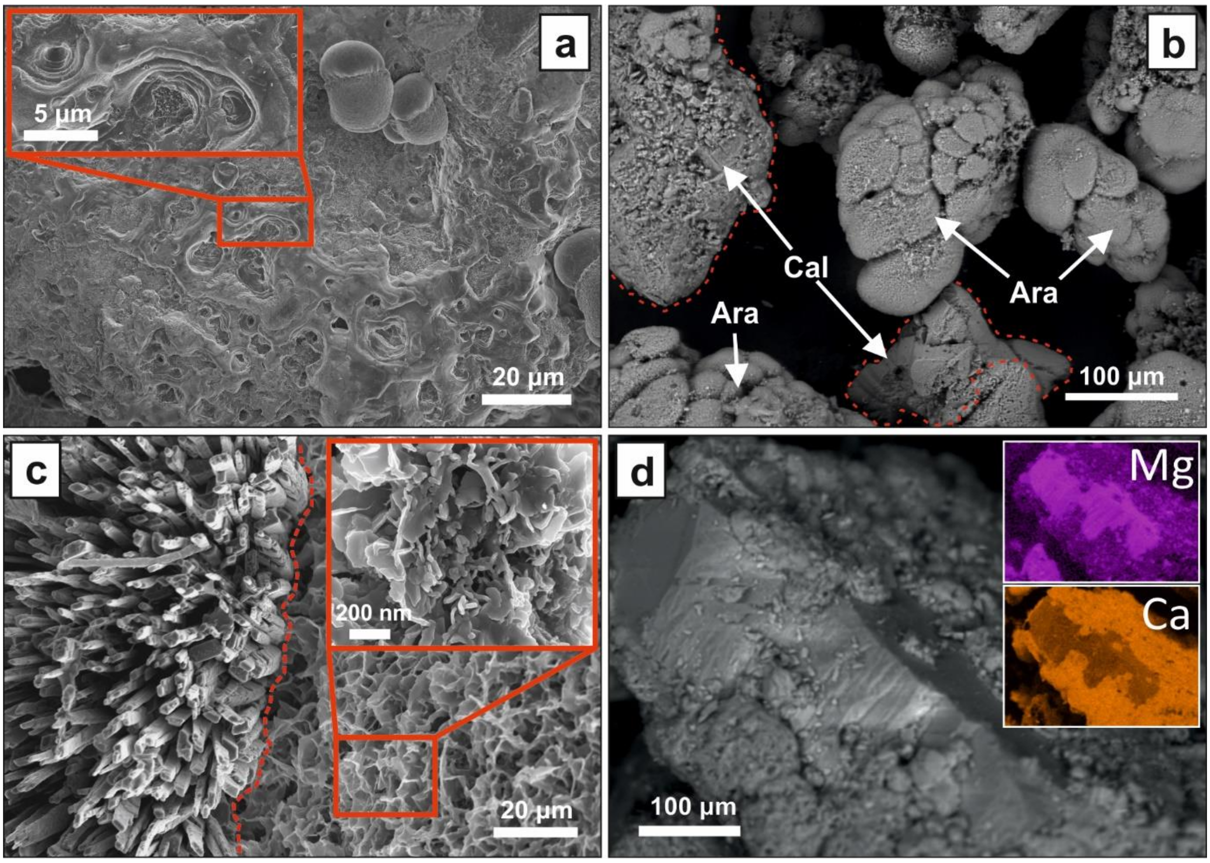

Figure 4.12. *Mineral phases and textures from BP site.* ***(a)*** *Lithified travertine with chaotic morphologies due to precipitation from multiple fluid generations.* ***Inset:*** *Zoomed image of vugs and clefts with step that are dispersed over the carbonate layers.* ***(b)*** *Sphere-like aragonite (Ara) co-existing with calcite (Cal) in submerged parts of travertine in river waters.* ***(c)*** *Acicular aragonite rods growing in association with clay minerals. Dashed red line separates aragonite (left) and Mg-rich clays (right).* ***Inset:*** *Zoomed image displays the interlocking flaky clay crystals.* ***(d)*** *Aragonite mantling a dolomite crystal in sediments of BP5 pool.*

4.7 Discussion

In order to better constrain the carbonation processes in the Ronda continental serpentinite-hosted alkaline fluids, we will first discuss the processes accounting for the physicochemical composition of the Ronda river waters (*section **4.7.1***) and hyperalkaline fluids (*section **4.7.2***) in the light of those already proposed for other continental serpentinite-hosted alkaline springs worldwide. We will then address the origin of the mineralogical and textural diversity of their associated mineral precipitates, and how it relates to the (hydro)dynamics of the Ronda alkaline spring systems (*section **4.7.3***).

4.7.1 Genesis of Ronda Mg–HCO$_3$ alkaline river waters

The relative enrichment of Ronda river waters in Mg and Si is characteristic of river waters running through serpentinites (Baumeister et al., 2015; Margiotta et al., 2012). Like surface alkaline waters in ophiolites worldwide (e.g., Barnes and O'Neil, 1969), the genesis of Ronda Mg–HCO$_3$ river waters is most likely due to hydrolysis of ferromagnesian peridotite minerals (**Eq. 4.3**) by the infiltration of meteoric water and shallow groundwater in equilibrium with the atmosphere following reactions such as (e.g., Paukert et al., 2012):

$$\underset{\textit{Olivine}}{Mg_2SiO_4} + 4\ CO_2 + 2\ H_2O \rightarrow 2\ Mg^{2+} + 4\ HCO_3^{-} + SiO_2\ (aq) \qquad (4.3)$$

Percolation reaction path modelling of freshwater and rainwater through serpentinite under atmospheric CO$_2$ conditions demonstrates that this type of mineral hydrolysis reactions increases the concentration in Mg and H$_4$SiO$_4$ and, to a lower extent, the pH of water leading to mildly alkaline ($pH > 8$) Mg–HCO$_3$-rich waters (e.g., Bruni et al., 2002; Marques et al., 2008; Palandri and Reed, 2004; Paukert et al., 2012). Similarly, Mg–HCO$_3$ river waters in the Ronda peridotites are most likely generated by shallow chemical weathering of serpentinized peridotites by meteoric waters equilibrated with atmospheric CO$_2$ and O$_2$. The correlation of alkalinity with DIC concentrations in the Ronda river waters (**Fig. 4.13**) indicate that carbonic species (i.e., HCO$_3^-$) are the main source of alkalinity in agreement with a shallow circulation and interaction of these waters with the vegetation and atmosphere. The Cl-normalized alkalinity of the Ronda river waters is conservative relative to Cl-normalized Ca, K and Na (**Fig. 4.14**), which likely reflects that they are in equilibrium with Ca-, K-, and Na-bearing minerals such as calcium carbonates and clays.

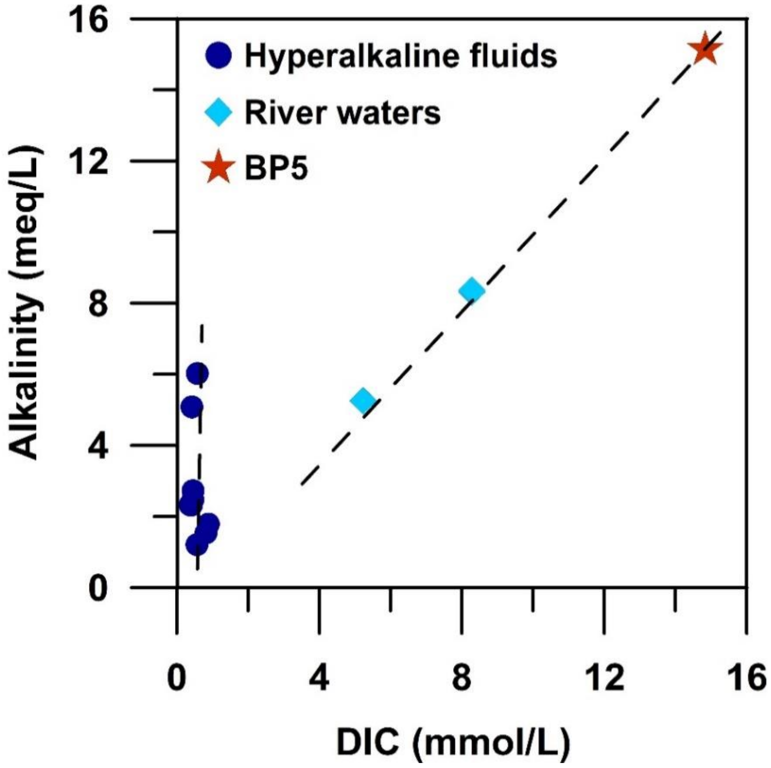

Figure 4.13. *Alkalinity versus DIC concentration of the different water types in the Ronda spring sites. Dashed lines indicate the different trends between the water types based on the alkalinity–DIC relationship.*

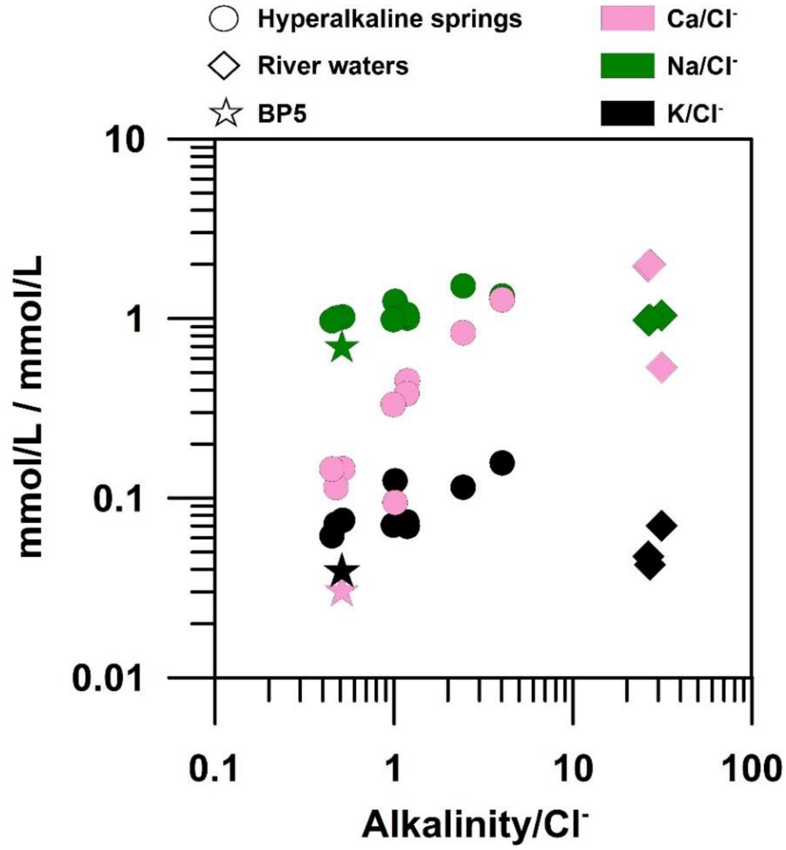

Figure 4.14. *Cl-normalized Ca, Na and K versus Cl-normalized alkalinity of the different water types in the Ronda spring sites.*

Despite being saturated in $CaCO_3$, Mg-carbonates, and quartz, the Ronda river waters lack any precipitates of these minerals (**Fig. 4.9a – d & h**). The absence of calcite in $CaCO_3$ supersaturated water is common in Mg–HCO_3 waters worldwide (e.g., Lu et al., 2000; Pentecost, 1992; Suarez, 1983) and usually attributed to inhibited nucleation of $CaCO_3$ due to high fluid flow, short resident times, and high sediment loads (Rogerson et al., 2014; and references therein). Under moderate atmospheric pressure and ambient temperature, the abiotic formation of anhydrous magnesium carbonates is kinetically hindered (e.g., Arvidson and Mackenzie,1999; Land, 1998), accounting for the lack of magnesite and dolomite in Ronda river waters.

4.7.2 Genesis of Ronda Ca–OH hyperalkaline fluids

4.7.2.1 Origin of hyperalkaline fluids by low-temperature serpentinization reactions

Ronda hyperalkaline fluids have physicochemical characteristics similar to other continental serpentinite-hosted Ca–OH hyperalkaline waters worldwide. The prevailing theory for the genesis of serpentinite-hosted, Ca–OH hyperalkaline fluids is that they form during low temperature serpentinization reactions driven by reactive percolation of meteoric Mg–HCO_3 surface waters in deep serpentinized peridotite aquifers isolated from the atmosphere (Barnes and O'Neil, 1969; Boschetti and Toscani, 2004; Bruni et al., 2002; Kelemen and Matter, 2008; Neal and Stanger, 1985; Palandri and Reed, 2004). Among other reactions, the hydration of olivine and pyroxene (**Eq. 4.4**) by fresh water in a closed system to atmospheric CO_2 accounts for the hyperalkalinity and chemistry of Ca–OH hyperalkaline fluids (Boschetti and Toscani, 2004; Bruni et al., 2002; Neal and Stanger, 1985; Palandri and Reed, 2004; Paukert et al., 2012):

$$\underset{(Olivine)}{4\,Mg_2SiO_4} + \underset{(Pyroxene)}{CaMgSi_2O_6} + 7\,H_2O \rightarrow \underset{(Serpentine)}{3\,Mg_3Si_2O_5(OH)_4} + Ca^{2+} + 2\,OH^- \qquad (4.4)$$

However, there are still many uncertainties about reaction path mechanism, residence time, and source of serpentinite-hosted hyperalkaline waters (Bruni et al., 2002; Chavagnac et al., 2013b; Paukert et al., 2012). Despite their long residence time in deep serpentine aquifers, the sluggish reaction rate of serpentinization reactions below 100 °C (McCollom et al., 2016) may call into question that low-temperature serpentinization is the sole origin for Ca–OH hyperalkaline fluids, but no alternative reactions pathways have yet been proposed.

The chemical similarity of deep coastal aquifer waters in the nearby Marbella (Malaga, Spain) area with Ronda Mg–HCO_3 river waters (Argamasilla et al., 2017) and the old ^{14}C age of the DIC in Ronda hyperalkaline fluids (c. 3 ka; Etiope et al., 2016), suggest that infiltration of meteoric-derived Mg–HCO_3 river waters are the potential source of Ronda Ca–OH hyperalkaline fluids. Alternatively, Ca–HCO_3 waters from nearby karst aquifers in western Alpujárrides limestones (**Fig. 4.1b**) (Barber_a and Andreo, 2015), may also be a potential source.

Figure 4.15 shows the chemical trends of Mg, Ca and DIC modelled for non-reactive (this study; dashed green line in **Fig. 4.15**; see figure caption for further details) and reactive peridotite/serpentinite percolation (Paukert et al., 2012; dashed and continuous black line in **Fig. 4.15**) of meteoric waters isolated from the atmosphere. The calculated trends for reactive percolation reproduce accurately the variations of Ca and Mg observed in Ronda river waters and hyperalkaline fluids, supporting that Ronda waters may form by deep percolation reaction of meteoric waters isolated from the atmosphere. As in the Oman Ophiolite hyperalkaline springs, at high pH, the Ca concentration of Ronda hyperalkaline fluids is less than those predicted in the Paukert et al. (2012) model (**Fig. 4.15a**). The lower Ca concentration may be due to precipitation of Ca-bearing carbonates (calcite and dolomite), because they are supersaturated at high pH as shown in our non-reactive models. Rempfert et al. (2017) reported higher Ca concentrations (> 3.5 mmol/L) in hyperalkaline fluids collected from deep wells in the Oman Ophiolite (up to 475m depth) than in the aerial hyperalkaline springs. This could indicate that Ca shows an upwards decrease due to precipitation of Ca-rich carbonates in the shallow subsurface due to mixing with DIC-rich shallow groundwater (Neal and Stanger, 1985).

The increase in Mg concentration in the pH range of 7.5 − 8.5 observed in the Ronda and Oman alkaline springs (**Fig. 4.15b**) is likely caused by hydration of Mg-silicates in the peridotites (**Eq. 4.4**) (Palandri and Reed, 2004; Paukert et al., 2012). The subsequent decrease in Mg concentration at increasing pH (**Fig. 4.15b**) is caused by the formation of Mg-bearing minerals —serpentine and brucite— during deeper fluid percolation (Palandri and Reed, 2004; Paukert et al., 2012).

Percolation reaction models greatly overestimated the observed decrease of the DIC from river waters to hyperalkaline fluids (**Fig. 4.15c**). The observed decrease in DIC is better accounted by non-reactive models due to the precipitation of Ca-bearing carbonates that become oversaturated at hyperalkaline pH (**Fig. 4.15c**). This process may also explain the formation of Mg-rich carbonate (e.g., magnesite) veins in serpentinized peridotites (Andreani et al., 2009; Bruni et al., 2002; Cipolli et al., 2004; Kelemen et al., 2011), as well as the potential formation of Ca-rich carbonates prior to fluid discharge and interaction with the atmosphere at the spring sites (Paukert et al., 2012).

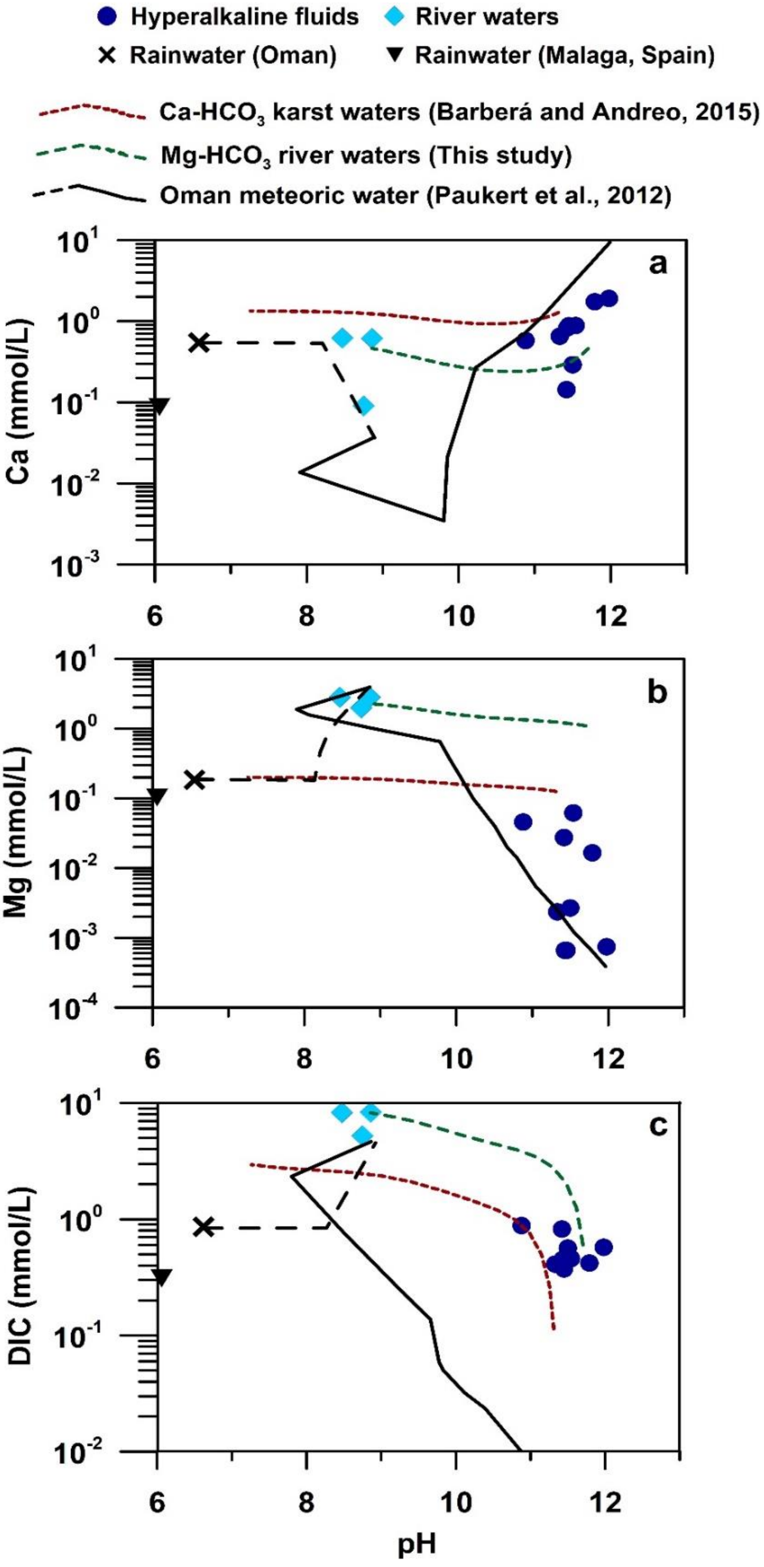

Figure 4.15. *Comparative graphs of non-reactive (this study) and reactive (Paukert et al., 2012) models of water isolation from the atmosphere. The graphs include* ***(a)*** *Ca,* ***(b)*** *Mg and* ***(c)*** *DIC versus pH in natural water samples from Ronda peridotites. The red and green dashed lines indicate the aqueous species evolution under non-reactive isolation from the atmosphere of Ca–HCO$_3$ waters (Barberá and Andreo, 2015) and Mg–HCO$_3$ (green line, this study), respectively. Dashed black line indicates model reaction progress in an open system. Solid black line indicates reaction progress under a closed system.*

4.7.2.2 The source of Ca of hyperalkaline fluids

In the low temperature serpentinization hypothesis, the main Ca source of hyperalkaline fluids comes from the hydrolysis of anhydrous Ca-bearing silicates in the peridotites such as clinopyroxene, orthopyroxene, and plagioclase (e.g., Palandri and Reed, 2004). These phases are minor component of peridotites and are almost absent in residual (i.e., recording high extent of melting) peridotites such as harzburgite in the mantle section of the Oman Ophiolite. Subcontinental mantle peridotites, such as the Ronda peridotite, are more fertile (i.e., richer in Ca and Al) than their ophiolitic counterparts (Bodinier and Godard, 2006). In the Ronda peridotites, Ca-silicates occur in lherzolites and harzburgites, wehrlite patches in dunites, pyroxenite layers, and rare intrusive gabbros (Garrido and Bodinier, 1999; Hidas et al., 2013b, 2015; Lenoir et al., 2001; Obata et al., 1980; Tubía, 1994; Varas-Reus et al., 2018).

Figure 4.16 shows the volume of reacted peridotite that accounts for the yearly amount of Ca discharged in hyperalkaline springs. The mass balance assumes that the total consumption of Ca by chemical weathering of Ca-bearing minerals in residual (dunite with 0.5 CaO wt%) to fertile (lherzolite with 4.0 CaO wt%) peridotite, is 1 mmol/L with a flow rate of $4.73 \cdot 10^{5}$ L/y per spring. The mass balance indicates that weathering of 0.21m^{3} of fertile lherzolite —or 1.68m^{3} of residual dunite— is required to account for the mass of Ca discharged yearly by one hyperalkaline spring (**Fig. 4.16**). Assuming a steady-state flow rate, the weathered volume of peridotite during the 3 ka residence time of these fluids in deep serpentinite aquifer (Etiope et al., 2016) is $6.3 \cdot 10^{-7}$ km^{3} of fertile lherzolite or $5.1 \cdot 10^{-6}$ km^{3} of residual dunite (**Fig. 4.16**). This volume of peridotite corresponds only to c. $1.0 - 7.5 \cdot 10^{-7}$ % of the total volume of the Ronda peridotites (c. 675 km^{3}; assuming a constant thickness of 1.5 km along the 450 km^{2} of exposed peridotites; **Fig. 4.1**). The volume of water discharged yearly in Ronda hyperalkaline fluid springs is unknown; assuming a total of 100 alkaline springs with Ca concentration and flow rates similar to those investigated here, the mass of Ca discharged in Ronda hyperalkaline springs in 1 Ma requires weathering of 0.003 % or 0.025 % of the total volume of the Ronda lherzolite or dunite, respectively. These are upper bound estimates as hyperalkaline fluids derive from meteoric waters that already contained Ca (**Fig. 4.15a & b**). The computation indicates that weathering (i.e., hydrolysis; **Eq. 4.4**) of Ca-silicates in the Ronda peridotites is a viable source to account for Ca concentration in hyperalkaline springs. However, it implies a steady-state dissolution rate of clinopyroxene of $1.6 \cdot 10^{-12}$ moL/cm^{2}·s (considering an average clinopyroxene grain size of 100 μm; Vauchez and Garrido, 2001) that is about eight order of magnitude faster than experimental values for steady-state dissolution rates of dissolution of

Ca-rich pyroxene (c. $10^{-20} - 10^{-19}$ moL/cm^2·s in the ranges of 20 − 100 °C and 6 < pH < 7; Zhang et al., 2013).

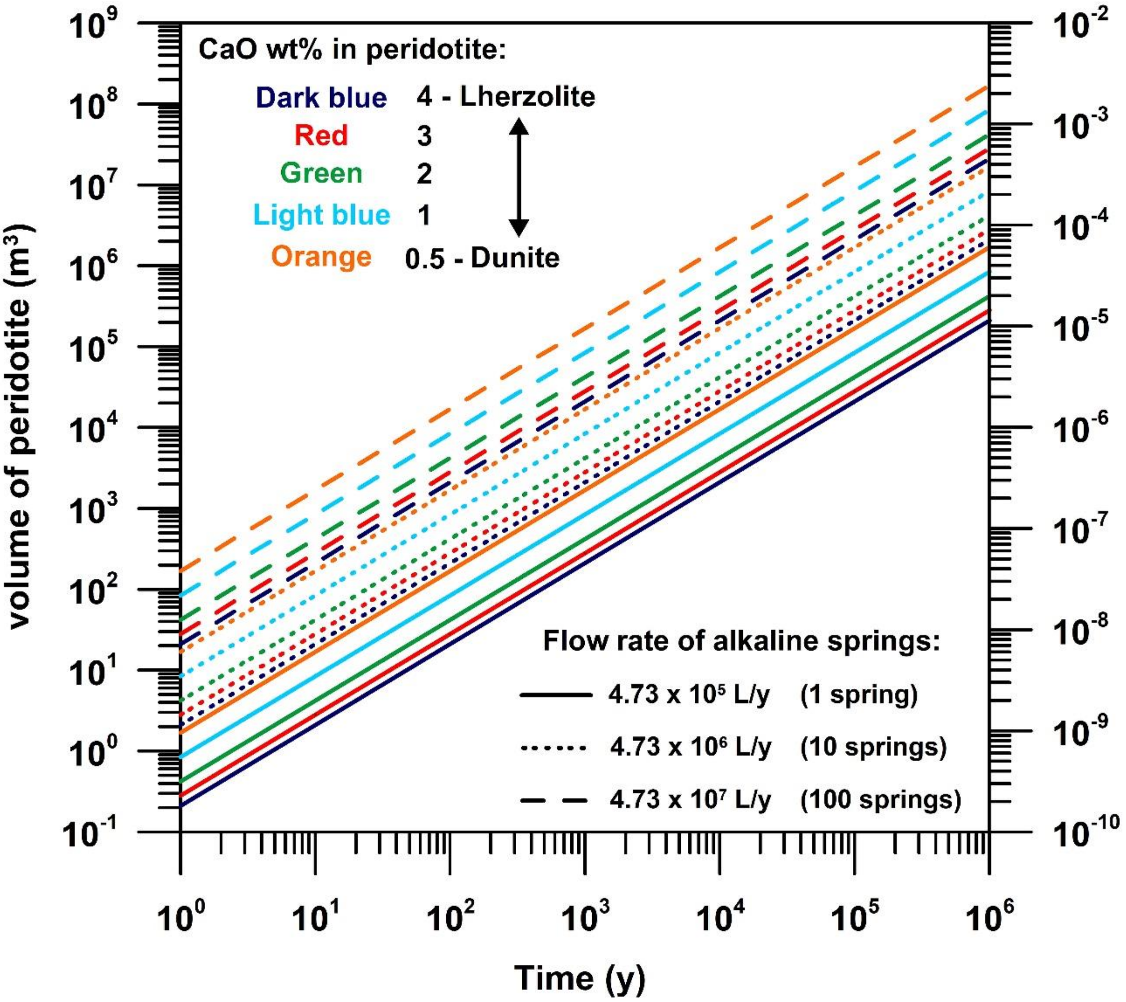

Figure 4.16. *Estimation of the reacted volume of peridotite (in m^3 and km^3) as a function of time under different CaO wt% and flow rates. Dark blue and orange colors correspond to lherzolite (4 CaO wt%) and dunite (0.5 CaO wt%) rock composition, respectively. Red, green and light blue colors correspond to intermediate rock compositions between 0.5 and 4 CaO wt%.*

De Obeso and Kelemen (2018) have shown that limestones can be an alternative source of Ca in some Oman Ophiolite hyperalkaline springs. An alternative source of Ca for the Ronda hyperalkaline fluids could be limestone karst aquifers (Sierra Blanca and Sierra de las Nieves) surrounding the Ronda peridotite massifs (**Fig. 4.1b**). Karst aquifers near the Ronda peridotite spring sites show the highest annual rainfall (> 800 mm), recharge (400 − 700 mm/y) and infiltration coefficient (40 − 70%) in the Betic Cordillera (Martos-Rosillo et al., 2015). These karst aquifers host Ca–HCO$_3$ waters that may infiltrate the peridotite along serpentinite-rich faults and become the source of the Ronda Ca–OH hyperalkaline fluids (**Fig. 4.15**).

4.7.2.3 *Genesis of methane bubbling in the spring sites*

Methane —bubbling in springs, pools, and rivers (**Fig. 4.2a**)— is the main gas emitted in some of the Ronda peridotite hyperalkaline spring sites (Etiope et al., 2016). In most continental peridotites, methane is the dominant gas in serpentinite-hosted hyperalkaline springs (e.g., Etiope and Whiticar, 2019; and references therein), but hydrogen can be also dominant in some sites such as the Oman Ophiolite hyperalkaline springs. Etiope et al. (2016) analyzed the C and H stable isotope composition of gases emitted from several Ronda hyperalkaline springs. They concluded that methane was predominantly abiotic and was genetically unrelated to the water DIC that has a younger ^{14}C age than methane (Etiope et al., 2016). Dating of $^{14}C – CH_4$ in serpentinite hosted hyperalkaline springs systematically shows that methane carbon is several thousands of years older than the ^{14}C – DIC ages (hundred to thousand years old) recording the residence time of water in the aquifer (Cipolli et al., 2004; Marques et al., 2008; Etiope et al., 2016; Etiope and Whiticar, 2019). Hypotheses proposed for the origin of abiotic methane in serpentinite-hosted hyperalkaline springs include gas-phase CO_2 hydrogenation (Sabatier's reactions) (Etiope and Sherwood Lollar, 2013; Etiope and Whiticar, 2019; McCollom, 2016; and references therein), and a deep magmatic or hydrothermal source (De Boer et al., 2007; Grozeva, 2018).

4.7.3 Mineralization and mineral textures in Ronda hyperalkaline spring

4.7.3.1 *Travertine*

Like other continental serpentinite-hosted alkaline springs (e.g., Chavagnac et al., 2013a & b; Neal and Stanger, 1984; Paukert et al., 2012; Stanger, 1987), travertines in the Ronda peridotites occur around the discharging outlets of hyperalkaline fluids, along their flow paths, and at the mixing areas of these waters with Mg–HCO_3 river waters (**Fig. 4.2a & d**). In the Ronda peridotites, the different stages and mechanisms of travertine formation are well illustrated in the BP spring site (**Fig. 4.2**; **Fig. 4.17**). Although aragonite and calcite are supersaturated in the BP hyperalkaline fluids (**Fig. 4.9a & b**), calcite is the only $CaCO_3$ polymorph present in the travertine at the discharging outlets (**Table 4.3**; **Fig. 4.2b**). Aragonite is occasionally observed in the crystalline crusts that form in the pools near the discharging outlets (see *section* ***4.6.4.1***). Precipitation of calcite upon uptake of atmospheric CO_2 is commonplace in hyperalkaline spring fluids with low Mg/Ca ratio (< 0.5) and T < 40 °C (Folk, 1994; Jones, 2017a; Pentecost, 2005; and references therein) such as those around the Ronda spring discharging outlets (Mg/Ca < 0.2 and avg. T: 19.9 °C) (**Fig. 4.17a**). The cause of the preponderance of calcite precipitation in Ca-rich and low Mg/Ca fluids is a matter of some debate (Jones, 2017a). Experimental studies show that aragonite forms at temperatures > 30 °C, while calcite is more stable at lower temperatures (e.g., Meldrum and Cölfen, 2008; Zeller and Wray, 1956). However, in natural settings, both $CaCO_3$ polymorphs precipitate in a wide range of temperature (Jones, 2017a). Degassing of CO_2 is the most common cause of travertine precipitation from $CaCO_3$-supersaturated fluids. Although rapid CO_2 degassing of CO_2-rich fluids promotes aragonite precipitation irrespective of their temperature and Mg/Ca ratio (e.g., Jones and Peng, 2016; Pentecost, 2005), degassing-induced aragonite precipitation is likely very limited in the Ronda hyperalkaline fluids because of their very low P_{CO_2} (**Fig. 4.10**).

A parallel mechanism for the formation of travertine in the Ronda spring sites is carbonate precipitation by mixing of Ca–OH-rich hyperalkaline fluids with Mg–HCO_3-rich river waters (**Fig. 4.17b & c**). In the BP site, the aragonite content of travertines gradually increases towards the riverside pointing to the mixing of Ca–OH-rich hyperalkaline fluids with Mg–HCO_3-rich river waters as the driving force for aragonite precipitation in this spring site (**Fig. 4.17b & c**). The phase of $CaCO_3$ polymorph that precipitates also depends on Mg content and Mg/Ca ratio of the fluid; Mg ions suppress the transformation of metastable $CaCO_3$ phases to calcite (Kitamura, 2001; Reddy andWang,1980) while higher Mg/Ca ratios favor aragonite precipitation (Burton, 1993; Falini et al., 1994; Lin and Singer, 2009). In the BP site, the increasing content of aragonite in travertine towards the riverside indicates that the main driver for aragonite precipitation is likely secular variations in the fluid Mg/Ca ratio likely due to seasonal flooding of the springs by the Mg–HCO_3 river waters, and mixing with Ca–OH hyperalkaline spring fluids (**Fig. 4.17b – d**).

Textures of $CaCO_3$ minerals in the BP travertines support fast supersaturation rates as expected by sudden changes in the fluid Mg/Ca ratio during secular flooding and water mixing. Polycrystalline aragonite with spherulitic, needle-like morphologies in BP travertines (**Fig. 4.18a**) is consistent with experimental and natural crystallization under high supersaturation states (Fernandez-Diaz et al., 1996; Jones, 2017b). In some instances, aragonite displays non-classical crystal growth textures that are consistent with growth by oriented aggregation of nanoparticles (**Fig. 4.18b**). During this process, $CaCO_3$ particles —probably amorphous— are self-assembled at the tips of the crystals, leading to a two-dimensional lateral re-organization on the surface of the previous flattened particle (Beniash et al., 1997; De Yoreo et al., 2015) (**Fig. 4.18b**).

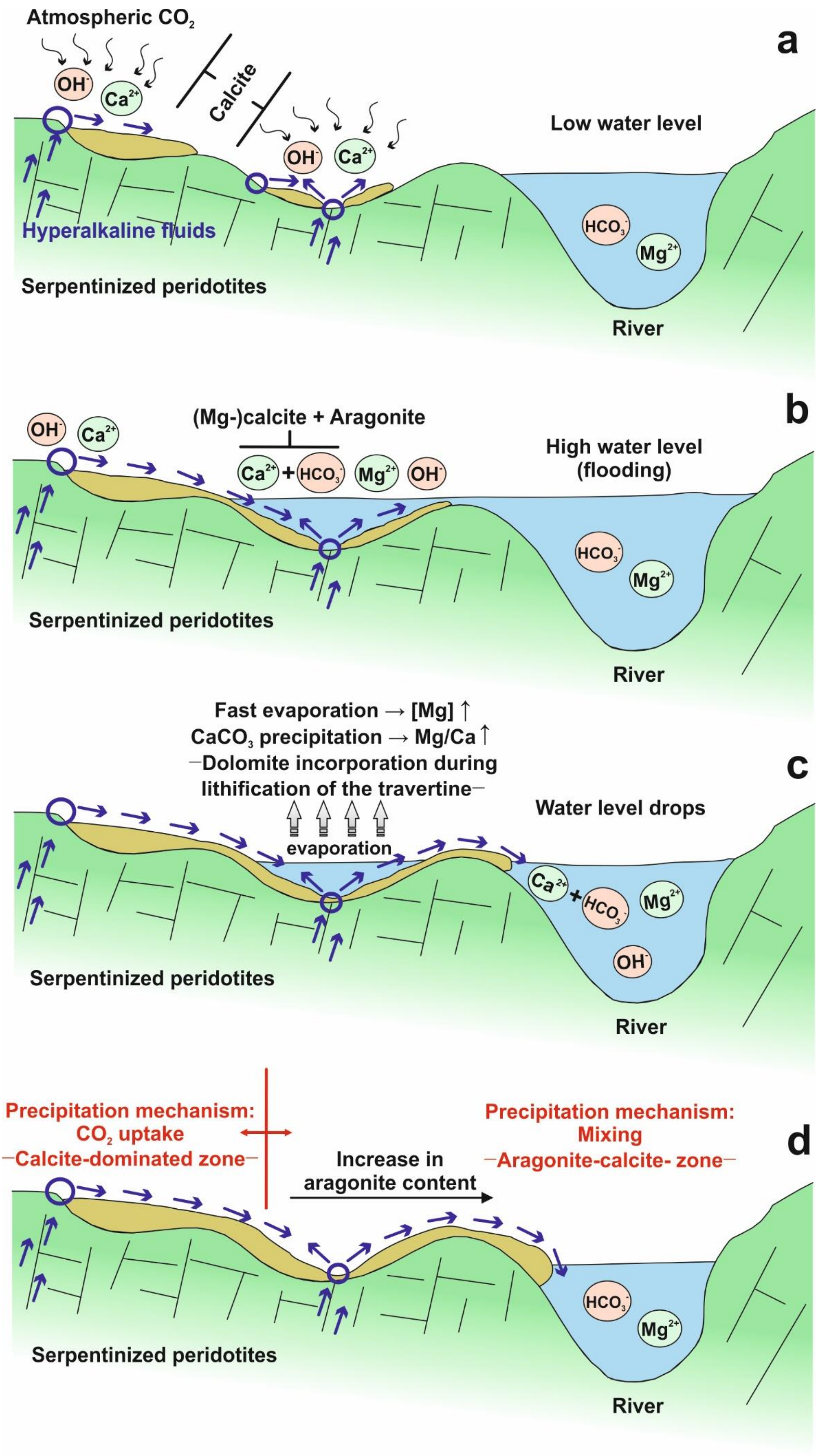
Atmospheric CO_2
a
OH^-
Ca^{2+}
Calcite
OH^-
Ca^{2+}
Low water level
HCO_3^-
Mg^{2+}
Hyperalkaline fluids
Serpentinized peridotites
River
b
OH^-
Ca^{2+}
(Mg-)calcite + Aragonite
Ca^{2+} + HCO_3^-
Mg^{2+}
OH^-
High water level (flooding)
HCO_3^-
Mg^{2+}
Serpentinized peridotites
River
Fast evaporation → [Mg] ↑
$CaCO_3$ precipitation → Mg/Ca ↑
–Dolomite incorporation during lithification of the travertine–
c
Water level drops
evaporation
Ca^{2+} + HCO_3^-
Mg^{2+}
OH^-
Serpentinized peridotites
River
Precipitation mechanism: CO_2 uptake –Calcite-dominated zone–
Precipitation mechanism: Mixing –Aragonite-calcite- zone–
d
Increase in aragonite content
HCO_3^-
Mg^{2+}
Serpentinized peridotites
River

◄ **Figure 4.17.** *Conceptual model of carbonate mineral precipitation during fluctuations of the river water level.* ***(a)*** *Hyperalkaline fluids form calcite-dominated travertine due to atmospheric CO_2 uptake upon discharge.* ***(b)*** *Flooding events of river water overflows the —previously— formed travertine. Aragonite and (Mg-)calcite precipitate as a result of the mixing of the two fluids.* ***(c)*** *Fast evaporation leads to dolomite formation during travertine lithification process. Water level retreats, and travertine formation continues to take place along the river bank due to mixing of hyperalkaline fluids with river waters.* ***(d)*** *Two zones of different precipitation mechanisms can be observed;* ***i)*** *precipitation due to CO_2 uptake leading to calcite-dominated travertine around the discharging outlets of hyperalkaline fluids, and* ***ii)*** *travertine enriched in aragonite due to mixing of the two water types as the river bank is approached. The straight blue, undulating black and dashed grey arrows correspond to the hyperalkaline fluid flow paths, CO_2 uptake and evaporation, respectively.*

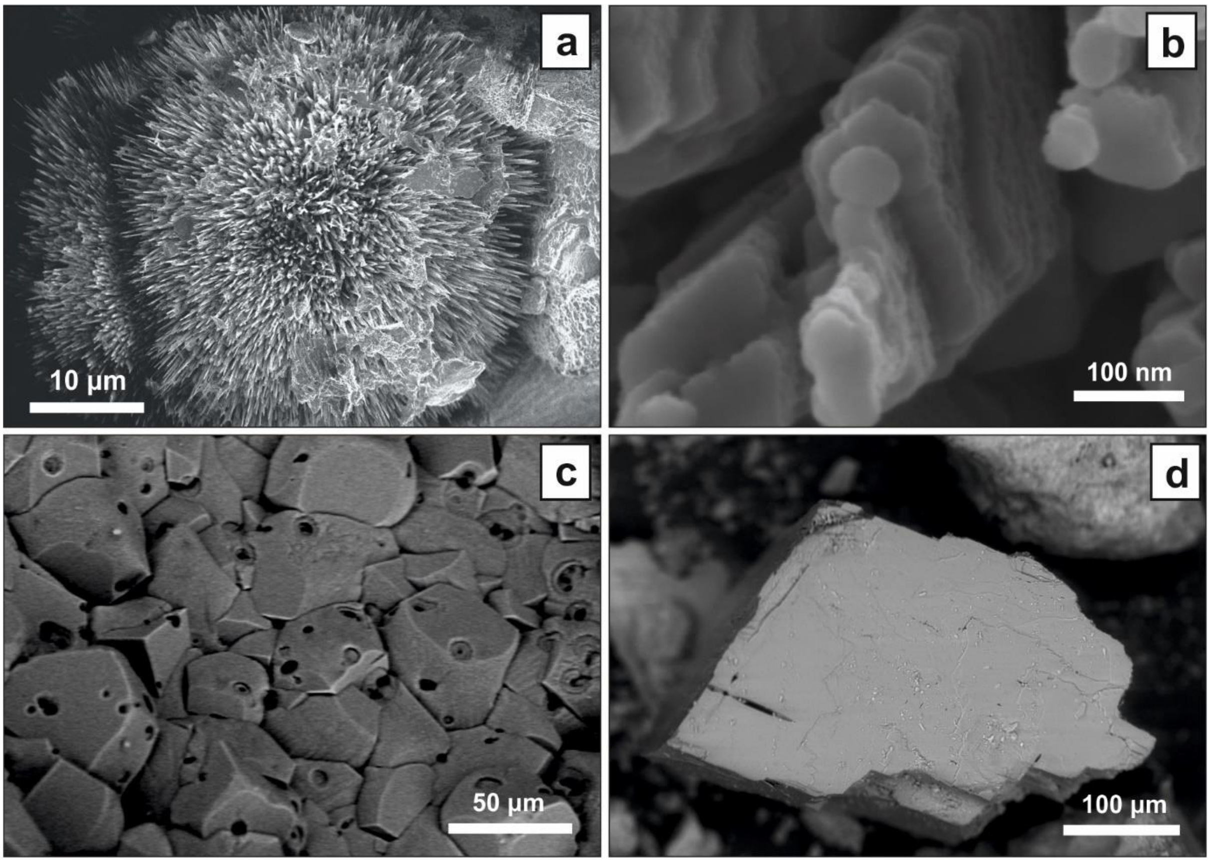

Figure 4.18. *Textural characteristics of mineral phases in BP site.* ***(a)*** *Polycrystalline aragonite with spherulitic, needle-like morphology in travertine.* ***(b)*** *Nano-rods of aragonite formed by aggregation of flat nano-particles with a thinning towards the tip of the crystal.* ***(c)*** *Holes on calcite surface indicating the presence of gas bubbles.* ***(d)*** *Large, euhedral dolomite crystal in BP5 sediments showing strong crystallographic symmetry.*

4.7.3.2 Crystalline crusts and sediment deposits

Precipitation of crystalline crusts upon discharge is common in serpentinite-hosted alkaline springs (e.g., Oman Ophiolite alkaline springs; Chavagnac et al., 2013a; Paukert et al., 2012).

In Ronda alkaline springs, crystalline crusts —mostly composed of calcite— only occur in hyperalkaline pools and discharging fluid outlets (see *section* ***4.6.4***) (**Fig. 4.11c**). Calcite-dominated travertine in the Ronda hyperalkaline discharging outlets and calcite floating crusts are formed by the precipitation of calcite upon uptake of atmospheric CO_2 by the hyperalkaline fluids. Flat-faced rhombohedral {104} and curved edges in calcite (**Fig. 4.11c**) indicate, respectively, events of slow and fast growth due to changes in supersaturation rate (Pope and Grotzinger, 2000). This variability in calcite morphology likely records spatial and temporal fluctuations in the supersaturation rate modulated by the supply of atmospheric CO_2 and the evaporation rate. The homocentric cavities in calcite surfaces may record that methane gas bubbles were attached during the growth of calcite clusters (**Fig. 4.18c**) (Taylor and Chafetz, 2004; Aquilano et al., 2003). Alternatively, they might be due to microbial activity (e.g., cyanobacteria) during calcite precipitation (Martinez et al., 2010; Bundeleva et al., 2014).

The BAL, AMAR, and HED sites do not display the natural hydrological features of the ALF and BP site, and we investigated travertine, crystalline crusts and sediments only at the discharging outlets. Calcite is the only carbonate phase in AMAR and HED sites, probably because of the absence of river waters as a Mg source. The BAL spring is aragonite-dominated, which is in agreement with the elevated Mg content and high Mg/Ca ratio of these fluids relative to other hyperalkaline springs (**Table 4.2**). Aragonite crystals in the BAL site show branching features (**Fig. 4.11d**) that may be indicative of high supersaturation level and fast supersaturation rates (Fernandez-Diaz et al., 1996) and may record sudden changes in the Mg concentration of fluids at this spring site.

4.7.3.3 Formation of dolomite in travertine and sediments

In Ronda, dolomite occurs in the aragonite-bearing travertine at BP site (**Table 4.3**) formed by mixing of Ca–OH hyperalkaline fluids with Mg–HCO_3 river waters (**Fig. 4.17b & c**). Several authors have reported variable amounts of dolomite in lithified travertines associated with serpentinite-hosted alkaline fluids (Barnes and O'Neil, 1971; Mervine et al., 2014; Renaut and Jones, 1997), where dolomite forms from trapped pore water with high Mg/Ca during lithification and early diagenesis (Fischbeck and Muller, 1971; Folk, 1993; Renaut and Jones, 1997).

Dolomite is absent in most of the investigated sediments in alkaline pools (**Table 4.3**); a remarkable exception is the sediments from the BP5 pool (**Fig. 4.2e**) that contain c. 90% dolomite. The elevated S and P concentrations in BP5 pool may be indicative of microbial activity, opening the possibility of dolomite precipitation by bacterial sulfate reduction (e.g., Vasconcelos et al., 1995), methanogenesis (e.g., Roberts et al., 2004), or sulfate-driven anaerobic oxidation of methane (e.g., Boetius et al., 2000; Peckmann and Thiel, 2004). Such biotic processes may seem inconsistent with the oxidative environment of the BP5 pool, but biotic dolomite formation under aerobic and hypersaline conditions may take place at the water–sediment interface (Sánchez-Román et al., 2009). Biotic crystallization of dolomite is, however, unlikely because dolomite crystals exhibit classical crystal growth with symmetrical features (**Fig. 4.18d**) unlike the typical spherical or dumbbell morphologies of biotic dolomite crystallization (e.g., Sánchez-Román et al., 2009; Van Lith et al., 2003; Warthmann et al., 2005; Zhang et al., 2012).

The abiotic precipitation of large amounts of dolomite is uncommon at atmospheric conditions even in dolomite supersaturated fluids (e.g., Land, 1998) such as most of the Ronda alkaline fluids (**Fig. 4.9c**). The supersaturation of dolomite in BP5 pool is expected, as this pool shows the highest Mg and DIC concentrations (**Fig. 4.7b & f**), as well as elevated Ca concentrations compared to river waters (**Fig. 4.7a**). Indeed, BP5 pool displays the highest supersaturation in dolomite (**Fig. 4.9c**) compared to river waters and hyperalkaline fluids. Thermodynamic calculations suggest that despite the very low Mg concentrations (minimum: $2.35 \cdot 10^{-6}$ mmol/L) in hyperalkaline fluids, dolomite reaches supersaturation when Mg/Ca ratio in the fluids is over $3.6 \cdot 10^{-3}$ (**Fig. 4.19a**), and Mg/OH ratio is over $1.1 \cdot 10^{-3}$ (**Fig. 4.19b**). Dolomite in pool BP5 sediments points that the fluids are already highly supersaturated in dolomite before their discharge at the pool (Badiozamani, 1973). In BP5 pool, the values of pH, Cl-normalized Mg, and DIC fall in between those of hyperalkaline fluids and river waters, showing characteristics of both water types. Thus, possible subsurface mixing of Ca–OH hyperalkaline fluids and shallow Mg–HCO_3 waters might induce dolomite supersaturation before discharge.

Alternatively, the formation of dolomite could be favored under conditions of high salinity (Orr Chazen and Ehrlich, 1973; Vasconcelos and McKenzie, 1997) or changing-salinity environments such as sabkhas (Müller et al., 1990). The very high conductivity (**Fig. 4.4b**) and Cl^- concentrations (**Fig. 4.6**) show that BP5 pool underwent high evaporation rates that could inhibit Mg ion hydration and promote dolomite precipitation under atmospheric conditions (Di Tommaso and de Leeuw, 2010). Furthermore, high alkalinity and conductivity of BP5 pool fluids (**Fig. 4.4b & c**) decrease the low-temperature kinetic barrier for dolomite precipitation (Sánchez-Román et al., 2009). Roberts et al. (2013) demonstrated that natural surfaces possessing a high density of carboxyl groups might be a mechanism by which abiotic dolomite nuclei forms. Roberts et al. (2013) suggested that carboxyl group formation is accelerated in environments of changing or high salinity, meteoric–saline water mixing, or in certain weathering settings (e.g., presence of clays). The physicochemical and hydrological characteristics of the BP5 pool seems to meet the conditions for abiotic, low-temperature dolomite precipitation so long-hypothesized, yet rarely documented in nature.

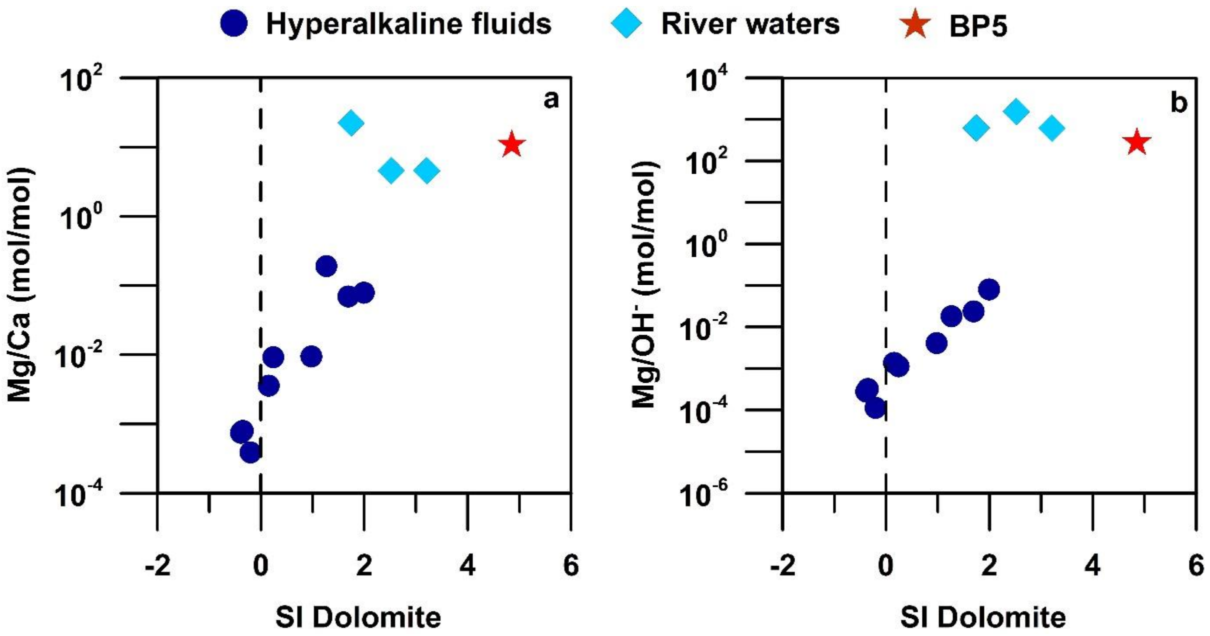

Figure 4.19. ***(a)*** *Mg/Ca and* ***(b)*** *Mg/OH versus dolomite saturation index (SI) of the different water types in the Ronda spring sites. Vertical dashed black line indicates the equilibrium state (SI = 0).*

4.8 Appendix

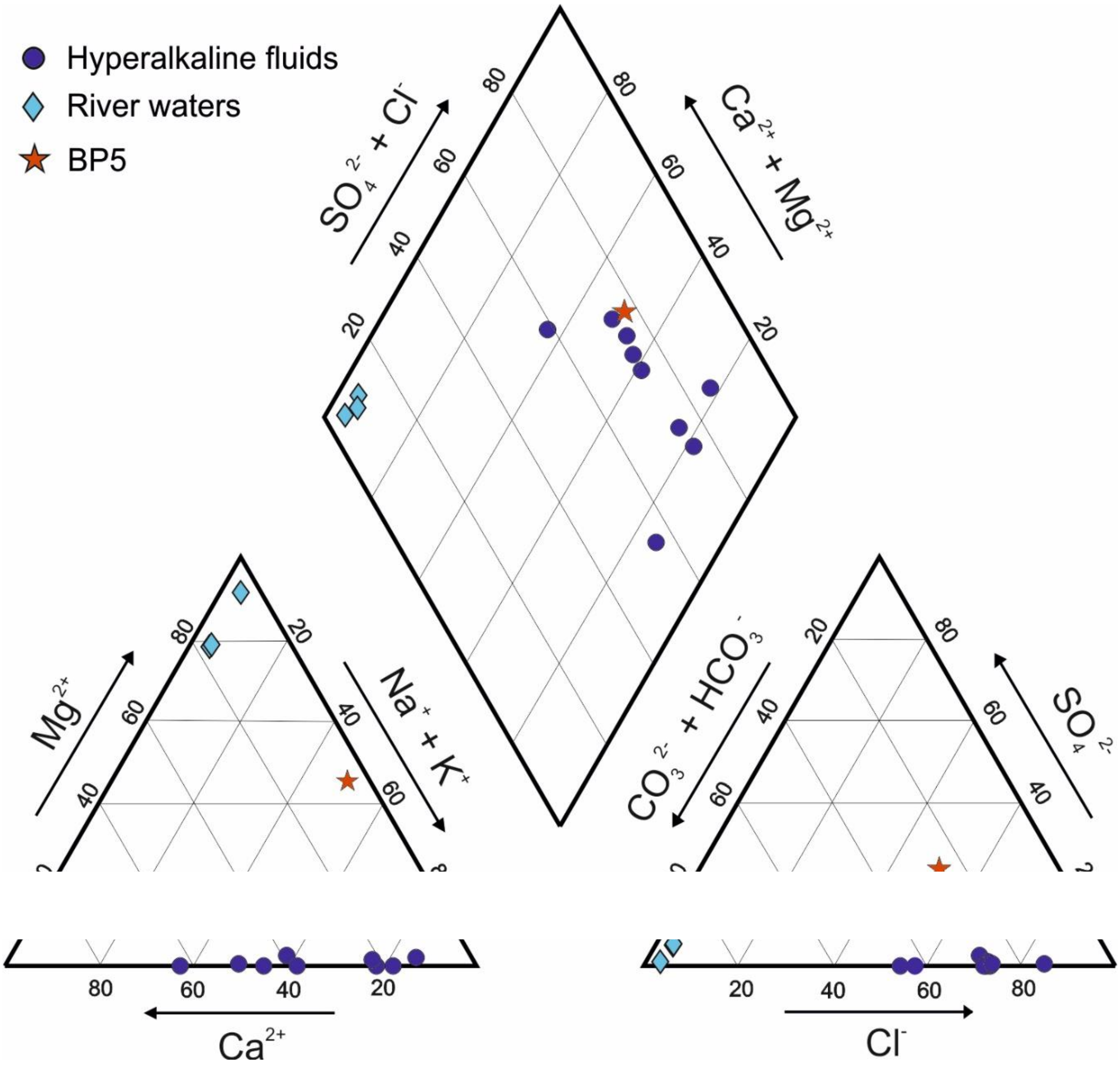

Figure A−4.1. *PIPER plot showing the relative proportions of major cations and anions.*

5 Crystallization experiments of hydrated magnesium carbonates at low temperature

5.1 Introduction

The crystallization of carbonate minerals in the $MgO–CO_2–H_2O$ system from aqueous solutions has recently attracted increasing research interest in various fields such as biomineralization and the design of new materials (e.g., Unluer and Taabaa, 2013; Mavromatis et al., 2012). Although numerous studies regarding Mg-carbonates have been already reported, the crystallization mechanisms and the role of amorphous magnesium carbonate (AMC) in the crystallization sequence are poorly understood.

Due to their ability to sequester anthropogenically generated CO_2 in a stable and long-lasting form, magnesium carbonates are currently of great interest as a part of the efforts to counter global warming, where the main goal is to capture and store excess CO_2, preventing its accumulation in the atmosphere and, therefore, slowing down its contribution to climate change. Magnesium carbonates exist in two main forms: anhydrous and hydrated. Anhydrous magnesium carbonate naturally exists as the mineral magnesite ($MgCO_3$), and $MgCO_3$ can form solid solutions to form carbonate minerals such as dolomite [$CaMg(CO_3)_2$] and huntite [$Mg_3Ca(CO_3)_4$]. The stability of long-term storage of CO_2 is highly associated with the degree of carbonation during fluid-rock interaction reactions (e.g., Matter and Kelemen, 2009). Carbonation is an essential process for capturing CO_2, where Mg-, Fe-, and Ca-silicates turn into carbonates such as calcite ($CaCO_3$), magnesite ($MgCO_3$), dolomite ($CaMg(CO_3)_2$), and siderite ($FeCO_3$) via a series of reactions.

The study of the Mg-bearing anhydrous carbonates is of high significance as they have a close relation to sites, where CO_2 is injected in basaltic rocks (Hansen et al., 2005; Matter et al., 2006) or show great potential for long-term CO_2 storage (Kelemen and Matter, 2008). However, numerous studies (e.g. Sayles and Fyfe, 1973; Konigsberger et al., 1999; Urosevic et al., 2012) have failed to precipitate anhydrous $MgCO_3$-bearing phases (magnesite and dolomite) at room temperature (e.g. Land 1998; Ardvison and Mackenzie, 1999; Mackenzie and Andersson, 2013). This could be attributed to the large dehydration energy associated with six molecules of H_2O comprising the solvation shell of the aqueous Mg^{2+} ions. The smaller size of Mg^{2+} compared to Ca^{2+} and Fe^{2+}, leads to greater charge density around Mg^{2+}, and thus, water molecules are more firmly bound to the ion. The high-energy barrier of Mg^{2+} solvation shell prevents the precipitation of anhydrous magnesium carbonate, but instead, favors the crystallization of hydrated magnesium carbonates and hydroxy-carbonates (Pokrovsky et al., 1999; Hanchen et al., 2008; Saldi et al., 2009; Benezeth et al., 2011). Nevertheless, recent reports on magnesite formation from non-aqueous solutions (Xu et al., 2013) suggest that a strained accommodation of the CO_3 molecules in the crystal lattice of magnesite inhibits its nucleation at low temperatures. The most common hydrated $MgCO_3$-bearing phases in the literature are: barringtonite [$MgCO_3 \cdot 2H_2O$], nesquehonite ($MgCO_3 \cdot 3H_2O$), lansfordite [$MgCO_3 \cdot 5H_2O$], hydromagnesite [$Mg_5(CO_3)_4(OH)_2 \cdot 4H_2O$], dypingite [$Mg_5(CO_3)_4(OH)_2 \cdot 5H_2O$], and artinite [$Mg_2CO_3(OH)_2 \cdot 3H_2O$]. In order to adequately investigate CO_2 sequestration in carbonate minerals, knowledge of the mechanisms and kinetics of the complex pathway of transformation reactions involving secondary magnesium carbonates is needed (e.g., Daval et al., 2009; Dufaud et al., 2009).

The vast majority of crystallization experiments in the $MgO–CO_2–H_2O$ system was conducted in a closed system or under negligible influence from atmospheric CO_2, while the observed phases were identified within few hours after the initiation of the experiments. In nature, hydrated Mg-carbonates are strongly related to environments characterized by weathering, evaporating waters and CO_2-rich conditions (*cf.* Power et al., 2019, and references therein). This indicates the tendency of these phases to form under open atmospheric conditions. A comparative study —which is the case in the present work— of Mg-carbonate crystallization in closed vs. open system could give information on the effect of atmospheric conditions on the phase occurrence and textural differentiation.

Although the conditions and parameters controlling the crystallization and transformation of Mg-carbonates are well studied (e.g. Ballirano et al., 2013; Bénézeth et al., 2011; Hänchen et al., 2008; Harrison et al., 2019; Hopkinson et al., 2008, 2012; Königsberger et al., 1999, among others), this research involves an in-depth examination of phases and textures, under a wide range of variable solution compositions and pH values. This study allows documenting different crystallization sequences and related morphologies of the synthesized Mg-carbonates both in the closed and open systems.

5.2 Materials and Methods

5.2.1 Crystallization setup - solution mixing at closed and open system

For the closed system experiments, the reagents used for the synthesis of the hydrated magnesium (hydroxy-) carbonates at room temperature were $MgCl_2.6H_2O$ (SIGMA-ALDRICH, Lot: 100M0075V) and $HNaCO_3$ (SIGMA-ALDRICH, Lot: 069k0084). The concentrations of the initial $MgCl_2.6H_2O$ and Na_2CO_3 solutions were 0.01 M, 0.02 M, 0.05 M, 0.1 M, 0.2 M, 0.5 M, 1 M, and 2 M for each solution used, respectively. MilliQ water was used for the preparation of the solutions, which were vigorously stirred (800 rpm) at 25 °C for 60 minutes. After stirring, all the solutions were transferred into a nitrogen glovebox —where the mixing and monitoring experimental procedures took place— to avoid any interaction with the atmosphere.

One millimeter (1 mL) of $MgCl_2.6H_2O$ and 1 mL of Na_2CO_3 were mixed in a 16 mm diameter Linbro plate wells under varying concentrations, generating a grid of mixed solutions (each solution had a final volume of 2 mL) with variable reactant concentrations (**Fig. 5.1**). Multiple Linbro plates were made to monitor the pH evolution, identify the phases and characterize their textural aspects, and observe the crystallization sequence.

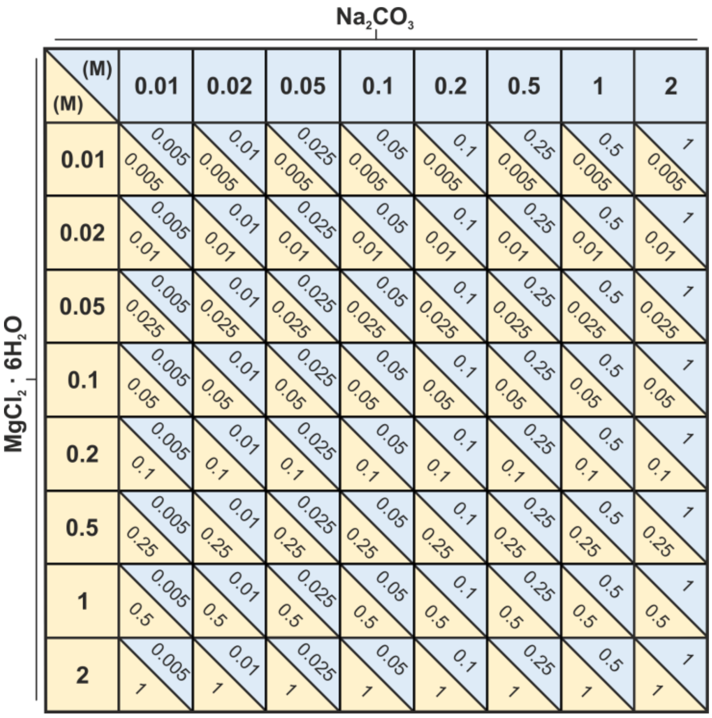

(M) (M)	0.01	0.02	0.05	0.1	0.2	0.5	1	2
0.01	0.005 0.005	0.01 0.005	0.025 0.005	0.05 0.005	0.1 0.005	0.25 0.005	0.5 0.005	1 0.005
0.02	0.005 0.01	0.01 0.01	0.025 0.01	0.05 0.01	0.1 0.01	0.25 0.01	0.5 0.01	1 0.01
0.05	0.005 0.025	0.01 0.025	0.025 0.025	0.05 0.025	0.1 0.025	0.25 0.025	0.5 0.025	1 0.025
0.1	0.005 0.05	0.01 0.05	0.025 0.05	0.05 0.05	0.1 0.05	0.25 0.05	0.5 0.05	1 0.05
0.2	0.005 0.1	0.01 0.1	0.025 0.1	0.05 0.1	0.1 0.1	0.25 0.1	0.5 0.1	1 0.1
0.5	0.005 0.25	0.01 0.25	0.025 0.25	0.05 0.25	0.1 0.25	0.25 0.25	0.5 0.25	1 0.25
1	0.005 0.5	0.01 0.5	0.025 0.5	0.05 0.5	0.1 0.5	0.25 0.5	0.5 0.5	1 0.5
2	0.005 1	0.01 1	0.025 1	0.05 1	0.1 1	0.25 1	0.5 1	1 1

Figure 5.1. *Mixing grid created by the mixing combinations of the two reagents* 1 mL) of $MgCl_2.6H_2O$ and 1 mL of Na_2CO_3. Note that the concentration of each reagent gets diluted 1:2 after mixing.

The pH values for the initial $MgCl_2.6H_2O$ solutions ranged from 6.1 to 6.7 and for Na_2CO_3 from 10.6 to 11.3 (**Table A-5.1**). The pH was monitored every 30 min for the first 12 h of the experiment, and every 24 h for the next 1000 h. **Figures A-5.1** to **A-5.3** contain the pH values of each initial solution (pH_0) (**Fig. A-5.1**), as well as the measured values at 6 different times (t_1 = 3 h (**Fig. A-5.1**), t_2 = 12 h (**Fig. A-5.2**), t_3 = 36 h (**Fig. A-5.2**), t_4 = 240 h (**Fig. A-5.3**), t_5 = 720 h (**Fig. A-5.3**), t_6 = 1000 h (**Fig. A-5.3**) during monitoring for the next 1000 h. This allowed determining the time needed for hydrated magnesium carbonates to nucleate at a specific pH value. The solutions of the wells that demonstrated instant precipitation upon mixing were collected via filtering (filter diameter) and analyzed with XRD and Raman without drying in order to avoid any potential transformation to occur during the drying process. The same procedure was followed with the samples dried at 32 °C for 24 hours. All the samples sent for textural characterization in with SEM were dried.

For the open system experiments, the reagents preparation and Linbro plate mixing grid construction (**Fig 5.1**) were the same as in the closed system experiments. The Linbro plates were left uncovered and in contact with the atmosphere, which triggered the evaporation of the mixed solutions. The pH was monitored at three steps: i) instantly upon the mixing of the solutions, ii) after 3 h, and iii) after 120 h. **Figure A-5.4** contains the measurements of the pH values in the evaporating wells. At 3 h and 72 h, the precipitated material in the wells was collected, dried at 32 °C for 24 hours, and sent for phase identification and textural characterization.

5.2.2 Solid phase characterization

The synthesized phases were identified by powder X-ray diffraction (XRD), using a PANalytical MPD diffractometer with a Bragg-Brentano parafocusing geometry and Cu K_a radiation (operating at 40 mA and 45 kV). Instrument configuration included programmable divergence slits in the incident and diffracted beams, placement of a 0.25º fix anti-scatter slit in the incident path and a PSD detector PIXel. Data processing was conducted by using the software HighScore Plus from PANalytical X'Pert PRO (mineral database: Pdf2HSP/PAN-ICSD). The identification of the synthesized phases was complemented by a field emission scanning electron microscope (FE-SEM) Zeiss Supra 40Vp connected to a Renishaw In Via Raman spectrometer fitted with a Nd:YAG 532 nm laser and a near-infrared diode 785 nm laser, with maximum powers of 500 mW and 100 mW, respectively. The SEMs were equipped with Energy Dispersive X-ray Spectrometers (EDS).

Textural and morphological characterization of the phases was carried out at the Instituto Andaluz de Ciencias de la Tierra (IACT) and Centro de Instrumentación Científica (CIC) of the University of Granada (Granada, Spain). Complementary Fourier Transform Infrared spectroscopy (FT–IR) was applied using a JASCO 6200 spectrometer at CIC. Crystallization sequence and transformation processes were initially observed using a NIKON AZ100 optical microscope coupled to JENOPTIK ProgRes CT3 camera. Further textural characterization and semi-quantitative chemical analysis of the solid samples were carried out using a Field Emission Scanning Electron Microscope (FE-SEM) ZEISS AURIGA (In- Lens mode at 3 kV) and an Environmental SEM (ESEM) FEI Quanta 400 (SE mode at 5 kV and BSE mode at 12 kV).

5.2.3 Ionic concentration product and PHREEQC calculations

Because of missing information (e.g., solute activities and solution ionic strength) for the calculation of the ionic activity product (IAP), the ionic concentration product (ICP) was used instead to determine the saturation (S) of $MgCO_3$ in the mixed solutions and —at least approximately— evaluate the role of saturation in the precipitation of $MgCO_3$-bearing minerals. The theoretical Saturation Index (SI), defined as the logarithm of the ratio between IAP and solubility product of the relevant mineral phases in the sampled waters was calculated using the PHREEQC-2 code (Parkhurst and Appelo, 2005) and the wateq4f.dat database (Ball and Nordstrom, 1991). The use of PHREEQC in this study was to compare the theoretical saturation index with the saturation values calculated by the solubility products from the literature and the concentration of initial solutions used for the experiments (**Table A-5.2**). Negative SI indicates that the final solutions are undersaturated with respect to a given phase and its dissolution is thermodynamically favored over precipitation; positive SI indicates that the solution is supersaturated and precipitation is favored, and SI of zero shows that the mineral phase is in equilibrium with the solution.

5.3 Results and Discussion

5.3.1 Crystallization experiments in closed system

5.3.1.1 Crystallization sequence of $MgCO_3$-bearing phases

Upon the mixing of the initial solutions, some wells showed no precipitation, whereas in others the precipitation of a transparent or white (cloudy) colloidal phase of various density was instantly triggered (**Fig. 5.2**). The higher the concentration and when Mg/CO_3 ratios are ~1 or 1, then the colloidal material gets denser. No instant crystallization —at least under observance with the optical microscope— was observed in any of the mixed solutions derived from all mixing combinations of $MgCl_2.6H_2O$ and Na_2CO_3 solutions with concentrations 0.01 and 0.02 M (**Fig. 5.2**).

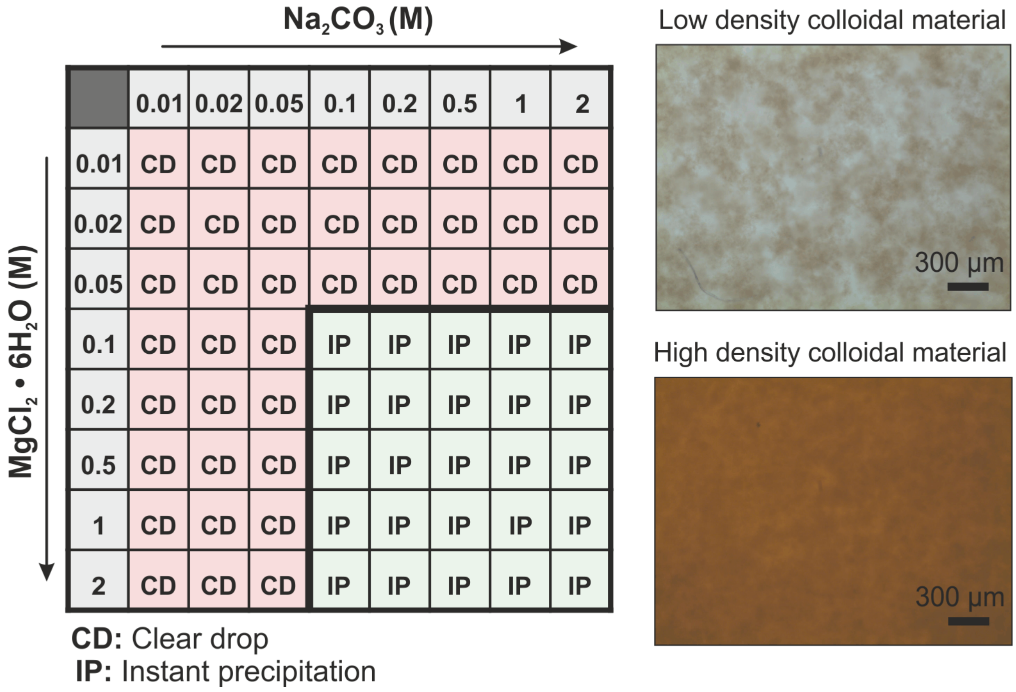

	0.01	0.02	0.05	0.1	0.2	0.5	1	2
0.01	CD	CD	CD	CD	CD	CD	CD	CD
0.02	CD	CD	CD	CD	CD	CD	CD	CD
0.05	CD	CD	CD	CD	CD	CD	CD	CD
0.1	CD	CD	CD	IP	IP	IP	IP	IP
0.2	CD	CD	CD	IP	IP	IP	IP	IP
0.5	CD	CD	CD	IP	IP	IP	IP	IP
1	CD	CD	CD	IP	IP	IP	IP	IP
2	CD	CD	CD	IP	IP	IP	IP	IP

Figure 5.2. *Grid of crystallization cells of mixed solutions that presented either clear drops (empty) or instant precipitation of a colloidal material of different density.*

The precipitated colloidal material from the wells with instant precipitation showed three different compositional profiles (**Fig. 5.3**): i) AMC, ii) AMC + nesquehonite, and iii) AMC + nesquehonite + dypingite. AMC is the only phase at Mg/CO_3 = 1 and ICP = 10^{-2} and 4 x 10^{-2} and S between 2.3 and 3, and at Mg/$CO_3 \neq 1$ and ICP between 2 x 10^{-1} and 10^{-2}. The co-existence of AMC + nesquehonite was observed at Mg/$CO_3 \neq 1$ and ICP > 2 x 10^{-1}. AMC + nesquehonite + dypingite were identified at both Mg/CO_3 = 1 and Mg/$CO_3 \neq 1$, and overall ICP > 10^{-1}, at high $MgCO_3$ saturation values between 3.3 and 4.9. The calculated ICP for each crystallization well and the respective saturation value are given in **Table 5.1** and **Table 5.2**, respectively. Although magnesite ($MgCO_3$) is the anhydrous product of the reaction between Mg^{2+} and CO_3^{2-}, the solubility product of —the hydrated $MgCO_3$— nesquehonite ($K_{sp}^{nesq} = 10^{-5.06}$ at 25 °C; from Harrison et al., 2019) was preferred, as it is readily fomred at room temperatures compared to magnesite.

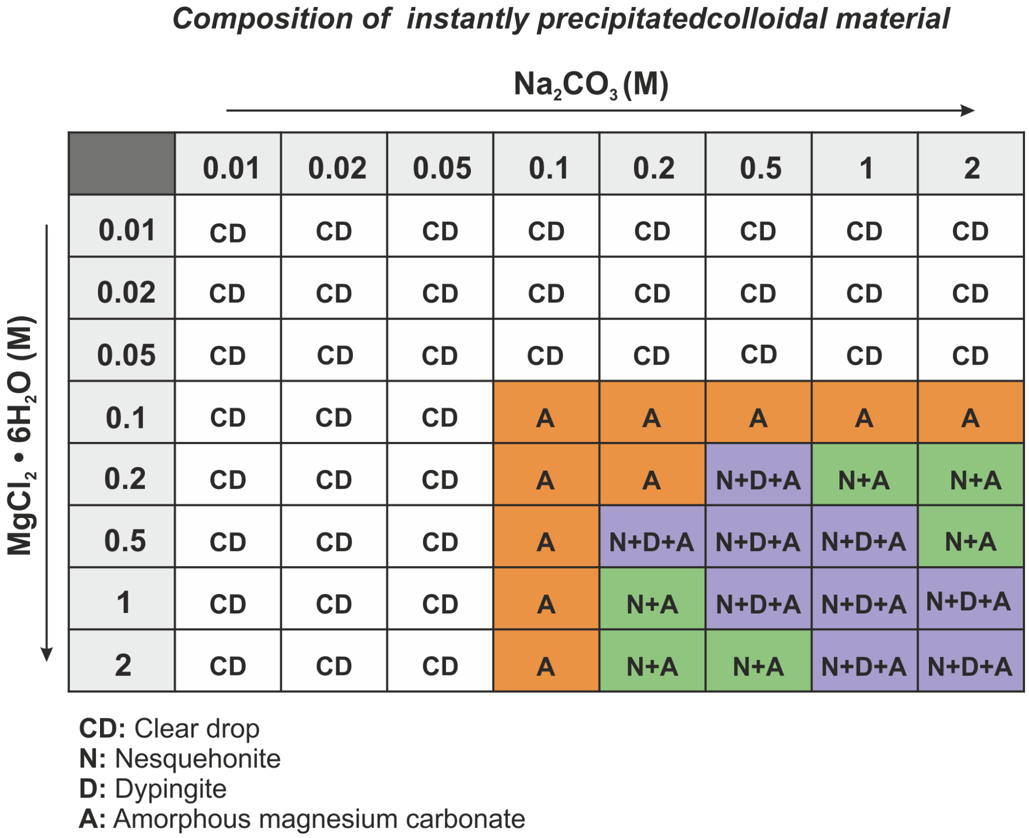

Composition of instantly precipitatedcolloidal material

Na_2CO_3 (M)

$MgCl_2 \cdot 6H_2O$ (M)

	0.01	0.02	0.05	0.1	0.2	0.5	1	2
0.01	CD	CD	CD	CD	CD	CD	CD	CD
0.02	CD	CD	CD	CD	CD	CD	CD	CD
0.05	CD	CD	CD	CD	CD	CD	CD	CD
0.1	CD	CD	CD	A	A	A	A	A
0.2	CD	CD	CD	A	A	N+D+A	N+A	N+A
0.5	CD	CD	CD	A	N+D+A	N+D+A	N+D+A	N+A
1	CD	CD	CD	A	N+A	N+D+A	N+D+A	N+D+A
2	CD	CD	CD	A	N+A	N+A	N+D+A	N+D+A

CD: Clear drop
N: Nesquehonite
D: Dypingite
A: Amorphous magnesium carbonate

Figure 5.3. *Mixing grid including the composition of colloidal material that precipitated instantly upon solution mixing.*

The majority of the XRD diffractograms showed ranges of broad peaks that could indicate an amorphous phase (i.e., between 16 and 48 2θ°) (Yang, 2018), as well as characteristic peaks of nesquehonite and dypingite (**Fig. A-5.5a & b**). In few instances, the precipitated colloidal material was exclusively made of AMC showing no apparent peaks, with exception of the characteristic AMC curve peaking at 28 2θ° (**Fig. A-5.5c**) (Yang, 2018). Complementary analyses by FTIR displayed characteristic bands of water and carbonate confirming that the amorphous phase was a hydrated carbonate (**Fig. A-5.6**) (White et al., 2014).

AMC seems to form in a wide range of saturation values but is the first phase to precipitate at intermediate saturation (2.6 – 3.9; **Table 5.2**) states of $MgCO_3$, indicating possible high supersaturation rates upon mixing of the solutions. AMC could present multiple water contents and is likely to have different structural and morphological characteristics among various studies (e.g., White et al, 2014). Nesquehonite forms readily after the solution mixing under numerous mixing combinations, which was already observed in many experimental studies in the MgO–CO_2–H_2O system at low temperature (e.g., Hanchen et al., 2008; Ferrini et al., 2009). The co-existence of amorphous and crystalline phases is common to other similar systems such as $CaCO_3$ crystallization, where concomitant precipitation of amorphous calcium carbonate with crystalline phases is observed both in experimental studies (Kellermeier et al., 2013) and in nature (Jones 2017a, b). However, in serpentinization-related environments, hydrated Ca-carbonates are absent or rare, compared to hydrated Mg-carbonate minerals that characterize such environments.

Table 5.1. *Table of ionic concentration product of $MgCO_3$ in each crystallization cell.*

		Ionic Concentration Product (ICP) of $MgCO_3$ in each crystallization well							
		CO_3^{2-} [M]							
		0.01	0.02	0.05	0.1	0.2	0.5	1	2
Mg^{2+} [M]	0.01	10^{-4}	2 x 10^{-4}	5 x 10^{-4}	10^{-3}	2 x 10^{-3}	5 x 10^{-3}	10^{-2}	2 x 10^{-2}
	0.02	2 x 10^{-4}	4 x 10^{-4}	10^{-3}	2 x 10^{-3}	4 x 10^{-3}	10^{-2}	2 x 10^{-2}	4 x 10^{-2}
	0.05	5 x 10^{-4}	10^{-3}	2.5 x 10^{-3}	5 x 10^{-3}	10^{-2}	2.5 x 10^{-2}	5 x 10^{-2}	10^{-1}
	0.1	10^{-3}	2 x 10^{-3}	5 x 10^{-3}	10^{-2}	2 x 10^{-2}	5 x 10^{-2}	10^{-1}	2 x 10^{-1}
	0.2	2 x 10^{-3}	4 x 10^{-3}	10^{-2}	2 x 10^{-2}	4 x 10^{-2}	10^{-1}	2 x 10^{-1}	4 x 10^{-1}
	0.5	5 x 10^{-3}	10^{-2}	2.5 x 10^{-2}	5 x 10^{-2}	10^{-1}	2.5 x 10^{-1}	5 x 10^{-1}	1
	1	10^{-2}	2 x 10^{-2}	5 x 10^{-2}	10^{-1}	2 x 10^{-1}	5 x 10^{-1}	1	2
	2	2 x 10^{-2}	4 x 10^{-2}	10^{-1}	2 x 10^{-1}	4 x 10^{-1}	1	2	4

Table 5.2. *Table of calculated saturation of $MgCO_3$ from ICP and nesquehonite solubility in each crystallization cell.*

		Saturation value of $MgCO_3$							
		Na_2CO_3 [M]							
		0.01	0.02	0.05	0.1	0.2	0.5	1	2
$MgCl_2.6H_2O$ [M]	0.01	0.3	0.6	1.0	1.3	1.6	2.0	2.3	2.6
	0.02	0.6	0.9	1.3	1.6	1.9	2.3	2.6	2.9
	0.05	1.0	1.3	1.7	2.0	2.3	2.7	3.0	3.3
	0.1	1.3	1.6	2.0	2.3	2.6	3.0	3.3	3.6
	0.2	1.6	1.9	2.3	2.6	2.9	3.3	3.6	3.9
	0.5	2.0	2.3	2.7	3.0	3.3	3.7	4.0	4.3
	1	2.3	2.6	3.0	3.3	3.6	4.0	4.3	4.6
	2	2.6	2.9	3.3	3.6	3.9	4.3	4.6	4.9

Although the occurrence of AMC was supported by complementation of various techniques, its initial —most likely nano-scale— nucleation and its role as a possible precursor for crystalline Mg-carbonates remains unclear. Implementation of ultrahigh-resolution analyses and *in situ* observation of mixed solutions could be useful for the confirmation and description of transformation processes between AMC and crystalline Mg-carbonate phases.

The ratio of Mg/CO_3 seems to play a critical role in which phase will crystallize; wells with theoretically high ICP, and thus saturation values, are characterized by Mg/CO_3 ratios << or >> than 1, show no precipitation or less amount of synthesized phases. On the contrary, wells with Mg/CO_3 ~ 1 or 1, they tend to show more crystalline phases. The quantitative analysis could provide useful insights into the relationship between ICP (and IAP) and Mg/CO_3 and how it affects Mg-carbonate crystallization.

5.3.1.2 Relation of pH evolution and $MgCO_3$-bearing phases

The coupling of pH and phase monitoring with time allowed to explain the pH evolution based on the phase (trans) formation sequence. Out of many mixing combinations, we will follow the pH evolution and crystallization sequence of three mixing combinations with Mg/CO_3 = 1: i) low saturation (S = 0.9) and ICP values (4 x 10^{-4}) (**Fig. 5.4**), ii) intermediate saturation (S = 2.9) and ICP (4 x 10^{-2}) (**Fig. 5.5**), and iii) high saturation (S = 4.9) and ICP (4) (**Fig. 5.6**).

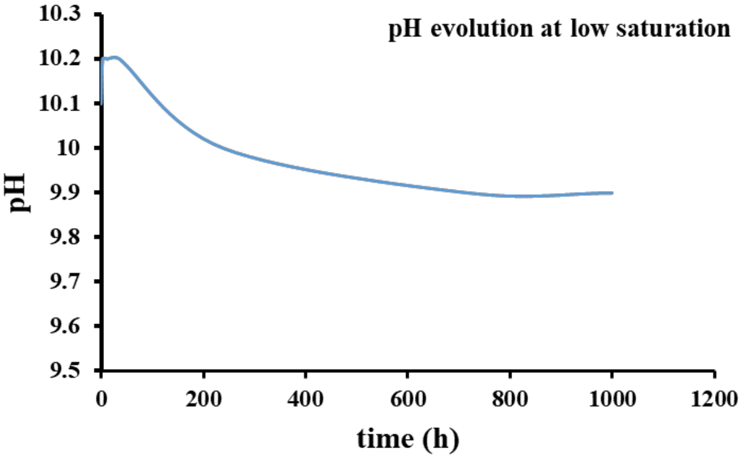

Figure 5.4. *Graph showing the pH evolution at low saturation in closed system.*

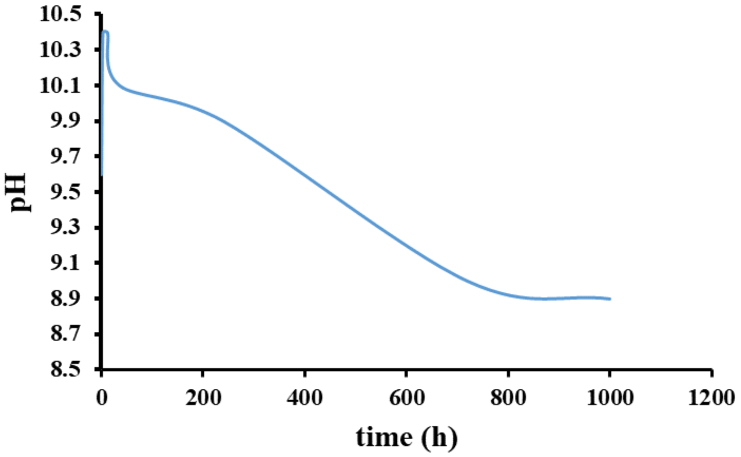

Figure 5.5. *Graph showing the pH evolution at intermediate saturation in closed system.*

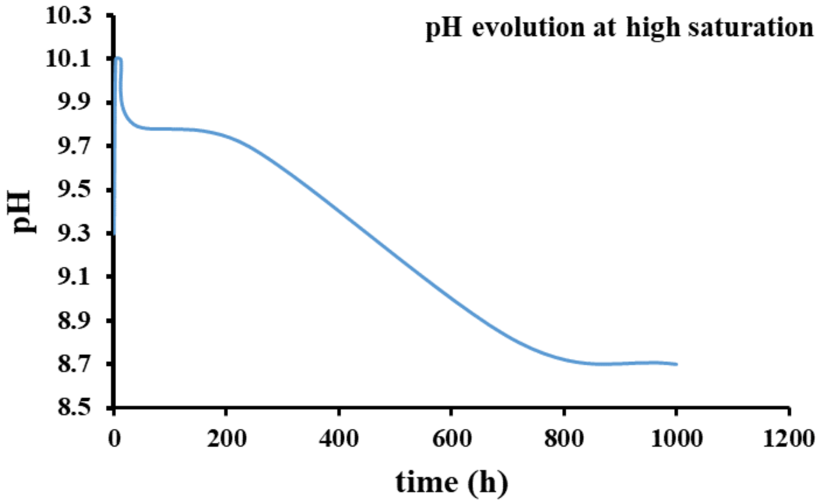

Figure 5.6. *Graph showing the pH evolution at high saturation in closed system.*

The initial colloid material can be composed of different phase assemblages based on the initial reactant concentration and pH (**Fig. 5.7a**), and afterward, it can transform into crystalline phases due to the Oswald ripening law. Under high OH^- concentration, brucite could be expected to form, yet the minimum pH for brucite supersaturation in natural alkaline waters was estimated to be 10.5 (e.g., Chavagnac et al., 2013). In most cases, our mixed solutions showed pH values < 10.5 and this could explain why no brucite was found in our experiments. In addition, Harrison et al. (2019) reported that brucite is constantly undersaturated during Mg-carbonate crystallization experiments.

At a low saturation state, the pH remained stable for c. 300 h, when it decreased from 10.1 to 9.8. Despite the slight pH decrease and the fact that the saturation value of $MgCO_3$ is close to 1, no precipitation occurred during the 1000 h of monitoring in this well. At intermediate saturation, the transformation into nesquehonite was observed when measured pH_0 of initial AMC formation was around 9.6 but gradually decreased slightly towards 9.5 in the next 50 min. After that, AMC began to dissolve with increasing pH reaching 10.3. At the same time, well–defined needles of nesquehonite crystals of several tens micrometers (1 µm – 50 mm) formed in the next 3 h (**Fig. 5.7b**). The nesquehonite growth continued for the next 190 h reaching crystal sizes up to 200 µm, followed by its transformation into dypingite that is in agreement with many experimental studies (e.g., Harrison et al., 2019). AMC was co-existed with the nesquehonite crystals, suggesting that the transformation probably was enhanced by a solvent-mediated mechanism. Nesquehonite initially forms with the rise of pH that may be caused by the dissolution of the initially formed AMC that consumes H^+ via the following reaction: $MgCO_3.2H_2O$ (AMC) + H^+ = Mg^{2+} + HCO_3^- + $2H_2O$.

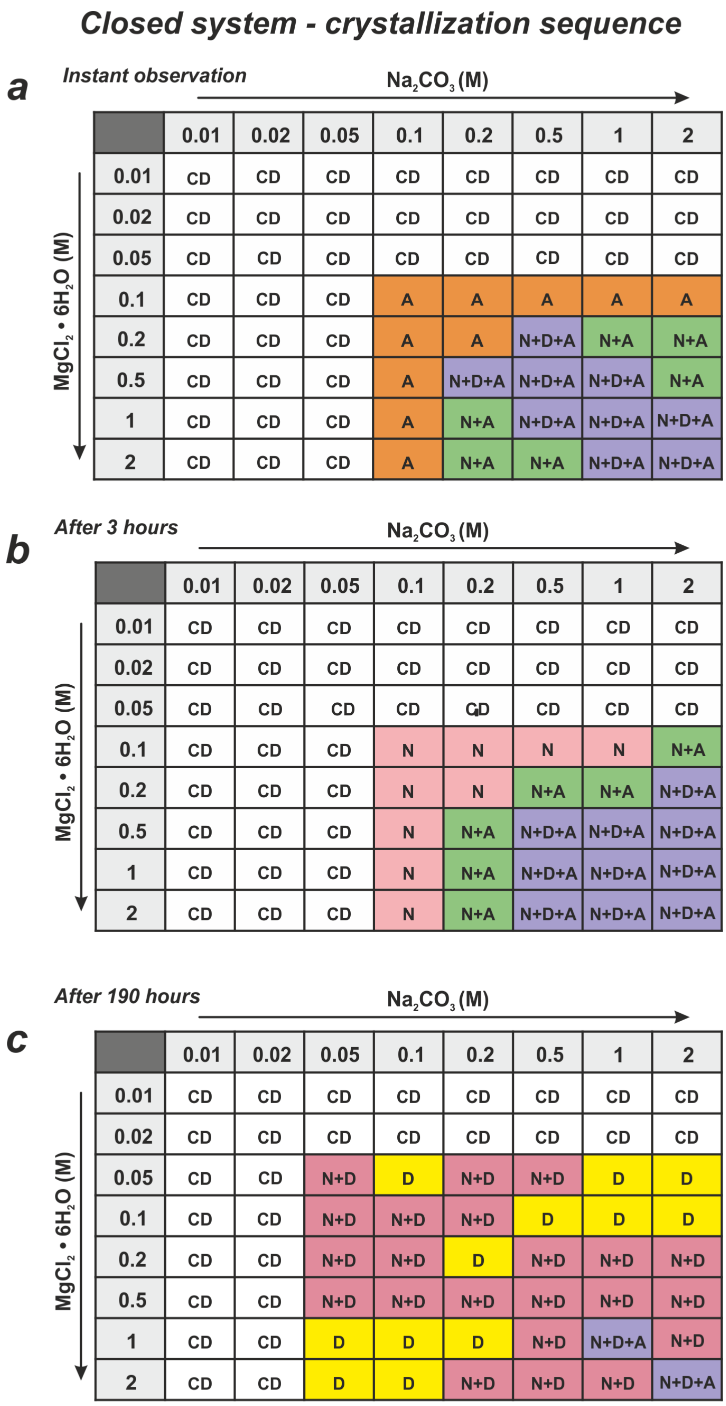

Closed system - crystallization sequence

a *Instant observation*

Na_2CO_3 (M) →

$MgCl_2 \cdot 6H_2O$ (M) ↓

	0.01	0.02	0.05	0.1	0.2	0.5	1	2
0.01	CD	CD	CD	CD	CD	CD	CD	CD
0.02	CD	CD	CD	CD	CD	CD	CD	CD
0.05	CD	CD	CD	CD	CD	CD	CD	CD
0.1	CD	CD	CD	A	A	A	A	A
0.2	CD	CD	CD	A	A	N+D+A	N+A	N+A
0.5	CD	CD	CD	A	N+D+A	N+D+A	N+D+A	N+A
1	CD	CD	CD	A	N+A	N+D+A	N+D+A	N+D+A
2	CD	CD	CD	A	N+A	N+A	N+D+A	N+D+A

b *After 3 hours*

Na_2CO_3 (M) →

$MgCl_2 \cdot 6H_2O$ (M) ↓

	0.01	0.02	0.05	0.1	0.2	0.5	1	2
0.01	CD	CD	CD	CD	CD	CD	CD	CD
0.02	CD	CD	CD	CD	CD	CD	CD	CD
0.05	CD	CD	CD	CD	CD	CD	CD	CD
0.1	CD	CD	CD	N	N	N	N	N+A
0.2	CD	CD	CD	N	N	N+A	N+A	N+D+A
0.5	CD	CD	CD	N	N+A	N+D+A	N+D+A	N+D+A
1	CD	CD	CD	N	N+A	N+D+A	N+D+A	N+D+A
2	CD	CD	CD	N	N+A	N+D+A	N+D+A	N+D+A

c *After 190 hours*

Na_2CO_3 (M) →

$MgCl_2 \cdot 6H_2O$ (M) ↓

	0.01	0.02	0.05	0.1	0.2	0.5	1	2
0.01	CD	CD	CD	CD	CD	CD	CD	CD
0.02	CD	CD	CD	CD	CD	CD	CD	CD
0.05	CD	CD	N+D	D	N+D	N+D	D	D
0.1	CD	CD	N+D	N+D	N+D	D	D	D
0.2	CD	CD	N+D	N+D	D	N+D	N+D	N+D
0.5	CD	CD	N+D	N+D	N+D	N+D	N+D	N+D
1	CD	CD	D	D	D	N+D	N+D+A	N+D
2	CD	CD	D	D	N+D	N+D	N+D	N+D+A

CD: Clear drop
N: Nesquehonite
D: Dypingite
A: Amorphous magnesium carbonate

Figure 5.7. *Grid of identified phases at i) the moment of mixing, ii) after 3 h, and iii) after 720 h. AMC turns into nesquehonite in the first 3 hours of the experiments, with nesquehonite transforming into dypingite within a priod of 720 h.*

After 36 h, the formation reaction of nesquehonite became predominant, and the pH dropped to 10 (**Fig. 5.5**). After 66 h of pH drop, solution pH was stable at around 10, indicating that nesquehonite was in quasi-equilibrium with the solution. The pH started decreasing again at 240 h, indicating that another phase started precipitating, following the dissolution of nesquehonite. Nesquehonite crystals were shortened and they showed dissolution at their edges, where new globular particles started to form (**Fig. 5.9a**). This result indicates the solvent-mediated transformation from nesquehonite to another phase occurred. From XRD pattern and Raman spectra, the newly occurring phase was dypingite.

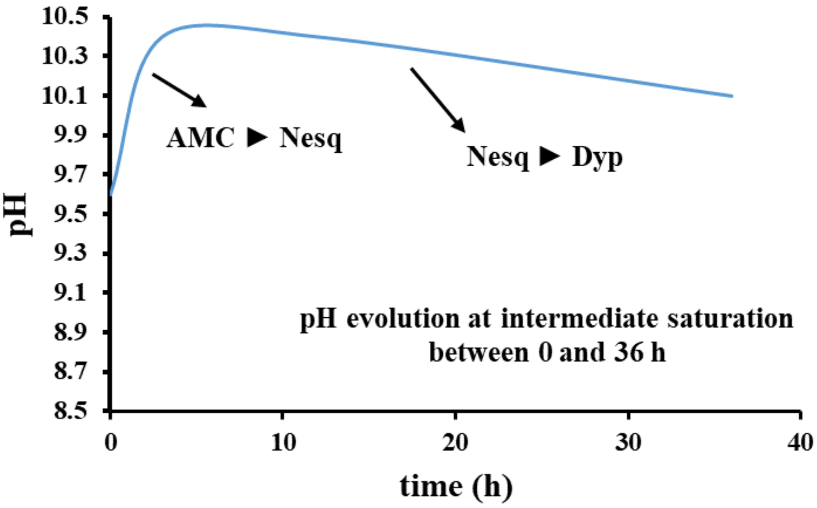

Figure 5.8. *Graph showing the pH evolution at intermediate saturation in closed system, zoomed at the first 40 h. Initially, the pH rises due to AMC dissolution and transformation into nesquehonite. Later, the pH decreases due to dypingite formation over dissolution of nesquehonite.*

Dypingite globules were polycrystalline particles with low crystallinity that eventually reorganized into the well-developed flakes (c. 50 – 100 μm) (**Fig. 5.9b**). The solution under decreasing pH conditions would be saturated with respect to nesquehonite, but supersaturated with dypingite. At the example of high supersaturation, the colloidal material was made of AMC + nesquehonite + dypingite. As in intermediate saturation, pH increased to 10.1 from the pH_0 = 9.3 in the next 12 h, probably due to AMC dissolution, and started decreasing after 36 h (pH = 9.8) to reach its lowest value (pH = 8.8) = and stabilize after 1000h.

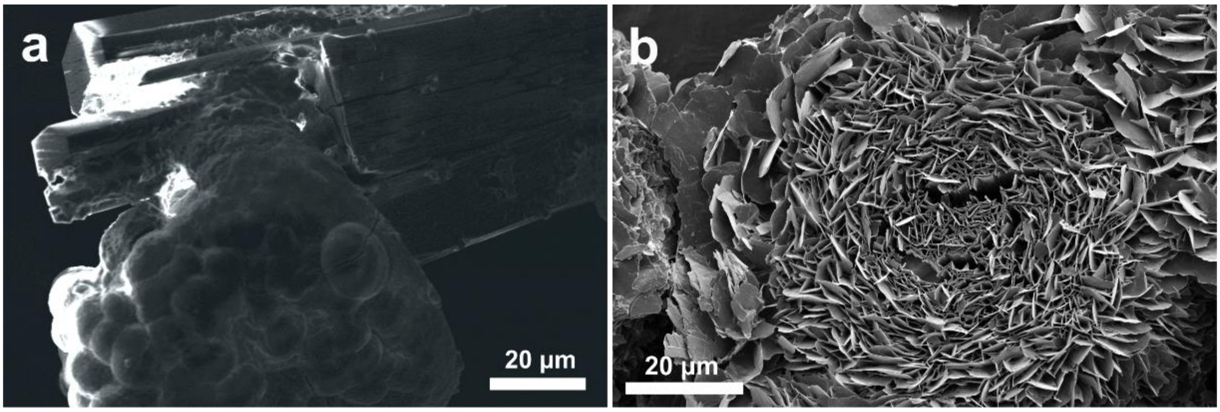

Figure 5.9. (a) *nesquehonite dissolution and dypingite precipitation at the dissolved surfaces after 240 h, and* ***(b)*** *well-defined flaky crystals of dypingite after 72o h after the initiation of the experiment.*

5.3.1.3 *Morphologies and textures of MgCO$_3$-bearing phases*

The morphology of nesquehonite is monotonous throughout the experiments and exbibit prismatic crystals, often with twinning, of variable sizes (Fig. **5.10a & b**). Dypingite exhibits spherical morphologies that are mostly composed of interlocking flakes that grow from small dypingite spheres (**Fig. 5.10 c & d**). The crystal or amorphous material sizes varying according to the initial reactant concentrations.

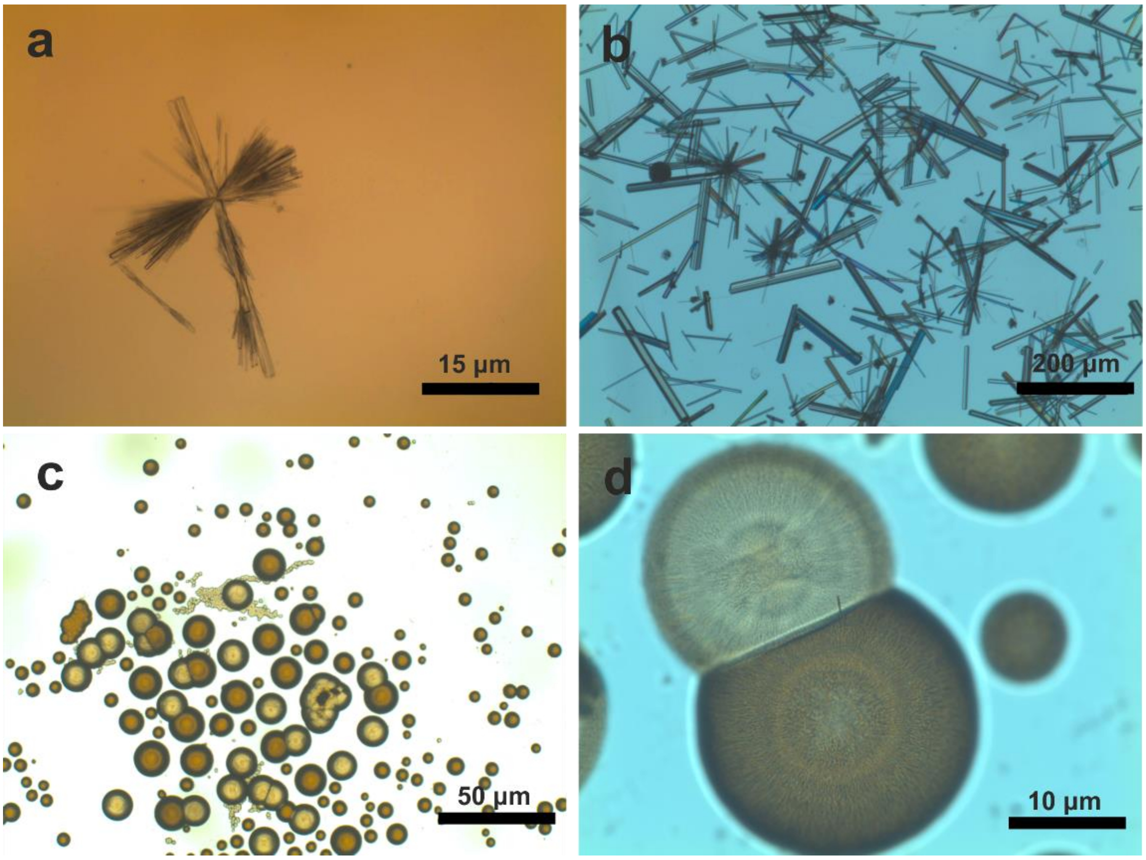

Figure 5.10. ***(a)*** *Nesquehonite crystals growing at low saturation and ICP values in the first 3 h of the experiment* ***(b)*** *Nesquehonite size and number of crystals is increased at intermediate saturation and Mg/CO$_3$ = 1* ***(c)*** *Dypingite spheres of variable sizes* ***(d)*** *Growth of dypingite clusters through aggregation that hinders the growth of one sphere and initiates a new nucleation for another sphere.*

At intermediate supersaturation (and Mg/CO$_3$ = 1), the crystal number increases compared to mixing combinations with the same ICP, but ratios $\neq$ 1. On the contrary, crystal sizes and crystal quality increase at solutions with Mg/CO$_3$ $\neq$ 1 and ICP $\leq 10^{-1}$. At high supersaturation and ICP $\geq$ 1, nesquehonite forms acicular morphologies made of prismatic or needle-like crystals with numerous dypingite spheres attached on its crystal surface. This observation could imply that nesquehonite could be forming before dypingite, though the amount of crystals is insufficient to confirm or discard this interpretation with a sufficient empirical basis.

5.3.2 Crystallization experiments in an open system

5.3.2.1 Crystallization sequence of $MgCO_3$-bearing phases

The second part of the crystallization experiments was conducted in an open system under present CO_2-rich conditions. The solutions were in contact with the atmosphere, and they were affected by CO_2 diffusion in the water and evaporation. These processes caused different crystallization sequences and morphologies compared to closed system experiments. **Figure 5.11** includes the phases observed after 3 h (**Fig. 5.11a**) and 72 h (**Fig. 5.11b**), The initial cloudy colloidal material is considered to have the same composition as in the closed system experiments. However, no AMC was identified in the evaporating wells, suggesting that the supply of CO_2 and an increase in saturation favors the formation of crystalline phases.

In open system experiments, evaporation and atmospheric CO_2 diffusion in the solution triggered different crystallization sequences and morphologies compared to the closed system experiments. Evaporation caused an increase in the values and rates of supersaturation, leading eventually to precipitation in all crystallization wells. Unlike closed system experiments, crystallization in clear drop wells started between 3 and 48 h after the initial mixing. The differentiation in the phases and textures is triggered after 3 h, where crystallization in the open system took place under increased values and rates of supersaturation in comparison to the closed system experiments. Under open-system conditions, crystallization was eventually triggered in every well due to the evaporation of the water that increased the solute concentration and led to supersaturation. In contrast, experiments in the closed system show no crystallization at initial concentrations of both reactants ≤ 0.02 M. The pH showed a decrease with time in every well, similar to low and high saturation pH evolution in closed system experiments (**Fig. A-5.4**). However, in this case, the atmospheric CO_2 diffusion in the solution is also contributing to the pH decline apart from carbonate precipitation.

As demonstrated in the previous section, the nesquehonite-dypingite transformation was initiated between 190 and 240 h in the closed system experiments. Unlike closed system experiments, nesquehonite did not transform into dypingite, as the solution was entirely evaporated after 120 h. This solvent-mediated process cannot take place due to the evaporation of the water. This could explain the persistence of nesquehonite in evaporative natural environments (Power et al., 2008). Moreover, this can support the assumption of Giampouras et al. (2020) that the observed pseudomorphs of dypingite replacing prismatic nesquehonite in Oman alkaline springs is due to occasional alkaline water influxes into pools that hosted evaporation-mediated nesquehonite.

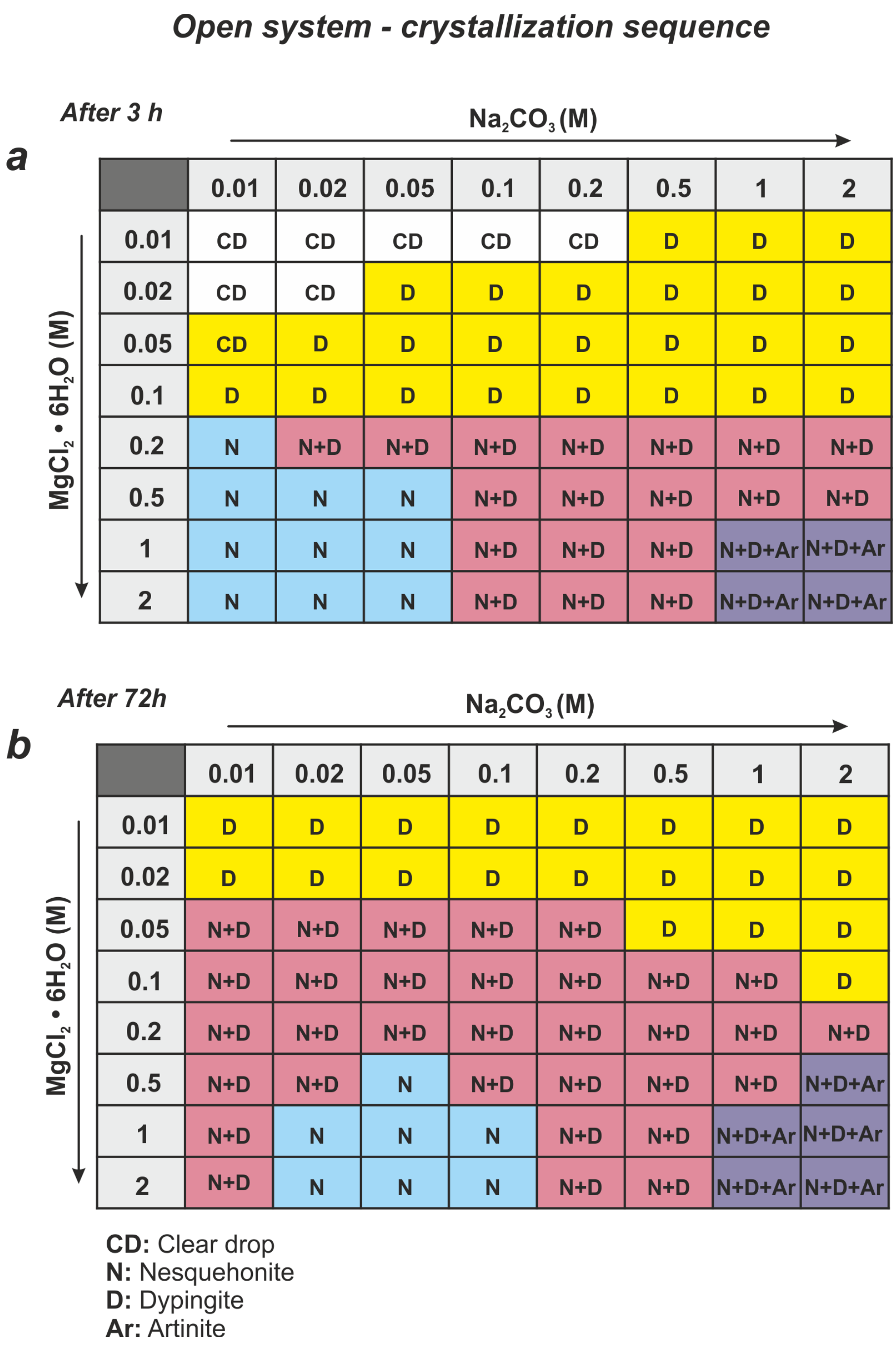

Open system - crystallization sequence

a

After 3 h

Na_2CO_3 (M) →

$MgCl_2 \bullet 6H_2O$ (M) ↓

	0.01	0.02	0.05	0.1	0.2	0.5	1	2
0.01	CD	CD	CD	CD	CD	D	D	D
0.02	CD	CD	D	D	D	D	D	D
0.05	CD	D	D	D	D	D	D	D
0.1	D	D	D	D	D	D	D	D
0.2	N	N+D	N+D	N+D	N+D	N+D	N+D	N+D
0.5	N	N	N	N+D	N+D	N+D	N+D	N+D
1	N	N	N	N+D	N+D	N+D	N+D+Ar	N+D+Ar
2	N	N	N	N+D	N+D	N+D	N+D+Ar	N+D+Ar

b

After 72h

Na_2CO_3 (M) →

$MgCl_2 \bullet 6H_2O$ (M) ↓

	0.01	0.02	0.05	0.1	0.2	0.5	1	2
0.01	D	D	D	D	D	D	D	D
0.02	D	D	D	D	D	D	D	D
0.05	N+D	N+D	N+D	N+D	N+D	D	D	D
0.1	N+D	N+D	N+D	N+D	N+D	N+D	N+D	D
0.2	N+D	N+D	N+D	N+D	N+D	N+D	N+D	N+D
0.5	N+D	N+D	N	N+D	N+D	N+D	N+D	N+D+Ar
1	N+D	N	N	N	N+D	N+D	N+D+Ar	N+D+Ar
2	N+D	N	N	N	N+D	N+D	N+D+Ar	N+D+Ar

CD: Clear drop
N: Nesquehonite
D: Dypingite
Ar: Artinite

Figure 5.11. *Grid of identified phases after i) 3 h, and iii) after 72 h in open system. Variable amounts of nesquehonite, dypingite and artinite form eventually in every mixing well until the total evaporation of the water.*

At low supersaturation, dypingite is the predominant phase, with nesquehonite forming at initial [Mg] ≥ 0.2 M (**Fig. 5.11**) This implies the importance of Mg concentration in order nucleation of nesquehonite to be triggered, while dypingite precipitates independently of the initial Mg concentration of the evaporating solutions. As Mg and CO_3 concentration increases during evaporation and constant CO_2 supply from the atmosphere, the excess in carbonic species due to CO_2 diffusion favors dypingite formation over nesquehonite. This could explain the tendency of dypingite to form at equilibrium with the atmosphere, and its absence at low and intermediate saturation in the closed system experiments (Harrison et al., 2019). Ballirano et al. (2010) reported that nesquehonite releases CO_2 molecules during its transformation into dypingite, suggesting that CO_2-rich conditions can favor dypingite formation. At a low saturation state of $MgCO_3$ ($S < 1$), Mg concentration does not exceed 0.16 M for 120 µL of the solution during evaporation. This observation is in agreement with our closed system experiments that demonstrated no nesquehonite precipitation under such conditions. At high supersaturation, artinite was identified co-precipitating with nesquehonite. This confirms the findings from some natural environments, where nesquehonite and artinite co-exist in evaporating environments (Klopporge et al., 2003). Similar to dypingite, the CO_2-rich environment and the evaporation rates could play a key role in artinite formation as it was not observed in the closed system crystallization experiments.

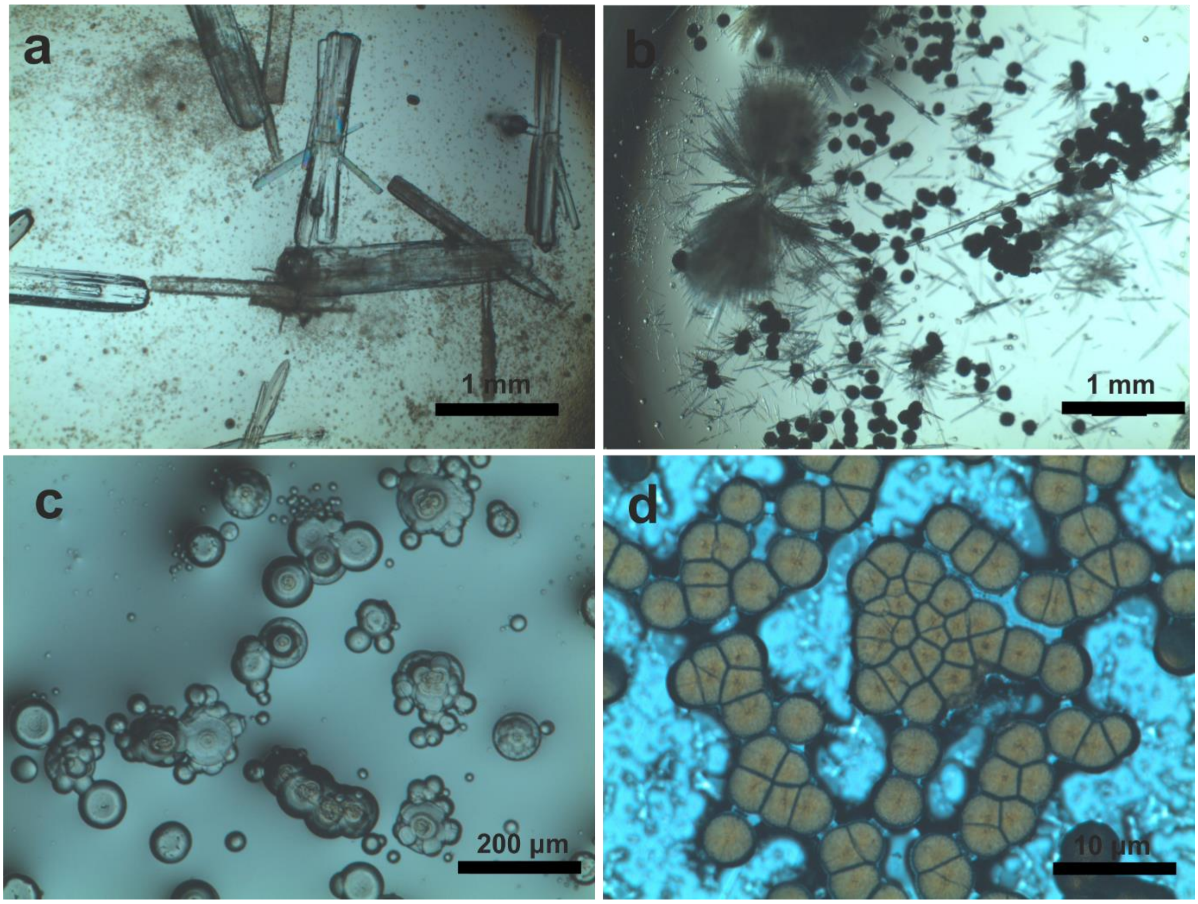

Figure 5.12. *Textures of the occurring phases in open system crystallization experiments:* ***(a)*** *Nesquehonite crystals growing along with dypingite globules at high initial Mg concentrations* ***(b)*** *Needles of artinite forming double fan morphologies at high initial reactan concentrations (high initial ICP and S)* ***(c)*** *Dypingite clusters made of variable size spheres in wells with intermediate initial S values* ***(d)*** *Cluster of dypingite spheres at wells with low initial Mg concentration.*

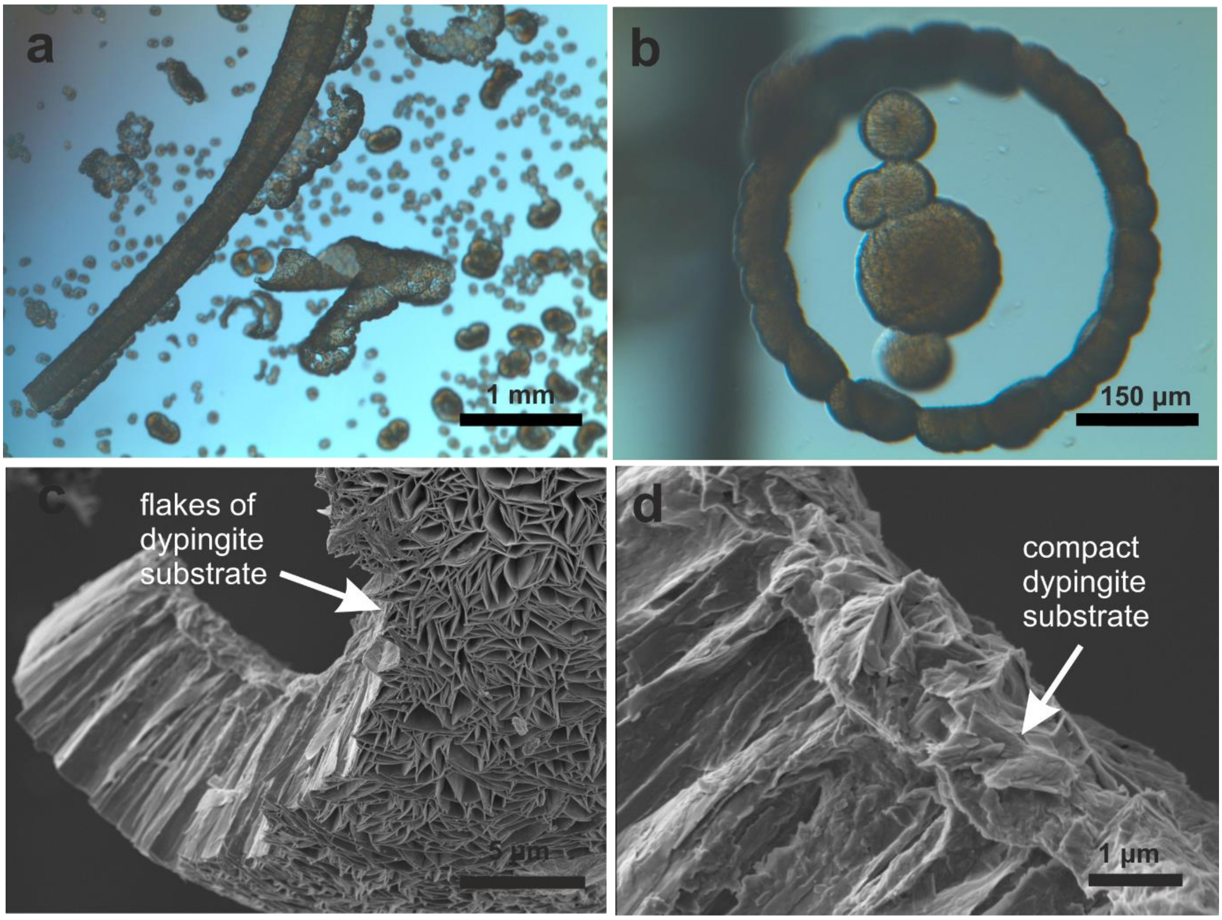

Figure 5.13. *Textures of dypingites in open system crystallization experiments:* ***(a)*** *Dypingite forming long chain-like structures* ***(b)*** *Aggregation of dypingite in a circular orientation generates perfect ring structures* ***(c)*** *SEM image of the chain like dypingite. The exterior part of the chain is made of interlocking flakes that grow vertical on a compact dypingite substrate* ***(d)*** *The interior part of chain-like dypingite that is composed of compacted flakes and acts as substrate for the flaky dypingite exterior part.*

5.3.2.1 Morphologies and textures of the occurring $MgCO_3$-bearing phases

The morphologies of nesquehonite crystals are similar to those from the closed system experiments (**Fig. 5.12a**); however, the crystals demonstrate poorer quality than those in closed system experiments. Where present, artinite occurs as acicular, double fan morphologies made of needles along with nesquehonite (**Fig 5.12b**). Unlike nesquehonite, dypingite exhibits a wide range of morphologies compared to those produced in the closed system experiments. In most cases, multiple growth stages can be observed at spherical crystals of dypingite (**Fig. 5.12c & d**) that indicate different nucleation events during evaporation.

Moreover, many peculiar morphologies of dypingite occur due to crystal aggregation, including chain-like structures, rings, and clusters (**Fig. 5.13a & b**). The chain-like dypingite has a hemispherical structure that exhibits the common interlocking flakes of dypingite at the exterior part (**Fig 5. 13c**), and a compact dypingite substrate in the interior part (**Fig 5.13d**). This interior part is most likely formed around initial Mg-CO_3-bearing nuclei, while the well-defined dypingite flakes of the exterior part grow at a later stage due to evaporation. The chain-like morphologies form after aggregation of dypingite hemispheres triggered by continuous supersaturation due to the evaporation of the solution. The rings exhibit similar to chain-like structures; the difference is on the crystal aggregation process that followed a circular growth orientation that led to the ring-like shape.

5.4 Appendix

pH$_0$ Instant

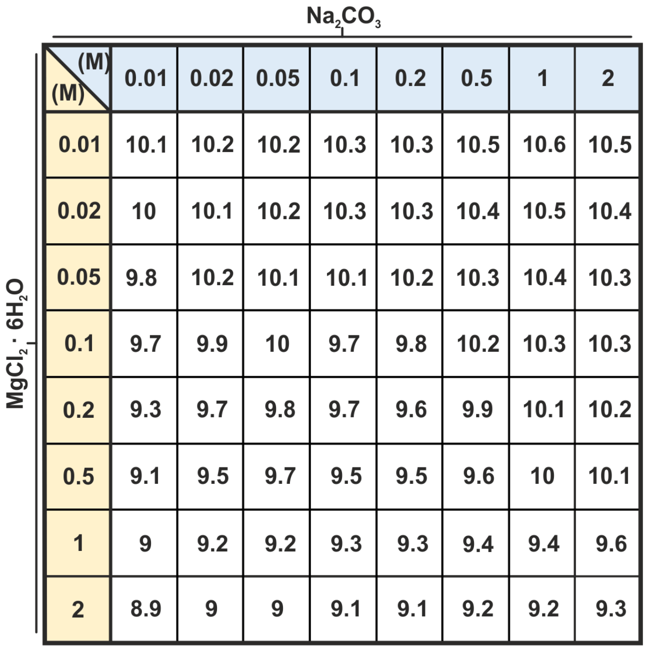

MgCl$_2$ · 6H$_2$O (M) \ Na$_2$CO$_3$ (M)	0.01	0.02	0.05	0.1	0.2	0.5	1	2
0.01	10.1	10.2	10.2	10.3	10.3	10.5	10.6	10.5
0.02	10	10.1	10.2	10.3	10.3	10.4	10.5	10.4
0.05	9.8	10.2	10.1	10.1	10.2	10.3	10.4	10.3
0.1	9.7	9.9	10	9.7	9.8	10.2	10.3	10.3
0.2	9.3	9.7	9.8	9.7	9.6	9.9	10.1	10.2
0.5	9.1	9.5	9.7	9.5	9.5	9.6	10	10.1
1	9	9.2	9.2	9.3	9.3	9.4	9.4	9.6
2	8.9	9	9	9.1	9.1	9.2	9.2	9.3

t$_1$ = 3 h

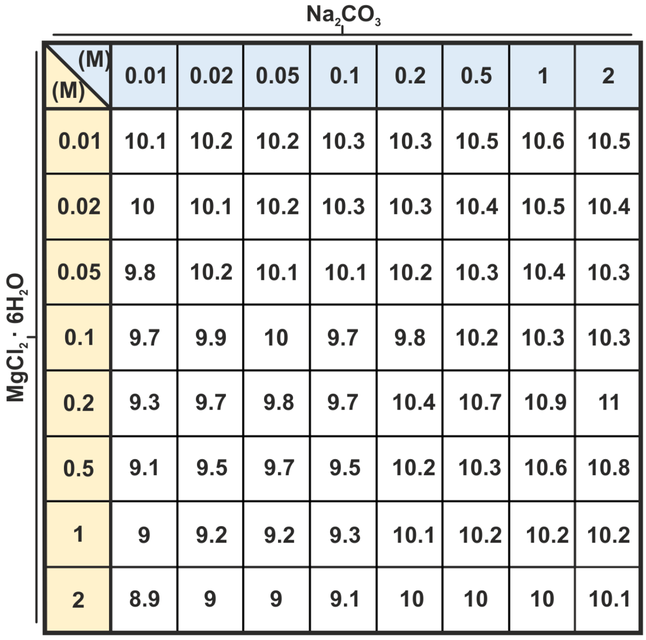

MgCl$_2$ · 6H$_2$O (M) \ Na$_2$CO$_3$ (M)	0.01	0.02	0.05	0.1	0.2	0.5	1	2
0.01	10.1	10.2	10.2	10.3	10.3	10.5	10.6	10.5
0.02	10	10.1	10.2	10.3	10.3	10.4	10.5	10.4
0.05	9.8	10.2	10.1	10.1	10.2	10.3	10.4	10.3
0.1	9.7	9.9	10	9.7	9.8	10.2	10.3	10.3
0.2	9.3	9.7	9.8	9.7	10.4	10.7	10.9	11
0.5	9.1	9.5	9.7	9.5	10.2	10.3	10.6	10.8
1	9	9.2	9.2	9.3	10.1	10.2	10.2	10.2
2	8.9	9	9	9.1	10	10	10	10.1

Figure A-5.1. *Grid of pH values of mixed solutions at the time of mixing (pH$_0$) and after 3 h of the initiation of closed system crystallization experiments.*

After t_2 = 12 h

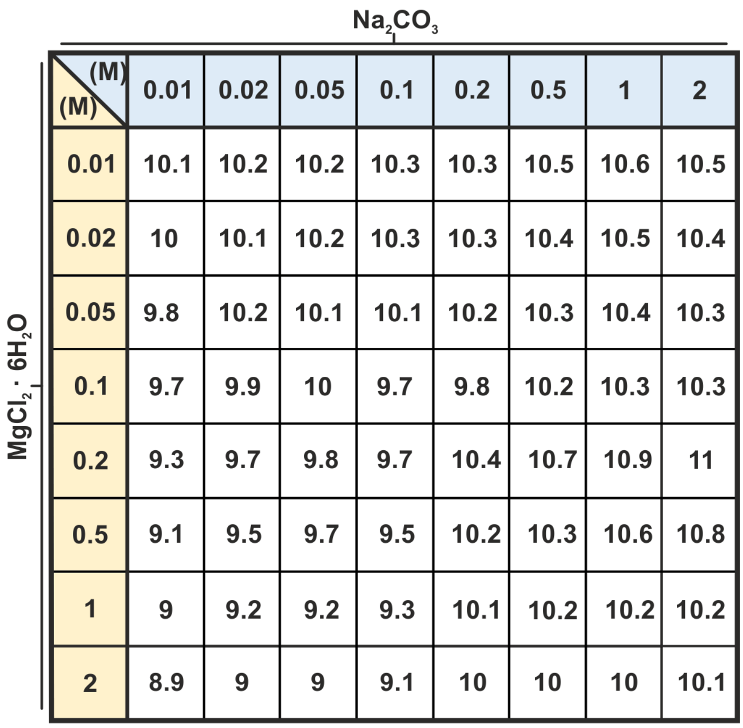

Na_2CO_3

$MgCl_2 \cdot 6H_2O$

(M) (M)	0.01	0.02	0.05	0.1	0.2	0.5	1	2
0.01	10.1	10.2	10.2	10.3	10.3	10.5	10.6	10.5
0.02	10	10.1	10.2	10.3	10.3	10.4	10.5	10.4
0.05	9.8	10.2	10.1	10.1	10.2	10.3	10.4	10.3
0.1	9.7	9.9	10	9.7	9.8	10.2	10.3	10.3
0.2	9.3	9.7	9.8	9.7	10.4	10.7	10.9	11
0.5	9.1	9.5	9.7	9.5	10.2	10.3	10.6	10.8
1	9	9.2	9.2	9.3	10.1	10.2	10.2	10.2
2	8.9	9	9	9.1	10	10	10	10.1

After t_3 = 36 h

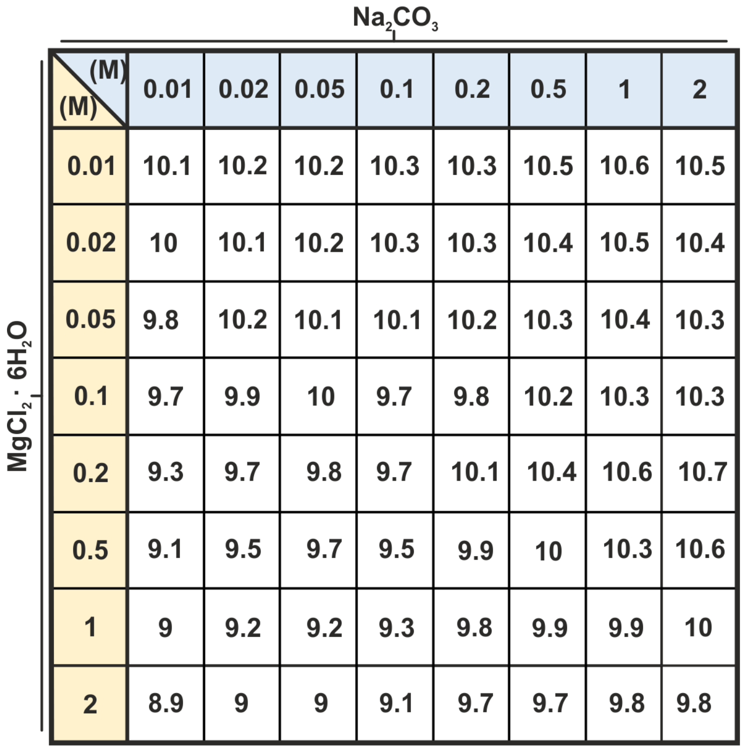

Na_2CO_3

$MgCl_2 \cdot 6H_2O$

(M) (M)	0.01	0.02	0.05	0.1	0.2	0.5	1	2
0.01	10.1	10.2	10.2	10.3	10.3	10.5	10.6	10.5
0.02	10	10.1	10.2	10.3	10.3	10.4	10.5	10.4
0.05	9.8	10.2	10.1	10.1	10.2	10.3	10.4	10.3
0.1	9.7	9.9	10	9.7	9.8	10.2	10.3	10.3
0.2	9.3	9.7	9.8	9.7	10.1	10.4	10.6	10.7
0.5	9.1	9.5	9.7	9.5	9.9	10	10.3	10.6
1	9	9.2	9.2	9.3	9.8	9.9	9.9	10
2	8.9	9	9	9.1	9.7	9.7	9.8	9.8

Figure A-5.2. *Grid of pH values of mixed solutions after 12 and 36 h of the initiation of closed system crystallization experiments.*

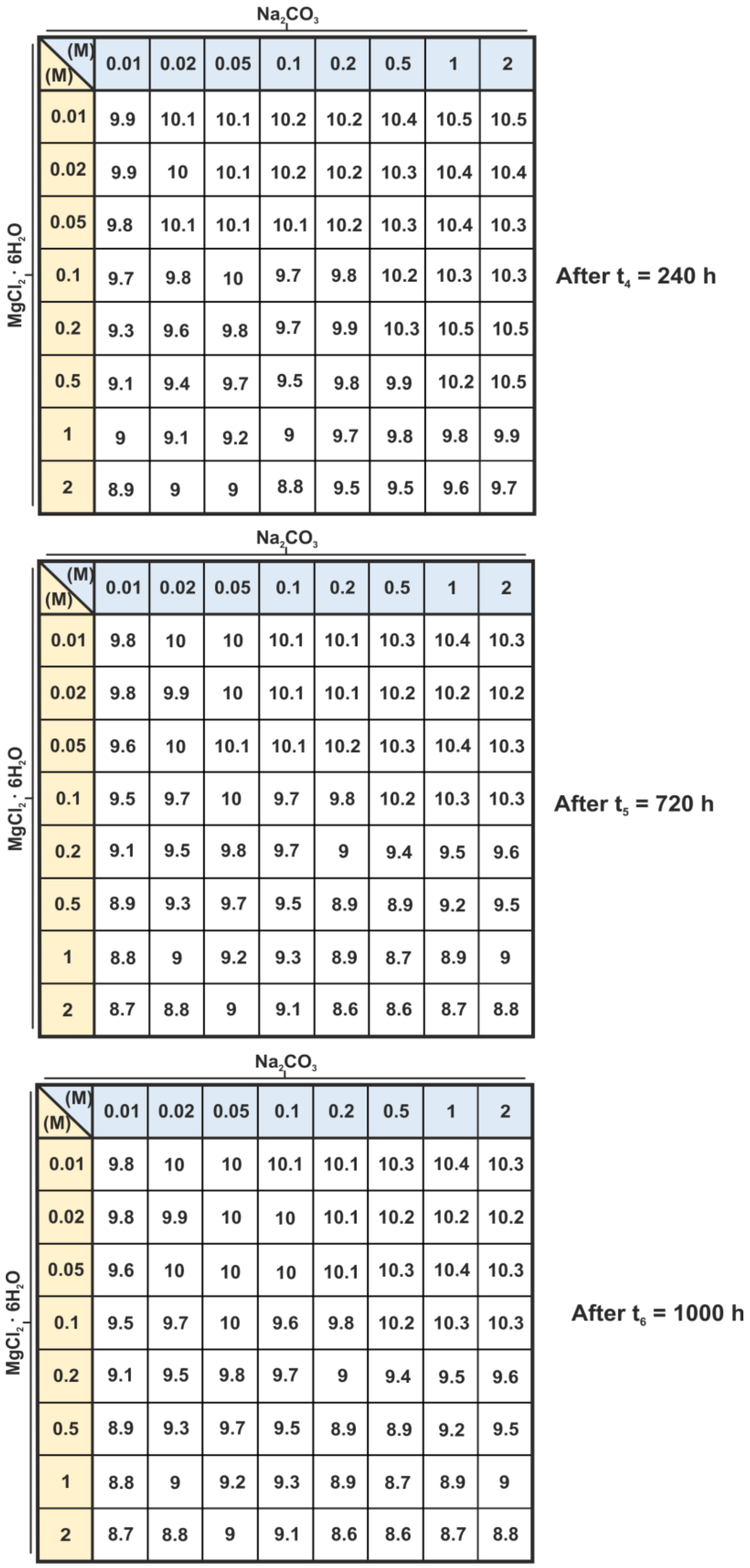

Na_2CO_3

$MgCl_2 \cdot 6H_2O$

(M) \ (M)	0.01	0.02	0.05	0.1	0.2	0.5	1	2
0.01	9.9	10.1	10.1	10.2	10.2	10.4	10.5	10.5
0.02	9.9	10	10.1	10.2	10.2	10.3	10.4	10.4
0.05	9.8	10.1	10.1	10.1	10.2	10.3	10.4	10.3
0.1	9.7	9.8	10	9.7	9.8	10.2	10.3	10.3
0.2	9.3	9.6	9.8	9.7	9.9	10.3	10.5	10.5
0.5	9.1	9.4	9.7	9.5	9.8	9.9	10.2	10.5
1	9	9.1	9.2	9	9.7	9.8	9.8	9.9
2	8.9	9	9	8.8	9.5	9.5	9.6	9.7

After t_4 = 240 h

Na_2CO_3

$MgCl_2 \cdot 6H_2O$

(M) \ (M)	0.01	0.02	0.05	0.1	0.2	0.5	1	2
0.01	9.8	10	10	10.1	10.1	10.3	10.4	10.3
0.02	9.8	9.9	10	10.1	10.1	10.2	10.2	10.2
0.05	9.6	10	10.1	10.1	10.2	10.3	10.4	10.3
0.1	9.5	9.7	10	9.7	9.8	10.2	10.3	10.3
0.2	9.1	9.5	9.8	9.7	9	9.4	9.5	9.6
0.5	8.9	9.3	9.7	9.5	8.9	8.9	9.2	9.5
1	8.8	9	9.2	9.3	8.9	8.7	8.9	9
2	8.7	8.8	9	9.1	8.6	8.6	8.7	8.8

After t_5 = 720 h

Na_2CO_3

$MgCl_2 \cdot 6H_2O$

(M) \ (M)	0.01	0.02	0.05	0.1	0.2	0.5	1	2
0.01	9.8	10	10	10.1	10.1	10.3	10.4	10.3
0.02	9.8	9.9	10	10	10.1	10.2	10.2	10.2
0.05	9.6	10	10	10	10.1	10.3	10.4	10.3
0.1	9.5	9.7	10	9.6	9.8	10.2	10.3	10.3
0.2	9.1	9.5	9.8	9.7	9	9.4	9.5	9.6
0.5	8.9	9.3	9.7	9.5	8.9	8.9	9.2	9.5
1	8.8	9	9.2	9.3	8.9	8.7	8.9	9
2	8.7	8.8	9	9.1	8.6	8.6	8.7	8.8

After t_6 = 1000 h

Figure A-5.3. *Grid of pH values of mixed solutions after 240, 720, and 1000 h of the initiation of closed system crystallization experiments.*

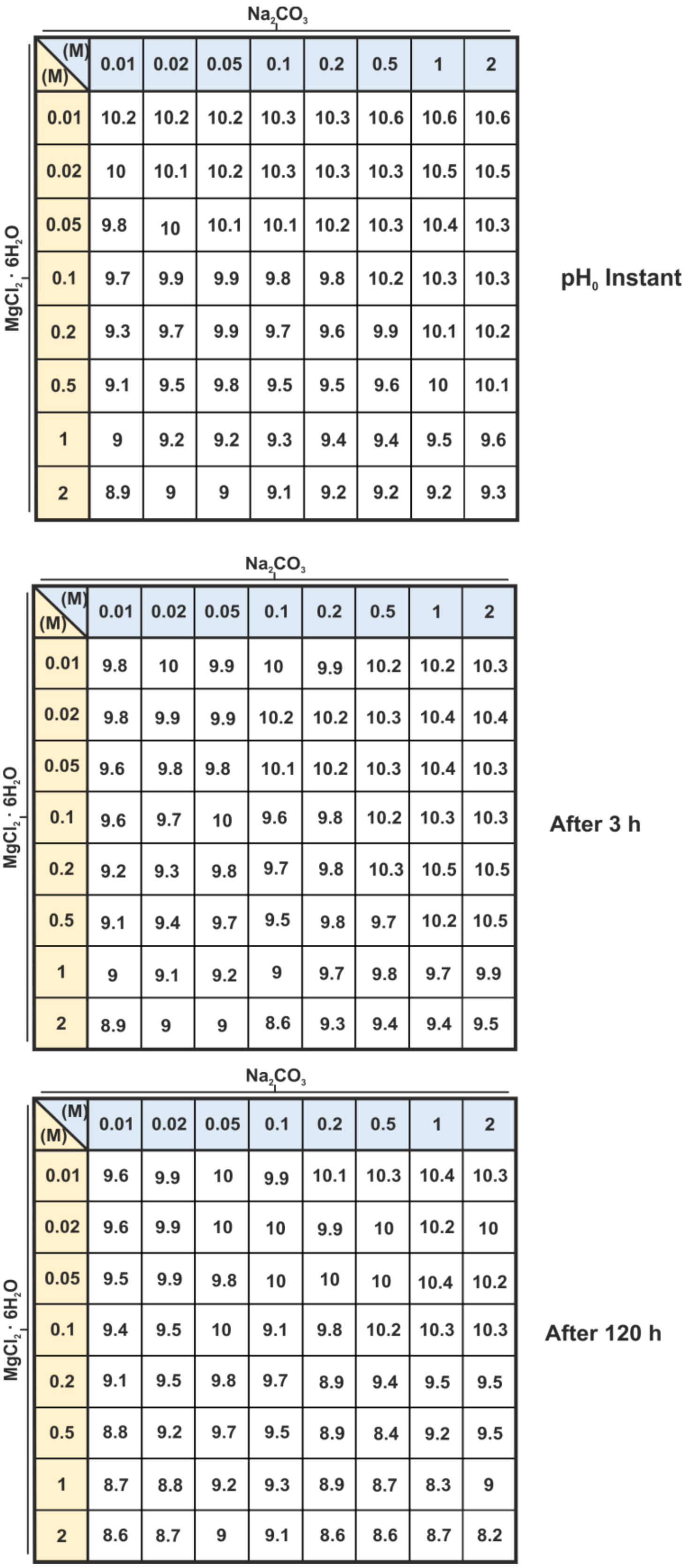

pH_0 Instant

$MgCl_2 \cdot 6H_2O$ (M) \ Na_2CO_3 (M)	0.01	0.02	0.05	0.1	0.2	0.5	1	2
0.01	10.2	10.2	10.2	10.3	10.3	10.6	10.6	10.6
0.02	10	10.1	10.2	10.3	10.3	10.3	10.5	10.5
0.05	9.8	10	10.1	10.1	10.2	10.3	10.4	10.3
0.1	9.7	9.9	9.9	9.8	9.8	10.2	10.3	10.3
0.2	9.3	9.7	9.9	9.7	9.6	9.9	10.1	10.2
0.5	9.1	9.5	9.8	9.5	9.5	9.6	10	10.1
1	9	9.2	9.2	9.3	9.4	9.4	9.5	9.6
2	8.9	9	9	9.1	9.2	9.2	9.2	9.3

After 3 h

$MgCl_2 \cdot 6H_2O$ (M) \ Na_2CO_3 (M)	0.01	0.02	0.05	0.1	0.2	0.5	1	2
0.01	9.8	10	9.9	10	9.9	10.2	10.2	10.3
0.02	9.8	9.9	9.9	10.2	10.2	10.3	10.4	10.4
0.05	9.6	9.8	9.8	10.1	10.2	10.3	10.4	10.3
0.1	9.6	9.7	10	9.6	9.8	10.2	10.3	10.3
0.2	9.2	9.3	9.8	9.7	9.8	10.3	10.5	10.5
0.5	9.1	9.4	9.7	9.5	9.8	9.7	10.2	10.5
1	9	9.1	9.2	9	9.7	9.8	9.7	9.9
2	8.9	9	9	8.6	9.3	9.4	9.4	9.5

After 120 h

$MgCl_2 \cdot 6H_2O$ (M) \ Na_2CO_3 (M)	0.01	0.02	0.05	0.1	0.2	0.5	1	2
0.01	9.6	9.9	10	9.9	10.1	10.3	10.4	10.3
0.02	9.6	9.9	10	10	9.9	10	10.2	10
0.05	9.5	9.9	9.8	10	10	10	10.4	10.2
0.1	9.4	9.5	10	9.1	9.8	10.2	10.3	10.3
0.2	9.1	9.5	9.8	9.7	8.9	9.4	9.5	9.5
0.5	8.8	9.2	9.7	9.5	8.9	8.4	9.2	9.5
1	8.7	8.8	9.2	9.3	8.9	8.7	8.3	9
2	8.6	8.7	9	9.1	8.6	8.6	8.7	8.2

Figure A-5.4. *Grid of pH values of mixed solutions at the time of mixing (pH_0) and after 3 and 120 h of the initiation of closed system crystallization experiments.*

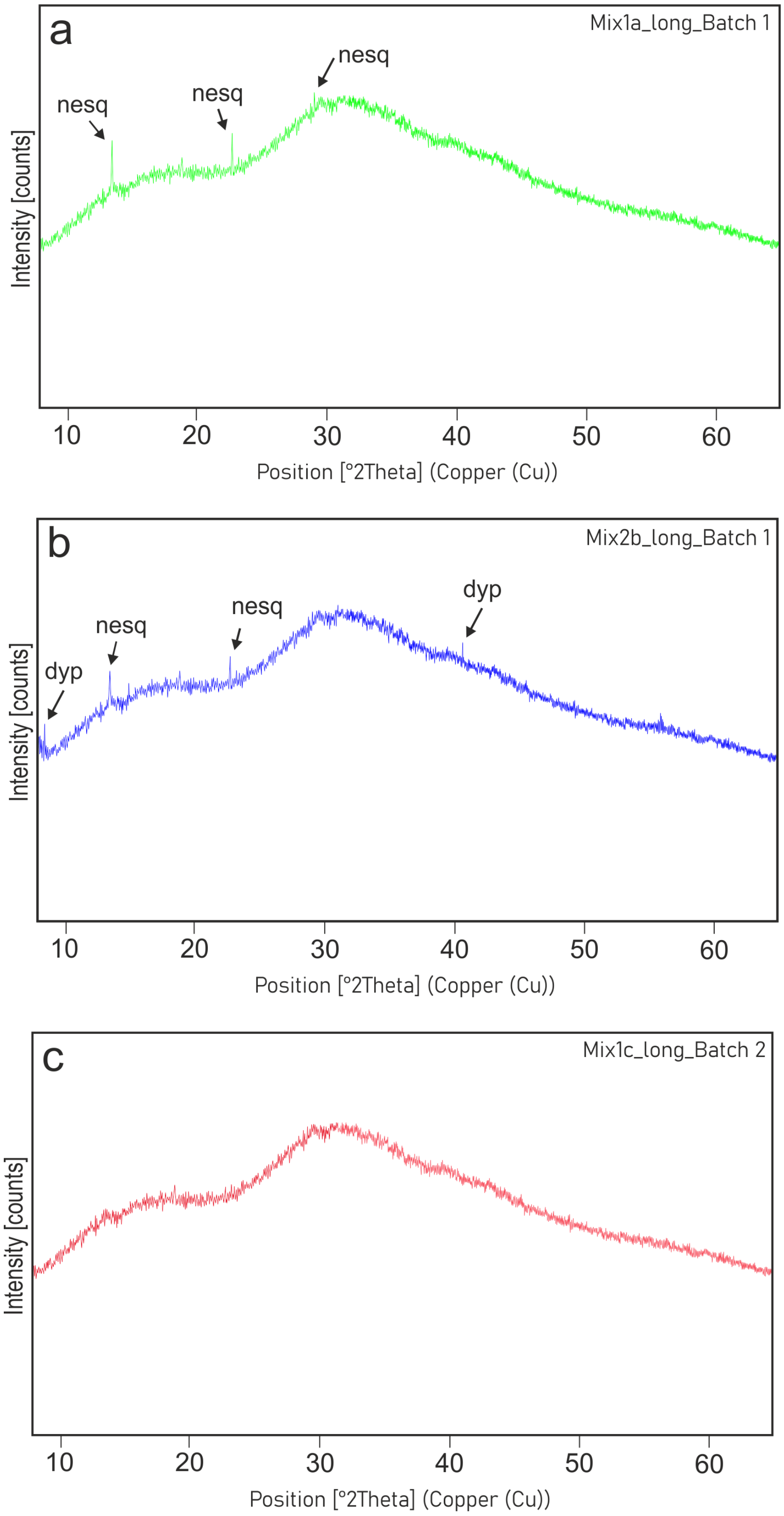

Figure A-5.5. *XRD patterns showing phases different phases in the instantly precipitated colloidal material:* ***(a)*** *AMC + nesquehonite (nesq),* ***(b)*** *AMC + nesquehonite +dypingite (dyp), and* ***(c)*** *AMC. The broad peaks in the diffractograms could be indicative of an amorphous phase.*

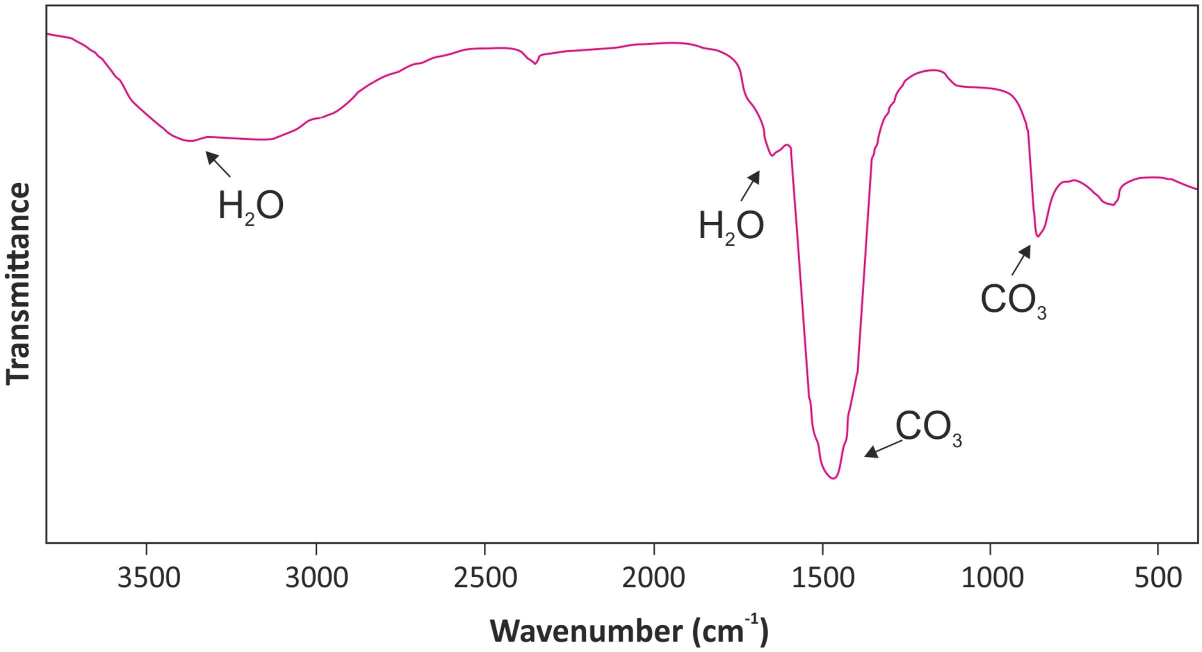

Figure A-5.5. *Fourier transform infrared (FTIR) spectra for AMC from the instantly precipitated colloidal material.*

Table A-5.1. *pH values of each initial solution used for the experiments.*

pH of initial solutions		
[M]	$MgCl_2.6H_2O$	Na_2CO_3
0.01	6.1	10.6
0.02	6.1	10.7
0.05	6.2	10.9
0.1	6.3	11
0.2	6.2	11.1
0.5	6.5	11.1
1	6.5	11.3
2	6.7	11.2

Table A-5.2. *Ionic concentration product, saturation of $MgCO_3$*, K_{sp} of nesquehonite (from Harrison et al., 2019), and SI value of nesquehonite form PHREEQC for all isotonic mixing combinations.

Mg^{2+} [M]	CO_3^{2-} [M]	ICP	K_{sp}^{nesq}	S = ICP / K_{sp}^{nesq}	SI^{nesq} - PHREEQC
0.01	0.01	10^{-4}	$10^{-5.06}$	0.30	-0.05
0.02	0.02	4×10^{-4}	$10^{-5.06}$	0.90	0.33
0.05	0.05	2.5×10^{-3}	$10^{-5.06}$	1.70	0.79
0.1	0.1	10^{-2}	$10^{-5.06}$	2.30	1.13
0.2	0.2	4×10^{-2}	$10^{-5.06}$	2.90	1.47
0.5	0.5	2.5×10^{-1}	$10^{-5.06}$	3.70	1.91
1	1	1	$10^{-5.06}$	4.30	2.28
2	2	4	$10^{-5.06}$	4.90	2.68

Part III

CONCLUSIONS AND PERSPECTIVES

6 Conclusions and Perspectives

6.1 Conclusions

This thesis provides new insights into the derived from the study of natural systems and laboratory experiments of carbonation of peridotites in forearc settings and the fate of serpentinite-hosted carbon during high-pressure metamorphism based on natural examples from ophiolites and metamorphic terranes and improves our understanding of the role of hydrated peridotites for deep carbon cycling in subduction zones.

Through the detailed study of the chemical profiles of alkaline waters and the mineralogy and textures of the occurring precipitates, the present research provides new information on i) how water composition, mixing, and mineral precipitation and textures co-evolve in serpentinization-driven alkaline springs in the Oman Ophiolite, and ii) the geochemical processes in alkaline spring sites in subcontinental mantle peridotites, and associated mineralizations formed by the interaction between hyperalkaline fluids and river waters in Ronda peridotite massifs. Furthermore, the results from crystallization experiments provide new constraints on the nucleation, growth, and transformation processes regarding the formation of hydrated Mg-carbonates.

Interaction between meteoric water and ultramafic rocks in the Oman Ophiolite generates waters of variable physicochemical characteristics. The discharge of these waters forms complex hydrological networks of streams and pools where waters mix, undergo evaporation, and take up atmospheric CO_2, leading to the generation of a broad diversity of mineral phases and textures. Coupling of textural and mineralogical studies with chemical analysis of waters allowed the estimation of the saturation state of a wide range of minerals and correlate them to the different water and precipitate types of the Oman spring sites. The systematic downstream—sampling of numerous pools in individual spring sites, and the detailed documentation of mineral assemblages and crystal morphologies, enabled to investigate the impact of water geochemistry and hydrodynamics on mineral precipitation and textures. Three types of waters were classified in the spring sites: Mg-type (mildly alkaline, $7.9 < pH < 9.5$; Mg^{2+}–HCO_3^--rich waters), Ca-type (hyperalkaline, $pH > 11.6$; Ca^{2+}–OH^--rich waters), and Mix-type waters (alkaline to hyperalkaline, $9.6 < pH < 11.5$; with intermediate chemical composition) formed by mixing of Mg-type and Ca-type.

The mineralogy and textures of different types of solid precipitates and deposits mostly record the local physicochemical characteristics of water, the hydrodynamic regime, and the evaporation rate of the spring sites. The identification of hydrated magnesium (hydroxy-) carbonates (e.g., nesquehonite and dypingite) in Oman Mg-type waters confirms the occurrence of weathering-related carbon mineralization observed in other environments (e.g., hydromagnesite playas and serpentinite mine tailings). Nesquehonite forms via evaporation and transforms into dypingite and hydromagnesite under local CO_2-rich conditions. In Ca-type waters, coupled atmospheric CO_2 uptake and evaporation trigger the formation of calcitic crystalline crusts at the air-water interface, while the instantaneous mixing of Mg-type and Ca-type waters into a single Mix-water pool leads to the formation of aragonite-dominated and brucite-bearing crystalline crusts. In this type of Mix-water pools, acicular aragonite acts as a substrate for the subsequent growth of brucite and calcite crystals. Throughout the spring sites, the Mix-type water pools also host massive aragonite-dominated deposits because the high Mg/Ca of these waters favors the formation of aragonite over calcite. The hydrodynamics of water mixing controls the occurrence of brucite, which is commonly restricted to mixing zones with a steady mixing rate and slow water flow. These low energy environments provide a constant supply of Mg^{2+} and OH^{-} for brucite formation and prevent the mobilization and dissolution of brucite.

Crystal morphologies record the effect on the values of supersaturation and supersaturation rates in the pools due to mixing processes, evaporation, and CO_2 uptake. In Ca-type waters, CO_2 uptake and evaporation dictate the supersaturation rate in the waters, and thus, the textural characteristics of calcite in crystalline crusts and rock coatings, where it mainly exhibits large euhedral crystals of high-quality. Textural evolution of aragonite in a single sample, from initial crystalline sheaves to spheroidal shapes in flocculent material, highlights the different supersaturation rates of calcium carbonate crystallization in Mix-type waters. Moreover, the spindle aragonite crystals in mud-like dam formations could be attributed to self-assembly processes via aggregation of nano-rod subunits. Mixing models between Mg-type and Ca-type waters reveal the evolution of mineral SIs under various mixing proportions and their relation to the observed mineral assemblages and chemistry of waters. Calcium carbonate is supersaturated in all water types, while brucite and hydrated Mg-carbonates display variations during water mixing. The range of mixing ratios of Mg-type and Ca-type waters that brucite shows the highest supersaturation values coincides with the calculated mixing ratios characterizing the natural Mix-type waters where brucite was found. Nesquehonite is persistently undersaturated in all water types, underlining the importance of evaporation in its precipitation. Therefore, hydrology, geochemistry and local hydrodynamics characterizing the spring sites control the mineral assemblages, textures, and precipitation rate of the different types of solid precipitates occurring in the Oman alkaline spring systems.

Waters in the Ronda peridotite spring sites can be classified into hyperalkaline fluids and river waters that are, respectively, similar to the Ca–OH-type (i.e., Ca^{2+}–OH^{-}-rich) and Mg–HCO_3-type (i.e., Mg^{2+}–HCO_3^{-}-rich) water types described in ophiolite-hosted alkaline springs elsewhere. Like the majority of other known alkaline spring sites worldwide, Ronda alkaline spring systems do not exhibit the complexity of the ophiolite-hosted spring sites of Oman, where pools of mixed waters are predominant, and the distinction of a third type of waters (i.e., Mix-type) is possible. Ronda hyperalkaline fluids are characterized by high pH (10.9 – 12), low Mg, and high Na, K, Ca, and Cl^{-} concentrations and occur in the spring outlets and in natural ponds formed along the flow path of discharging fluids. River waters are enriched in Mg and DIC compared to Na, K, Ca and Cl^{-}, and are mildly alkaline ($8.5 < pH < 8.9$). As suggested for other serpentinite-hosted (sub-) surface waters, the chemistry of Ronda Mg–HCO_3 river waters is due to the hydrolysis of ferromagnesian peridotite minerals by infiltrated meteoric waters and shallow groundwater that are in equilibrium with the atmosphere. The physicochemical composition of the Ronda Ca–OH hyperalkaline fluids was derived via low-temperature serpentinization reactions from Mg–HCO_3 river waters or Ca–HCO_3 waters from near karst aquifers that infiltrate the peridotites with brecciated serpentinite along brittle faults. Mass balance calculations indicate that weathering of Ca-bearing peridotite is a feasible source of Ca in Ronda Ca–OH hyperalkaline fluids, but it would require relatively high steady-state dissolution rates. Assuming a total of 100 alkaline springs with Ca concentration and flow rates similar to those investigated here, the mass of Ca discharged in Ronda hyperalkaline springs in 1 Ma requires the weathering of 0.003 % or 0.025 % of the total volume of the Ronda lherzolite or dunite, respectively.

Travertine, crystalline crusts, and sediment deposits are the main precipitate types found in the Ronda hyperalkaline spring sites. Calcite and aragonite, minor dolomite and Mg-Al-rich clays are the main minerals identified in the spring sites. As illustrated in the Baños del Puerto spring (BP) site, (i) calcite-dominated precipitation occurs at atmospheric CO_2-driven uptake of hyperalkaline fluids at their discharging outlet, and (ii) aragonite-dominated precipitation occurs by mixing of Ca–OH hyperalkaline fluids with Mg–HCO_3 river waters. Aragonite and dolomite contents increase away from the springs and toward the river waters. The main factors driving the precipitation of aragonite over calcite are the Mg concentration, Mg/Ca ratio, and carbonic species abundance in the fluids. Textures of calcium carbonates indicate fast supersaturation rates in lithified travertine, and variations in supersaturation rate at calcitic crystalline crusts floating on the surface of the hyperalkaline springs. Variability in aragonite textures reflects fast supersaturation rates as evidenced by crystal branching. Dolomite most likely forms during lithification processes of travertines, and sporadic flooding of river water combined with subsequent evaporation. Despite the abiotic precipitation of large amounts of dolomite is uncommon at atmospheric conditions, specific alkaline pools of high salinity seem to meet the conditions for abiotic, low-temperature dolomite precipitation so long-hypothesized, yet rarely documented in nature.

The crystallization sequence and morphologies of hydrated magnesium carbonates were investigated in an open and closed system at room temperature. Mixing of $MgCl_2.6H_2O$ and Na_2CO_3 solutions resulted either in no precipitation (clear drops) or instant precipitation of a cloudy colloidal material of micro- to nano-particles. Instantly precipitated, colloidal material was either amorphous magnesium carbonate (AMC), or AMC–nesquehonite, or AMC–nesquehonite–dypingite, with increasing supersaturation.

In closed system experiments, the transformation of the initial colloidal material took place in three steps: i) dissolution of AMC with increasing pH, followed by the formation of well-defined needles of nesquehonite prismatic crystals (1 μm – 50 μm), ii) nesquehonite growth (up to 200 μm crystal sizes) with slight rise of pH due to the dissolution AMC, and iii) solvent-mediated transformation of nesquehonite into dypingite particles (< 1 to 5 μm crystal sizes).

Open system experiments were affected by atmospheric CO_2 uptake and diffusion in water, and evaporation, which caused different crystallization sequences and morphologies compared to the closed system experiments. Evaporation caused an increase in the values and rates of supersaturation, leading to precipitation in all crystallization wells. Unlike closed system experiments, crystallization in clear drop wells started between 3 and 48 h after the initial mixing. Nesquehonite did not transform into dypingite, as the solution entirely evaporated between 90 and 120 h after initial mixing. This solvent-mediated process cannot take place due to the evaporation of the water, explaining the persistence of nesquehonite in evaporation-affected natural environments. Dypingite exhibits a wide range of morphologies including chain-like structures, rings, and clusters. The chain-like dypingite has a hemispherical structure that exhibits interlocking flakes of dypingite at the exterior part, and a compact dypingite substrate in the interior part. This interior part is most likely formed around initial $Mg\text{-}CO_3$-

bearing nuclei, while the well-defined dypingite flakes of the exterior part grow at a later stage due to evaporation. The chain-like morphologies form after aggregation of dypingite hemispheres triggered by continuous supersaturation due to the evaporation of the solution.

6.2 Perspectives

The results of the present Ph.D. thesis complemented the existing knowledge on the ophiolite-hosted alkaline springs in Oman and described for the first time key processes regarding the geochemistry and mineralogy of Ronda alkaline springs in subcontinental mantle peridotites. Moreover, the results of crystallization experiments in the $MgO–CO_2–H_2O$ system contribute to the further understanding of the factor and mechanisms controlling the formation of hydrated Mg-carbonates low temperature.

However, both natural and experimental studies in this thesis addressed open questions that require further investigation. In particular, the concept of "active serpentinization" is still unclear, with the processes leading to Ca–OH-type hyperalkaline waters remaining subjects to future investigations. The source of Ca in the Ca-OH waters is still a subject of debate that could possibly be resolved by isotopic studies. In addition, the role of redox reactions in the generation of alkalinity is a topic of interest, not only for water-rock reactions but also for the development of microbial communities in deep aquifers.

Although it is challenging to crystallize anhydrous magnesium carbonate at low temperatures, isotopic studies on extensive Mg-carbonate occurrences (e.g., magnesite veins) in Oman have shown that these minerals have been formed at c. 60 °C. The detailed study of the formation conditions of hydrated Mg-carbonates in the $Mg–HCO_3$-type alkaline springs coupled to subsurface carbonation of circulating fluids could advance our knowledge on low-temperature Mg-carbonate formation. Similarly, occurrences of abiotic dolomite in Ronda springs is an exciting finding in order to investigate Mg-carbonate precipitation under low-temperature and high salinity conditions further. In alkaline spring systems, active precipitation of mineral phases such as brucite seems to form randomly in the spring sites, despite its supersaturation. Experimental studies and improvements in modeling could be proven useful for a better understanding of this issue. Generally, studying mineral phases and textures in natural systems is a complicated, and sometimes chaotic, task compared to the "perfect" conditions of the laboratory. However, mineral textures and morphologies can be utilized to define the prevailing environmental conditions during precipitation. Experimental studies could provide useful insights into the conditions characterizing any precipitation environment through comparison with natural examples.

Nucleation and crystallization are by nature probabilistic phenomena that prove difficult to control and observe. Novel techniques that incorporate in-situ observations of nucleation at the nano-scale could set boundaries on the controlling factors of hydrated Mg-carbonate crystallization sequence, and the role of precursor phases. Detailed studies on the relationship of supersaturation state and rate and textures could give insights into the mechanisms behind the morphogenesis of Mg-carbonates.

Part IV

REFERENCES

References

Abbate E., Bortolotti V., Passerini P., Principi G., 1985. The rhythm of Phanerozoic ophiolites. *Ophioliti* **10**, 109–138.

Abe, N., 2001. Petrochemistry of serpentinized peridotite from the Iberia Abyssal Plain (ODP Leg 173): its character intermediate between suboceanic and sub-continental upper mantle. *Geological Society, London, Special Publications,* **187**, 143-159.

Acosta-Vigil, A., Rubatto, D., Bartoli, O., Cesare, B., Meli, S., Pedrera, A., Azor, A., Tajcmanova, L., 2014. Age of anatexis in the crustal footwall of the Ronda peridotites, S Spain. *Lithos,* **210**, 147-167.

Afiri, A., Gueydan, F., Pitra, P., Essaifi, A., Précigout, J., 2011. Oligo-Miocene exhumation of the Beni-Bousera peridotite through a lithosphere-scale extensional shear zone. *Geod. Acta,* **2**, 49-60.

Alt, J.C., Garrido, C.J., Shanks III, W.C., Turchyn, A., Padrón-Navarta, J.A., López Sánchez-Vizcaíno, V., Gómez Pugnaire, M.T., Marchesi, C., 2012. Recycling of water, carbon, and sulfur during subduction of serpentinites: a stable isotope study of Cerro del Almirez, Spain. *Earth Planet. Sci. Lett.,* **327**, 50-60.

Alt, J.C., Schwarzenbach, E.M., Früh-Green, G.L., Shanks, W.C., Bernasconi, S.M., Garrido, C.J., Crispini, L., Gaggero, L., Padrón-Navarta, J.A., Marchesi, C., 2013. The role of serpentinites in cycling of carbon and sulfur: seafloor serpentinization and subduction metamorphism. *Lithos,* **178**, 40–54.

Alt, J.C., Shanks III, W.C., Crispini, L., Gaggero, L., Schwarzenbach, E.M., Früh-Green, G.L., Bernasconi, S.M., 2012. Uptake of carbon and sulfur during seafloor serpentinization and the effects of subduction metamorphism in Ligurian peridotites. *Chem.l Geol.*, **322**, 268–277.

Andreani, M., Luquot, L., Gouze, P., Godard, M., Hoise, E., Gibert, B., 2009. Experimental study of carbon sequestration reactions controlled by the percolation of CO_2-rich brine through peridotites. *Environ. Sci. Technol.,* **43**, 1226-1231.

Andreo, B., Gervilla, F., 2007. Las peridotitas de Ronda. En: J.J. Durán (Coord.), Atlas Hidrogeológico de la Provincia de Málaga 2. *Instituto Geológico y Minero de España* – Diputación de Málaga, Madrid, 212–216.

Andreo, B., 1997. Hidrogeología de acuíferos carbonatados en las Sierras Blanca y Mijas (Cordillera Bética, Sur de España). *SPICUM UMA*, Málaga, 489.

Anraku, S., Morimoto, K., Sato, T., Yoneda, T., 2009. Formation of secondary minerals and uptake of various anions under naturally-occurring hyperalkaline conditions in Oman. In: *ASME 2009 12th International Conference on Environmental Remediation and Radioactive Waste Management 2*. Liverpool, UK, 851–856.

Argamasilla, M., Barberá, J.A., Andreo, B., 2017. Factors controlling groundwater salinization and hydrogeochemical processes in coastal aquifers from southern Spain. *Sci. Total Environ.,* **580**, 50-68.

Arvidson, R.S., Mackenzie, F.T., 1999. The dolomite problem; control of precipitation kinetics by temperature and saturation state. *Am. J. Sci.,* **299**, 257-288.

Aquilano, D., Costa, E., Genovese, A., Massaro, F.R., Pastero, L., Rubbo, M., 2003. Hollow rhombohedral calcite crystals encompassing CO2 microcavities nucleated in solution. *J. Cryst. Growth,* **247**, 516–522.

Bach, W., Paulick, H., Garrido, C.J., Ildefonse, B., Meurer, W.P., Humphris, S.E., 2006. Unraveling the sequence of serpentinization reactions: petrography, mineral chemistry, and petrophysics of serpentinites from MAR 15 N (ODP Leg 209, Site 1274). *Geophys. Res. Lett.,* **33**, L13306.

Badiozamani, K., 1973. The dorag dolomitization model, application to the middle Ordovician of Wisconsin. *J. Sediment. Res.,* **43**, 965-984.

Balanyá, J.C., García-Duenas, V., Azañón, J.M., Sánchez-Gómez, M., 1997. Alternating contractional and extensional events in the alpujarride nappes of the alboran domain (Betics, Gibraltar arc). *Tectonics,* **16**, 226-238.

Ball, J.W., Nordstrom, D.K., 1991. User's manual for WATEQ4F, with revised thermodynamic data base and test cases for calculating speciation of major, trace, and redox elements in natural waters. USGS *Open-File Report* 91–183.

Ballirano P., De Vito C., Mignardi S., Ferrini V., 2013. Phase transitions in the Mg–CO_2–H_2O system and the thermal decomposition of dypingite, $Mg_5(CO_3)_4(OH)_2\cdot{}_5H_2O$: Implications for geosequestration of carbon dioxide. *Chem. Geol.,* **340**, 59–67.

Batuev, B.N., Krotov, A.G., Markov, V.F., Cherkashev, G.A., Krasnov, S.G., Lisitzin, Y.D., 1994. Massive sulfide deposits discovered at 14°N45', Mid-Atlantic Ridge. *BRIDGE Newsletter*, **6**, 6–10.

Barberá, J.A., Andreo, B., 2015. Hydrogeological processes in a fluviokarstic area inferred from the analysis of natural hydrogeochemical tracers. The case study of eastern Serranía de Ronda (S Spain). *J. Hydrol.* **523**, 500e514.

Barnes, I., La Marche, V.C., Himmelberg, G., 1967. Geochemical evidence of present-day serpentinization. *Science* **156**, 830–832.

Barnes, I., O'Neil, J.R., 1969. The relationship between fluids in some fresh alpine-type ultramafics and possible modern serpentinization, western United States. *Geol. Soc. Am. Bull.* **80**, 1947–1960.

Barnes, I., O'Neil, J.R., 1971. Calcium-magnesium carbonate solid solutions from Holocene conglomerate cements and travertines in the Coast Range of California. *Geochem. Cosmochim. Acta* **35**, 699-718.

Barnes, I., O'neil, J.R., Trescases, J.J., 1978. Present day serpentinization in New Caledonia, Oman and Yugoslavia. *Geochim. Cosmochim. Acta* **42**, 144–145.

Barnes, I., Rapp, J.B., 1972. Metamorphic assemblages and the direction of flow of metamorphic fluids in four instances of serpentinization. *Contrib. Mineral. Petrol.* **35**, 263–276.

Baumeister, J.L., Hausrath, E.M., Olsen, A.A., Tschauner, O., Adcock, C.T., Metcalf, R.V., 2015. Biogeochemical weathering of serpentinites: an examination of incipient dissolution affecting serpentine soil formation. *Appl. Geochem.* **54**, 7–84.

Beinlich, A., Austrheim, H., 2012. In situ sequestration of atmospheric CO_2 at low temperature and surface cracking of serpentinized peridotite in mine shafts. *Chem. Geol., **332***, 32–44.

Bénézeth P., Saldi G. D., Dandurand J. L., Schott J., 2011. Experimental determination of the solubility product of magnesite at 50 to 200°C. *Chem. Geol.* **286**, 21–31.

Beniash, E., Aizenberg, J., Addadi, L.,Weiner, S., 1997. Amorphous calcium carbonate transforms into calcite during sea urchin larval spicule growth. *Proc. R. Soc. Lond. B. Biol. Sci.,* **264**, 461-465.

Berner, R.A., 1975. The role of magnesium in the crystal growth of calcite and aragonite from seawater. *Geochim. Cosmochim. Acta,* **39**, 489–504.

Berninger U.-N., Jordan G., Schott J., Oelkers E. H. 2014. The experimental determination of hydromagnesite precipitation rates at 22.5–75 °C. *Mineral. Mag.* **78**, 1405–1416.

Blank, J.G., Green, S.J., Blake, D., Valley, J.W., Kita, N.T., Treiman, A., Dobson, P.F., 2009. An alkaline spring system within the Del Puerto Ophiolite (California, USA): a Mars analog site. *Planet. Space Sci.,* **57**, 533–540.

Bodinier, J.L., 1988. Geochemistry and petrogenesis of the Lanzo peridotite body, western Alps. *Tectonophysics*, ***149***, 67-88.

Bodinier, J.L., Garrido, C.J., Chanefo, I., Bruguier, O., Gervilla, F., 2008. Origin of pyroxenite-peridotite veined mantle by refertilization reactions: evidence from the Ronda peridotite (Southern Spain). *J. Petrol.* **49**, 999–1025.

Bodinier, J.L., Godard, M., 2006. Orogenic, ophiolitic and abyssal peridotites. In: *Carlson, R.W. (Ed.), Treatise on Geochemistry. 2. Geochemistry of the Mantle and Core*. Elsevier.

Bodinier, J.-L., Godard, M., 2014. Orogenic, ophiolitic, and abyssal peridotites. In: *Carlson, R.W. (Ed.), 2nd Edition Treatise on Geochemistry* Vol. 3. Elsevier, 103–167 (Ch. 4).

Boetius, A., Ravenschlag, K., Schubert, C.J., Rickert, D., Widdel, F., Gieseke, A., Amann, R., Jorgensen, B.B., Witte, U., Pfannkuche, O., 2000. A marine microbial consortium apparently mediating anaerobic oxidation of methane. *Nature* **407**, 623.

Boillot G, Winterer EL, Meyer AW, et al., 1988. Galicia Margin: Covering Leg 103 of the Cruises of the Drilling Vessel JOIDES Resolution. Ponta Delgada, Azores, to Bremerhaven, Germany, April 25, 1985–June 19, 1985. *Proceeding of the Ocean Drilling Program, Scientific Results*, **103**, 858. College Station, TX: Ocean Drilling Program.

Booth-Rea, G., Martínez-Martínez, J.M., Giaconia, F., 2015. Continental subduction, intracrustal shortening, and coeval upper-crustal extension: P–T evolution of subducted south Iberian paleomargin metapelites (Betics, SE Spain). *Tectonophysics* **663**, 122–139.

Bonatti, E., Emiliani, C., Ferrara, G., Honnorez, J., Rydell, H., 1974. Ultramafic-carbonate breccias from the equatorial Mid Atlantic Ridge. *Mar. Geol.*, ***16***, 83–102.

Bonatti, E., Peyve, A., Kepezhinskas, P., Kurentsova, N., Seyler, M., Skolotnev, S., Udintsev, G., 1992. Uppermantle heterogeneity below the Mid-Atlantic Ridge, 0°–15°N. *J. of Geoph. Res.*, **97**, 4461–4476.

Bosch D, Jamais M, Boudier F, Nicolas A, Dautria JM, Agrinier P. 2004. Deep and high-temperature hydrothermal circulation in the Oman ophiolite—petrological and isotopic evidence. *J. Petrol.*, **45**, 1181–208.

Boschetti, T., Toscani, L., 2008. Springs and streams of the TaroeCeno Valleys (Northern Apennine, Italy): reaction path modeling of waters interacting with serpentinized ultramafic rocks. *Chem. Geol.*, **257**, 76–91.

Boschetti, T., Toscani, L., Iacumin, P., Selmo, E., 2017. Oxygen, hydrogen, boron and lithium isotope data of a natural spring water with an extreme composition: a fluid from the dehydrating slab? *Aquat. Geochem.*, **23**, 299–313.

Boschi, C., Früh-Green, G.L., Delacour, A., Karson, J.A., Kelley, D.S., 2006. Mass transfer and fluid flow during detachment faulting and development of an oceanic core complex, Atlantis Massif (MAR 30 N). *Geochem. Geoph. Geosys.*, ***7***. 10.1029/2005GC001074.

Botha, A., Strydom, C.A., 2001. Preparation of a magnesium hydroxy carbonate from magnesium hydroxide. *Hydrometallurgy* **62**, 175–183.

Boudier, F., Coleman, R.G., 1981. Cross section through the peridotite in the Samail ophiolite, southeastern Oman Mountains. *J. of Geoph. Res.: Sol. Earth*, **86**, 2573-2592.

Boudier, F., Nicolas, A., 1985. Harzburgite and lherzolite subtypes in ophiolitic and oceanic environments. *Earth Planet. Sci. Lett*, ***76***, 84–92.

Boudier, F., Baronnet, A., Mainprice, D., 2010. Serpentine mineral replacements of natural olivine and their seismic implications: Oceanic lizardite versus subduction-related antigorite. *J. Petrol.*, **51**, 495–512.

Boulart C., et al., 2013. Differences in gas venting from ultramafic-hosted warm springs: the example of Oman and Voltri ophiolites. *Ofioliti.* **38**, 143–156.

Brazelton, W.J., Schrenk, M.O., Kelley, D.S., Baross, J.A., 2006. Methane- and sulfur-metabolizing microbial communities dominate the Lost City hydrothermal field ecosystem. *Appl. Environ. Microbiol.*, **72**, 6257–6270.

Bruguier, O., Hammor, D., Bosch, D., Caby, R., 2009. Miocene incorporation of peridotite into the Hercynian basement of the Maghrebides (Edough massif, NE Algeria): implications for the geodynamic evolution of the Western Mediterranean. *Chem. Geol.*, ***261***,172–184.

Bruni, J., Canepa, M., Chiodini, G., Cioni, R., Cipolli, F., Longinelli, A., Marini, L., Ottonello, G., Zuccolini, M.V, 2002. Irreversible water–rock mass transfer accompanying the generation of the neutral, Mg–HCO_3 and high-pH, Ca–OH spring waters of the Genova province, Italy. *Appl. Geochem.*, **17**, 455–474.

Bundeleva, I.A., Shirokova, L.S., Pokrovsky, O.S., Bénézeth, P., Ménez, B., Gérard, E., Balor, S., 2014. Experimental modeling of calcium carbonate precipitation bycyanobacterium Gloeocapsa sp. *Chem. Geol.*, **374**, 44–60.

Burg J.P., Bodinier J.L., Chaudhry S., Hussain S.S., Dawood H., 1998. Infra-arc mantle–crust transition and intra-arc mantle diapirs in the Kohistan Complex (Pakistani Himalaya): Petro-structural evidence. *Terra Nova*, **10**, 74–80.

Burton, E.A., 1993. Controls on marine carbonate cement mineralogy: review and reassessment. *Chem. Geol.*, **105**, 163–179.

Canales, J., Detrick, R.S., Toomey, D.R., Wilcock, W.S., 2003. Segment-scale variations in the crustal structure of 150–300 kyr old fast spreading oceanic crust (East Pacific Rise, 8º 15′ N–10º 5’ N) from wide-angle seismic refraction profiles. *Geoph. J. Intern.*, ***152***, 766–794.

Cann, J.R., 1971. Petrology of basement rocks from Palmer Ridge, NE Atlantic. *Philosophical Transactions of the Royal Society of London. Series A, Mathematical and Physical Sciences*, ***268***, 605–617.

Cann, J.R., Blackman, D.K., Smith, D.K., Mcallister, E., Janssen, B., Mello, S., Avgerinos, E., Pascoe, A.R., Escartín, J., 1997, Corrugated slip surfaces formed at ridge-transform intersections on the Mid-Atlantic Ridge: *Nature,* **385**, 329–332.

Cannat, M., Fontaine, F., Escartín, J., 2010. Serpentinization and associated hydrogen and methane fluxes at slow spreading ridges. In: Diversity of Hydrothermal Systems on Slow Spreading Ocean Ridges, *Geophys. Monogr. Ser.*, **188**, edited by P. A. Rona et al., AGU, Washington, D. C. 241–264,

Canterford J. H., Tsambourakis G., Lambert B., 1984. Some observations on the properties of dypingite, $Mg_5(CO_3)_4(OH)_2$ $5H_2O$, and related minerals. *Mineral. Mag.* **48**, 437–442.

Cardace, D., Meyer-Dombard, D.A.R., Woycheese, K.M., Arcilla, C.A., 2015. Feasible metabolisms in high pH springs of the Philippines. *Front. in microb.*, ***6***, p.10.

Carlson, R.L., Miller, D.J., 2003. Mantle wedge water contents estimated from seismic velocities in partially serpentinized peridotites. *Geoph. Res. Lett.*, ***30***, 1250, 0.1029/2002GL016600.

Cawood, P.A., Kröner, A., Collins, W.J., Kusky, T.M., Mooney, W.D., Windley, B.F., 2009. Accretionary orogens through Earth history. *Geological Society, London, Special Publications*, ***318***, 1-36.

Ciazela, J., Koepke, J., Dick, H.J., Muszynski, A., 2015. Mantle rock exposures at oceanic core complexes along mid-ocean ridges. *Geologos*, **21**, 207–231.

Chaka, A.M., Felmy, A.R., 2014. Ab initio thermodynamic model for magnesium carbonates and hydrates. *J. Phys. Chem.*, ***118***, 7469–7488.

Chaka A. M., Felmy A. R., Qafoku O., 2016. *Ab initio* thermodynamics of magnesium carbonates and hydrates in water-saturated supercritical CO_2 and CO_2-rich regions. *Chem. Geol.*, **434**, 1–11.

Charlou, J.L., Donval, J.P., Fouquet, Y., Jean-Baptiste, P. Holm, N., 2002. Geochemistry of high H_2 and CH_4 vent fluids issuing from ultramafic rocks at the Rainbow hydrothermal field (36° 14′ N, MAR). *Chem. Geol.*, ***191***, 345-359.

Chavagnac, V., Monnin, C., Ceuleneer, G., Boulart, C., Hoareau, G., 2013a. Characterization of hyperalkaline fluids produced by low-temperature serpentinization of mantle peridotites in the Oman and Ligurian ophiolites. *Geochem. Geophys. Geosyst.* **14**, 2496–2522.

Chavagnac, V., Ceuleneer, G., Monnin, C., Lansac, B., Hoareau, G., Boulart, C., 2013b. Mineralogical assemblages forming at hyperalkaline warm springs hosted on ultramafic rocks: a case study of Oman and Ligurian ophiolites. *Geochem. Geophys. Geosyst.* **14**, 2474–2495.

Cheng W., Li Z., 2009. Precipitation of nesquehonite from homogeneous supersaturated solutions. *Cryst. Res. Technol.* **44**, 937–947.

Cheng W., Li Z., Demopoulos G. P., 2009. Effects of temperature on the preparation of magnesium carbonate hydrates by reaction of $MgCl_2$ with Na_2CO_3. *Chinese J. Chem. Eng.* **17**, 661–666.

Cipolli, F., Gambardella, B., Marini, L., Ottonello, G., Zuccolini M., 2004. Geochemistry of high-pH waters from serpentinites of the Gruppo di Voltri (Genova, Italy) and reaction path modeling of CO_2 sequestration in serpentinite aquifers. *Appl. Geochem.* **19**, 787–802.

Clark, I.D., Fontes, J.-C., Fritz, P., 1992. Stable isotope disequilibria in travertine from high pH waters: laboratory investigations and field observations from Oman. *Geochim. Cosmochim. Acta* **56**, 2041–2050.

Coleman, R.G., 1971. Plate tectonic emplacement of upper mantle peridotites along continental edges. *J. Geophys. Res.*, ***76***, 1212–1222.

Coleman R.G, 1977. Ophiolites: Ancient Oceanic Lithosphere? Heidelberg, Berlin, NY: Springer.

Coleman, R.G., 1981. Tectonic setting for ophiolite obduction in Oman. *J. Geophys. Res.* **86**, 2497–2508.

Cölfen, H., Mann, S., 2003. Higher-order organization by mesoscale self-assembly and transformation of hybrid nanostructures. *Angew. Chem. Inter. Ed.* **42**, 2350–2365.

Cornen G, Beslier M.–O., Girardeau J, 1996. Petrologic characteristics of the ultramafic rocks from the ocean/continent transition in the Iberia Abyssal Plain. Iberia Abyssal Plain; Leg 149, Sites 891–901, Proceedings of the Ocean Drilling Program; *Scientific reports*, **149**, 377–396. College Station, TX: Ocean Drilling Program.

Daae, F.L., Okland, I., Dahle, H., Jørgensen, S.L., Thorseth, I.H., Pedersen, R.B., 2013. Microbial life associated with low-temperature alteration of ultramafic rocks in the Leka ophiolite complex. *Geobiology*, **11**, 318–339.

D'Alessandro, W., Yüce, G., Italiano, F., Bellomo, S., Gülbay, A.H., Yasin, D.U., Gagliano, A.L., 2018. Large compositional differences in the gases released from the Kizildag ophiolitic body (Turkey): Evidences of prevailingly abiogenic origin. *Mar. and petrol. Geol.*, **89**, 174–184.

D'Alessandro, W., Daskalopoulou, K., Calabrese, S., Bellomo, S., 2018. Water chemistry and abiogenic methane content of a hyperalkaline spring related to serpentinization in the Argolida ophiolite (Ermioni, Greece). *Mar. and petrol. Geol.*, **89**, 185–193.

Dasgupta, R., Hirschmann, M.M., 2010. The deep carbon cycle and melting in Earth’s interior. Earth Planet. *Sci. Lett.* **298**, 1–13.

Daval, D., Martínez, I., Corvisier, J., Findling, N., Goffé, B., Guyot, F., 2009. Carbonation of Ca-bearing silicates, the case of wollastonite: Experimental investigations and kinetic modeling. *Chem. Geol.*, **265**, 63–78.

Davies P. J., Bubela B., 1973. The transformation of nesquehonite into hydromagnesite. *Chem. Geol.* **12**, 289–300.

Deelman, J.C., Low–temperature formation of dolomite and magnesite. Open-access e-book. 2011. **512**.

De Boer, J.Z., Chanton, J., Zeitlh€ofler, M., 2007. Homer’s Chimaera fires (SW of Antalya Turkey); burning abiogenic methane gases; are they generated by a serpentinization process related to alkalic magmatism? *Z. Dtsch. Ges. Geowiss*., **158**, 997–1003.

de Gramont, X., Le Métour, J., Villey, M., 1986. Samad geologic map, sheet NF40-7C. In: *Minist. of Commer. and Ind., Direct. Gen. of Miner., Muscat.*

De Obeso, J.C., Kelemen, P.B., 2018. Fluid rock interactions on residual mantle peridotites overlain by shallow oceanic limestones: insights from Wadi Fins, Sultanate of Oman. *Chem. Geol*., **498**, 139–149.

Den Tex, E., 1969. Origin of ultramafic rocks, their tectonic setting and history: a contribution to the discussion of the paper. In: The origin of ultramafic and ultrabasic rocks. Edited by PJ Wyllie. *Tectonophysics*, **7**, 457-488.

Deschamps, F., Godard, M., Guillot, S., Hattori, K., 2013. Geochemistry of subduction zone serpentinites: A review. *Lithos*, **178**, 96–127.

Dewandel, B., Lachassagne, P., Bakalowicz, M., Weng, P., Al-Malki A., 2003. Evaluation of aquifer thickness by analyzing recession hydrographs: application to the Oman ophiolite hard-rock aquifer. *J. Hydrol*., **274**, 248–269.

Dewandel, B., Lachassagne, P., Qatan, A., 2004. Spatial measurements of stream baseflow, a relevant method for aquifer characterization and permeability evaluation: application to a hard rock aquifer, Oman ophiolite. *Hydrol. Process*, **18**, 3391–3400.

Dewandel B, Lachassagne P, Boudier F, Al-Hattali S, Ladouche B, et al. 2005. A conceptual hydrogeological model of ophiolite hard-rock aquifers in Oman based on a multiscale and a multidisciplinary approach. *Hydrogeol. J.* **13**, 708–26.

De Yoreo, J.J., Gilbert, P.U., Sommerdijk, N.A., Penn, R.L., Whitelam, S., Joester, D., Zhang, H., Rimer, J.D., Navrotsky, A., Banfield, J.F., Wallace, A.F., Michel, F.M., Meldrum, F.C., Colfen, H., Dove, P.M., 2015. Crystallization by particle attachment in synthetic, biogenic, and geologic environments. *Science* **349**, 6760.

Dick H.J.B, Fisher R.L., Bryan W.L., 1984. Mineralogic variability of the uppermost mantle along mid-ocean ridges. *Earth Planet. Sci. Lett.*, **69**, 88–106.

Dijkstra, A.H., Cawood, P.A., 2004. Base-up growth of ocean crust by multiple phases of magmatism: field evidence from Macquarie Island. *J. Geol. Soc.*, **161**, 739–742.

Dilek, Y., Flower, M.F., 2003. Arc-trench rollback and forearc accretion: 2. A model template for ophiolites in Albania, Cyprus, and Oman. *Geological Society, London, Special Publications*, **218**, 43–68.

Dilek, Y., Furnes, H., 2011. Ophiolite genesis and global tectonics: Geochemical and tectonic fingerprinting of ancient oceanic lithosphere. *Bulletin*, **123**, 387–411.

Di Lorenzo, F., Rodriguez-Galan, R.M., Prieto, M., 2014. Kinetics of the solvent-mediated transformation of hydromagnesite into magnesite at different temperatures. *Mineral. Mag.*, **78**, 1363–1372.

Ding W., Ouyang J., Yang H., 2016. Synthesis and characterization of nesquehonite ($MgCO_3·3H_2O$) powders from natural talc. *Powder Technol.,* **292**, 169–175.

Di Tommaso, D., de Leeuw, N.H., 2010. Structure and dynamics of the hydrated magnesium ion and of the solvated magnesium carbonates: insights from first principles simulations. Phys. Chem. Chem. Phys. **12**, 894e901.

Dixon, J.C., Campbell, S.W., Thorn, C.E., Darmody, R.G. (2006) Incipient weathering rind development on introduced machine-polished granite discs in an Arctic alpine environment, northern Scandinavia. *Earth Surf. Proc. and Landf.,* **31**, 111–121.

Doljak, D., Jojić Glavonjić, T., 2016. State and prospects of geothermal energy usage in Serbia. *Journal of the Geographical Institute" Jovan Cvijic", SASA*, **66**, 221-236.

Dong M., Cheng W., Li Z., Demopoulos G. P., 2008. Solubility and stability of nesquehonite ($MgCO_3·H_2O$) in mixed NaCl + $MgCl_2$, NH_4Cl + $MgCl_2$, LiCl, and LiCl + $MgCl_2$ solutions. *J. Chem. Eng. Data*, **53**, 2586–2593.

Dufaud, F., Martínez, I., Shilobreeva, S., 2009. Experimental study of Mg-rich silicates carbonation at 400 and 500 ºC and 1 kbar. *Chem. Geol.*, **265**,79–87.

Emmanuel S, Berkowitz B. 2006. Suppression and stimulation of seafloor hydrothermal convection by exothermic mineral hydration. *Earth Planet. Sci. Lett.*, **243**, 657–68.

Ernst, W.G., 1981. Petrogenesis of eclogites and peridotites from the Western and Ligurian Alps. *Am. Mineral.,* **66**, 443–472.

Esteban, J.J., Cuevas, J., Tubía, J.M., Sergeev, S., Larionov, A., 2011. A revised Aquitanian age for the emplacement of the Ronda peridotites (Betic Cordilleras, southern Spain). *Geol. Mag.*, **148**, 183–187.

Etiope, G., Judas, J., Whiticar, M.J., 2015. Occurrence of abiotic methane in the eastern United Arab Emirates ophiolite aquifer. *Arab. J. Geosc.*, **8**, 11345–11348.

Etiope, G., Samardžić, N., Grassa, F., Hrvatović, H., Miošić, N., Skopljak, F., 2017. Methane and hydrogen in hyperalkaline groundwaters of the serpentinized Dinaride ophiolite belt, Bosnia and Herzegovina. *Appl. Geochem.*, **84**, 286–296.

Etiope, G., Sherwood Lollar, B., 2013. Abiotic methane on Earth. *Rev. Geophys.,* **51**, 276–299.

Etiope, G., Tsikouras, B., Kordella, S., Ifandi, E., Christodoulou, D. Papatheodorou, G., 2013. Methane flux and origin in the Othrys ophiolite hyperalkaline springs, Greece. *Chem. Geol.*, **347**, 161–174.

Etiope, G., Vadillo, I., Whiticar, M.J., Marques, J.M., Carreira, P.M., Tiago, I., Benavente, J., Jiménez, P., Urresti, B., 2016. Abiotic methane seepage in the Ronda peridotite massif, southern Spain. *Appl. Geochem*., **66**, 101–113.

Etiope, G., Whiticar, M.J., 2019. Abiotic methane in continental ultramafic rock systems: towards a genetic model. *Appl. Geochem*., **102**, 139–152.

Evans, B.W., Hattori, K., Baronnet, A., 2013. Serpentinite: what, why, where? *Elements*, **9**, 99–106.

Fabriès, J., Lorand, J.P., Bodinier, J.L. Dupuy, C., 1991. Evolution of the upper mantle beneath the Pyrenees: evidence from orogenic spinel lherzolite massifs. *J. Petrol.*, **2**, 55–76.

Faccenna, C., Piromallo, C., Crespo-Blanc, A., Jolivet, L., Rossetti, F., 2004. Lateral slab deformation and the origin of the western Mediterranean arcs. *Tectonics,* **23**. 10.1029/2002TC001488.

Falk, E.S., Guo, W., Paukert, A.N., Matter, J.M., Mervine, E.M., Kelemen, P.B., 2016. Controls on the stable isotope compositions of travertine from hyperalkaline springs in Oman: insights from clumped isotope measurements. *Geochim. Cosmochim. Acta*, **192**, 1–28.

Falini, G., Gazzano, M., Ripamonti, A., 1994. Crystallisation of calcium carbonate in presence of magnesium and polyelectrolytes. *J. Cryst. Growth,* **137**, 577–584.

Fenter, P., Sturchio, N.C., 2012. Calcite (104)–water interface structure, revisited. *Geochim. Cosmochim. Acta*, **97**, 58–69.

Fernández-Díaz, L., Putnis, A., Prieto, M., Putnis, C.V., 1996. The role of magnesium in the crystallization of calcite and aragonite in a porous medium. *J. Sediment. Res.*, **66**, 482–491.

Ferrini, V., De Vito, C., Mignardi, S., 2009. Synthesis of nesquehonite by reaction of gaseous CO2 with Mg chloride solution: its potential role in the sequestration of carbon dioxide. *J. Hazard. Mater.*, **168**, 832–837.

Ferris, F.G., Wiese, R.G., Fyfe, W.S., 1994. Precipitation of carbonate minerals by microorganisms: Implications for silicate weathering and the global carbon dioxide budget. *Geomicrob. J.*, **121**, 1–13.

Fischbeck, R., Müller, G., 1971. Monohydrocalcite, hydromagnesite, nesquehonite, dolomite, aragonite, and calcite in speleothems of the Fr€ankische Schweiz, Western Germany. *Contrib. Mineral. Petrol.*, **33**, 87–92.

Folk, R.L., 1993. SEM imaging of bacteria and nannobacteria in carbonate sediments and rocks. *J. Sediment. Res.*, **63**, 990-999.

Folk, R. L., 1994. Interaction between bacteria, nannobacteria, and mineral precipitation in hot springs of central Italy. *Géogr. Phys. et Quat.*, **48**, 233–246.

Frets, E.C., Tommasi, A., Garrido, C.J., Vauchez, A., Mainprice, D., Targuisti, K., Amri, I., 2014. The Beni Bousera peridotite (Rif belt, Morocco): an oblique-slip low-angle shear zone thinning the subcontinental mantle lithosphere. *J.* Petrol., **55**, 283–313.

Frost, B.R., Beard, J.S., 2007. On silica activity and serpentinization. *J. Petrol.*, **48**, 1351–1368.

Früh-Green, G.L., Connolly, J.A., Plas, A., Kelley, D.S., Grobéty, B., 2004. Serpentinization of oceanic peridotites: implications for geochemical cycles and biological activity. *The subseafloor biosphere at mid-ocean ridges*, **144**, 119–136.

Früh-Green, G.L., Kelley, D.S., Bernasconi, S.M., Karson, J.A., Ludwig, K.A., Butterfield, D.A., Boschi, C., Proskurowski, G., 2003. 30,000 years of hydrothermal activity at the Lost City vent field. *Science*, **301**, 495–498.

Fryer, P., Wheat, C.G., Mottl, M.J., 1999. Mariana blueschist mud volcanism: Implications for conditions within the subduction zone. *Geology*, **27**, 103–106.

Fyfe WS. 1974. Heats of chemical reactions and submarine heat production. *Geophys. J. R. Astron. Soc.*, **37**, 213–15.

García-Ruíz, J.M., Hyde, S.T., Carnerup, A.M., Christy, A.G., Van Kranendonk, M.J., Welham, N.J., 2003. Self-assembled silica-carbonate structures and detection of ancient microfossils. *Science*, **302**, 1194–1197.

García-Ruíz, J.M., Nakouzi, E., Kotopoulou, E., Tamborrino, L., Steinbock, O., 2017. Biomimetic mineral self-organization from silica-rich spring waters. *Sci. Adv*., **3**, 1602285.

Garrido, C.J., Bodinier, J.L., 1999. Diversity of mafic rocks in the Ronda peridotite: evidence for pervasive melt-rock reaction during heating of subcontinental lithosphere by upwelling asthenosphere. *J. Petrol.*, **40**, 729–754.

Garrido, C.J., Gueydan, F., Booth-Rea, G., Précigout, J., Hidas, K., Padrón-Navarta, J.A., Marchesi, C., 2011. Garnet lherzolite and garnet-spinel mylonite in the Ronda peridotite: Vestiges of Oligocene backarc mantle lithospheric extension in the western Mediterranean. *Geology*, ***39***, 927–930.

Gerdemann, S.J., O'Connor, W.K., Dahlin, D.C., Penner, L.R., Rush, H., 2007. Ex situ aqueous mineral carbonation. *Environ. Sci. Technol*., **41**, 2587–2593.

Gervilla, F., Leblanc, M., 1990. Magmatic ores in high-temperature alpine-type lherzolite massifs (Ronda, Spain, and Beni Bousera, Morocco). *Econ. Geol.*, **44**, 112–132.

Giampouras, M., Garrido, C.J., Zwicker, J., Vadillo, I., Smrzka, D., Bach, W., Peckmann, J., Jiménez, P., Benavente, J., García-Ruíz, J.M., 2019. Geochemistry and mineralogy of serpentinization-drivenhyperalkaline springs in the Ronda peridotites. *Lithos*, **350-351**, 105215.

Giampouras, M., Garrido, C.J., Bach, W., Los, C., Fussmann, D., Monien, P., García-Ruíz, J.M., 2020. On the controls of mineral assemblages and textures in alkaline springs, Samail Ophiolite, Oman. *Chem. Geol.*, **533**, 119435.

Gislason, S.R., Oelkers, E.H., 2014. Carbon storage in basalt. *Science*, **344**, 373–374.

Glennie, K.W., Bouef, M.G.A., Hughes-Clark, M.W., Moody-Stuart, M., Pilaar, W.F.H., Reinhardt, B.M., 1973. Late Cretaceous nappes in the Oman mountains and their geological evolution. *Am. Assoc. Pet. Geol. Bull.*, **57**, 5–27.

Glennie K.W., Bouef M.G.A., Hughes-Clarke M.W., Moody-Stuart M., Pilaar W.F.H., Reinhardt B.M. 1974. Geology of the Oman Mountains, vol 31. *Verhundelingen van het koninklijk Nederlnnds Geologisch-Mijnbouwkundig Genootschap.*

Godard, M., Awaji, S., Hansen, H., Hellebrand, E., Brunelli, D., Johnson, K., Yamasaki, T., Maeda, J., Abratis, M., Christie, D., Kato, Y., 2009. Geochemistry of a long in-situ section of intrusive slow-spread oceanic lithosphere: Results from IODP Site U1309 (Atlantis Massif, 30 N Mid-Atlantic-Ridge). *Earth Planet. Sci. Lett.*, **279**, 110–122.

Godard, M., Dautria, J.M., Perrin, M., 2003. Geochemical variability of the Oman ophiolite lavas: relationship with spatial distribution and paleomagnetic directions. *Geochem. Geophys. Geosyst.*, **4**, 8609.

Godard, M., Jousselin, D., Bodinier, J.L., 2000. Relationships between geochemistry and structure beneath a palaeo-spreading centre: a study of the mantle section in the Oman ophiolite. *Earth Planet. Sci. Lett.*, **180**, 133–148.

Godard, M., Lagabrielle, Y., Alard, O., Harvey, J., 2008. Geochemistry of the highly depleted peridotites drilled at ODP Sites 1272 and 1274 (Fifteen-Twenty Fracture Zone, Mid-Atlantic Ridge): implications for mantle dynamics beneath a slow spreading ridge. *Earth Planet. Sci. Lett.*, **267**, 410–425.

González-Jiménez, J.M., Marchesi, C., Griffin, W.L., Gervilla, F., Belousova, E.A., Garrido, C.J., Romero, R., Talavera, C., Leisen, M., O'Reilly, S.Y., Barra, F., Martin, L., 2017. Zircon recycling and crystallization during formation of chromite- and Ni-arsenide ores in the subcontinental lithospheric mantle (Serranía de Ronda, Spain). *Ore Geol. Rev.*, **90**, 193–209.

González, L.A., Carpenter, S.J., Lohmann, K.C., 1992. Inorganic calcite morphology; roles of fluid chemistry and fluid flow. *J. Sediment. Res.*, **62**, 382–399.

Gránásy, L., Pusztai, T., Tegze, G., Warren, J.A., Douglas, J.F., 2005. Growth and form of spherulites. *Phys. Rev.*, **72**, 11605.

Gregory R.T, Taylor H.P., 1981. An oxygen isotope profile in a section of Cretaceous oceanic crust, Samail Ophiolite, Oman - Evidence for delta-^{18}O buffering of the oceans by deep (less than 5 km) seawater-hydrothermal circulation at mid-ocean ridges. *J. Geoph. Res.* **86**, 2737–2755.

Grozeva, N.G., Klein, F., Seewald, J.S.,, Sylva, S.P., 2017. Experimental study of carbonate formation in oceanic peridotite. *Geochim. Cosmochim. Acta*, **199**, 264–286.

Grozeva, N.G., 2018. Mineral Transformations in Seafloor Serpentinization Systems. *Ph.D. Thesis. MIT*, p. 198.

Guerrera, F., Martín-Martín, M., Perrone, V., Tramontana, M., 2005. Tectono-sedimentary evolution of the southern branch of the western tethys (maghrebian flysch basin and lucanian ocean): consequences for western Mediterranean geodynamics. *Terra. Nova*, **17**, 358–367.

Gysi, A.P., Jagoutz, O., Schmidt, M.W., Targuisti, K., 2011. Petrogenesis of pyroxenites and melt infiltrations in the ultramafic complex of Beni Bousera, Northern Morocco. *J.Petrol.*, **52**, 1679–1735.

Hacker B.R., Mosenfelder J.L., Gnos E., 1996. Rapid emplacement of the Oman ophiolite: Thermal and geochronologic constraints. *Tectonics*, **15**, 1230–1247.

Hamilton J. L., Wilson S. A., Morgan B., Turvey C. C., Paterson D. J., MacRae C., McCutcheon J., Southam G., 2016. Nesquehonite sequesters transition metals and CO_2 during accelerated carbon mineralisation. *Int. J. Greenhouse Gas Control.*, **55**, 73–81.

Hamlyn, P.R., Bonatti, E., 1980. Petrology of mantle-derived ultramafics from the Owen Fracture Zone, northwest Indian Ocean: implications for the nature of the oceanic upper mantle. *Earth Planet. Sci. Lett.*, **48**, 65–79.

Hammer, O., Dysthe, D.K., Jamtveit, B., 2007. The dynamics of travertine dams. *Earth Planet. Sci. Lett.*, **256**, 258–263.

Hammer, O., Dysthe, D.K., Jamtveit, B., 2010. Travertine terracing: patterns and mechanisms. *J. Geol. Soc.*, **336**, 345–355.

Hänchen M., Prigiobbe V., Baciocchi R., Mazzotti M., 2008. Precipitation in the Mgcarbonate system—effects of temperature and CO_2 pressure. *Chem. Eng. Sci.*, **63**, 1012–1028.

Hanghoj, K., Kelemen, P.B., Hassler, D., Godard, M., 2010. Composition and genesis of depleted mantle peridotites from the Wadi Tayin Massif, Oman Ophiolite; major and trace element geochemistry, and Os isotope and PGE systematics. *J. Petrol.*, **51**, 201–227.

Harrison A. L., Dipple G. M., Power I. M., Mayer K. U., 2016. The impact of evolving mineral-water-gas interfacial areas on mineral-fluid reaction rates in unsaturated porous media. *Chem. Geol.,* **421**, 65–80.

Harrison A. L., Dipple G. M., Power I. M., Mayer K. U., 2015. Influence of surface passivation and water content on mineral reactions in unsaturated porous media: Implications for brucite carbonation and CO_2 sequestration. *Geochim. Cosmochim. Acta,* **148**, 477–495.

Harrison, A.L., Mavromatis, V., Oelkers, E.H., Bénézeth, P., 2019. Solubility of the hydrated Mg-carbonates nesquehonite and dypingite from 5 to 35 °C: Implications for CO_2 storage and the relative stability of Mg-carbonates. *Chem. Geol.,* **504**, 123–135.

Harrison A. L., Power I. M., Dipple G. M., 2013. Accelerated carbonation of brucite in mine tailings for carbon sequestration. *Environ. Sci. Technol.,* **47**, 126–134.

Hartmann J., West J., Renforth P., Kohler P., De La Rocha C., Wolf-Gladrow D. A., Durr H., Scheffran J., 2013. Enhanced chemical weathering as a geoengineering strategy to reduce atmospheric carbon dioxide, a nutrient source and to mitigate ocean acidification. *Rev. Geophys.,* **51**, 113–149.

Hausrath, E.M., Treiman, A.H., Vicenzi, E., Bish, D.L., Blake, D., Sarrazin, P., Hoehler, T., Midtkandal, I., Steele, A., Brantley, S.L., 2008. Short-and long-term olivine weathering in Svalbard: implications for Mars. *Astrobiology*, **8**, 1079-1092.

Hekinian, R., Bideau, D., Francheteau, J., Cheminee, J.L., Armijo, R., Lonsdale, P., Blum, N., 1993. Petrology of the East Pacific Rise crust and upper mantle exposed in Hess Deep (eastern equatorial Pacific). *J. Geoph. Res.: Sol. Earth*, **98**, 8069-8094.

Helffrich, G.R., Wood, B.J., 2001. The Earth's mantle. *Nature,* **412**, 501–507.

Hellebrand, E., Snow, J.E., Mühe, R., 2002. Mantle melting beneath Gakkel Ridge (Arctic Ocean): abyssal peridotite spinel compositions. *Chem. Geol.*, **182**, 227–235.

Hellebrand, E., Snow, J.E., 2003. Deep melting and sodic metasomatism underneath the highly oblique-spreading Lena Trough (Arctic Ocean). *Earth Planet. Sci. Lett.*, **216**, 283–299.

Hidas, K., Booth-Rea, G., Garrido, C.J., Martínez-Martínez, J.M., Padrón-Navarta, J.A., Konc, Z., Giaconia, F., Frets, E., Marchesi, C., 2013a. Backarc basin inversion and subcontinental mantle emplacement in the crust: kilometre-scale folding and shearing at the base of the proto-Albor_an lithospheric mantle (Betic Cordillera, southern Spain). *J. Geol. Soc.,* **170**, 47–55.

Hidas, K., Garrido, C.J., Tommasi, A., Padr_on-Navarta, J.A., Thielmann, M., Konc, Z., Frets, E., Marchesi, C., 2013b. Strain localization in pyroxenite by reaction-enhanced softening in the shallow subcontinental lithospheric mantle. *J. Petrol.,* **54**, 1997–2031.

Hidas, K., Varas-Reus, M.I., Garrido, C.J., Marchesi, C., Acosta-Vigil, A., Padrón-Navarta, J.A., Targuisti, K., Konc, Z., 2015. Hyperextension of continental to oceanic-like lithosphere: the record of late gabbros in the shallow subcontinental lithospheric mantle of the westernmost Mediterranean. *Tectonophysics,* **650**, 65–79.

Hoehler, T.M., Roberts, B.A., Foster, A.L., 2009. Actively serpentinizing seeps in the Bay of island ophiolites, western newfoundland: a window into the deep biosphere. In: *Annual Meeting Geological Society of America Abstracts with Programs,* **41**, 378.

Homma, A., Tsukahara, H., 2008. Chemical characteristics of hot spring water and geological environment in the northernmost area of the Itoigawa Shizuoka tectonic line. *Bull Earthw. Res. Inst. Univ. Tokyo,* **83**, 217–225.

Hopkinson L., Kristova P., Rutt K., Cressey G. (2012) Phase transitions in the system MgO – CO2 – H2O during CO2 degassing of Mg-bearing solutions. *Geochim. Cosmochim. Acta,* **76**, 1–13.

Hopkinson L., Rutt K., Cressey G. (2008) The transformation of nesquehonite to hydromagnesite in the system CaO-MgO-H2O-CO2: An experimental spectroscopic study. *J. Geol.,* **116**, 387–400.

Hostetler, P.B., Coleman, R.G., Mumpton, F.A., 1966. Brucite in alpine serpentinites. *Am. Mineral.,* **51**, 75–98.

Hseu, Z.Y., Tsai, H., Hsi, H.C., Chen, Y.C., 2007. Weathering sequences of clay minerals in soils along a serpentinitic toposequence. *Clays and Clay Min.,* **55**, 389–401.

Hyndman, R.D., Peacock, S.M., 2003. Serpentinization of the forearc mantle. *Earth Planet. Sci. Lett.*, **212**, 417-432.

Ildefonse, B., Blackman, D.K., John, B.E., Ohara, Y., Miller, D.J., MacLeod, C.J., 2007. Oceanic core complexes and crustal accretion at slow-spreading ridges. *Geology*, **35**, 623–626.

Jackson, M.P., Cramez, C., Fonck, J.M., 2000. Role of subaerial volcanic rocks and mantle plumes in creation of South Atlantic margins: implications for salt tectonics and source rocks. *Marine and Petroleum Geology*, ***17***, 477–498.

Jauffret G., Morrison J., Glasser F. P., 2015. On the thermal decomposition of nesquehonite. *J. Therm. Anal. Calorim.*, 5–10.

Johnson, K.T.M., Dick, H.J.B., 1992. Open system melting and temporal and spatial variation of peridotite and basalt at the Atlantis II Fracture Zone. *J. Geoph. Res.*, **97**, 9219–9241.

Jones, B., 2017a. Review of calcium carbonate polymorph precipitation in spring systems. *Sediment. Geol.*, **353**, 64–75.

Jones, B., 2017b. Review of aragonite and calcite crystal morphogenesis in thermal spring systems. *Sediment. Geol.*, **354**, 9–23.

Jones, B., Peng, X., 2016. Mineralogical, crystallographic, and isotopic constraints on the precipitation of aragonite and calcite at Shiqiang and other hot springs in Yunnan Province, China. *Sediment. Geol.*, **345**, 103–125.

Kelemen, P.B., Koga, K., Shimizu, N., 1997. Geochemistry of gabbro sills in the crust-mantle transition zone of the Oman ophiolite: Implications for the origin of the oceanic lower crust. *Earth Planet. Sci. Lett.*, **146**, 475–488.

Kelemen, P.B., Manning, C.E., 2015. Reevaluating carbon fluxes in subduction zones, what goes down, mostly comes up. *Proc. Natl. Acad. Sci.*, **112**, 3997-4006.

Kelemen, P.B., Matter, J.M., 2008. In situ carbonation of peridotite for CO2 storage. *Proc. Natl. Acad. Sci. U. S. A.* **105**, 17295–17300.

Kelemen, P.B., Matter, J., Streit, E.E., Rudge, J.F., Curry, W.B., Blusztajn, J., 2011. Rates and mechanisms of mineral carbonation in peridotite: natural processes and recipes for enhanced, in situ CO2 capture and storage. *Annu. Rev. Earth Planet Sci.*, **39**, 545–576.

Kelley, D.S., Karson, J.A., Blackman, D.K., Früh-Green, G.L., Butterfield, D.A., Lilley, M.D., Olson, E.J., Schrenk, M.O., Roe, K.K., Lebon, G.T., Rivizzigno, P., 2001. An off-axis hydrothermal vent field near the Mid-Atlantic Ridge at 30º N. *Nature*, **412**, 145–149.

Kelley, D.S., Karson, J.A., Früh-Green, G.L., Yoerger, D.R., Shank, T.M., Butterfield, D.A., Hayes, J.M., Schrenk, M.O., Olson, E.J., Proskurowski, G., Jakuba, M., Bradley, A., Larson, B., Ludwig, K., Glickson, D., Buckman, K., Bradley, A.S., Brazelton, W.J., Roe, K., Elend, M.J., Delacour, A., Bernasconi, S.M., Lilley, M.D., Baross, J.A., Summons, R.E., Sylva, S.P., 2005. A serpentinite-hosted ecosystem: the Lost City hydrothermal field. *Science*, **307**, 1428–1434.

Kellermeier, M., Melero-Garcia, E., Glaab, F., Klein, R., Drechsler, M., Rachel, R., García-Ruíz, J.M., Kunz, W., 2010. Stabilization of amorphous calcium carbonate in inorganic silica-rich environments. *J. Amer. Chem. Soc.*, **132**, 17859–17866.

Kerrick, D.M., Connolly, J.A.D., 1998. Subduction of ophicarbonates and recycling of CO2 and H_2O. *Geology*, **26**, 375–378.

Kitamura, M., 2001. Crystallization and transformation mechanism of calcium carbonate polymorphs and the effect of magnesium ion. *J. Colloid. Interface Sci.*, **236**, 318–327.

Klein, F., Bach, W., Humphris, S.E., Kahl, W.A., Jöns, N., Moskowitz, B. and Berquó, T.S., 2014. Magnetite in seafloor serpentinite—Some like it hot. *Geology*, **42**, 135–138.

Klein, F., Bach, W. and McCollom, T.M., 2013. Compositional controls on hydrogen generation during serpentinization of ultramafic rocks. *Lithos*, **178**, 55–69.

Klein, F., Bach, W., Jöns, N., McCollom, T., Moskowitz, B., Berquó, T., 2009. Iron partitioning and hydrogen generation during serpentinization of abyssal peridotites from 15º N on the Mid-Atlantic Ridge. *Geochim. Cosmochim. Acta*, **73**, 6868–6893.

Klein, F., Garrido, C.J., 2011. Thermodynamic constraints on mineral carbonation of serpentinized peridotite. *Lithos*, **126**, 147–160.

Klein, F., McCollom, T.M., 2013. From serpentinization to carbonation: new insights from a CO2 injection experiment. *Earth Planet. Sci. Lett.*, **379**, 137–145.

Kloprogge, J.T., Martens, W.N., Nothdurft, L., Duong, L.V., Webb, G.E., 2003. Low temperature synthesis and characterization of nesquehonite. *J. Mater. Sci. Lett.*, **22**, 825–829.

Königsberger E., Königsberger L.-C., Gamsjäger H., 1999. Low-temperature thermodynamic model for the system Na_2CO_3-$MgCO_3$–$CaCO_3$–H_2O. *Geochim. Cosmochim. Acta,* **63**, 3105–3119.

Kristova P., Hopkinson L. J., Rutt K. J., Hunter H. M. A., Cressey G., 2014. Carbonate mineral paragenesis and reaction kinetics in the system MgO–CaO–CO_2–H_2O in presence of chloride or nitrate ions at near surface ambient temperatures. *Appl. Geochemistry,* **50**, 16–24.

Kumar, N., Reisberg, L., Zindler, A., 1996. A major and trace element and strontium, neodymium, and osmium isotopic study of a thick pyroxenite layer from the Beni Bousera ultramafic complex of northern Morocco. *Geochim. Cosmochim. Acta,* **60**, 1429–1444.

Lacelle, D., Lauriol, B., Clark, I.D., 2009. Formation of seasonal ice bodies and associated cryogenic carbonates in Caverne de l'Ours, Québec, Canada: kinetic isotope effects and pseudo-biogenic crystal structures. J. *Cave Karst Stud.*, **71**, 48–62.

Lackner, K.S., Wendt, C.H., Butt, D.P., Joyce, E.L., Sharp, D.H., 1995. Carbon dioxide disposal in carbonate minerals. *Energy*, **20**, 1153–1170.

Lagabrielle, Y., Guivel, C., Maury, R.C., Bourgois, J., Fourcade, S., Martin, H., 2000. Magmatic–tectonic effects of high thermal regime at the site of active ridge subduction: the Chile Triple Junction model. *Tectonophysics*, **326**, 255–268.

Lanas J., Alvarez J. I., 2004. Dolomitic lime: Thermal decomposition of nesquehonite. *Thermochim. Acta,* **421**, 123–132.

Land, L.S., 1998. Failure to precipitate dolomite at 25 ºC from dilute solution despite 1000-fold oversaturation after 32 years. *Aquat. Geochem.*, **4**, 361–368.

Lane, N., Martin, W., 2010. The energetics of genome complexity. *Nature*, **467**, 929.

Lang, S.Q., Butterfield, D.A., Schulte, M., Kelley, D.S., Lilley, M.D., 2010. Elevated concentrations of formate, acetate and dissolved organic carbon found at the Lost City hydrothermal field. *Geochim. Cosmochim. Acta,* **74**, 941–952.

Langmuir D., 1965. Stability of carbonates in the system MgO–CO_2–H_2O. *J. Geol.,* **73**, 730–754.

Leleu, T., Chavagnac, V., Delacour, A., Noiriel, C., Ceuleneer, G., Aretz, M., Rommevaux, C., Ventalon, S., 2016. Travertines associated with hyperalkaline springs: evaluation as a proxy for paleoenvironmental conditions and sequestration of atmospheric CO_2. *J. Sediment. Res.*, **86**, 1328–1343.

Lenoir, X., Garrido, C., Bodinier, J., Dautria, J., Gervilla, F., 2001. The recrystallization front of the Ronda peridotite: evidence for melting and thermal erosion of subcontinental lithospheric mantle beneath the Alboran basin. *J. Petrol.*, **42**, 141–158.

Levy, D.B., Schramke, J.A., Esposito, K.J., Erickson, T.A., Moore, J.C., 1999. The shallow ground water chemistry of arsenic, fluorine, and major elements: Eastern Owens Lake, California. *Appl. Geochem.*, **14**, 53–65.

Lewis, J.F., Draper, G., Proenza, J.A., Espaillat, J., Jiménez, J., 2006. Ophiolite-related ultramafic rocks (serpentinites) in the Caribbean region: a review of their occurrence, composition, origin, emplacement and Nilaterite soil formation. *Geolog. Acta: an international earth science journal*, **4**, 237–263.

Liou J.G., Zhang R.Y., Ernst W.G., 2007. Very high-pressure orogenic garnet peridotites. *PNAS,* **104**, 9116–9121.

Lin, Y.P., Singer, P.C, 2009. Effect of Mg^{2+} on the kinetics of calcite crystal growth. *J. Cryst. Growth*, **312**, 136–140.

Lippard, S.J., Shelton, A.W., Gass, I.G., 1986. The ophiolite of Northern Oman. Published for *The Geological Society by Blackwell Scientific Publications.*

Lister, G., Forster, M., 2009. Tectonic mode switches and the nature of orogenesis. *Lithos*, **113**, 274–291.

Loomis, T.P., 1972. Diapiric emplacement of the Ronda high-temperature ultramafic intrusion, southern Spain. *Geol. Soc. Am. Bul.*, **83**, 2475–2496.

Loomis, T.P., 1975. Tertiary mantle diapirism, orogeny, and plate tectonics east of the Strait of Gibraltar. *Am. J. Sci.*, **275**, 1–30.

Lonergan, L., White, N., 1997. Origin of the Betic-Rif mountain belt. *Tectonics,* **16**, 504–522.

Lu, G., Zheng, C., Donahoe, R.J., Lyons, W.B., 2000. Controlling processes in a $CaCO_3$ precipitating stream in Huanglong natural scenic district, sichuan, *China. J. Hydrol.*, **230**, 34–54.

Ludwig, K.A., Kelley, D.S., Butterfield, D.A., Nelson, B.K., Früh-Green, G., 2006. Formation and evolution of carbonate chimneys at the Lost City Hydrothermal Field. *Geochim. Cosmochim. Acta*, **70**, 3625–3645.

Matter, J., Assayag, N., Goldberg, D., 2006. Basaltic rocks and their potential to permanently sequester industrial carbon dioxide emissions. GHGT- 8:https://events.adm.ntnu.no/ei/

Matter, J.M., Kelemen, P.B., 2009. Permanent storage of carbon dioxide in geological reservoirs by mineral carbonation. *Nat. Geosci.*, **2**, 837–841.

Matter J., Stute M., Snæbjörnsdottir S.Ó., Oelkers E., Gislason S. R., Aradottir E. S., Sigfusson B., Gunnarsson I., Alfredsson H. A., Wolff-boenisch D., Mesfin K., Fernandez de la Reguera Taya D., Hall J., Dideriksen K., Broecker W. S., 2016. Rapid carbon mineralization for permanent disposal of anthropogenic carbon dioxide emissions. *Science* **352**, 1312–1314.

Marchesi, C., Garrido, C.J., Bosch, D., Bodinier, J.-L., Hidas, K., Padron-Navarta, J.A., Gervilla, F., 2012. A late Oligocene suprasubduction setting in the Westernmost Mediterranean revealed by intrusive pyroxenite dikes in the Ronda Peridotite (Southern Spain). *J. Geol.*, **120**, 237–247.

Margiotta, S., Mongelli, G., Summa, V., Paternoster, M., Fiore, S., 2012. Trace element distribution and Cr(VI) speciation in Ca–HCO_3 and Mg–HCO_3 spring waters from the northern sector of the Pollino massif, southern Italy. *J. Geochem. Explor.*, **115**, 1–12.

Martín-Algarra, A., 1987. Evolucion geológica alpina del contacto entre las zonas internas y las zonas externas de la cordillera Betica (sector centro-occidental). *Doctoral dissertation, Universidad de Granada, Spain*.

Martin, W., Baross, J., Kelley, D., Russell, M.J., 2008. Hydrothermal vents and the origin of life. *Nat. Rev. Microbiol.* **6**, 805.

Martin, W., Russell, M.J., 2007. On the origin of biochemistry at an alkaline hydrothermal vent. Philos. *Trans. R. Soc. Biol. Sci.*, **362**, 1887–1926.

Martinez, F., Taylor, B., 2002. Mantle wedge control on back-arc crustal accretion. *Nature*, **416**, 417–420.

Martinez, R.E., Gardes, E., Pokrovsky, O.S., Schott, J., Oelkers, E.H., 2010. Do photosynthetic bacteria have a protective mechanism against carbonate precipitation at their surfaces? *Geochem. Cosmochim. Acta***, 74**, 1329–1337.

Martos-Rosillo, S., González-Ramón, A., Jiménez-Gavilán, P., Andreo, B., Durán, J.J., Mancera, E., 2015. Review on groundwater recharge in carbonate aquifers from SW Mediterranean (Betic Cordillera, S Spain). *Environ. Earth Sci.* **74**, 7571–7581.

Marques, J.M., Carreira, P.M., Carvalho, M.R., Matias, M.J., Goff, F.E., Basto, M.J., Graça, R.C., Aires-Barros, L., Rocha, L., 2008. Origins of high pH mineral waters from ultramafic rocks, Central Portugal. *Appl. Geochem.* **23**, 3278–3289.

Mavromatis V., Pearce C. R., Shirokova L. S., Bundeleva I. A., Pokrovsky O. S., Bénézeth P., Oelkers E. H., 2012. Magnesium isotope fractionation during hydrous magnesium carbonate precipitation with and without cyanobacteria. *Geochim. Cosmochim. Acta* **76**, 161–174.

Mazzoli, S., Martin-Algarra, A., 2011. Deformation partitioning during transpressional emplacement of a ’mantle extrusion wedge’: the Ronda peridotites, western Betic Cordillera, Spain. *J. Geol. Soc.*, **168**, 373-382.

Mazzoli, S., Martín-Algarra, A., Reddy, S.M., López Sánchez-Vizcaíno, V., Fedele, L., Noviello, A., 2013. The evolution of the footwall to the Ronda subcontinental mantle peridotites: insights from the Nieves Unit (western Betic Cordillera). *J. Geol. Soc.* **170**, 385-402.

McCollom, T.M., 2016. Abiotic methane formation during experimental serpentinization of olivine. *Proc. Natl. Acad. Sci.* **113**, 13965–13970.

McCollom, T.M., Bach, W., 2009. Thermodynamic constraints on hydrogen generation during serpentinization of ultramafic rocks. *Geochim. Cosmochim. Acta,* **73**, 856–875.

McCollom, T.M., Klein, F., Robbins, M., Moskowitz, B., Berqu_o, T.S., Jons, N., Bach, W., Templeton, A., 2016. Temperature trends for reaction rates, hydrogen generation, and partitioning of iron during experimental serpentinization of olivine. Geochem. Cosmochim. Acta, **181**, 175–200.

McCollom, T.M., Seewald, J.S., 2013. Serpentinites, hydrogen, and life. *Elements*, **9**, 129–134.

McCutcheon, J., Dipple, G.M., Wilson, S.A., Southam, G., 2015. Production of magnesium-rich solutions by acid leaching of chrysotile: A precursor to field-scale deployment of microbially enabled carbonate mineral precipitation. *Chem. Geol.*, **413**, 119–131.

McCutcheon, J., Power, I.M., Harrison, A.L., Dipple, G.M., Southam, G., 2014. A greenhouse-scale photosynthetic microbial bioreactor for carbon sequestration in magnesium carbonate minerals. *Environ. Sci. Technol.*, **48**, 9142–9151.

Mehl, M.R. Pennebaker, J.W., 2003. The social dynamics of a cultural upheaval: Social interactions surrounding September 11, 2001. *Psychol. Sci.*, **14**, 579–585.

Meldrum, F.C., Colfen, H., 2008. Controlling mineral morphologies and structures in biological and synthetic systems. *Chem. Rev.*, **108**, 4332–4432.

Melson W.G., Jarosewich E., Bowen V.T., Thompson G., 1967. Saint Peter and Saint Paul Rocks: A high-temperature, mantle-derived intrusion. *Science*, **156**, 1532–1535.

Ménez, B., Pasini, V., Brunelli, D., 2012. Life in the hydrated suboceanic mantle. *Nat. Geosci.*, **5**, 133-137.

Ménez, B., Pisapia, C., Andreani, M., Jamme, F., Vanbellingen, Q.P., Brunelle, A., Richard, L., Dumas, P., Réfrégiers, M., 2018. Abiotic synthesis of amino acids in the recesses of the oceanic lithosphere. *Nature*, **564**, 59–63.

Menzel, M.D., Garrido, C.J., López Sánchez-Vizcaíno, V., Marchesi, C., Hidas, K., Escayola, M.P., Delgado Huertas, A., 2018. Carbonation of mantle peridotite by CO_2-rich fluids: the formation of listvenites in the Advocate ophiolite complex (Newfoundland, Canada). *Lithos*, **323**, 238–261.

Menzel, M.D., Garrido, C.J., López Sánchez-Vizcaíno, V., Hidas, K., Marchesi, C., 2019. Subduction metamorphism of serpentinite-hosted carbonates beyond antigorite serpentinite dehydration (Nevado-Filábride Complex, Spain). *J. Metamorph. Geol.*, **37**, 681–715.

Menzies, M.A., Dupuy, C., 1991. Orogenic massifs: protolith, process and provenance. *J. Petrol.*, 1–16.

Mervine, E.M., Humphris, S.E., Sims, K.W., Kelemen, P.B., Jenkins, W.J., 2014. Carbonation rates of peridotite in the Samail Ophiolite, Sultanate of Oman, constrained through 14C dating and stable isotopes. *Geochim. Cosmochim. Acta*, **126**, 371–397.

Mignardi, S., De Vito, C., Ferrini, V., Martin, R.F., 2011. The efficiency of CO_2 sequestration via carbonate mineralization with simulated wastewaters of high salinity. *J. Hazard. Mater.*, **191**, 49–55.

Miller, H.M., Matter, J.M., Kelemen, P., Ellison, E.T., Conrad, M.E., Fierer, N., Ruchala, T., Masako, T., Templeton, A.S., 2016. Modern water/rock reactions in Oman hyperalkaline peridotite aquifers and implications for microbial habitability. *Geochim. Cosmochim. Acta*, **179**, 217–241.

Miošić, N., Samardžić, N., 2016. Mineral, thermal and thermomineral Waters of Bosnia and Herzegovina. In *Mineral and Thermal Waters of Southeastern Europe*, 147–171. Springer, Cham.

Miyashiro, A., Shido, F., Ewing, M., 1969. Composition and origin of serpentinites from the Mid-Atlantic Ridge near 24 and 30 north latitude. *Contrib. Mineral. Petr.*, **23**, 117–127.

Monnier, C., Girardeau, J., Le Mée, L., Polvé, M., 2006. Along-ridge petrological segmentation of the mantle in the Oman ophiolite. *Geochem. Geophys. Geosyst.*, **7**, 11008.

Monnin, C., Chavagnac, V., Boulart, C., Ménez, B., Gérard, M., Gérard, E., Pisapia, C., Quéméneur, M., Erauso, G., Postec, A., Guentas-Dombrowski, L., Payri, C., Pelletier, B., 2014. Fluid chemistry of the low temperature hyperalkaline hydrothermal system of Prony Bay (New Caledonia). *Biogeosciences*, **11**, 5687.

Montes-Hernandez G., Renard F., Chiriac R., Findling N., Toche F., 2012. Rapid precipitation of magnesite microcrystals from $Mg(OH)_2$–H_2O–CO_2 slurry enhanced by NaOH and a heat-aging step (from ~20 to 90 °C). *Cryst. Growth Des.*, **12**, 5233–5240.

Montserrat F., Renforth P., Hartmann J., Knops P., Leermakers M., Meysman F. J. R., 2017. Olivine dissolution in seawater: Implications for CO2 sequestration through Enhanced Weathering in coastal environments. *Environ. Sci. Technol.*, **51**, 3960–3972.

Mottl, M.J., Wheat, C.G., Fryer, P., Gharib, J., Martin, J.B., 2004. Chemistry of springs across the Mariana forearc shows progressive devolatilization of the subducting plate. *Geochim. Cosmochim.Acta*, **68**, 4915–4933.

Morgan B., Wilson S. A., Madsen I. C., Gozukara Y. M., Habsuda J., 2015. Increased thermal stability of nesquehonite ($MgCO_3 \cdot 3H_2O$) in the presence of humidity and CO_2: Implications for low temperature CO_2 storage. *Int. J. Greenhouse Gas Control,* **39**, 366–376.

Morrill, P.L., Kuenen, J.G., Jonhson, O.G., Suzuki, S., Rietze, A., Sessions, A.L., Fogel, M.L., Nealson, K.H., 2013. Geochemistry and geobiology of a present-day serpentinization site in California: The Cedars. *Geochim. Cosmochim. Acta*, **109**, 222–240.

Müller, G., Irion, G., Förstner, U., 1972. Formation and diagenesis of inorganic Ca–Mg carbonates in the lacustrine environment. *Naturwissenschaften*, **59**, 158–164.

Müller, D.W., McKenzie, J.A., Mueller, P.A., 1990. Abu Dhabi sabkha, Persian Gulf, revisited: application of strontium isotopes to test an early dolomitization model. *Geology*, **18**, 618–621.

Müller, R.D., Sdrolias, M., Gaina, C., Roest, W.R., 2008. Age, spreading rates, and spreading asymmetry of the world's ocean crust. *Geochem., Geophys., Geosys.*, **9**. 10.1029/2007GC001743.

Müntener, O., Hermann, J., 1996. The Val Malenco lower crust–upper mantle complex and its field relations (Italian Alps). *Schweizerische Mineralogische und Petrographische Mitteilungen*, **76**, 475–500.

Müntener, O., Manatschal, G., 2006. High degrees of melt extraction recorded by spinel harzburgite of the Newfoundland margin: The role of inheritance and consequences for the evolution of the southern North Atlantic. *Earth Planet. Sci. Lett.*, **252**, 437–452.

Neal, C., Shand, P., 2002. Spring and surface water quality of the Cyprus ophiolites. *Hydrol. Earth Syst. Sci.*, **6**, 797–817.

Neal, C., Stanger, G., 1983. Hydrogen generation from mantle source rocks in Oman. *Earth Planet. Sci. Lett.*, **66**, 315–320.

Neal, C., Stanger, G., 1984. Calcium and magnesium hydroxide precipitation from alkaline groundwaters in Oman, and their significance to the process of serpentinization. *Mineral. Mag.* **48**, 237–241.

Neal, C., Stanger, G., 1985. Past and present serpentinization of ultramafic rocks: an example from the Semail ophiolite nappe of northern Oman. In: Drewer, J.I. (Ed.), The Chemistry of Weathering. D. Reidel Publishing Company, Holland, 249–275.

Nicolas A., 1989. Structure of Ophiolites and Dynamics of Oceanic Lithosphere. Dordrecht, Boston: Kluwer Academic Press.

Nicolas, A., Boudier, F., 2003. Where ophiolites come from and what they tell us. *Special papers-Geological Society of America*, 137–152.

Nicolas, A., Boudier, F., Ildefonse, V., Ball, E., 2000. Accretion of Oman and United Arab Emirates ophiolite—discussion of a new structural map. *Mar. Geophys.* Res., **21**, 147–149.

Nicula, A.M.,, Baciu, C., 2010. Potential occurrence of alkaline waters in ophiolites from Banat and Apuseni Mountains (Western Romania). www.ecoterra-online.ro/files/1578765678.pdf.

Niu, Y., Hékinian, R., 1997. Basaltic liquids and harzburgitic residues in the Garrett Transform: a case study at fast-spreading ridges. *Earth Planet. Sci. Lett.*, **146**, 243–258.

Nixon, P.H., Rogers, N.W., Gibson, I.L., Grey, A., 1981. Depleted and fertile mantle xenoliths from southern African kimberlites. *Ann. Rev.Earth Planet. Sci. Lett.*, **9**, 285–309.

Obata, M., Suen, C.J., Dickey, J.S., 1980. The origin of mafic layers in the Ronda hightemperature peridotite intrusion, S. Spain: an evidence of partial fusion and fractional crystallization in the upper mantle. *Colloques Internationaux CNRS*, **272**, 257–268.

O'Hara M. J., 1967. Mineral parageneses in ultramafic rocks. In: *Wyllie PJ (ed.) Ultramafic and Related Rocks*, 393–403. New York: Wiley.

Okland, I., Huang, S., Dahle, H., Thorseth, I.H., Pedersen, R.B., 2012. Low temperature alteration of serpentinized ultramafic rock and implications for microbial life. *Chem. Geol.*, **318**, 75–87.

Olsson, J., Stipp, S.L.S., Gislason, S.R., 2014. Element scavenging by recently formed travertine deposits in the alkaline springs from the Oman Semail Ophiolite. *Min. Mag.*, **78**, 1479–1490.

O'Neil, J.R., Barnes, I., 1971. ^{13}C and ^{18}O compositions in some fresh-water carbonates associated with ultramafic rocks and serpentinites: western United States. *Geochim. Cosmochim. Acta*, **35**, 687–697.

Oskierski H. C., Dlugogorski B. Z., Jacobsen G., 2013. Sequestration of atmospheric CO_2 in chrysotile mine tailings of the Woodsreef Asbestos Mine, Australia: Quantitative mineralogy, isotopic fingerprinting and carbonation rates. *Chem. Geol.*, **358**, 156–169.

Oskierski H. C., Dlugogorski B. Z., Oliver T. K., Jacobsen G., 2016. Chemical and isotopic signatures of waters associated with the carbonation of ultramafic mine tailings, Woodsreef Asbestos Mine, Australia. *Chem. Geol,*. **436**, 11–23.

Orr Chazen, P., Ehrlich, R., 1973. Low-temperature synthesis of dolomite from aragonite. *Geol. Soc. Am. Bull.*, **84**, 3627–3634.

Oudech, S., Djokic, I., 2015. Geothermal energy use, country update for Serbia. In *Proceeding, World Geothermal Congress*, 10.

Palandri, J.L., Reed, M.H., 2004. Geochemical models of metasomatism in ultramafic systems: serpentinization, rodingitization, and sea floor carbonate chimney precipitation. *Geochem. Cosmochim. Acta*, **68**, 1115–1133.

Pallister J. S., Hopson C. A., 1981. Samail ophiolite plutonic suite: Field relations, phase variation, cryptic variation and layering, and a model of a spreading ridge magma chamber. *J. Geophys. Res.*, **86**, 2593–2644.

Parkhurst, D.L., Appelo, C.A.J., 1999. User's guide to PHREEQC (version 2): a computer program for speciation, batch-reaction, one-dimensional transport, and inverse geochemical calculations. In: *US Geol. Survey Water Resour. Invest. Rep.*, **99**, 312.

Parkhurst, D.L., Appelo, C.A.J., 2005. PHREEQC-2 Version 2.12: A Hydrochemical Transport Model. US Geological Survey Central Region Research, USGS Water Resources Division. http://wwwbrr.cr.usgs.gov/projects/GWC_coupled/phreeqc.

Parkinson, I.J., Pearce, J.A., 1998. Peridotites from the Izu–Bonin–Mariana forearc (ODP Leg 125): evidence for mantle melting and melt–mantle interaction in a supra-subduction zone setting. *J. Petrol.*, **39**, 1577–1618.

Paukert, A.N., Matter, J.M., Kelemen, P.B., Shock, E.L., Havig, J.R., 2012. Reaction path modeling of enhanced in situ CO_2 mineralization for carbon sequestration in the peridotite of the Samail Ophiolite, Sultanate of Oman. *Chem. Geol.*, **330–331**, 86–100.

Pawson, J.F., 2015. Abiotic Methane Formation at the Dun Mountain Ophiolite, New Zealand. *M.Sc. Thesis*, University of Canterbury, New Zealand. http://hdl.handle.net/10092/10280.

Pearson, D.G., Nowell, G.M., 2004. Re–Os and Lu–Hf isotope constraints on the origin and age of pyroxenites from the Beni Bousera peridotite massif: implications for mixed peridotite–pyroxenite mantle sources. *J.Petrol.*, **45**, 439-455.

Pearson, D.G., Canil, D., Shirey, S.B., 2003. Mantle samples included in volcanic rocks: xenoliths and diamonds. *Treatise on Geochemistry*, **2**, 568. Springer.

Peckmann, J., Thiel, V., 2004. Carbon cycling at ancient methaneeseeps. *Chem. Geol.*, **205**, 443-467.

Pentecost, A., 1992. Carbonate chemistry of surface waters in a temperate karst region: the southern Yorkshire Dales, UK. *J. Hydrol.*, **139**, 211–232.

Pentecost, A., 2005. Travertine. Springer-Verlag, Berlin.

Platt, J.P., Anczkiewicz, R., Soto, J.I., Kelley, S.P., Thirlwall, M., 2005. Early Miocene continental subduction and rapid exhumation in the western Mediterranean. *Geology*, **34**, 981-984.

Platt, J.P., Behr, W.M., Johanesen, K., Williams, J.R., 2013. The betic-rif arc and its orogenic hinterland: a review. *Annu. Rev. Earth Planet Sci.*, **41**, 313–357.

Pfiffner, M., Trommsdorff, V., 1998. The high-pressure ultramafic-mafic-carbonate suite of Cima Lunga-Adula, Central Alps: excursions to Cima di Gagnone and Alpe Arami. *Schweizerische Mineralogische und Petrographische Mitteilungen*, **78**, 337–354.

Pokrovsky, O.S., 1998. Precipitation of calcium and magnesium carbonates from homogeneous supersaturated solutions. *J. Cryst. Growth*, **186**, 233–239.

Pokrovsky, O.S., Schott, J., Thomas, F., 1999. Dolomite surface speciation and reactivity in aquatic systems. *Geochim. Cosmochim. Acta*, **63**, pp.3133-3143.

Pope, M.C., Grotzinger, J.P., 2000. Controls on fabric development and morphology of tufas and stromatolites, uppermost Pethel Group (1.8 Ga), Great Slave Lake, northwest Canada. In: Grotzinger, J.P., James, N.P. (Eds.), Carbonate Sedimentation and Diagenesis in the Evolving Precambrian World. SEPM Special Publication, Tulsa, OK.

Power, I.M., Wilson, S.A., Thom, J.M., Dipple, G.M., Southam, G., 2007. Biologically induced mineralization of dypingite by cyanobacteria from an alkaline wetland near Atlin, British Columbia, Canada. *Geochem. Trans.*, **8**, 13.

Power, I.M., Wilson, S.A., Thom, J.M., Dipple, G.M., Gabites, J.E., Southam, G., 2009. The hydromagnesite playas of Atlin, British Columbia, Canada: a biogeochemical model for CO2 sequestration. *Chem. Geol.*, **260**, 286–300.

Power, I.M., Dipple, G.M., Southam, G., 2010. Bioleaching of ultramafic tailings by *Acidithiobacillus* spp. for CO_2 sequestration. *Environ. Sci. Technol.*, **44**, 456–462.

Power, I.M., Wilson, S.A., Dipple, G.M., 2013a. Serpentinite carbonation for CO_2 sequestration. *Elements*, **9**, 115–121.

Power, I.M., Harrison, A.L., Dipple, G.M., Wilson, S.A., Kelemen, P.B., Hitch, M., Southam, G., 2013b. Carbon mineralization: from natural analogues to engineered systems. Rev. Mineral. *Geochem.*, **77**, 305–360.

Power, I.M., Harrison, A.L., Dipple, G.M., Wilson, S.A., Barker, S.L., Fallon, S.J., 2019. Magnesite formation in playa environments near Atlin, British Columbia, Canada. *Geochim. Cosmochim. Acta*, **255**, 1–24.

Power, I.M., Wilson, S.A., Harrison, A.L., Dipple, G.M., McCutcheon, J., Southam, G., Kenward, P.A., 2014. A depositional model for hydromagnesite–magnesite playas near Atlin, British Columbia, Canada. *Sedimentology*, **61**, 1701-1733.

Precigout, J., Gueydan, F., Garrido, C.J., Cogné, N., Booth-Rea, G., 2013. Deformation and exhumation of the Ronda peridotite (Spain). *Tectonics*, **32**, 1011–1025.

Prinz, M., Keil, K., Green, J.A., Reid, A.M., Bonatti, E., Honnorez, J., 1976. Ultramafic and mafic dredge samples from the equatorial Mid-Atlantic ridge and fracture zones. *J. Geophys. Res.*, **81**, 4087-4103.

Pronost, J., Beaudoin, G., Lemieux, J.M., Hébert, R., Constantin, M., Marcouiller, S., Klein, M., Duchesne, J., Molson, J.W., Larachi, F., Maldague, X., 2012. CO_2-depleted warm air venting from chrysotile milling waste (Thetford Mines, Canada): Evidence for in-situ carbon capture from the atmosphere. *Geology*, **40**, 275–278.

Proskurowski, G., Lilley, M.D., Kelley, D.S., Olson, E.J., 2006. Low temperature volatile production at the Lost City Hydrothermal Field, evidence from a hydrogen stable isotope geothermometer. *Chem. Geol.*, **229**, 331–343.

Rabenhorst, M.C., Foss, J.E., Fanning, D.S., 1982. Genesis of Maryland soils formed from serpentinite. *Soil Sci. Soc. Am. J.*, **46**, 607–616.

Reddy, M.M., Wang, K.K., 1980. Crystallization of calcium carbonate in the presence of metal ions: I. Inhibition by magnesium ion at pH 8.8 and 25 ºC. *J. Cryst. Growth*, **50**, 470-480.

Reisberg, L., Zindler, A, Jagoutz, E., 1989. Further Sr and Nd isotopic results from peridotites of the Ronda ultramafic complex. *Earth Planet. Sci. Lett.*, **96**, 161–180.

Rempfert, K.R., Miller, H.M., Bompard, N., Nothaft, D., Matter, J.M., Kelemen, P., Fierer, N., Templeton, A.S., 2017. Geological and geochemical controls on subsurface microbial life in the Samail Ophiolite, Oman. *Front. Microbiol.*, **8**, 56.

Renaut, R.W., 1993. Morphology, distribution, and preservation potential of microbial mats in the hydromagnesite-magnesite playas of the Cariboo Plateau, British Columbia, Canada. *Hydrobiologia*, **267**, 75–98.

Renaut, R.W., Jones, B., 1997. Controls on aragonite and calcite precipitation in hot spring travertines at Chemurkeu, Lake Bogoria, Kenya. Can. *J. Earth Sci.*, **34**, 801-818.

Renaut, R.W., Stead, D., 1990. Recent magnesite-hydromagnesite sedimentation in playa basins of the Cariboo plateau, British Columbia. *Geol. Soc. Geol. Fieldwork*, 1991-1.

Reuber, I., Michard, A., Chalouan, A., Juteau, T., Jermoumi, B., 1982. Structure and emplacement of the Alpine-type peridotites from Beni Bousera, Rif, Morocco: a polyphase tectonic interpretation. *Tectonophysics*, **82**, 231–251.

Rietveld, H., 1969. A profile refinement method for nuclear and magnetic structures. *J. Appl. Crystallogr.*, **2**, 65–71.

Rigopoulos I., Harrison A. L., Delimitis A., Ioannou I., Efstathiou A. M., Kyratsi T., Oelkers E. H. (2018) Carbon sequestration via enhanced weathering of peridotites and basalts in seawater. *Appl. Geochem.*, **91**, 197–207.

Roberts, J.A., Bennett, P.C., González, L.A., Macpherson, G.L., Milliken, K.L., 2004. Microbial precipitation of dolomite in methanogenic groundwater. *Geology*, **32**, 277–280.

Roberts, J.A., Kenward, P.A., Fowle, D.A., Goldstein, R.H., Gonz_alez, L.A., Moore, D.S., 2013. Surface chemistry allows for abiotic precipitation of dolomite at low temperature. *Proc. Natl. Acad. Sci.*, **110**, 14540–14545.

Rogerson, M., Pedley, H.M., Kelham, A., Wadhawan, J.D., 2014. Linking mineralisation process and sedimentary product in terrestrial carbonates using a solution thermodynamic approach. *Earth Surf. Dyn.*, **2**, 197.

Rosca, M., Bendea, C. Vîjdea, A.M., 2016. Mineral and Thermal Waters of Romania. In *Mineral and Thermal Waters of Southeastern Europe*, 97–114. Springer, Cham.

Royden, L.H., 1993. Evolution of retreating subduction boundaries formed during continental collision. *Tectonics*, **12**, 629-638.

Rowling, J., 2004. Studies on aragonite and its occurrence in caves, including New South Wales caves. *J. proc. R. Soc. N.S.W.*, **137**, 123–149.

Ruíz-Agudo, E., Putnis, C.V., Putnis, A., 2014. Coupled dissolution and precipitation at mineral–fluid interfaces. *Chem. Geol.*, **383**, 132–146.

Russell, M.J., Hall, A.J., Martin, W., 2010. Serpentinization as a source of energy at the origin of life. *Geobiology*, **8**, 355–371.

Russell, M.J., Ingham, J.K., Zedef, V., Maktav, D., Sunar, F., Hall, A.J. and Fallick, A.E., 1999. Search for signs of ancient life on Mars: expectations from hydromagnesite microbialites, Salda Lake, Turkey. *J. Geol. Soc.*, **156**, 869–888.

Saldi G. D., Jordan G., Schott J., Oelkers E. H., 2009. Magnesite growth rates as a function of temperature and saturation state. *Geochim. Cosmochim. Acta*, **73**, 5646–5657.

Sánchez-Murillo, R., Gazel, E., Schwarzenbach, E.M., Crespo-Medina, M., Schrenk, M.O., Boll, J., Gill, B.C., 2014. Geochemical evidence for active tropical serpentinization in the Santa Elena Ophiolite, Costa Rica: an analog of a humid early Earth? *Geochem. Geophys. Geosyst.*, **15**, 1783–1800.

Sánchez-Roman, M., McKenzie, J.A., Wagener, A.D.L.R., Riva de Neyra, M.A., Vasconcelos, C., 2009. Presence of sulfate does not inhibit low-temperature dolomite precipitation. *Earth Planet. Sci. Lett.*, **285**, 131–139.

Saumur, B.M., Hattori, K.H. Guillot, S., 2010. Contrasting origins of serpentinites in a subduction complex, northern Dominican Republic. *Bulletin*, **122**, 292–304.

Schaef H. T., Windisch C. F., McGrail B. P., Martin P. F., Rosso K. M., 2011. Brucite [$Mg(OH_2)$] carbonation in wet supercritical CO_2: An in situ high pressure X-ray diffraction study. *Geochim. Cosmochim. Acta*, **75**, 7458–7471.

Schmidt, K., Koschinsky, A., Garbe-Schönberg, D., de Carvalho, L.M.,, Seifert, R., 2007. Geochemistry of hydrothermal fluids from the ultramafic-hosted Logatchev hydrothermal field, 15 N on the Mid-Atlantic Ridge: Temporal and spatial investigation. *Chem. Geol.*, **242**, 1–21.

Schrenk, M.O., Brazelton, W.J., Lang, S.Q., 2013. Serpentinization, carbon, and deep life. *Rev. Mineral. Geochem.*, **75**, 575–606.

Schuiling RD. 1964. Serpentinization as a possible cause of high heat-flow values in and near the oceanic ridges. *Nature*, **201**, 807–8

Schwartzman, D.W., Volk, T., 1989. Biotic enhancement of weathering and the habitability of Earth. *Nature*, **340**, 457-460.

Schwarzenbach, E.M., Früh-Green, G.L., Bernasconi, S.M., Alt, J.C., Plas, A., 2013. Serpentinization and carbon sequestration: A study of two ancient peridotite-hosted hydrothermal systems. *Chem. Geol.*, **351**, 115–133.

Searle, M.P., Cox, J., 2002. Subduction zone metamorphism during formation and emplacement of the Semail ophiolite in the Oman Mountains. *Geol. Mag.*, **139**, 241–255.

Seifritz, W., 1990. CO_2 disposal by means of silicates. *Nature*, **345**, 486.

Seyler, M., Lorand, J.-P., Toplis, M.J., Godard, G., 2004. Asthenospheric metasomatism beneath the mid-ocean ridge: evidence from depleted abyssal peridotites. *Geology*, **32**, 301–304.

Shirokova L. S., Mavromatis V., Bundeleva I. A., Pokrovsky O. S., Bénézeth P., Gérard E., Pearce C. R., Oelkers E. H., 2013. Using Mg isotopes to trace cyanobacterially mediated magnesium carbonate precipitation in alkaline lakes. *Aquat. Geochemistry*, **19**, 1–24.

Simandl, G.J., Paradis, S., Irvine, M., 2008. Brucite–uses, exploration guidelines and selected grass-root exploration targets. *Can. Inst. Min. Bull.*, **101**, 1–7.

Sleep, N.H., Bird, D.K., Pope, E.C., 2011. Serpentinite and the dawn of life. Philos. Trans. *R. Soc. Lond. Ser. B Biol. Sci.*, **366**, 2857–2869.

Soustelle, V., Tommasi, A., Bodinier, J.L., Garrido, C.J., Vauchez, A., 2009. Deformation and reactive melt transport in the mantle lithosphere above a large-scale partial melting domain: the Ronda Peridotite massif, Southern Spain. *J. Petrol.*, **50**, 1235–1266.

Stanger, G., 1986. The Hydrogeology of the Oman Mountains. Ph. D. thesis. Department of Earth Sciences, The Open University, U.K.

Stanger G., Laver J., Neal C., 1988. Black Carbonaceous Calcite Associated with Serpentinite from Oman. *Mineral. Mag.*, **52**, 403–408

Stanger G., Neal C., 1994. The occurrence and chemistry of huntite from Oman. *Chem. Geol.*, **112**, 274–254

Streit, E., Kelemen, P., Eiler, J., 2012. Coexisting serpentine and quartz from the carbonate bearing serpentinized peridotite in the Samail Ophiolite, Oman. Contrib. *Mineral. Petrol.*, **164**, 82–837.

Stumm, W., Morgan, J.J., 1996. Aquatic Chemistry: Chemical Equilibria and Rates in Natural Waters, 3^{erd} Edition. John Wiley and Sons.

Suarez, D.L., 1983. Calcite supersaturation and precipitation kinetics in the lower Colorado river, all-American canal and east highline canal. *Water Resour. Res.*, **19**, 653-661.

Suda, K., Gilbert, A., Yamada, K., Yoshida, N., Ueno, Y., 2017. Compound–and position–specific carbon isotopic signatures of abiogenic hydrocarbons from on–land serpentinite–hosted Hakuba Happo hot spring in Japan. *Geochim. Cosmochim. Acta*, **206**, 201–215.

Sayles, F.L., Fyfe, W.S., 1973. The crystallization of magnesite from aqueous solution. *Geochim. Cosmochim. Acta*, **37**(1), pp.87-99.

Szponar, N., Brazelton, W.J., Schrenk, M.O., Bower, D.M., Steele, A., Morrill, P.L., 2013. Geochemistry of a continental site of serpentinization, the Tablelands Ophiolite, Gros Morne National Park: a Mars analogue. *Icarus*, **224**, 286–296.

Takai, K., Moyer, C.L., Miyazaki, M., Nogi, Y., Hirayama, H., Nealson, K.H., Horikoshi, K., 2005. Marinobacter alkaliphilus sp. nov., a novel alkaliphilic bacterium isolated from subseafloor alkaline serpentine mud from Ocean Drilling Program Site 1200 at South Chamorro Seamount, Mariana Forearc. *Extremophiles*, **9**, 17–27.

Taylor, P.M., Chafetz, H.S., 2004. Floating rafts of calcite crystals in cave pools, central Texas, USA: crystal habit vs. saturation state. *J. Sediment. Res.*, **74**, 328–341.

Thayer T.P., 1960. Some critical differences between alpine-type and stratifor peridotite–gabbro complexes. In: *21st International Geolological Congress, Copenhagen,* 247–259.

Tilley, C.E., 1947. The dunite-mylonites of Saint Paul's Rocks (Atlantic). *Am. J. Sci.*, **245**, 483-491.

Todorović, M., Štrbački, J., Ćuk, M., Andrijašević, J., Šišović, J., Papić, P., 2016. Mineral and thermal waters of Serbia: multivariate statistical approach to hydrochemical characterization. In: *Mineral and Thermal Waters of Southeastern Europe*, 81–95. Springer, Cham.

Tubía, J.M., 1994. The Ronda peridotites (Los Reales nappe) - an example of the relationship between lithospheric thickening by oblique tectoniques and late extensional deformation within the Betic Cordillera (Spain). *Tectonophysics*, **238**, 381–398.

Tubía, J.M., Cuevas, J., 1986. High-temperature emplacement of the Los Reales peridotite nappe (Betic Cordillera, Spain). *J. Struct. Geol.*, **8**, 473–482.

Tubía, J.M., Cuevas, J., Esteban, J.J., 2004. Tectonic evidence in the Ronda peridotites, Spain, for mantle diapirism related to delamination. *Geology*, **32**, 941–944.

Tubía, J.M., Cuevas, J., Ibarguchi, J.G., 1997. Sequential development of the metamorphic aureole beneath the Ronda peridotites and its bearing on the tectonic evolution of the Betic Cordillera. *Tectonophysics*, **279**, 227–252.

Tucholke, B.E., Lin, J., Kleinrock, M.C., 1998, Megamullions and mullion structure defining oceanic metamorphic core complexes on the mid-Atlantic ridge, *J. Geophys. Res.*, **103**, 9857–9866.

Ulven, O.I., Beinlich, A., Hövelmann, J., Austrheim, H.,, Jamtveit, B., 2017. Subarctic physicochemical weathering of serpentinized peridotite. *Earth Planet. Sci. Lett.*, **468**, 11–26.

Unluer, C., Al-Tabbaa, A., 2013. Impact of hydrated magnesium carbonate additives on the carbonation of reactive MgO cements. *Cem. and Concr. Res.*, **54**, 87–97.

Uqba, K.A., 1991. The water resources of the United Arab Emirates: a comprehensive empirical appraisal of their status and management. Doctoral dissertation, Durham University.

Urosevic, M., Rodríguez-Navarro, C., Putnis, C.V., Cardell, C., Putnis, A., Ruíz-Agudo, E., 2012. In situ nanoscale observations of the dissolution of {101 4} dolomite cleavage surfaces. *Geochim. Cosmochim. Acta*, **80**, 1–13.

Vadillo, I., Urresti, B., Jiménez, P., Martos, S., Durán, J., Benavente, J., Carrasco, F., Pedrera, A., 2015. Preliminary hydrochemical study of Ronda ultramafic massif (South Spain). In: *European Geosciences Union General Assembly, Conference Abstracts*, **18**, 13275.

Van Tongeren J.A., Kelemen P.B., Hanghoj K., 2008. Cooling rates in the lower crust of the Oman ophiolite: Ca in olivine, revisited. *Earth Planet Sci. Lett.*, **267**, 69–82.

Van der Wal, D., Vissers, R.L., 1993. Uplift and emplacement of upper mantle rocks in the western Mediterranean. *Geology*, **21**, 1119-–1122.

Van der Wal, D., Vissers, R.L., 1996. Structural petrology of the Ronda peridotite, SW Spain: deformation history. *J. Petrol.*, **37**, 23–43.

Van Lith, Y., Warthmann, R., Vasconcelos, C., McKenzie, J.A., 2003. Microbial fossilization in carbonate sediments: a result of the bacterial surface involvement in dolomite precipitation. *Sedimentology*, **50**, 237-245.

Varas-Reus, M.I., Garrido, C.J., Marchesi, C., Bodinier, J.L., Frets, E., Bosch, D., Tommasi, A., Hidas, K., Targuisti, K., 2016. Refertilization processes in the subcontinental lithospheric mantle: the record of the Beni Bousera orogenic Peridotite (Rif Belt, Northern Morocco). *J. Petrol.*, **57**, 2251–2270.

Varas-Reus, M.I., Garrido, C.J., Marchesi, C., Bosch, D., Hidas, K., 2018. Genesis of ultra-high pressure garnet pyroxenites in orogenic peridotites and its bearing on the compositional heterogeneity of the Earth's mantle. *Geochem. Cosmochim. Acta*, **232**, 303–328.

Varne R., Rubenach M.J., 1972. Geology of Macquarie Island and its relationship to oceanic crust. *Ant. Res. Ser.*, **19**, 251–266.

Vasconcelos, C., McKenzie, J.A., Bernasconi, S., Grujic, D., Tiens, A.J., 1995. Microbial mediation as a possible mechanism for natural dolomite formation at low temperatures. *Nature*, **377**, 220.

Vasconcelos, C., McKenzie, J.A., 1997. Microbial mediation of modern dolomite precipitation and diagenesis under anoxic conditions (Lagoa Vermelha, Rio de Janeiro, Brazil). *J. Sediment. Res.*, **67**, 378–390.

Vauchez, A., Garrido, C.J., 2001. Seismic properties of an asthenospherized lithospheric mantle: constraints from lattice preferred orientations in peridotite from the Ronda massif. *Earth Planet. Sci. Lett.*, **192**, 235–249.

Voutsis, N., Kelepertzis, E., Tziritis, E., Kelepertsis, A., 2015. Assessing the hydrogeochemistry of groundwaters in ophiolite areas of Euboea Island, Greece, using multivariate statistical methods. *J. Geochem. Explor.*, **159**, 79–92.

Wang D., Li Z., 2012. Chemical modeling of nesquehonite solubility in Li + Na + K + H4 + Mg + Cl + H_2O System with a speciation-based approach. *Chinese J. Chem. Eng.*, **20**, 2670276.

Wang Y., Li Z., Demopoulos G. P., 2008. Controlled precipitation of nesquehonite ($MgCO_3·3H_2O$) by the reaction of $MgCl_2$ with $(NH_4)_2CO_3$. J. Critical Growth, **310**, 1220–1227.

Warren, J.M., 2016. Global variations in abyssal peridotite compositions. *Lithos*, **248**, 193-219.

Warren, J.M., Shimizu, N., 2010. Cryptic variations in abyssal peridotite compositions: evidence for shallow level melt infiltration in the oceanic lithosphere. *J. Petrol.*, **51**, 395–423.

Warthmann, R., Vasconcelos, C., Sass, H., McKenzie, J.A., 2005. Desulfovibrio brasiliensis sp. nov., a moderate halophilic sulfate-reducing bacterium from Lagoa Vermelha (Brazil) mediating dolomite formation. *Extremophiles,* **9**, 255–261.

Weyhenmeyer CE (2000) Origin and evolution of groundwater in the alluvial aquifer of the eastern Batinah coastal plain, Sultanate of Oman: A hydrogeochemical approach. Ph.D. Thesis, Universität Bern, Bern, Switzerland.

White, R.S., McKenzie, D.P., O'Nions, R.K., 1992. Oceanic crustal thickness from seismic measurements and rare earth element inversions. *J. Geophys. Res.*, **97**, 19683–19715.

White, C.E., Henson, N.J., Daemen, L.L., Hartl, M., Page, K., 2014. Uncovering the true atomic structure of disordered materials: The structure of a hydrated amorphous magnesium carbonate ($MgCO_3 \cdot 3D_2O$). *Chem. Mater.,* **26**, 2693–2702.

Wilson, S.A., Dipple, G.M., Power, I.M., Thom, J.M., Anderson, R.G., Raudsepp, M., Gabites, J.E., Southam, G., 2009. Carbon dioxide fixation within mine wastes of ultramafic-hosted ore deposits: examples from the Clinton Creek and Cassiar chrysotile deposits, Canada. *Econ. Geol.,* **104**, 95–112.

Wilson S. A., Barker S. L. L., Dipple G. M., Atudorei V., 2010. Isotopic disequilibrium during uptake of atmospheric CO_2 into mine process waters: Implications for CO_2 sequestration. *Environ. Sci. Technol.*, **44**, 9522–9529.

Xiong Y., 2011. Experimental determination of solubility constant of hydromagnesite (5424) in NaCl solutions up to 4.4 m at room temperature. *Chem. Geol.,* **284**, 262–269.

Xiong Y., Lord A. S., 2008. Experimental investigations of the reaction path in the $MgO–CO_2–H_2O$ system in solutions with various ionic strengths, and their applications. *Appl. Geochemistry*, **23**, 6, 1634–1659.

Xu, J., Yan, C., Zhang, F., Konishi, H., Xu, H., Teng, H.H., 2013. Testing the cation-hydration effect on the crystallization of $Ca–Mg–CO_3$ systems. *Proc. Nat. Acad. Sc.*, **110**, 17750–17755.

Yang, J., 2018. Amorphous magnesium carbonate nanomaterials: Synthesis, characterization and applications. Ph.D. Thesis, dissertation. Uppsala University. Dissertations from the Faculty of Science and Technology 1685. 82 pp. Uppsala: Acta Universitatis Upsaliensis.

Yuce, G., Italiano, F., D'Alessandro, W., Yalcin, T.H., Yasin, D.U., Gulbay, A.H., Ozyurt, N.N., Rojay, B., Karabacak, V., Bellomo, S., Brusca, L., Yang, T., Fu, C.C., Lai, C.W., Ozacar, A., Walia, V., 2014. Origin and interactions of fluids circulating over the Amik Basin (Hatay, Turkey) and relationships with the hydrologic, geologic and tectonic settings. *Chem. Geol.*, **388**, 23–39.

Zeller, E.J., Wray, J.L., 1956. Factors influencing precipitation of calcium carbonate. *AAPG (Am. Assoc. Pet. Geol.) Bull.,* **40**, 140–152.

Zhao L., Sang L., Chen J., Ji J., Teng H. H., 2010. Aqueous carbonation of natural brucite: Relevance to CO_2 sequestration. *Environ. Sci. Technol.*, **44**, 406–411.

Zhao L., Zhu C., Ji J., Chen J., Teng H. H., 2013. Thermodynamic and kinetic effect of organic solvent on the nucleation of nesquehonite. *Geochem. Cosmochim. Acta,* **106**, 192–202.

Zhang, F., Xu, H., Konishi, H., Kemp, J.M., Roden, E.E., Shen, Z., 2012. Dissolved sulfide-catalyzed precipitation of disordered dolomite: implications for the formation mechanism of sedimentary dolomite. *Geochem. Cosmochim. Acta*, **97**, 148–165.

Zhang, R., Zhang, X., Guy, B., Hu, S., De Ligny, D., Moutte, J., 2013. Experimental study of dissolution rates of hedenbergitic clinopyroxene at high temperatures: dissolution in water from 25 ºC to 374 ºC. *Eur. J. Mineralogy,* **25**, 3, 353–372.

Zhang, Z., Zheng, Y., Ni, Y., Liu, Z., Chen, J., Liang, X., 2006. Temperature and pH-dependent morphology and FT–IR analysis of magnesium carbonate hydrates. *J. Phys. Chem.*, **110**, 12969–12973.

Zhou, G.T., Yao, Q.Z., Ni, J., Jin, G., 2009. Formation of aragonite mesocrystals and implication for biomineralization. *Am. Mineral.,* **94**, 293–302.

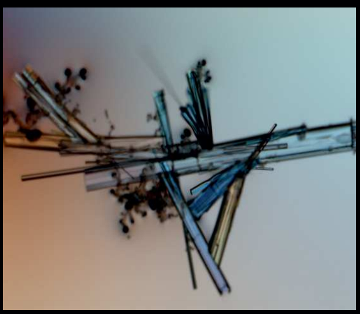

In continental settings, the interaction between meteoric water and ultramafic rocks generates waters of variable physicochemical characteristics due to serpentinization and weathering. The discharge of these waters forms aerial alkaline to hyperalkaline spring systems where waters mix, undergo evaporation, and take up atmospheric CO_2 leading to the precipitation of carbonate minerals. The understanding of natural carbonation in these serpentinite-hosted alkaline environmentsis critical, among others, for assessing the role of this process in the global carbon cycle throughout the Earth's history, and the viability of CO_2 sequestration techniques for permanent carbon storage.

The main objective of the present Ph.D. thesis is to advance in our understanding of serpentinization-related alkaline spring systems and the precipitation of calcium carbonate minerals in these alkaline environments. To attain this goal, this thesis investigates the factors controlling carbon mineralization in two natural case studies of active alkaline spring systems hosted in serpentinized peridotites in oceanic (Samail Ophiolite, Oman) and subcontinental mantle (Ronda peridotites, Spain) tectonically emplaced in continental orogens. The detailed study of the chemical composition of alkaline waters, along with the mineralogy and textures of precipitates, allows to unveil the geochemical and mineralogical characteristics of these alkaline springs and evaluate how the interaction of hyperalkaline fluids with meteoric waters and the atmosphere affects carbonate precipitation. Furthermore, the thesis presents new results of crystallization experiments aimed at constraining the nucleation, crystal growth, and transformation conditions and the mechanisms of formation of hydrated Mg-carbonates in alkaline environments. By combining the study of active alkaline spring systems and experimental work, the present Ph.D. thesis contributes to filling gaps in our current knowledge on the mechanisms and conditions of carbonate precipitation in alkaline environments.

Laboratorio
de Estudios
Cristalográficos

IACT
INSTITUTO ANDALUZ DE CIENCIAS DE LA TIERRA

PROMETHEUS

erc

Research Group on
Petrology, Geochemisty and Geochronology
Thesis Memoir n° 10

MARIE CURIE ACTIONS

itn Abyss

CSIC
CONSEJO SUPERIOR DE INVESTIGACIONES CIENTÍFICAS

UNIVERSIDAD
DE GRANADA